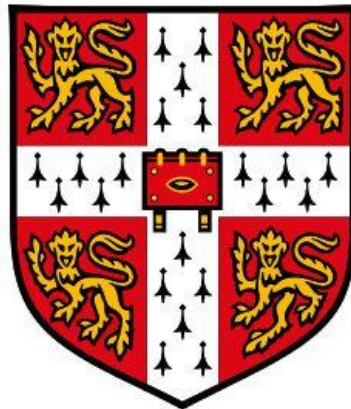


Stabilisation of metal nanoparticles by confinement on curved supports



Tamsin Elizabeth Bell

Clare College, Cambridge, UK

Department of Chemical Engineering and Biotechnology

University of Cambridge

This dissertation is submitted for the degree of Doctor of Philosophy

May 2018

Preface declaration

This dissertation is the result of my own work and includes nothing which is the outcome of work done in collaboration except as declared in the Preface and specified in the text.

It is not substantially the same as any that I have submitted, or, is being concurrently submitted for a degree or diploma or other qualification at the University of Cambridge or any other University or similar institution except as declared in the Preface and specified in the text. I further state that no substantial part of my dissertation has already been submitted, or, is being concurrently submitted for any such degree, diploma or other qualification at the University of Cambridge or any other University or similar institution except as declared in the Preface and specified in the text. It does not exceed the prescribed word limit (65,000) for the Engineering Degree Committee.

Contents

Preface declaration.....	i
List of figures.....	vii
List of tables.....	xiii
Nomenclature.....	xvi
Abbreviations and acronyms.....	xvi
Chemical formulae.....	xvii
Acknowledgements.....	xviii
Abstract.....	xix
Dissemination of research.....	xx
Publications.....	xx
Oral presentations.....	xx
Poster presentations.....	xxi
Chapter 1 – Introduction.....	1
1.1 Novel metal nanoparticle stabilisation hypothesis.....	2
1.2 Aims and objectives.....	4
1.3 Impact.....	4
1.4 Thesis structure.....	5
Chapter 2 – Literature review.....	7
2.1 Metal nanoparticles.....	8
2.1.1 Methods for synthesis of metal nanoparticles.....	9
2.1.2 Strategies for metal nanoparticle stabilisation.....	10
2.2 Al ₂ O ₃ as a catalyst support.....	12
2.2.1 Synthesis of nanostructured Al ₂ O ₃	12
2.2.1.1 Hydrothermal synthesis of nanostructured Al ₂ O ₃	14
2.3 Catalytic applications of Co/ γ -Al ₂ O ₃	17

2.3.1	Ammonia decomposition.....	18
2.3.2	Fischer-Tropsch synthesis	23
2.4	Au/ γ -Al ₂ O ₃ catalysts for CO oxidation.....	29
2.5	Literature review conclusions	33
Chapter 3 - Experimental methodology		35
3.1	Hydrothermal synthesis of nanostructured γ -Al ₂ O ₃	35
3.2	Synthesis of supported nanoparticles.....	36
3.2.1	Incipient wetness impregnation (IWI).....	36
3.2.2	Wet impregnation (imp)	37
3.2.3	Adsorption/ion exchange (ads).....	37
3.2.4	Precipitation.....	38
3.2.5	Methods summary	39
3.2.6	Processing conditions	40
3.2.7	Summary of catalysts.....	40
3.3	Materials characterisation	43
3.3.1	N ₂ sorption.....	43
3.3.2	Electron microscopy	43
3.3.3	Powder X-ray diffraction.....	44
3.3.4	Temperature programmed reduction	46
3.3.5	CO pulse chemisorption	46
3.3.6	²⁷ Al nuclear magnetic resonance (NMR)	49
3.3.7	Thermogravimetric analysis	49
3.3.8	Inductively coupled plasma optical emission spectroscopy	49
3.3.9	X-ray photoelectron spectroscopy	50
3.4	CO oxidation catalytic rig design and construction.....	50
3.4.1	Rig safety.....	54
3.4.2	Calibrations: Furnace, mass flow controller and gas analyser	55

3.4.3	Data reproducibility	56
3.4.4	Operation of the CO oxidation rig	57
3.4.5	Catalytic data processing	58
3.4.6	Pressure drop	58
3.5	Catalyst testing for NH ₃ decomposition	59
3.6	Catalyst testing for Fischer-Tropsch synthesis	63
Chapter 4 – Hydrothermal synthesis of nanostructured γ -Al ₂ O ₃		65
4.1	Mechanism of the hydrothermal synthesis of nanostructured γ -Al ₂ O ₃	66
4.1.1	Effect of NaOH:Al on product yield and overall mechanism	66
4.1.2	Detailed mechanism of AlOOH formation.....	67
4.2	Effect of NaOH:Al ratio on synthesis pH and γ -Al ₂ O ₃ morphology	72
4.2.1	Characterisation of γ -Al ₂ O ₃ nanorods and nanoplates.....	74
4.3	Understanding the nanorod formation mechanism to achieve curvature control	76
4.3.1	Mechanism of formation of 1D AlOOH nanorods	76
4.3.2	Nanorod size control.....	79
4.3.3	Nanorod formation mechanism overview	82
4.4	γ -Al ₂ O ₃ nanorod yield maximisation with morphological control	84
4.5	Materials used as catalyst supports	90
Chapter 4 conclusions		95
Chapter 5 – Effect of cobalt loading methods on Co/ γ -Al ₂ O ₃ properties and catalytic activity		97
5.1	Effect of synthesis methods on Co/ γ -Al ₂ O ₃ properties	98
5.1.1	Characterisation of calcined <i>Co/plate</i> catalysts.....	100
5.1.2	Characterisation of reduced catalysts	106
5.1.3	Discussion of chemical composition of catalysts	109
5.1.4	Discussion of cobalt reducibility	112
5.1.5	Discussion of particle size	115
5.2	NH ₃ decomposition catalytic activity	117

5.2.1	Effect of calcination on NH ₃ decomposition activity	117
5.2.2	Effect of reduction temperature on NH ₃ decomposition activity	122
5.2.3	Effect of synthesis method on NH ₃ decomposition activity	125
Chapter 5 conclusions		128
Chapter 6 – Effect of support morphology on Co/γ-Al ₂ O ₃ catalytic activity and stability		131
6.1	NH ₃ decomposition	132
6.1.1	Catalysts synthesised by NaOH precipitation	132
6.1.1.1	Characterisation of fresh <i>Co/γ-Al₂O₃-NaOH</i> catalysts	132
6.1.1.2	Characterisation of reduced <i>Co/γ-Al₂O₃-NaOH</i> catalysts	137
6.1.1.3	Catalytic activity of <i>Co/γ-Al₂O₃-NaOH-red580</i> catalysts	138
6.1.2	Catalysts synthesised by incipient wetness impregnation	143
6.1.2.1	Characterisation of calcined <i>Co/γ-Al₂O₃-IWI-cal250</i> catalysts	143
6.1.2.2	Characterisation of reduced <i>Co/γ-Al₂O₃-IWI-cal250</i> catalysts	148
6.1.2.3	Catalytic activity of <i>Co/γ-Al₂O₃-IWI-cal250-red580</i> catalysts	154
6.1.3	Discussion of the effect of synthesis method on catalytic activity of Co/γ-Al ₂ O ₃	157
6.1.4	Thermal stability of Co/γ-Al ₂ O ₃ catalysts	162
6.2	Fisher-Tropsch synthesis	165
6.2.1	Effect of sodium on FTS activity of <i>Co/γ-Al₂O₃-IWI-cal250</i>	165
6.2.2	Activity and selectivity of <i>Co/γ-Al₂O₃-IWI-cal250</i> catalysts	166
6.2.3	Discussion of the effect of loading and support morphology on FTS activity, selectivity and stability	170
Chapter 6 conclusions		172
Chapter 7 – Effect of support morphology on Au/γ-Al ₂ O ₃ catalytic activity and stability		175
7.1	Optimisation of Au/γ-Al ₂ O ₃ synthesis procedure	175
7.2	Effect of support morphology on Au/γ-Al ₂ O ₃ catalysts synthesised by IWI and adsorption	179

7.2.1	Characterisation of <i>Au/γ-Al₂O₃-IWI</i> catalysts	179
7.2.2	Catalytic testing of <i>Au/γ-Al₂O₃-IWI</i> catalysts	182
7.2.3	Characterisation of <i>Au/γ-Al₂O₃-adsorption</i> catalysts.....	183
7.2.4	Catalytic testing of <i>Au/γ-Al₂O₃-adsorption</i> catalysts.....	187
7.2.5	Discussion of the effect of loading, support morphology and synthesis method on CO oxidation catalytic activity	189
7.2.5.1	Effect of support morphology of <i>Au/γ-Al₂O₃-IWI</i> catalysts	189
7.2.5.2	Effect of gold loading and support morphology of <i>Au/γ-Al₂O₃-ads-wash</i> catalysts.....	191
7.2.5.3	Effect of gold synthesis method and support morphology.....	194
7.3	Thermal stability of <i>Au/γ-Al₂O₃</i> catalysts	197
	Chapter 7 conclusions	199
	Chapter 8 – Conclusions and future work.....	201
8.1	Hypothesis of metal nanoparticle stabilisation by confinement using curved supports	201
8.2	Hydrothermal synthesis of nanostructured <i>γ-Al₂O₃</i>	203
8.3	Effect of cobalt loading methods on <i>Co/γ-Al₂O₃</i> properties and catalytic activity	204
8.4	Effect of support morphology on <i>Co/γ-Al₂O₃</i> catalytic activity and stability.....	204
8.5	Effect of support morphology on <i>Au/γ-Al₂O₃</i> catalytic activity and stability	206
	Appendix.....	207
	References.....	213

List of figures

Figure 1. Melting temperature with respect to particle diameter for different metals.	2
Figure 2. Agglomeration of metal nanoparticles (MNPs) on conventional flat supports (a) compared to the novel stabilisation hypothesis of using curved supports (b).	3
Figure 3. Change in electronic structure and band gap with respect to metal diameter.	8
Figure 4. Methods for nanoparticle stabilisation a) electrostatic stabilisation b) steric stabilisation c) encapsulation and d) immobilisation on a solid support.	11
Figure 5. Reported electron micrographs of nanostructured Al ₂ O ₃ a) 1D nanorods, b) 2D nanoplates and c) 3D hierarchical flowers.	13
Figure 6. Stepwise mechanism of NH ₃ decomposition on the (111) Co fcc surface.	19
Figure 7. NH ₃ decomposition activity with respect to nitrogen binding energy (Q _N).	19
Figure 8. Size-activity dependency for reported cobalt-based NH ₃ decomposition catalysts.	21
Figure 9. Relationship between C ₅₊ selectivity and Co crystallite size.	25
Figure 10. Deactivation by re-oxidation, aluminate formation and sintering in FTS Co/Al ₂ O ₃ catalysts.	26
Figure 11. TCD signal during pulse chemisorption of γ -Al ₂ O ₃ <i>plate</i> support.	48
Figure 12. TCD signal during pulse chemisorption of <i>0.5Au/10hrod-IE-WRT</i>	48
Figure 13. Annotated photograph of the CO oxidation catalytic testing rig.	51
Figure 14. P&ID schematic of the CO oxidation catalytic rig.	53
Figure 15. Response of gas analyser upon introduction of CO into the gas stream.	54
Figure 16. Temperature calibration curve for the furnace.	55
Figure 17. CO oxidation activity of <i>0.5Au/10hrod-IE-wash-red200</i> repeated three times.	56
Figure 18. CO conversion data of <i>0.1Au/plate-ads-wash-red200</i> analysed by continuous logging (black line) and by averaging the values from holding at three set point (red cross).	58
Figure 19. P&ID of the NH ₃ decomposition catalytic rig.	60
Figure 20. Polynomial relationship between NH ₃ conversion and outlet H ₂ composition.	61
Figure 21. NH ₃ decomposition activity for a reactor filled with SiC only (○) and SiC mixed with γ -Al ₂ O ₃ <i>plate</i> support (x).	62
Figure 22. Yield of γ -Al ₂ O ₃ product as a function of NaOH:Al reagent ratio.	67
Figure 23. ²⁷ Al NMR spectra for Al solutions.	68
Figure 24. Transformation of planar gibbsite fragments to AlOOH building blocks by thermolysis above 170 °C.	70

Figure 25. TEM micrographs of γ -AlOOH (i) and γ -Al ₂ O ₃ (ii) after 20 hours hydrothermal synthesis at 200 °C.	72
Figure 26. TGA of γ -AlOOH nanorods (grey) and nanoplates (black) synthesised at 200 °C for 20 hours with different NaOH:Al reagent ratios.....	73
Figure 27. pXRD pattern of unwashed γ -Al ₂ O ₃ calcined at 500 °C after 20 hours hydrothermal synthesis at 200 °C with different initial NaOH:Al reagent ratios.....	75
Figure 28. N ₂ adsorption-desorption isotherms of γ -Al ₂ O ₃ from 20 hours hydrothermal synthesis at 200 °C with different NaOH:Al reagent ratios.....	75
Figure 29. TEM micrographs of γ -Al ₂ O ₃ samples obtained from hydrothermal treatment for 20 hours with NaOH:Al 0.77:1.....	77
Figure 30. SEM micrographs of γ -Al ₂ O ₃ nanorods synthesised with 0.77:1 NaOH:Al ratio for 20 hours.....	78
Figure 31. High resolution TEM micrographs of nanorods synthesised with 0.77:1 NaOH:Al molar ratio at 200 °C for 20 hours.	78
Figure 32. TEM micrographs of γ -Al ₂ O ₃ calcined at 500 °C synthesised with 0.77:1 NaOH:Al ratio.	79
Figure 33. Average sizes of <i>short/thick NR</i> γ -Al ₂ O ₃ produced by hydrothermal synthesis for different durations at 180 °C (grey) and 200 °C (black).	82
Figure 34. Summary of the six step mechanism determined for γ -Al ₂ O ₃ nanorod formation by hydrothermal synthesis under acidic conditions.	83
Figure 35. Hydrothermal synthesis of morphologically pure γ -Al ₂ O ₃ nanorods by a) conventional batch process and b) semi-continuous recycle procedure.	85
Figure 36. pXRD patterns of γ -Al ₂ O ₃ synthesised at 200 °C with 0.77NaOH:1Al for 20 hours, calcined at 500 °C.	86
Figure 37. TEM micrographs and distributions of γ -Al ₂ O ₃ synthesised for 20 hours at 200 °C with 0.77NaOH:1Al.....	87
Figure 38. pXRD of unwashed γ -Al ₂ O ₃ synthesised with 0.77NaOH:1Al at 200°C for 20 hours.	87
Figure 39. pXRD of γ -Al ₂ O ₃ synthesised with 0.77NaOH:1Al at 200°C for 20 hours.....	88
Figure 40. Composition of γ -Al ₂ O ₃ supports determined by different methods.....	91
Figure 41. pXRD of washed support materials obtained by hydrothermal synthesis.....	92
Figure 42. Electron microscopy of γ -Al ₂ O ₃	92
Figure 43. N ₂ adsorption-desorption isotherms of γ -Al ₂ O ₃	93
Figure 44. Pore size distributions of γ -Al ₂ O ₃	93

Figure 45. TGA under N ₂ of washed γ -Al ₂ O ₃ supports after calcination at 500 °C.....	94
Figure 46. The feasibility of Co ²⁺ adsorption in aqueous solution onto Al ₂ O ₃ surface at different pH conditions.....	99
Figure 47. TPR profiles for <i>Co/plate-cal250</i> catalysts synthesised by different methods. ...	101
Figure 48. pXRD spectra of fresh <i>Co/plate-cal250</i> samples synthesised by different methods.	103
Figure 49. Representative TEM micrographs and particle size distributions of <i>Co/plate-cal250</i> catalysts.....	104
Figure 50. Co 2p XPS spectra for <i>Co/plate-cal250</i> catalysts synthesised by different methods	105
Figure 51. pXRD patterns of <i>Co/plate-cal250</i> catalysts reduced at 580 °C synthesised by different methods.	106
Figure 52. Representative bright (LHS) and dark (centre) field SEM micrographs with associated Co ⁰ particle size distribution (RHS) of <i>7.6Co/plate-carb-cal250-red580</i>	107
Figure 53. Co 2p XPS spectra for <i>Co/plate-cal250</i> catalysts reduced <i>in situ</i> at 580 °C synthesised by different methods.....	108
Figure 54. Proportion of Co ⁰ in <i>Co/plate-cal250</i> catalysts synthesised by different methods after reduction at 580 °C calculated from XPS spectra of the reduced samples (black bar) and from the TPR profiles (white bar).....	114
Figure 55. NH ₃ decomposition catalytic data (pre-reduced <i>in situ</i> at 580 °C under H ₂) for <i>Co/plate</i> catalysts synthesised by IWI (●) and NaOH precipitation (X) calcined at 250 °C (black) and uncalcined (grey).	118
Figure 56. Deconvoluted TPR profile of <i>Co/plate</i> catalysts synthesised by a) IWI and b) NaOH precipitation methods with different calcination pre-treatments.	120
Figure 57. pXRD pattern of <i>Co/plate</i> catalysts reduced at 580 °C under H ₂ synthesised by IWI (b) and NaOH precipitation (c) methods with different calcination pre-treatments.....	121
Figure 58. NH ₃ decomposition TOF at 500 °C (i) and E _a (ii) for <i>Co/plate</i> catalysts reduced under H ₂ at different temperatures synthesised by a) IWI and b) NaOH precipitation.	122
Figure 59. NH ₃ decomposition catalytic data for the calcined <i>Co/plate-cal250</i> catalysts synthesised by different methods.....	125
Figure 60. pXRD patterns of <i>Co/γ-Al₂O₃-NaOH</i> catalysts synthesised by NaOH precipitation with different loadings on γ -Al ₂ O ₃ supports with different morphologies.	134

Figure 61. Deconvoluted TPR profiles of <i>Co/γ-Al₂O₃-NaOH</i> catalysts with different loadings on γ -Al ₂ O ₃ supports with different morphologies.....	135
Figure 62. pXRD of <i>Co/γ-Al₂O₃-NaOH</i> catalysts reduced <i>ex situ</i> (580 °C) synthesised by NaOH precipitation with different loadings on γ -Al ₂ O ₃ supports with different morphologies.	138
Figure 63. NH ₃ decomposition activity of <i>Co/γ-Al₂O₃-NaOH</i> catalysts with different target cobalt loadings on different γ -Al ₂ O ₃ supports.....	139
Figure 64. pXRD patterns of calcined <i>Co/γ-Al₂O₃-IWI-cal250</i> catalysts (unreduced) with different loadings on γ -Al ₂ O ₃ supports with different morphologies.	145
Figure 65. Co 2p XPS spectra for calcined <i>Co/γ-Al₂O₃-IWI-cal250</i> catalysts (unreduced) with different loadings on γ -Al ₂ O ₃ supports with different morphologies.	145
Figure 66. Deconvoluted TPR profiles of calcined <i>Co/γ-Al₂O₃-IWI-cal250</i> catalysts with different loadings on γ -Al ₂ O ₃ with different morphologies.	146
Figure 67. Co 2p XPS spectra for <i>Co/γ-Al₂O₃-IWI-cal250</i> catalysts synthesised by IWI reduced <i>in situ</i> at 580 °C on γ -Al ₂ O ₃ supports with different morphologies.	148
Figure 68. Proportion of Co ⁰ from XPS of <i>Co/γ-Al₂O₃-IWI-cal250</i> supported on γ -Al ₂ O ₃ with different morphologies.....	149
Figure 69. pXRD of <i>Co/γ-Al₂O₃-IWI-cal250</i> catalysts (4.8 wt% and 9.1 wt%) reduced <i>in situ</i> from room temperature to 600 °C.	149
Figure 70. pXRD <i>Co/γ-Al₂O₃-IWI-cal250</i> reduced <i>ex situ</i> (580 °C under H ₂) with different loadings on γ -Al ₂ O ₃ supports with different morphologies.	150
Figure 71. Average particle size for different cobalt species calculated from pXRD with sequential <i>in situ</i> reduction up to 600 °C for <i>Co/γ-Al₂O₃-IWI</i> catalysts.....	152
Figure 72. Bright field TEM (i) and HAADF-STEM (ii) micrographs of <i>Co/γ-Al₂O₃-IWI-red580</i>	153
Figure 73. NH ₃ decomposition activity of <i>Co/γ-Al₂O₃-IWI-cal250</i> catalysts.....	155
Figure 74. Apparent NH ₃ rate of reaction (TOF) at 500 °C with respect to Co loading for <i>Co/γ-Al₂O₃</i> catalysts synthesised by a) NaOH precipitation (x) and b) IWI (●).....	158
Figure 75. NH ₃ decomposition activity of <i>Co/γ-Al₂O₃-NaOH</i> catalysts tested herein compared to the literature.	159
Figure 76. Stabilisation by nanorods related to their diameter (R) and the size of the nanoparticle (P).....	161
Figure 77. FTS activity of <i>Co/γ-Al₂O₃-IWI-cal250</i>	165

Figure 78. FTS activity and selectivity of 4.9Co/40hfat-IWI-cal250-red425 (green) and 4.2Co/10hthin-IWI-cal250-red425 (blue).....	166
Figure 79. FTS activity and selectivity of 9.2Co/40hfat-IWI-cal250-red425 (green) and 9.7Co/10hthin-IWI-cal250-red425 (blue).....	168
Figure 80. TEM micrographs of Co/ γ -Al ₂ O ₃ -IWI catalysts after i) reduction <i>ex situ</i> at 425 °C and ii) FTS testing.....	169
Figure 81. TPR profiles of a) γ -Al ₂ O ₃ plate support, b) 1.42Au/plate-IWI, c) 0.69Au/plate-IWI-wash and d) 0.69Au/plate-IWI-wash-cal250.....	177
Figure 82. CO oxidation catalytic activity of Au/ γ -Al ₂ O ₃ -IWI-wash.....	178
Figure 83. TPR profile of Au/ γ -Al ₂ O ₃ -IWI-wash catalysts.....	180
Figure 84. Representative HAADF-STEM micrographs and Au particle size distributions for a) 0.7Au/plate-IWI-wash-red200 and b) 0.3Au/10hthin-IWI-wash-red200.....	181
Figure 85. CO oxidation activity for Au/ γ -Al ₂ O ₃ -IWI catalysts a) conversion-temperature and b) Arrhenius plot.....	182
Figure 86. TPR profile of washed Au/ γ -Al ₂ O ₃ -ads-wash catalysts prepared by adsorption with different loadings.....	185
Figure 87. Representative HAADF-STEM micrographs and gold particle size distributions for a) 1.0Au/plate-ads-wash-red200 and b) 0.5Au/10hthin-ads-wash-red200.....	186
Figure 88. CO oxidation catalytic activity for Au/ γ -Al ₂ O ₃ -ads-wash catalysts pre-reduced at 200 °C under H ₂ flow.....	188
Figure 89. TOF at 450 °C with respect to average gold size calculated by pulse CO chemisorption for Au/ γ -Al ₂ O ₃	195
Figure 90. CO oxidation thermal stability test for Au/ γ -Al ₂ O ₃ -wash catalysts.....	197
Figure 91. Metal nanoparticle stabilisation by confinement on curved supports.....	202
Figure A92. pXRD pattern for γ -Al ₂ O ₃ rods synthesised with 0.77NaOH:1Al, 20 hours and different temperature.....	207
Figure A93. Pore size distributions of γ -Al ₂ O ₃ synthesised with 0.77NaOH:1Al for 20 hours 170 °C (pale blue), 180 °C (red) and 200 °C (purple).....	207
Figure A94. pXRD pattern for γ -Al ₂ O ₃ rods synthesised with 0.77NaOH:1Al and different synthesis conditions.....	208
Figure A95. Length and diameter size distributions obtained from analysis of TEM micrographs of γ -Al ₂ O ₃ rods.....	208

Figure A96. N ₂ adsorption-desorption isotherms at -196 °C of γ -Al ₂ O ₃ synthesised with 0.77 NaOH:Al molar ratio.	209
Figure A97. Pore size distributions of γ -Al ₂ O ₃ synthesised with 0.77NaOH:1Al at a) 180 °C and b) 200 °C.	209
Figure A98. TPR (LHS) and MS (RHS) data for <i>6.8Co/plate-NaOH-cal250</i>	210
Figure A99. EELS mapping of <i>7.7Co/plate-IWI-cal250</i>	210
Figure A100. pXRD of <i>plate</i> γ -Al ₂ O ₃ support (grey) and <i>9.1Co/plate-NaOH-cal500</i> calcined at 500 °C (black).	211
Figure A101. TPR profile of unsupported CoOOH (<i>42.6Co-unsupported</i>).	211
Figure A102. Bright field TEM micrographs of fresh <i>16.6Co/180thin-NaOH</i> showing a large hexagonal structure	211

List of tables

Table 1. Summary of hydrothermal syntheses of γ -AlOOH and γ -Al ₂ O ₃ without a SDA.	15
Table 2. Properties and NH ₃ decomposition activity of reported cobalt catalysts.....	20
Table 3. Reported synthesis conditions, properties and FTS performance of some Co/Al ₂ O ₃ catalysts.....	27
Table 4. Reported properties, pre-treatment conditions and T ₅₀ CO oxidation catalytic activity of Au/Al ₂ O ₃ catalysts synthesised by different methods.	31
Table 5. Range of parameters varied during the hydrothermal synthesis of γ -Al ₂ O ₃	36
Table 6. Pore volume with H ₂ O solvent for different γ -Al ₂ O ₃ materials.	37
Table 7. Amount of precipitant used for precipitation of unsupported cobalt.....	38
Table 8. Amount of precipitant used for the synthesis of supported cobalt nanoparticles.	39
Table 9. Summary of methods for supported metal nanoparticle synthesis.	39
Table 10. Calcination conditions used for different catalyst samples.	40
Table 11. Summary of cobalt-based catalysts discussed in Chapters 5 and 6.	41
Table 12. Summary of gold-based catalysts discussed in Chapter 7.	42
Table 13. Approximate dominant peak angles and corresponding JCPDS card numbers for relevant compounds.	45
Table 14. Parameters used for cobalt and gold CO pulse chemisorption.	47
Table 15. Estimated dispersion and particle size of <i>0.5Au/10hRod-IE-WRT</i> from pulse CO chemisorption at different cryogenic conditions.....	49
Table 16. CO conversion at different temperature for three separate catalytic trials of <i>0.5Au/10hrod-IE-wash-red200</i>	56
Table 17. Yield of γ -Al ₂ O ₃ after hydrothermal treatment for 20 hours with 0.77NaOH:1Al molar ratio at different synthesis temperatures.	70
Table 18. The properties of γ -Al ₂ O ₃ obtained from hydrothermal synthesis at 200 °C for 20 hours.....	74
Table 19. Properties of γ -Al ₂ O ₃ synthesised at 170, 180 and 200 °C for 20 hours with 0.77:1 NaOH:Al ratio.....	77
Table 20. Properties of γ -Al ₂ O ₃ nanorods hydrothermally synthesised with 0.77:1 NaOH:Al molar ratio at 180 °C and 200 °C for 10 to 80 hours.....	80
Table 21. Physical properties of γ -Al ₂ O ₃ produced from recycle syntheses at 200 °C for 20 hours with constant NaOH:Al ratio of 0.77:1 and initial pH values of 3.2 – 3.5.	86

Table 22. Properties of γ -Al ₂ O ₃ materials calcined at 500 °C produced at 200 °C for 20 hours with 0.77:1 NaOH:Al ratio with 5, 10 and 20 equivalent mol of NaNO ₃ including reference <i>Batch</i> sample for comparison.....	89
Table 23. Details of the γ -Al ₂ O ₃ materials selected for use as catalyst supports.....	90
Table 24. Synthesis parameters and properties of calcined <i>Co/plate-cal250</i> catalysts synthesised by different methods.....	100
Table 25. TPR peak temperatures of <i>Co/plate-cal250</i> assigned to different reductive chemical processes.	102
Table 26. ICP results for <i>Co/plate-cal250</i> catalyst synthesised by different methods with 0.848 mmol of Co(NO ₃) ₂ ·6H ₂ O (0.2469 g).....	109
Table 27. Average cobalt particle size of calcined <i>Co/plate-cal250</i> catalysts synthesised by different methods.	116
Table 28. Catalytic activity and particle size of <i>Co/plate</i> catalysts produced by IWI and NaOH precipitation either fresh (uncalcined) or calcined at 250 °C.....	119
Table 29. Third run NH ₃ decomposition activation energy (E _a) and turnover frequency (TOF) of <i>Co/plate</i> catalysts prepared by IWI and NaOH precipitation with different <i>in situ</i> reduction procedures.	123
Table 30. Catalytic data and actual loading of <i>Co/plate-cal250</i> catalysts synthesised by different methods.	126
Table 31. Content and colour of fresh <i>Co/γ-Al₂O₃-NaOH</i> catalysts (unreduced) with different loadings on γ -Al ₂ O ₃ supports with different morphologies.	133
Table 32. TPR peak temperatures of <i>Co/γ-Al₂O₃-NaOH</i> catalysts assigned to different chemical processes.	136
Table 33. NH ₃ decomposition data and Co ⁰ size of <i>Co/γ-Al₂O₃-NaOH</i> catalysts with different loadings supported on γ -Al ₂ O ₃ with distinct morphologies.	140
Table 34. Content and colour of <i>Co/γ-Al₂O₃-IWI-cal250</i> catalysts synthesised by IWI with different loadings on γ -Al ₂ O ₃ supports with different morphologies.	144
Table 35. TPR peak temperatures of <i>Co/γ-Al₂O₃-IWI-cal250</i> catalysts assigned to different chemical processes.....	147
Table 36. Average Co ⁰ particle size for <i>Co/γ-Al₂O₃-IWI-cal250</i> catalysts with different loadings on γ -Al ₂ O ₃ supports with different morphologies.....	151
Table 37. NH ₃ decomposition catalytic data of <i>Co/γ-Al₂O₃-IWI-cal250</i> catalysts with different loadings supported on γ -Al ₂ O ₃ with different morphologies (<i>plate</i> , <i>40hfat</i> and <i>10hthin</i>) reduced <i>in situ</i> at 580 °C.....	156

Table 38. Change in NH ₃ decomposition activity and Co ⁰ crystallite size of <i>Co/γ-Al₂O₃</i> after exposure to 750 °C.	163
Table 39. Properties and third run CO oxidation catalytic data for <i>Au/γ-Al₂O₃-IWI</i> catalysts synthesised by IWI with different treatment conditions.	176
Table 40. Physical properties of washed <i>Au/γ-Al₂O₃-IWI-wash</i>	180
Table 41. CO oxidation catalytic data for <i>Au/γ-Al₂O₃-IWI-wash</i> catalysts supported on γ-Al ₂ O ₃ with different morphologies.	183
Table 42. Physical properties of <i>Au/γ-Al₂O₃-ads-wash</i> catalysts synthesised by adsorption with different support morphologies and loadings.	184
Table 43. Third run CO oxidation catalytic data for different loadings of <i>Au/γ-Al₂O₃-ads-wash</i> catalysts supported on different γ-Al ₂ O ₃ morphologies.	189

Nomenclature

Abbreviations and acronyms

BET	Brunauer–Emmett–Teller
BJH	Barrett-Joyner-Halenda
DP	Deposition-precipitation
E _a	Activation energy
EELS	Electron energy loss spectroscopy
FTS	Fisher-Tropsch synthesis
fcc	Face-centred cubic
FWHM	Full width at half maximum
GHSV	Gas hourly space velocity
HAADF-STEM	High angle annular dark field scanning transmission electron microscopy
hcp	Hexagonal close-packed
IWI	Incipient wetness impregnation
ICP-OES	Inductively coupled plasma optical emission spectroscopy
ID	Internal diameter
JCPDS	Joint Committee on Powder Diffraction Standards
MFC	Mass flow controllers
MS	Mass spectrometry
MNP	Metal nanoparticle
MWCNT	Multi-walled carbon nanotube
NP	Nanoparticle
NR	Nanorod
NMR	Nuclear magnetic resonance
P&ID	Piping and instrumentation diagram
PZC	Point of zero charge
pXRD	Powder X-ray diffraction
PEMFC	Proton exchange membrane fuel cell
SF	Stoichiometry factor
SDA	Structure directing agent
TPR	Temperature programmed reduction

TCD	Thermal conductivity detector
TGA	Thermogravimetric analyses
TOL	Time on line
TEM	Transmission electron microscopy
TOF	Turnover frequency
WI	Wet impregnation
XPS	X-ray photoelectron spectroscopy

Chemical formulae

AgNO ₃	Silver nitrate
Au/ γ -Al ₂ O ₃	Gold nanoparticles supported on γ -Alumina
Co/ γ -Al ₂ O ₃	Cobalt nanoparticles supported on γ -Alumina
CoOOH	Cobalt oxy hydroxide
Co ₂ CO ₃ (OH) ₂	Cobalt hydroxyl carbonate
Co(NO ₃) ₂ ·(H ₂ O) ₆	Cobalt (II) nitrate hexahydrate
CO(NH ₂) ₂	Urea
γ -AlOOH	γ -Boehmite
γ -Al ₂ O ₃	γ -Alumina
HAuCl ₄	Chloroauric acid
NH ₃	Ammonia
SiC	Silicon carbide

Acknowledgements

I would like to thank the Department of Chemical Engineering and Biotechnology at the University of Cambridge for allowing me to carry out my doctoral research in an academically stimulating environment. Moving to the new building was certainly an adventure but I feel privileged to have worked in such a historic place. I would like to extend my gratitude to my academic supervisor, Dr Torrente, for continuous inspiration, guidance and support. I would also like to thank the Process Integration research group, notably Julien Mahin for help acquiring microscopy images. In addition, I thank the Combustion group for allowing me to work in their laboratory and specifically, Zach Bond for help setting up the gas lines in the new building. The lab set up and daily conundrums were aided by the technical support staff. In particular I would like to thank Peter Claxton and Chris Bawden for their assistance.

Within the University of Cambridge, I am grateful to the Departments of Engineering, Geography and Material Science & Metallurgy for access to their characterisation equipment and expertise, notably from Anthony Dennis and Laura Healy. Many thanks to Clare College and the MCR. I have loved being part of such a vibrant and friendly graduate community.

The involvement of Sasol UK as the industrial sponsor has been a significant advantage for this project. I would like to thank Dr Juan-María González-Carballo and Professor Robert Tooze for their time spent discussing my results in our regular meetings and for sharing their industrial knowledge, which ultimately improved the research project outcomes. I thank Professor Robert Tooze for access to state-of-the-art equipment and to Dr Herve Menard and Dr Phil Landon for their help. I am grateful for the opportunity to test my materials in an industrial testing rig and to Dr Hendrik Van Rensburg for carrying out the experiments.

Thanks are due to the University of Bath and the Centre for Sustainable Chemical Technologies for training and support during the first phase of my doctoral research. I would like to thank Dr Alf Hill (University of Bath) for training on the NH₃ decomposition rig and Dr John Lowe (University of Bath) for acquiring the NMR spectra.

Many thanks to my friends and family for their support. I am eternally indebted to my parents for providing me with an excellent education, leading to the discovery of my interest in science. Amelia, Laurel, Céline, James, Mum and Dad thank you all for helping with proof reading. Finally, I would like to thank James for his patience, understanding and eternal optimism!

Abstract

Supported metal nanoparticles present unique chemical and physical properties compared to their bulk counterparts. Their high surface energy provides outstanding catalytic activities, opening the door not only to improved catalytic systems but also to new catalytic routes. However, their high surface energy and liquid-like properties are responsible for their instability, usually leading to agglomeration under reaction conditions.

This thesis seeks to investigate a novel nanoparticle stabilisation approach by physical confinement on curved supports. Specifically, the project focusses on the stabilisation of cobalt and gold nanoparticles on nanostructured γ -Al₂O₃ supports, motivated by the industrial interest of Sasol UK. The research hypothesis is validated by detailed characterisation and catalytic testing of a range of catalysts using different metal loadings and support morphologies.

To enable this study, the mechanism of the hydrothermal synthesis of a series of nanostructured γ -Al₂O₃ supports with either flat or curved surfaces and differing degrees of curvature has been elucidated, leading to the development of a semi-continuous manufacturing process. Varying the method for loading cobalt onto γ -Al₂O₃ supports highlights the implications of method selection on the particle size, reducibility, composition and the tendency to form irreducible cobalt oxides, all of which affect the catalytic activity. The ability to obtain and stabilise small nanoparticles with low loading (1 wt% Co) without the formation of irreducible cobalt oxides exposes the beneficial effect of the support curvature. Specifically, the stabilisation effect is theorised to be effective under the condition where the ratio of the diameter of the nanoparticle (P) and the nanorod (R) is less than one, $P:R < 1$. In several cases, after cobalt or gold reduction, elongation of the nanoparticles, as opposed to agglomeration, is observed by electron microscopy confirming that the particles are physical confined by the curved surface in all directions except along the nanorod axis. In these cases, highly active Co/ γ -Al₂O₃ and Au/ γ -Al₂O₃ catalysts are reported for NH₃ decomposition and CO oxidation respectively. For higher metal loadings (> 5 wt% Co), where the particles are the same size or larger than the diameter of the nanorod cross-section, no noticeable stabilisation effect is reported.

The results of this thesis are scientifically and industrially important. If applied correctly, this novel nanoparticle stabilisation strategy could be used to design catalysts with improved activity and stability, resulting in lower operational costs and improved resource efficiency.

Dissemination of research

The research presented in this thesis has been disseminated throughout the course of the project through publication in relevant journals and presentations at international conferences and internal events.

Publications

- T. E. Bell, J. M. González-Carballo, R. P. Tooze and L. Torrente-Murciano, High yield manufacturing of γ -Al₂O₃ nanorods, *ACS Sustain. Chem. Eng.*, 2018, **6**, 88–92.
- T. E. Bell, G. Zhan, K. Wu, H. Chun Zeng and L. Torrente-Murciano, Modification of ammonia decomposition activity of ruthenium nanoparticles by N-doping of CNT supports, *Top. Catal.*, 2017, **60**, 1251–1259.
- T. E. Bell, J. M. Gonzalez-Carballo, R. P. Tooze and L. Torrente-Murciano, γ -Al₂O₃ nanorods with tuneable dimensions – a mechanistic understanding of their hydrothermal synthesis, *RSC Adv.*, 2017, **7**, 22369-22377.
- L. Torrente-Murciano, A. K. Hill and T. E. Bell, Ammonia decomposition over cobalt/carbon catalysts – Effect of carbon support and electron donating promoter on activity, *Catal. Today*, 2017, **286**, 131–140.
- T. E. Bell and L. Torrente-Murciano, H₂ production via ammonia decomposition using non-noble metal catalysts: A review, *Top. Catal.*, 2016, **59**, 1438–1457.
- T. E. Bell, J. M. Gonzalez-Carballo, R. P. Tooze and L. Torrente-Murciano, γ -Al₂O₃ nanorods with tuneable dimensions – a mechanistic understanding of their hydrothermal synthesis, *J. Mater. Chem. A*, 2015, **3**, 6196–6201.

Oral presentations

- *Ammonia decomposition catalyst design for in situ hydrogen production*, iChemE Catalysis and Reaction Engineering Symposium, Sheffield, UK, May 2017.
- *Stabilisation of metal nanoparticles using curved supports*, Department of Chemical Engineering Graduate Conference, Cambridge, UK, April 2017.
- *Morphologically selective synthesis of nanostructured γ -Al₂O₃ with tuneable dimensions*, EuCheMS 6th European Chemistry Congress, Seville, Spain, September 2016.
- *Low temperature catalysts for on demand hydrogen production via ammonia decomposition*, EuCheMS 6th European Chemistry Congress, Seville, Spain, September 2016.

- *Hydrothermal synthesis of nanostructured γ -Al₂O₃ with controlled size and morphology in a recyclable process*, Department of Chemical Engineering Research Day, Cambridge, UK, January 2016. (Flash presentation)
- *What are catalysts and how can they be used to unlock the potential of the hydrogen economy?*, Clarity Evening Talk, Clare College, Cambridge, UK, November 2015.
- *Low temperature in-situ hydrogen production by ammonia decomposition using cobalt-based catalysts*, Europacat XII “Catalysis: Balancing the use of fossil and renewable resources”, Kazan, Russia, August 2015.
- *Stabilisation of metal nanoparticles by confinement on curved supports*, Department of Chemical Engineering Research Afternoon, University of Bath, UK, April 2015.

Poster presentations

- *Ammonia decomposition catalyst design for in situ hydrogen production*, Department of Chemical Engineering Research Day, Cambridge, UK, June 2017.
- *In situ hydrogen production from ammonia using cheap cobalt catalysts*, STEM for Britain event at Houses of Parliament, March 2017. (Shortlisted)
- *Stabilisation of metal nanoparticles using curved supports*, Department of Chemical Engineering Graduate Conference, Cambridge, UK, April 2016. (Poster prize awarded)
- *Hydrothermal synthesis of nanostructured γ -Al₂O₃ with controlled size and morphology in a recyclable process*, Department of Chemical Engineering Research Day, Cambridge, UK, January 2016.
- *Curved surfaces to reduce waste of expensive metals in catalysts*, National Women in Engineering Day (NWED) at the University of Bath, UK, June 2015.

Chapter 1 – Introduction

Over 95% of all industrial products are manufactured in the presence of a catalyst.¹ As a result, there is a high demand for the development of low cost catalysts with improved catalytic activity, selectivity and stability as well as reduced toxicity. Metal nanoparticles exhibit novel and unprecedented catalytic properties due to their small size and high surface area to volume ratio. However, under-coordinated surface atoms in these small particles give rise to high surface energy, leading to instability and a tendency to agglomerate (sinter), especially at high temperatures. This irreversible deactivation has a detrimental effect on their catalytic activity since performance is often size-specific.

Deactivation of metal nanoparticles in heterogeneous catalysts represents a significant challenge and cost for industry. Based on the commercial relevance, Sasol UK partially funded and co-supervised this project. Sasol Ltd are worldwide experts in Fischer-Tropsch synthesis (FTS), which employs a heterogeneous catalyst comprised of cobalt or iron nanoparticles supported on Al_2O_3 . Cobalt FTS is typically carried out at 210 to 240 °C and therefore the metal nanoparticles are susceptible to deactivation by sintering during catalytic operation.²

Accordingly, a new stabilisation approach is investigated in this thesis for $\text{Co}/\text{Al}_2\text{O}_3$ materials, which are tested for NH_3 decomposition as a model reaction. During the project some of the $\text{Co}/\text{Al}_2\text{O}_3$ materials were tested for FTS at Sasol UK. For $\text{Co}/\text{Al}_2\text{O}_3$ catalysts, characterisation techniques for size determination are challenging. Therefore, in order to directly correlate nanoparticle size with the activity, another system based on $\text{Au}/\text{Al}_2\text{O}_3$ was explored. Investigating a second metal also reveals the applicability of the stabilisation technique to different metal systems. In this case, CO oxidation is used as a model reaction to test the stabilisation theory for $\text{Au}/\text{Al}_2\text{O}_3$.

The aim of this thesis is to develop a novel stabilisation strategy for metal nanoparticles. The theory will be validated by characterisation and catalytic testing of the catalysts in relevant model reactions.

1.1 Novel metal nanoparticle stabilisation hypothesis

The concept of this novel stabilisation hypothesis is based on metal nanoparticles supported on a solid surface, a typical structure in heterogeneous catalysis. Below a certain size in the nanoscale metal nanoparticles begin to melt at a given temperature, as shown in Figure 1.³ Even above the melting temperature, the outer layers of the nanoparticle contract because the surface atoms are undercoordinated, resulting in a loss of crystallinity, which gives rise to liquid-like properties. Thus, nanoparticles resemble liquid droplets wetting a solid surface.⁴ This liquid-like behaviour enables their mobility on the support surface resulting in agglomeration and catalyst deactivation.

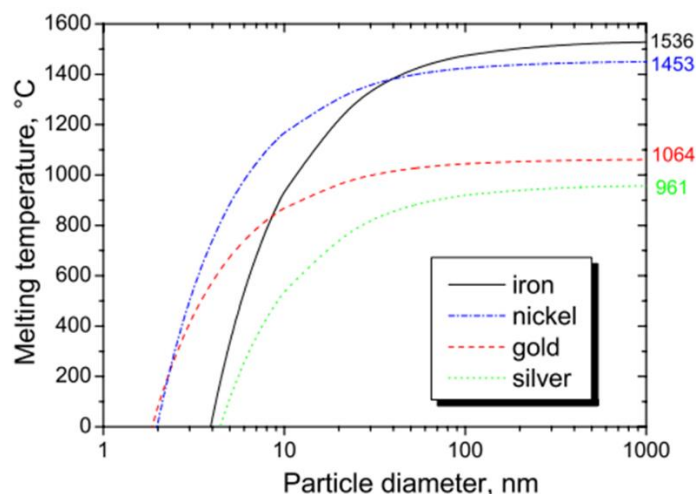


Figure 1. Melting temperature with respect to particle diameter for different metals. Iron (black), nickel (blue), gold (red) and silver (green). Directly reproduced from Moiala *et al.*³.

This project investigates a novel strategy for the stabilisation of metal nanoparticles by their physical confinement on the external surface of curved supports. Depending on the strength of the interaction between a metal nanoparticle and the surface, there will be a different contact angle (θ_c) between them, classified as either strong ($\theta_c < 1$) or weak ($\theta_c > 1$). If one considers that the metal nanoparticles have liquid-like properties then the Young equation for surface wetting applies. The relationship is shown in its simplified form in Equation (1) in terms of the surface tension vectors at the solid-liquid (γ_{SL}), solid-gas (γ_{SG}) and liquid-gas (γ_{LG}) interfaces.

$$\gamma_{SG} = \gamma_{SL} + \gamma_{LG} \cdot \cos \theta_c \quad (1)$$

$$\gamma_{\pi} = \gamma_{LG} \cdot \sin \theta_c \quad (2)$$

The resulting surface tension vector (γ_π) acts perpendicular to the surface and is a function of the contact angle (θ_c) and γ_{LG} (Equation (2)).

The wetting of metal nanoparticles on both flat and curved solid support surfaces is shown in Figure 2. In the case of metal nanoparticles on a conventional flat surface (Figure 2a), γ_π acts in parallel directions so the mobility of the nanoparticles is unrestricted and they are able to agglomerate with the provision of energy. However, when the support is curved (Figure 2b), γ_π of two adjacent nanoparticles acts in opposing directions, theoretically reducing their mobility and physically confining the particle against agglomeration. The stabilisation effect is further enhanced by the fact that the metal-support surface area increases from the use of a curved support. This spatial confinement is likely to be particularly useful at higher reaction temperatures, in which sintering is unrestricted with a flat support.

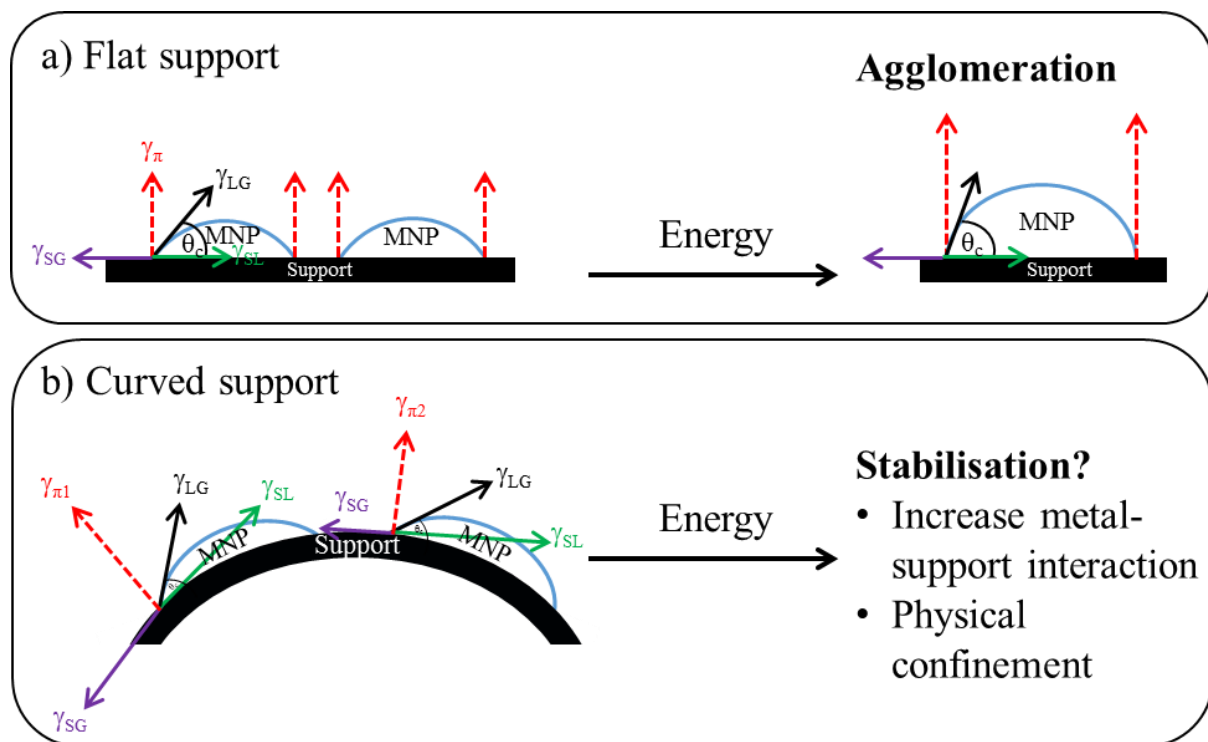


Figure 2. Agglomeration of metal nanoparticles (MNPs) on conventional flat supports (a) compared to the novel stabilisation hypothesis of using curved supports (b).

The novel stabilisation technique proposed herein hypothesises that the use of a curved support will result in enhanced metal nanoparticle stability compared to a conventional flat support under reaction conditions.

1.2 Aims and objectives

The overall PhD aim is to investigate the hypothesis of stabilisation of metal nanoparticles by confinement on the surface of curved supports. In order to achieve this aim and validate the research hypothesis, a series of objectives are identified:

1. Develop a reproducible synthesis of Al_2O_3 with controlled morphologies selectively containing flat or curved surfaces.
2. Examine the effect of different metal loading methods on the metal- Al_2O_3 interaction and metal particle size distribution.
3. Assess the catalytic activity of Co and Au nanoparticles supported on Al_2O_3 for NH_3 decomposition and CO oxidation respectively as model reactions, as well as for commercially relevant Fischer-Tropsch synthesis.
4. Study the thermal stability of Co and Au nanoparticles supported on Al_2O_3 with different morphologies under experimental conditions.

1.3 Impact

The need for effective stabilisation of metal nanoparticles is of paramount importance. Agglomeration of metal nanoparticles represents a huge cost to the chemical industry. A reduction in operational costs or precious metal waste associated with an industrial process resulting from superior catalyst stability plays an important role for sustainable development.

If the stabilisation strategy proposed herein proves to be effective, the impact on the scientific and industrial community would be enormous. Improved stability of catalysts results in higher productivity and reduced metal waste, leading to an overall reduction in operational costs. Heterogeneous catalysis usually employs precious and expensive metals, so an improvement in catalyst stability also prevents unnecessary depletion of these scarce resources.

Since dispersed metal nanoparticles are widely used in heterogeneous catalysis, the extent of the benefits of highly stable catalysts are virtually endless. Additionally, improved stability may encourage additional uptake of metal nanoparticles for other applications that strongly depend on stability, particularly as emerging catalytic research reveals applications for highly unstable 1 to 2 nm particles.

1.4 Thesis structure

The thesis is divided into the following chapters:

- Chapter 1: *Introduction*

- Chapter 2: *Literature review*

This chapter reviews the properties of metal nanoparticles and existing routes for their stabilisation. In addition, the known hydrothermal syntheses of nanostructured γ -Al₂O₃ are summarised. Finally, the properties and activity of relevant catalysts for NH₃ decomposition, Fischer-Tropsch synthesis and CO oxidation reactions are summarised.

- Chapter 3: *Experimental methodology*

This chapter provides details of the experimental protocols used for the support synthesis, nanoparticle synthesis, materials characterisation and catalytic testing.

- Chapter 4: *Hydrothermal synthesis of nanostructured γ -Al₂O₃*

This chapter devises a hydrothermal synthesis for the production of morphologically pure γ -Al₂O₃ nanostructures. The synthesis parameters are varied in order to vary the nanostructure type and develop a mechanistic understanding.

- Chapter 5: *Effect of cobalt loading methods on Co/ γ -Al₂O₃ properties and catalytic activity*

This chapter explores different methods for the formation of cobalt nanoparticles on γ -Al₂O₃. The catalysts are characterised and tested for NH₃ decomposition.

- Chapter 6: *Effect of support morphology on Co/ γ -Al₂O₃ catalytic activity and stability*

This chapter builds upon Chapter 5 by selecting two methods for metal loading to produce a range of catalysts with different loadings supported on γ -Al₂O₃ and distinct support morphology. All the materials are characterised and tested for NH₃ decomposition. A selection of catalysts are tested for their thermal stability under high temperature conditions up to 750 °C. In addition, some of the materials are tested for Fischer-Tropsch synthesis (FTS) under industrially relevant conditions.

- Chapter 7: *Effect of support morphology on Au/ γ -Al₂O₃ catalytic activity and stability*

The final research chapter focuses on optimising the synthesis of Au/ γ -Al₂O₃ based on characterisation and catalytic tests. Subsequently a series of catalysts with different loadings supported on γ -Al₂O₃ with different support morphology are characterised and tested for CO oxidation.

- Chapter 8: *Conclusions and future work.*

Chapter 2 – Literature review

This thesis investigates stabilisation of metal nanoparticles on curved supports. As such, the existing literature has been reviewed in the areas relevant to the research carried out. Initially, the behaviour of metal nanoparticles are addressed, highlighting their novel properties and inherent instability and the implications on catalytic activity. Subsequently the existing methods for nanoparticle synthesis and strategies for their stabilisation are considered.

The merits of Al_2O_3 as a catalyst support, particularly when in its nanostructured form, are addressed. Different methods of synthesis for nanostructured Al_2O_3 are discussed, including a comprehensive study of the nature of the $\gamma\text{-Al}_2\text{O}_3$ nanostructures obtained from hydrothermal synthesis as this is the chosen method, owing to its simplicity and reproducibility.

Previous studies of cobalt-based catalysts for NH_3 decomposition and Fischer-Tropsch synthesis, as well as gold-based catalysts for CO oxidation, are reviewed.

The areas for improvement and the scientific challenges that will be addressed herein are highlighted in the conclusion section of this literature review.

2.1 Metal nanoparticles

A nanoparticle typically possesses a diameter within the range of 1 to 100 nm.⁵ Metal nanoparticles are more catalytically active than their bulk counterparts due to the quantum confinement effects occurring at the nano-scale, which changes their chemical behaviour and properties.^{6,7} More specifically, the decrease in size results in more discrete energy levels due to a reduction in density of electronic states as shown in Figure 3.^{5,8} Dispersed metal nanoparticles are excellent catalysts because the exposed metallic surface possesses a high concentration of surface active sites relative to the total volume of the particle. This surface area to volume ratio increases with decreasing particle size.⁹ In addition, when clusters of atoms are constrained to such small sizes, there is a dramatic increase in the concentration of surface defects such as edges, terraces, kinks and corners, which are believed to act as the active sites in numerous structure-sensitive catalytic applications.^{10,11}

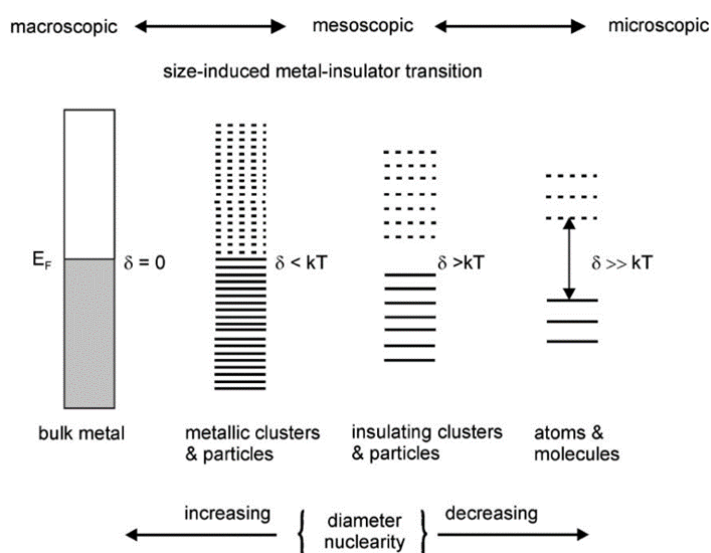


Figure 3. Change in electronic structure and band gap with respect to metal diameter. δ is the Kubo gap. Directly reproduced from Roduner.⁸

There is usually an optimal nanoparticle size for each metal catalyst and reaction, which maximises the concentration of the active sites responsible for accelerating the catalytic activity. However, nanoparticles possess high surface energy and as such, it is energetically and thermodynamically favourable to agglomerate with adjacent nanoparticles to minimise their surface energy, forming larger and more stable particles. This irreversible agglomeration process, known as sintering, is detrimental in catalysis because catalytic activity is often size dependent and larger particles are usually less active.

As such, the scientific community seeks not only a reproducible method for the synthesis of tuneable nanoparticles with a narrow particle size distribution, but also an effective stabilisation technique to preserve the particle size during use.

2.1.1 Methods for synthesis of metal nanoparticles

There are many methods available to synthesise heterogeneous metal nanoparticles onto supports, ranging in cost and complexity. The choice of method and conditions of synthesis are critical because they dictate the properties of the resulting nanoparticles such as particle size and distribution.¹² Ideally the synthesis method should deliver highly disperse metal nanoparticles within a narrow particle size range. Impregnation, deposition-precipitation and adsorption techniques are favoured due to their relative simplicity, which is valued in industry for the production of catalysts at a large scale.^{13,14}

Impregnation is a popular method for metal nanoparticle preparation as it consists of few synthetic steps but is criticised for poor particle size control and a weak metal support-interaction.¹⁵ In essence, impregnation involves contact of an aqueous or solvated metal salt solution with a solid support followed by drying to remove the solvent.¹⁴ There are two variations: incipient wetness impregnation (IWI) and wet impregnation. IWI employs a volume of metal precursor solution equal to the pore volume of the solid support whereas wet impregnation uses an excess solution, which is usually removed by rotary evaporation.¹³ In IWI, pore filling occurs due to capillary pressure and as the solvent is evaporated, the solution becomes super saturated, resulting in nucleation and growth of nanocrystallites.¹⁰

During adsorption synthesis, metal ions are adsorbed onto a support surface. A variation of this is ion exchange whereby the metal ions replace support surface ions. The isoelectric point or point of zero charge (PZC) of the support determines the pH of the support in solution and as such determines whether cations or anions will adsorb to the surface in an aqueous solution. Acidic supports ($\text{SiO}_2\text{-Al}_2\text{O}_3$, SiO_2) preferentially adsorb cations whereas basic supports (ZnO , MgO) adsorb anions. Due to its amphoteric nature, Al_2O_3 adsorbs cations in basic solutions and anions in acidic conditions. An aqueous suspension of the support and metal precursor can be stirred at elevated temperatures to increase the rate of adsorption, until an equilibrium is established.¹³ In order to determine the exact metal loading, analysis by inductively coupled plasma atomic/optical emission spectroscopy (ICP-A/OES) of the solid catalyst or the supernatant solution is needed.

The deposition-precipitation or precipitation method is commonly used for the synthesis of metal nanoparticles in industry as it is low cost, high yield and not energy intensive.¹⁶ Higher loadings can be achieved with deposition-precipitation than impregnation methods as the latter is limited by solubility or pore volume.¹⁰ In practice, the precipitation method is similar to adsorption but with the addition of a precipitant to induce the precipitation of metal compounds followed by deposition on the support surface.^{13,14} Care must be taken when adding the precipitant so as not to encourage precipitation in the bulk phase by exceeding the critical supersaturation point.¹⁰ Precipitants such as NH_3 , NaOH or Na_2CO_3 are commonly used due to their high solubility and ability to raise the pH of the suspension.^{13,17} Uniform precipitation can also be achieved by urea hydrolysis as an alternative source of hydroxide but higher synthesis temperatures are required to release the anions.¹³ In some instances, metallic nanoparticles are formed in solution by the addition of a reducing agent such as NaBH_4 or citrate compounds. Alternatively, the nanoparticles can be reduced after drying using hydrogen flow.

2.1.2 Strategies for metal nanoparticle stabilisation

Nanoparticles are thermodynamically unstable and as such stabilisation is critical to inhibit their growth via sintering, particularly since their properties and catalytic activity are normally size dependent. The mechanism of thermal deactivation process is highly debated in the literature and is said to proceed via two possible mechanisms: particle migration and coalescence or Ostwald ripening.¹⁸

The most common routes for nanoparticle stabilisation are represented in Figure 4. One possibility is to surround the metal cation core with oppositely charged counter anions to electrostatically stabilise the nanoparticles (Figure 4a). Stabilisation can also be achieved using compounds with steric bulk (Figure 4b) such as organic capping agents, inorganic ligands, colloids, soluble polymers or by creating a core-shell structure with another metal or oxide material.⁵ Both of these strategies produce unsupported metal nanoparticles, which can be later supported if desired. However, if the particles remain unsupported they can be difficult to separate from product streams. These stabilisation techniques may also have implications on catalytic activity, for example capping agents can block the active sites leading to mass transfer limitations or the stabiliser can interfere in the reaction.

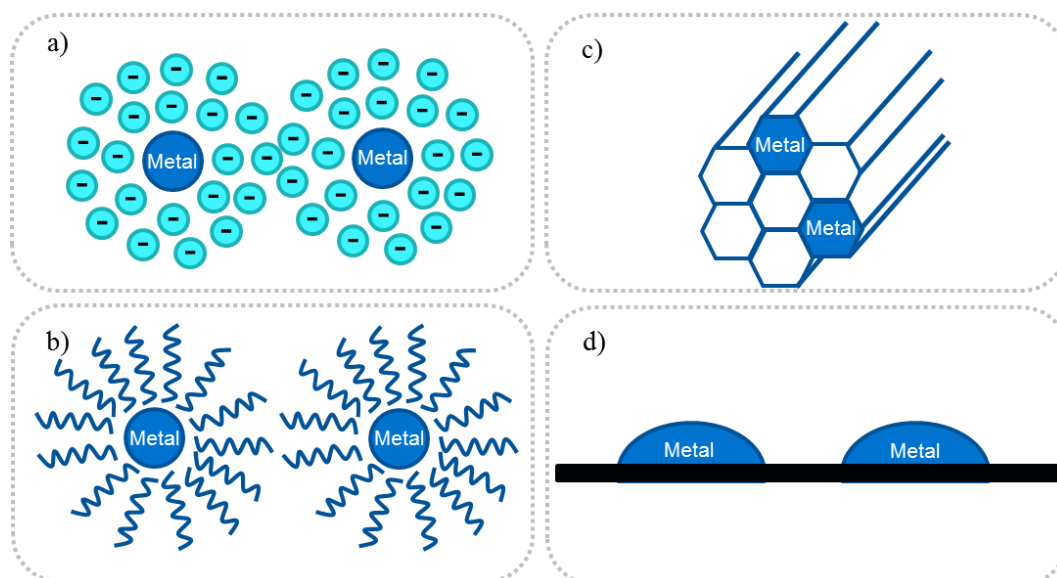


Figure 4. Methods for nanoparticle stabilisation a) electrostatic stabilisation b) steric stabilisation c) encapsulation and d) immobilisation on a solid support.

Metal nanoparticles can alternatively be stabilised using solid materials. They can either be encapsulated within the porous channels of solids such as zeolites and metal organic frameworks (Figure 4c) or located on the surface of high surface area materials such as ceramics or carbons (Figure 4d).^{10,19} Encapsulation within porous materials can effectively limit nanoparticle growth and thus size by controlling the channel diameter, which can result in catalytic stereo-selectivity. However this technique can lead to mass transfer limitations in catalytic applications depending on the size of the reacting molecules.¹⁹

The focus herein is supporting MNPs on solid metal oxide surfaces. In industrial processes, heterogeneous supported nanoparticle catalysts are advantageous as they can be easily separated from fluid streams, avoiding the need for complicated and costly separation steps. Commonly used solid support materials include porous ceramics (SiO_2 , TiO_2 , CeO_2 , Al_2O_3 , MnO_x , Fe_2O_3 , zeolites) and carbon nanostructures.⁷ Silica is the most extensively researched ceramic support and is employed in numerous industrial processes. However, alumina (Al_2O_3) is also widely used as a support in numerous industrial catalytic processes including Fischer-Tropsch synthesis (FTS), the Haber process, Ziegler-Natta polymerisation and hydrodesulfurisation to name a few.

Nanoparticle dependent technologies in industry exist and their implementation is rapidly increasing, beyond the field of catalysis, making the need for robust and effective nanoparticle stabilisation techniques a research priority.²⁰

2.2 Al₂O₃ as a catalyst support

The popularity of alumina, Al₂O₃, as a catalyst support is driven by its useful properties such as high strength, corrosion resistance, chemical and thermal stability, low thermal conductivity and electrical insulation.²¹ Based on these properties, Al₂O₃ is also used industrially as catalysts, adsorbents and abrasives.^{22–24} The under coordinated Al³⁺ Lewis acid sites of the Al₂O₃ surface provide anchoring points for stabilising metal nanoparticles.²⁵ The amphoteric nature of Al₂O₃ means that it possesses both basic and acidic surface hydroxyl groups.²⁵

Al₂O₃ is synthesised from polymorphs of aluminium hydroxide and oxy hydroxide precursors.²⁵ Boehmite (γ -AlOOH) forms various polymorphs of Al₂O₃ after calcination at 300 to 1000 °C following the order γ to δ to θ to α .^{26,27} The latter, is the most abundant and thermodynamically stable form, however its dense, cubic crystal structure results in low specific surface areas.²⁸ Conversely, calcination between 300 and 500 °C yields γ -Al₂O₃, which has the highest specific surface area making it the most suitable catalyst support material.^{29,30}

γ -AlOOH is composed of layers of octahedral AlO₆ units linked by hydrogen bonding in the (010) direction.³¹ During the thermal dehydration of γ -AlOOH, Al³⁺ cations migrate to tetrahedral positions resulting in the spinel-type crystal structure in γ -Al₂O₃ with tetragonal distortion arising from the absence of divalent cations.^{32,33}

2.2.1 Synthesis of nanostructured Al₂O₃

Recently there has been significant interest in the use of nanostructured materials as catalyst supports due to their novel properties compared to their bulk counterparts.³⁴ The ability to control the morphology at the nano-scale exposes different crystal planes, leading to distinct physical and chemical properties resulting in their use in numerous applications to date.^{35,36} For example, anisotropic 1D nanostructured Al₂O₃ possesses additional benefits compared to bulk Al₂O₃ such as a high elastic modulus, distinct optical properties and improved chemical and thermal stability.²¹

A wide range of ceramic support materials have been synthesised with well-defined shapes and pore structures, capable of supporting metallic particles with high metal dispersion, high concentration of active sites and unique electronic properties. The pore diameter of the support

is significant as it has implications on the resulting metallic crystallite size, even if the particle is located outside the pores.³⁷

1D morphologies of nanostructured Al_2O_3 reported in the literature include nanobelts, nanoribbons, nanowires, nanotubes and nanorods.³⁸ The diameter of a nanowire is between 0.5 nm and 2.5 nm, typically resulting in an aspect ratio (length:diameter) greater than 1000.³⁹ By contrast, nanorods and nanotubes have relatively larger diameters and smaller aspect ratios.³⁹ 2D nanostructured morphologies of Al_2O_3 have also been reported, such as nanosheets or nanoplates with dimensions from 10 to 1000 nm.^{39,40} More complicated 3D hierarchical morphologies such as flowers have been synthesised.⁴¹ Some examples of these different morphologies are shown in Figure 5.

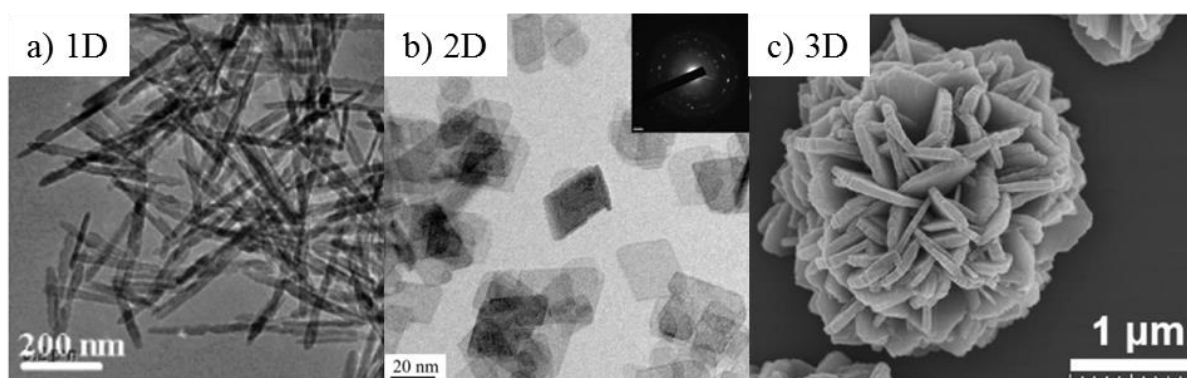


Figure 5. Reported electron micrographs of nanostructured Al_2O_3 a) 1D nanorods³⁸, b) 2D nanoplates⁴⁰ and c) 3D hierarchical flowers⁴¹.

The lowest energy surface planes of $\gamma\text{-Al}_2\text{O}_3$ in increasing order are (110), (100) and (111).⁴² Due to the change in atomic surface structure of nanostructured $\gamma\text{-Al}_2\text{O}_3$, these surfaces may be prevalent in different ratios and higher Miller index surfaces may become exposed compared to an unstrained model particle. The acidic properties of the support can therefore be mediated to provide anchoring sites for chemisorption of metal nanoparticles.⁴³ In other words, the morphology at the nano-scale changes the chemical properties of hydroxyl groups found on the alumina surface and the environment of the coordinated Al^{3+} cations.⁴³ Thus, shape control of the support material is critical as the nano-morphology can alter the catalytic ability as the metal nanoparticles bound to different crystal planes.⁴³ These interactions can be exploited as a means to offer additional stability to supported metal nanoparticles. This aspect will be explored in this thesis.

Despite the huge potential of nanostructured materials, their wide spread implementation is currently limited by the lack of economically feasible and consistent production methods at a

large scale. The range of synthetic methods developed for the formation of γ - Al_2O_3 nanostructures vary in cost and complexity. The choice of synthetic route is critical for defining the micro- and macro-structure of the product.³² Some commonly used methods include hydrothermal, sol-gel, atomic layer deposition, anodisation and wet etching.

Hydrothermal methods are widely used as they are cheap, reproducible, simple and can be easily scaled up for large scale manufacturing. During hydrothermal synthesis a sealed autoclave containing a liquid phase is heated to less than 300 °C, resulting in a pressure increase capable of producing crystalline nanostructured materials from precipitates, flocculates or gels. Hydrothermal methods offer many advantages for nanostructured material synthesis but are inherently limited due to their nature as batch processes. This is undesirable at an industrial scale mainly due to batch to batch variation, dead time in operation and large volumes of solvent waste.^{35,36} Hydrothermal synthesis will be used throughout the research herein for the synthesis of γ - Al_2O_3 nanostructures, with one research section devoted to addressing these shortcomings.

2.2.1.1 Hydrothermal synthesis of nanostructured Al_2O_3

Hydrothermal synthesis of nanostructured boehmite was first reported by Bugosh⁴⁴ in 1961 and has since been widely used. Hydrothermal routes enable facile control over the crystallinity and morphology of the resulting boehmite by modifying the reaction conditions.⁴⁵ Many different factors including the choice of aluminium precursor or precipitant and the use of additives, metal dopants or anions can affect the morphology and physical properties of the resulting nanostructure. Additionally, synthetic conditions such as pH, synthesis time and temperature and calcination temperature all play an important role in determining the nature of the product, however the effect is not always consistent in the literature.

Often syntheses are carried out with the addition of a structure directing agent (SDA), which acts as a template to control the resulting morphology. SDAs are classified as either hard (e.g. carbon nanotubes, mesoporous silica, nanoglass) or soft (liquid crystals, polymers, surfactants, acids).³⁸ However, the quality of the final product may be compromised by residual SDA or defects in the crystal lattice.³⁴ The price of the surfactant must also be considered as they are typically expensive, increasing the hydrothermal process cost, which is usually relatively low.⁴⁵ Alternatively, the morphology can be directed by anions such as sulphate, chloride and nitrate

by preferential adsorption to selected crystal planes, limiting their growth.⁴⁶ Unlike SDAs, anions are easily removed by washing or calcination without compromising the product purity.

Table 1. Summary of hydrothermal syntheses of γ -AlOOH and γ -Al₂O₃ without a SDA.

Precipitant	pH	Temperature (°C)	Time (hours)	Morphology	Size (nm)		S _{ABET} ^a (m ² ·g ⁻¹)	Ref.
					Length	Diameter		
None	n/a	240	3	Nanostrip (AlOOH)	190 - 210	40 - 80	n/a	47
Urea	n/a	200	3	Nanoflower (AlOOH)	3,000	100	n/a	41
NaOH	4	200	24	Nanorod (γ -AlOOH)	200 - 300	10 - 30	85	21
NaOH	5	200	24	Nanorod (γ -AlOOH)	200 - 300	10 - 30	24	21
C ₆ H ₅ NH ₂	n/a	200	24	Nanorod (γ -AlOOH)	300 - 700	25 - 40	n/a	22
NaNH ₂	n/a	200	4-6	Lamellar (γ -AlOOH)	20 - 40	20 - 25	n/a	48
NaNH ₂	n/a	200	12	Nanotube (γ -AlOOH)	100	2 - 5	n/a	48
NaNH ₂	n/a	200	20	Nanorod (γ -AlOOH)	< 180	15 - 20	n/a	48
NH ₄ OH	5	200	48	Nanorod (γ -AlOOH)	100 - 400	20 - 30	n/a	38
NH ₃	5	200	48	Nanorod (γ -AlOOH)	140 - 320	n/a	n/a	49
N ₂ H ₄ ·H ₂ O	5	200	12	Nanorod (γ -AlOOH)	100 - 150	8	n/a	40
N ₂ H ₄ ·H ₂ O	10	200	12	Nanoflake (γ -AlOOH)	20 - 30	n/a	n/a	40
(NH ₄) ₂ CO ₃	n/a	100	24	Nanorod (γ -Al ₂ O ₃)	90 - 140	35 - 45	165	50
(NH ₄) ₂ CO ₃	n/a	100	36	Nanorod (γ -Al ₂ O ₃)	90 - 140	35 - 45	152	50
HCO-N(CH ₃) ₂	2.5	150	24	Nanorod (γ -Al ₂ O ₃)	< 50	~ 5	457	51
(C ₂ H ₅) ₄ N(OH)	n/a	170	72	Nanofibre (γ -Al ₂ O ₃)	300 - 1000	8 - 15	210	7

^a S_{ABET} is the specific surface area calculated using the BET approximation using N₂ sorption data at -196 °C.

The reported hydrothermal syntheses of nanostructured γ -AlOOH and γ -Al₂O₃ without the use of SDAs are summarised in Table 1. γ -AlOOH is easily converted to γ -Al₂O₃ by calcination with conservation in morphology as protons are ejected and some Al³⁺ ions migrate to tetrahedral positions.³³ A decrease in size is observed due to the contraction of the crystal lattice following dehydration by calcination. The ability to consistently control the morphology and size of nanostructured alumina is not yet feasible despite work in this area. For example, Table 1 shows that hydrothermal syntheses at the same temperature and time (200 °C, 24 hours) yields γ -AlOOH nanorods either 200 to 300 nm²¹ or 300 to 700 nm²² long. This may be due to variations in other synthesis parameters.

2.3 Catalytic applications of Co/ γ -Al₂O₃

Cobalt-based catalysts provide low cost, abundant alternatives to platinum group metals commonly used in catalysis. Cobalt nanoparticles supported on Al₂O₃ have been implemented for use as a catalyst in industrial-scale reactions such as Fisher-Tropsch synthesis (FTS). Additionally Co/ γ -Al₂O₃ materials are potential candidates for NH₃ decomposition, which has recently gained interest due to the promising role of NH₃ as an energy vector for the hydrogen economy.^{37,52}

For these reactions, the active cobalt species is believed to be metallic Co⁰, therefore, the choice of suitable reduction conditions prior to the reaction is essential.^{53,54} For supported Co, the ease of reduction depends on the strength of the metal-support interaction, crystallite size, support porosity and surface area.^{53,55} The choice of the catalyst calcination temperature can also affect the reduction temperature due to the difference in resulting particle size.⁵⁶

Cobalt and Al₂O₃ have a strong interaction (relative to Co-C) resulting in high reduction temperatures from 400 to 800 °C, relative to unsupported cobalt which is reduced below 380 °C depending on the size.⁵⁶⁻⁵⁸ A strong metal-support interaction is beneficial as it can result in smaller particles and a higher Co⁰ active site density.⁵³

The strong interaction can unfortunately lead to the formation of new compounds or metal-oxides at the interface since Al³⁺ polarises and weakens the Co-O bonds.⁵⁷ The crystal structures of Co₃O₄ and Al₂O₃ are isomorphic with respect to Co³⁺ and Al³⁺, which have similar ionic radii, permitting the migration and diffusion of ions during high temperature calcination or reduction treatments (> 500 °C) to yield irreducible and inactive cobalt aluminate spinel (CoAl₂O₄).⁵⁹ Cobalt aluminate species have been widely reported to form when cobalt is supported on Al₂O₃ and are referred to as irreducible as they require reduction above 800 °C.³⁷ The extent of their formation depends on the treatment conditions, loading, particle size, metal-support interaction and synthesis method. For example, low cobalt loading less than 5 wt% encourages their formation, generally due to the smaller, more disperse particles obtained.⁶⁰ However, with suitable conditions, it is possible to reduce a Co/Al₂O₃ catalyst without forming cobalt aluminates.⁵⁹

2.3.1 Ammonia decomposition

Hydrogen presents a clean fuel option for portable applications, with water as the only by-product.⁶¹ The uptake of hydrogen powered technologies is limited by our current inability to economically store hydrogen with a sufficiently high density, in addition to public acceptance regarding safety concerns of its storage and transportation.⁶² As an alternative to physical storage, hydrogen can be stored chemically in molecules such as methanol, methane, ammonia and related compounds (e.g. NH_3BH_3), metal amine salts (e.g. $\text{Mg}(\text{NH}_3)_6\text{Cl}_2$ or $\text{Ca}(\text{NH}_3)_8\text{Cl}_2$) and hydrides (e.g. LaNi_5H_6 or NaAlH_4).^{63,64}

Ammonia presents a viable option because of its high 17.6 wt% hydrogen content (above the 9 wt% US Department of Energy target), absence of carbon, narrow flammability range in air (16 to 25 vol% for NH_3 cf 4 to 75 vol% for H_2), ambient temperature liquefaction at 8 bar, existing transportation and distribution network, established safety protocols and large scale production (> 100 million tonnes annually).^{63,65–68} The sustainability of the overall process can be achieved by using NH_3 generated from H_2 obtained from water splitting using excess renewable energy source or heat waste derived from the nuclear industry.⁶⁸ The toxicity of ammonia may be a concern but the strong smell is practical for identifying leaks or alternatively metal amines can be used.^{64,67}



Ammonia decomposition via Reaction (3) is an attractive solution for *in situ* production of CO_x -free hydrogen which can directly feed a proton exchange membrane fuel cell (PEMFC), a concept first proposed in 1982.⁶⁹ However, for ammonia decomposition to be viable for hydrogen storage, the decomposition needs to take place at the operating temperature of a PEMFC (90 to 180 °C).⁷⁰ The development of catalysts capable of effectively operating under these low temperature conditions is essential but inherently challenging due to catalyst poisoning by N-adatoms at low temperatures and the endothermic nature of the reaction limiting decomposition at low temperatures.

To date, the most effective catalysts for ammonia decomposition capable of H_2 release at 180 °C are based on electronically promoted ruthenium, which have been developed in our research group.^{62,71} However, the cost and scarcity of ruthenium inhibits its large scale implementation.⁷² Thus, catalysts based on readily available, non-noble metals need to be

developed, but current published research in the area tends to compromise on activity.⁷² The activity of some metals supported on activated alumina follows the trend $Ru > Ni > Rh > Co > Ir > Fe \gg Pt > Cr > Pd > Cu \gg Te, Se, Pb$.⁷³

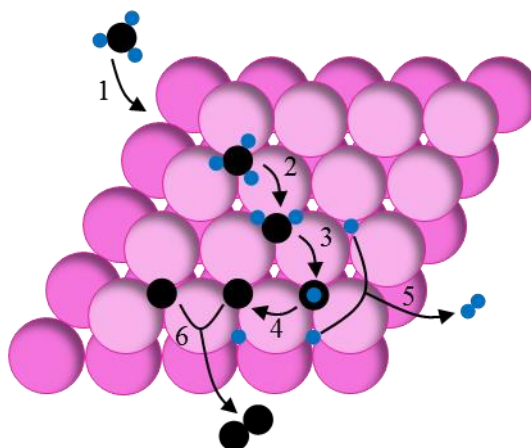
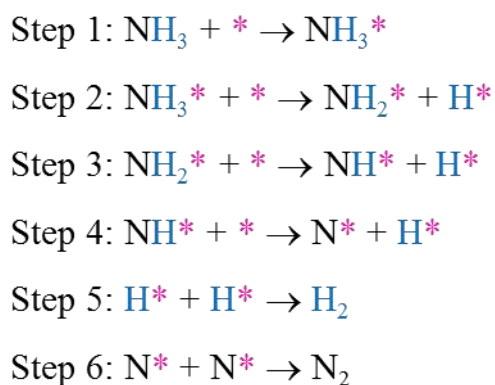


Figure 6. Stepwise mechanism of NH_3 decomposition on the (111) Co fcc surface.

The mechanism of ammonia decomposition over a solid catalyst is shown in Figure 6. Initially, NH_3 adsorbs to the metal surface and subsequently undergoes successive N-H bond scission. The released hydrogen atoms recombine to form molecular hydrogen. Finally the nitrogen atoms undergo recombinative desorption, evolving N_2 .⁷⁴

At low temperatures, the final nitrogen desorption step is the slowest and thus rate limiting step.⁷⁵ Consequently, the metal-N binding energy is a key parameter for catalyst design. An optimum binding energy is sought after to enable adsorption of ammonia as well as the release of nitrogen adatoms.

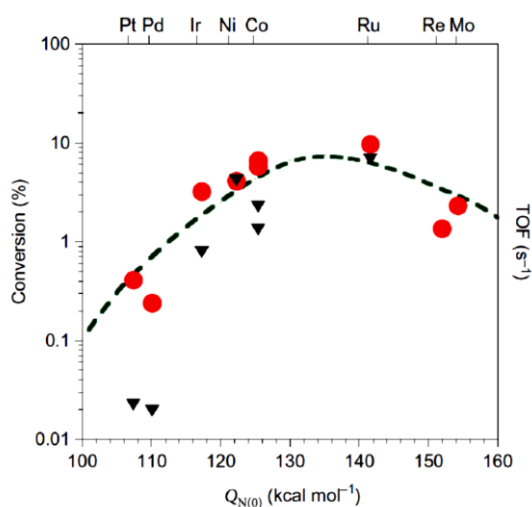


Figure 7. NH_3 decomposition activity with respect to nitrogen binding energy (Q_N). Directly reproduced from Hansgen *et al.*⁷⁴.

There is a volcano-type relationship of ammonia decomposition conversion with respect to nitrogen binding enthalpy, as shown in Figure 7.⁷⁶ Ruthenium sits at the maxima because it possesses an optimum nitrogen binding enthalpy, within the range of 130 to 140 kcal·mol⁻¹. This relationship forms the basis of the fundamental guidelines for the development of alternative low temperature NH₃ decomposition catalysts, which may be achieved with suitable combinations of metal, support and promoter or bimetallic systems.

Cobalt, nickel and iron have attracted attention as sustainable alternatives to ruthenium as the binding energy is close to ruthenium. A range of cobalt based catalysts have been reported with promising activity for NH₃ decomposition including core-shells,⁷⁷ cobalt incorporated within silica^{78,79} or alumina⁸⁰ matrices and supported on ceramics⁵⁷ or carbon^{55,81,82}. Some properties and the ammonia decomposition catalytic activity of the cobalt catalysts reported for NH₃ decomposition are summarised in Table 2.

Table 2. Properties and NH₃ decomposition activity of reported cobalt catalysts.

Catalyst details	Co (wt%)	Co size (nm)	Reduction T (°C)	Conversion @ 500 °C (%)	TOF @ 500 °C (mol _{H₂} ·mol _{Co} ⁻¹ ·h ⁻¹)	Ref.
Co incorporated in Na silicate	5	n/a	400	5	7	78
Co incorporated in silicate	17	n/a	400	5	3	79
Co with 2.9 Al, 1.6 Ca, 0.5 K, 0.2 Cr wt%	94.8	34	600	35	11	52
Co with 2.8 Al, 2.4 Ca, 0.6 K wt%	94	18	600	84	15	83
Co-SiO ₂ core-shell	83	n/a	550	15	3	77
Co in C matrix	18.7	4.5 - 6	350	55	89	84
Co in Al ₂ O ₃ matrix	95	10 - 20	650	72	36	80
Co/2MgAl-oxide	5	170	500	8	3	57
Co/2MgCe-oxide	5	12	500	40	71	57
Co/2MgLa-oxide	5	22	500	48	102	57
Co/MgO-La ₂ O ₃	5	2.5	500	60	60	85
Co/CNT	4.1	4 - 20	None	8	3	86
Co/MWCNT	5	4.3	500	60	159	55,81
Co/MWCNT	10	8.0	500	70	108	82
Co/Al ₂ O ₃	1	n/a	550	n/a	n/a	73

The preparation and pre-treatment conditions are important considerations for the synthesis of the optimum ammonia decomposition catalyst. For example, the choice of cobalt precursor can affect the catalytic activity with improved results observed with cobalt acetate compared to cobalt acetyl acetonate and commonly used cobalt nitrate.⁷⁹ Additionally, activity has been improved with nitric acid washing of the carbon support resulting in enhanced dispersion and control of the cobalt particle size.⁸⁷

All the catalysts included in Table 2 are pre-reduced prior to analysis or catalytic testing in the range 400 to 650 °C, except one material⁸⁴ reduced at 350 °C and one publication⁸⁶ in which no reductive treatments were reported. The latter unreduced material (cobalt supported on carbon nanotubes) resulted in a very poor catalyst, suggesting Co^0 is the catalytically active phase.⁸⁶

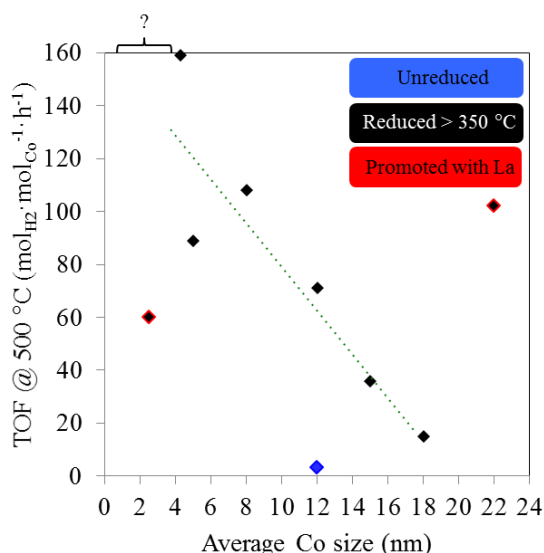


Figure 8. Size-activity dependency for reported cobalt-based NH_3 decomposition catalysts. Green dashed line represents a general size-activity relationship. Data acquired from publications are cited in Table 2.

Particle size is of critical importance in ammonia decomposition but since cobalt catalysts for this application are a relatively nascent research area, there are no clear guidelines for the optimum particle size to maximise the concentration of active sites. In addition, the arrangement of surface Co^0 atoms which act as the active site (or sites) has not yet been elucidated. The average cobalt particle size of the materials summarised in Table 2 ranges from 2 to 20 nm, which are shown in Figure 8 highlighting the size-activity dependency for the reported cobalt materials. A few catalysts from Table 2 were not included in Figure 8 due to lack of relevant reported data or because they contain on average larger cobalt crystallites (34 to 70 nm) leading to poor catalytic activity.

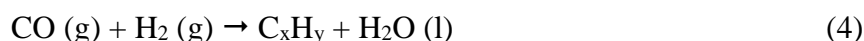
With the exception of the unreduced and lanthanum promoted catalysts, a significant enhancement of activity is observed in Figure 8 with decreasing particle size up to 4.3 nm, achieved from the use of multi-walled carbon nanotubes (MWCNT) support.^{55,81} The lack of NH₃ decomposition studies reporting cobalt materials less than 4 nm without promoters needs to be addressed by the research community as Figure 8 suggests potential for improvement. However, the absence of these reports may be due to the difficulty of their synthesis with a narrow particle size distribution or their instability.

A range of promoters for cobalt catalysts have been studied with a view to enhancing the activity of cobalt active sites. Oxides of Al, Ce, La, K, Mn and Cr have been employed as cobalt promoters in which La was found to make the most significant improvement, possibly due to the enhancement of the support basicity.^{52,57,80} For example the TOF at 500 °C increased from 3 to 71 to 102 mol_{H₂}·mol_{Co}⁻¹·h⁻¹ by exchanging Al, Ce and La respectively in a mixed magnesium oxide (2Mg:1Al/Ce/La) to support cobalt nanoparticles.⁵⁷ The promotional effect of potassium has been speculated to be due to an increase in surface area and a decrease in pore diameter.⁷⁸ Interestingly, chromium and manganese have a detrimental effect on the activity of cobalt supported on a mixed oxide.⁵²

In general, the catalytic activity based on the rate of reaction or turnover frequency (TOF) at 500 °C in Table 2 highlights one catalyst as the most active (5 wt% Co/MWCNT),^{55,81} capable of producing H₂ from NH₃ at a rate of 159 mol_{H₂}·mol_{Co}⁻¹·h⁻¹. A few catalysts have activities ranging from 60 to 102 mol_{H₂}·mol_{Co}⁻¹·h⁻¹ and the rest exhibit relatively poor activity below 36 mol_{H₂}·mol_{Co}⁻¹·h⁻¹. Evaluation of the literature suggests that there is scope for further improvement for cobalt-based NH₃ decomposition catalysts by research efforts into optimum cobalt particle size, ideal support properties, cobalt nanoparticle stabilisation techniques, synthesis methods and activity enhancing promoters.

2.3.2 Fischer-Tropsch synthesis

Fischer-Tropsch synthesis (FTS) (Reaction (4)) is an industrially useful reaction because it allows the conversion of a mixture of CO and H₂ called synthesis gas (obtained from gasification of natural gas, coal and biomass) into a range of useful hydrocarbons.^{2,88,89}



Most of the group 8 metals can catalytically accelerate the rate of FTS but only iron and cobalt are used industrially.² The metal choice governs the product selectivity with cobalt typically used to produce linear middle distillates and heavier wax fractions, which are subsequently cracked into the diesel fraction.^{2,90,91} Cobalt catalysts produce less oxygenate and isomer by-products compared to Fe materials and as such are widely used despite their relatively higher cost.^{2,90} As a compromise, costs are minimised by producing a highly disperse catalyst, usually containing 15 to 30 wt% Co.^{2,59,60} Cobalt-based FTS is operated at low temperature conditions from 210 to 240 °C under 20 to 30 bar pressure with a 2H₂:1CO reagent ratio.²

A range of support materials have been used to support cobalt particles for FTS in the literature, most commonly mesoporous metal oxides or carbons.⁵⁴ Only a few supports have been used in pilot or commercial scale FTS plants including titania, silica, alumina, aluminate and zinc oxide because they favour the production of long chain paraffins and waxes.^{2,90}

As expected, the rate of FTS is proportional to the number of cobalt active sites, which is determined by the active particle size, morphology, degree of metal reduction and stability.² Specifically, the activity of Co/Al₂O₃ FTS catalysts is influenced by the cobalt precursor, cobalt loading, support properties, synthesis method, heat treatments (calcination and reduction) and promoters.⁹¹ Thus, the catalyst design and synthesis conditions must be optimised in order to produce the target particle size, whilst suppressing the tendency to form irreducible mixed oxides and maximising the Co⁰ content. The shape of the resulting nanoparticle can also be modified by the method selection, for example spherical Co₃O₄ particles are obtained by impregnation but cubic Co₃O₄ is obtained from atomic layer deposition (ALD).⁹¹

The particle size can be tuned by the support pore size, loading and choice of method.^{91,92} For example, IWI in ethanol solvent results in smaller cobalt crystallites compared to the use of water solvent.⁹² Adsorption and IWI synthesis methods reportedly produce disperse catalysts suitable for FTS, contrary to the unsuitability of IWI for use in catalyst preparation for other

reactions.⁹² A double IWI technique can be used to achieve higher loadings when the pore volume is small.⁹⁰ Deposition-precipitation (with urea or $(\text{NH}_4)_2\text{CO}_3$ precipitants) and impregnation achieve higher loading but poorer dispersion with the latter forming a wide particle size distribution.^{91,92} Impregnation of pre-synthesised Co_3O_4 particles is a potential solution, which has been reported for the synthesis of active FTS catalyst.⁹¹

Catalysts may be calcined after synthesis to remove surface nitrates, often yielding Co_3O_4 . The choice of calcination temperature affects dispersion and reducibility, with higher temperatures usually resulting in lower dispersion.⁹¹ Interestingly, calcination in H_2 (reduction) leads to a hcp structural arrangement whereas calcination in air favours fcc formation.⁹¹ In order to expose the active oxidation state, Co^0 , reduction in H_2 gas flow is most commonly used prior to catalytic testing or characterisation.⁵⁴ Note that metallic cobalt usually has a fcc or hcp structure.⁹¹

As shown in Table 3, the most commonly employed reduction temperature prior to FTS is 400 °C, resulting in 15 to 70 % unreduced cobalt remaining as CoO . The unreduced proportion is higher when cobalt is strongly interacting with the support, such as in the case of alumina.⁶⁰ Cobalt reducibility is related to size because larger particles (> 20 nm) have less contact with support relative to the total volume and are therefore easier to reduce.⁵³ Cobalt aluminate modified alumina was investigated as an alternative support, which lowered the reduction temperature and resulted in the formation of hcp Co rather than fcc Co arrangement, which is more common with an Al_2O_3 support.⁹³

Since the cobalt surface is the active FTS site, the reaction is highly size and structure sensitive. Whilst there is some debate in the literature about the size dependent activity, as some authors claim it may be linked to the lower reducibility of smaller cobalt particles, in general the most active reported cobalt FTS catalysts are in the range of 5 to 30 nm cobalt diameter.^{54,60,92} Cobalt particles greater than 6 to 8 nm in diameter are needed to maximise the concentration of active sites to increase the activity and control the selectivity.^{2,60,92} Industrial cobalt catalysts typically contain ~ 20 nm particles, likely compromising on activity for their higher stability.⁹² An interesting computational study demonstrated the increase in B_5 and B_6 site concentrations in fcc cobalt clusters as the cluster diameter increases up to 8 nm.⁹⁴ This phenomenon may provide an alternative explanation for the FTS size sensitivity, however the nature of the active site for FTS is not well understood and as such this hypothesis remains conjecture.

Catalysts for FTS are often described by their CH₄ selectivity, as its formation is undesirable but regrettably common.³⁷ An effective FTS catalyst produces less than 4 % CH₄. Cobalt catalysts are favoured for their high C₅₊ selectivity, however smaller particles (less than 4 nm) are less selective to C₅₊, more selective to CH₄ (53 % cf 40 % for particles larger than 10 nm) and exhibit lower rates of reaction.⁹² The volcano-type relationship between cobalt crystallite size and C₅₊ selectivity when γ - and θ -alumina supports are used is evident in Figure 9.⁹⁰

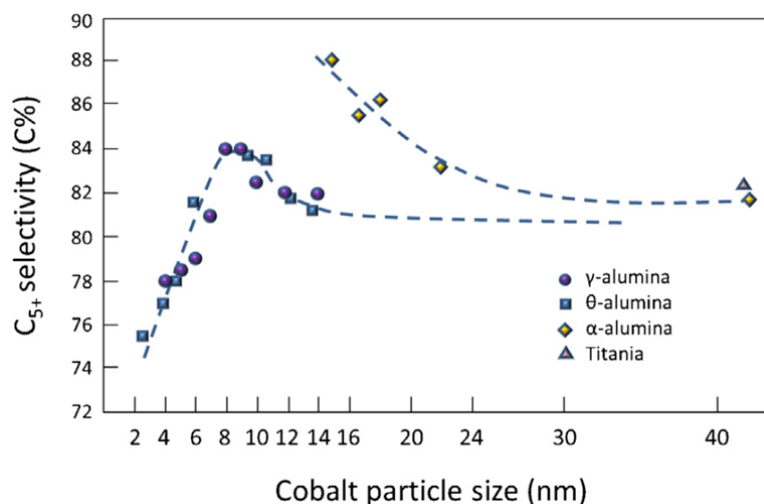


Figure 9. Relationship between C₅₊ selectivity and Co crystallite size. Directly reproduced from Rytter and Holmen.⁹⁰

Promoters are often added to FTS catalysts in order to increase reducibility, stability and FTS activity.⁹¹ The choice of promoter is significant and has been fairly extensively studied. The most common cobalt FTS noble metal promoters are platinum, rhenium and ruthenium, usually added in 0.05 to 0.1 wt% content.⁶⁰ Platinum and ruthenium catalyse the first reduction step (Co^{3+/2+} to Co²⁺) whereas rhenium decreases the temperature of the second step (Co²⁺ to Co⁰), due to the different promoter reduction temperatures.⁶⁰ Platinum and rhenium are most effective at decreasing the cobalt reduction temperature and maintaining cobalt in the metallic state.⁵³ For example, TPR profiles show the Co²⁺ reduction temperature decreases from 620 to 440 °C from the addition of platinum.³⁷ This promotion effect takes place by the accepted mechanism of hydrogen dissociation and spillover onto the promoter surface.^{2,91} The addition of rhenium offers further benefits such as increased dispersion, inhibition of nanoparticle agglomeration and improved catalyst lifetime.^{88,95} However, promoters can encourage sintering if the cobalt clusters formed as a result of the promotion effect are in close proximity.⁶⁰

Chromium and manganese have been found to increase the Co/Al₂O₃ reduction temperature. Copper poisons the catalyst surface and some metals (copper, palladium and gold) encourage undesirable C₁ to C₄ selectivity.^{52,60} Other metal oxides can also be added to the cobalt FTS catalyst in 1 to 10 wt% equivalent concentrations.² A range of metal oxides promoters has been studied, including Mg, Ca, Sr, Ba, Y, La, Ce, Ti, V, Mn, Zn, Zr and Mo, with La and V resulting in an increase in FTS activity.⁹⁶

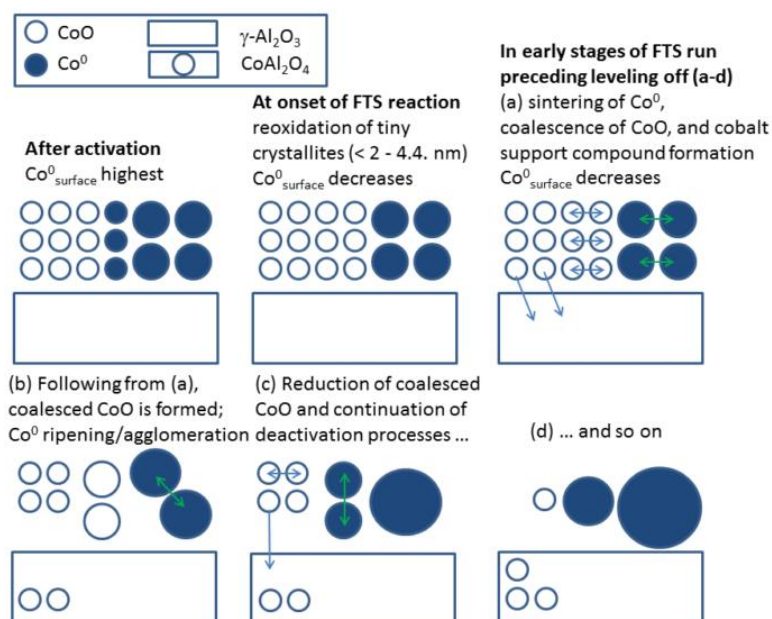


Figure 10. Deactivation by re-oxidation, aluminate formation and sintering in FTS Co/Al₂O₃ catalysts. Directly reproduced from Jacobs *et al.*⁹⁷.

During FTS testing, the catalysts often deactivate resulting in reduced productivity, representing a high cost for industry and a challenge for scientific research to overcome.⁹⁸ Some routes for cobalt FTS catalyst deactivation include poisoning by sulphur or nitrogen, cobalt surface reconstructions, formation of inert Co-carbon phases, re-oxidation of Co⁰, diffusion of cobalt into the support to form irreducible cobalt aluminates and sintering of the cobalt particles.^{60,98} The last three deactivation mechanisms are represented in Figure 10.

Oxidic supports tend to form irreducible and inactive mixed oxides during FTS operation, especially when the active metallic phase is highly disperse, containing particles 2 to 3 nm in diameter.^{59,92} Thus, Co/Al₂O₃ catalysts can be deactivated during FTS by the formation of cobalt aluminate, facilitated by the presence of H₂O, at the expense of Co⁰, the FTS active site.^{53,59,99} Water is always present at approximately 4 to 6 bar partial pressure during FTS but does not initiate the conversion of CO to CO₂ as cobalt is a poor water gas shift catalyst.⁵⁹ Oxidation of Co⁰ by the released H₂O is favoured under high temperature FTS operation (340

°C) or high CO conversion.⁵⁴ Small particles less than 6 nm are particularly susceptible to re-oxidation at high CO conversion.^{60,92} Higher loadings make the catalyst less susceptible to re-oxidation and results in less cobalt aluminate formation (~ 3 %) due to the formation of larger particles, making them attractive for use industrially as they are less prone to deactivation.⁶⁰

Owing to the FTS size-activity dependency, agglomeration of the metallic cobalt particles has detrimental and irreversible consequences on the catalytic activity. The issue of cobalt nanoparticle deactivation by sintering is the primary focus of the research carried out herein.

Table 3. Reported synthesis conditions, properties and FTS performance of some Co/Al₂O₃ catalysts.

Catalyst	Method ^a	Co (wt%)	Co size (nm)	Reduction T (°C)	FTS conditions	CO conversion (%)	Selectivity (%)		Ref.
							CH ₄	C ₅₊	
Co/Al ₂ O ₃	IWI	5	15.5	400	250 °C, 2H ₂ :1CO	12.5	56	31	99
Co/Al ₂ O ₃	Imp	15	9.3	450	210 °C, 10 bar 2H ₂ :1CO	35.6	15	72.8	100
Co/Al ₂ O ₃	Imp	13.5	16.4	400	230 °C, 1 bar 2H ₂ :1CO	40	36	38	91
Co/Al ₂ O ₃	ALD	13.8	8.3	400	230 °C, 1 bar 2H ₂ :1CO	60	32	31	91
Co/Al ₂ O ₃	DFP	10	n/a	500	230 °C, 20 bar 2H ₂ :1CO	n/a	19.4	64	101
CoPt/Al ₂ O ₃	IWI	25 (0.1 Pt)	7 - 15	400	220 °C, 20 bar 2H ₂ :1CO	69.9	8.6	84	54
CoRe/Al ₂ O ₃	Coimp	10 (1 Re)	n/a	400	220 °C, 18 bar ?H ₂ :1CO	57.6	n/a	n/a	102

^a IWI = incipient wetness impregnation, Imp = impregnation, ALD = atomic layer deposition, DFP = double flame pyrolysis, Coimp = co-impregnation.

Due to the industrial importance of Co/Al₂O₃ catalysts for FTS, there is an expansive literature addressing the subject of their activity, promotion and deactivation. As such, only a representative selection of publications have been summarised in Table 3 to highlight the effect of synthesis method, presence of promoters and reduction conditions on the catalytic activity and selectivity.

The temperature, pressure and $H_2:CO$ are quoted in Table 3 as it is worth noting that the change in operating conditions could contribute to differences in activity or selectivity. Due to these differences in experimental procedure and the absence of reported flow rates, the activity is presented as CO conversion, CH_4 selectivity and C_{5+} selectivity in Table 3.

The particle size of the materials summarised in Table 3 are all within the same order of magnitude so no effect on activity or selectivity can be deduced, despite the variation in loading from 5 to 25 wt% cobalt. The unpromoted catalyst synthesised by IWI with low loading exhibits very poor selectivity to C_{5+} , possibly because there may be some smaller particles which are more selective to CH_4 .¹⁰⁰ By contrast, Table 3 highlights the improved selectivity to C_{5+} from the addition of Pt promoter in the Co/Al_2O_3 catalyst produced by the same method.

2.4 Au/ γ -Al₂O₃ catalysts for CO oxidation

The toxicity of CO means that its conversion to CO₂ at low temperatures has a wide number of practical applications in mining, environmental and domestic sectors. For example in gas masks, gas sensors, H₂ purification and indoor air quality control.¹⁰³ Low temperature CO removal is also essential from H₂ feeds for fuel cells since the anode is poisoned by concentrations in excess of 10 ppm CO.¹⁰⁴

The unexpectedly high catalytic activity of nanoparticulate gold was first reported by Haruta¹⁰⁵ in 1987 for low temperature CO oxidation (Equation (5)). Since then, gold nanoparticles (NPs) have been extensively studied and have been found to be active for other catalytic applications including propene oxidation, water-gas shift reaction and the oxidation of ammonia and alcohols.¹⁰⁶ However, the long term stability of nanoparticulate gold catalysts needs to be addressed before large scale use in industrial applications is feasible.¹⁰⁷ Despite the high cost of gold, it is 1,000 times more active than platinum resulting in lower metal requirements.¹⁰³



The catalytic activity of gold for CO oxidation is dependent upon the interaction with the support, the particle size and dispersion, all of which are affected by the method of nanoparticle synthesis.¹⁵ The oxidation of CO by supported gold NPs is debated to proceed via either a water-assisted or an oxygen defect site mechanism, but recent evidence strongly supports the involvement of water.¹⁰⁸ At room temperature and below, CO oxidation is believed to take place at the perimeter interface between the metal and the support whereas above 60 °C, the reaction takes place on the gold surfaces, likely at the defect sites.¹¹ Gold itself does not adsorb O₂ well, and as such the role of the support in some cases is more than just for MNP stabilisation, it is also needed to activate the oxygen reagent.¹⁰⁹

A wide range of metal oxides have been reported to be effective supports for gold catalysts for CO oxidation at -70 °C by adsorbing O₂, including TiO₂, Fe₂O₃, Co₃O₄, NiO, Mg(OH)₂ and Be(OH)₂.¹⁵ Al₂O₃ does not adsorb CO or O₂ unlike the previously mentioned supports and is thus considered inert or irreducible, which usually results in lower catalytic activity of Au/Al₂O₃ materials.¹⁰⁸ The activity of Au/Al₂O₃ catalyst systems, which do not strongly adsorb CO or O₂ on the support, is thus attributed solely to the size effect of gold NPs.¹¹⁰ As such,

effective low temperature CO oxidation catalysts based on Au/Al₂O₃ are scarce due to the challenge to synthesise gold with a narrow particle size distribution and controllable sizes.

Nanoparticles larger than 10 nm are considered to be inert for CO oxidation but gold NPs smaller than 10 nm have a high concentration of peripheral edge and corner sites, which are capable of CO adsorption.¹⁰⁸ With an inert support, the particle size control is critical and must be within the range of 2 to 3 nm in order to enable and maximise adsorption of both CO and O₂ on the gold surface.^{109,111} It is worth noting that the optimum active particle size is dependent on the support. For example, 3d transition metal oxides require a particle size larger than 2 nm but Mg(OH)₂ and Be(OH)₂ supported catalysts are more active with gold NPs smaller than 2 nm.¹⁵

The choice of Au/Al₂O₃ preparation method is therefore critical in order to produce a narrow particle size distribution of gold nanoparticles less than 10 nm in diameter with a high concentration of 2 to 3 nm diameter particles. The impregnation method reportedly fails to synthesise highly dispersed gold nanoparticles for numerous reasons including a lower affinity to oxygen, the presence of chlorine impurities which encourage aggregation, the need for high temperature pre-treatment to form metallic gold and the relatively low melting point of gold (1064 °C) compared to other noble metals, which permits low temperature mobility.^{15,103,112} However, washing with a base (e.g. NH₃·H₂O) has been reported to be effective at removing chloride ions and producing small gold particles (2.4 nm).¹¹³

Co-precipitation and deposition-precipitation methods routinely lead to the formation of gold NPs smaller than 5 nm with loadings up to 3.3 wt% on various metal oxide supports.^{15,112} The deposition-precipitation is most suitable for gold addition to Al₂O₃, in which size of gold nanoparticles obtained is highly sensitivity to pH.^{15,103} Reportedly pH 8 to 10 results in the lowest temperature CO oxidation activity for Au/Al₂O₃, whilst materials obtained from acidic pH synthesis are active at higher temperatures.¹² This is due to the sequential hydroxylation of AuCl₄⁻ under basic conditions to yield Au(OH)₄⁻.¹¹⁴

Some reported pre-treatment conditions and resulting average particle size of Au/Al₂O₃ catalysts tested for CO oxidation are summarised in Table 4. For adsorption synthesis, HAuCl₄ has been demonstrated to be the most suitable gold precursor compared to NaAuCl₄ and NaAuBr₄, due to the presence of protons needed to form highly disperse gold catalysts.¹¹⁵ Washing procedures must also be carried out after Au/Al₂O₃ preparation, particularly if

H₂AuCl₄ is used, since chloride is a known poison for gold catalysts as it encourages gold agglomeration.¹⁷

Table 4. Reported properties, pre-treatment conditions and T₅₀ CO oxidation catalytic activity of Au/Al₂O₃ catalysts synthesised by different methods.

Method ^a	Au (wt%)	Au size (nm)	Calcination	Pre-treatment	T ₅₀ (°C)	Total GHSV (mL·g _{cat} ⁻¹ ·h ⁻¹)	Ref.
Imp (base wash)	1	2.4	400 °C, air	-	n/a	n/a	113
Imp	3	n/a	400 °C, air	-	333	20,000	116
CVD	5.3	3.5	300 °C, air	250 °C, air	-12	20,000	117
Ads (70°C)	2	1.9	300 °C, air	300 °C, air	150	23,000	115,118,119
DP (60°C, Na ₂ CO ₃ , pH 8-9)	2.4	2	250 °C, air	-	-20	80,000	120
DP (60°C, pH 8)	2.7	n/a	250 °C, air	-	-11	80,000	50
DP (70°C, Na ₂ CO ₃ , pH 8-9)	2.4	n/a	300 °C, air	150 °C, air	2	20,000	12
DP (60°C, Na ₂ CO ₃ , pH 8-9)	2.4	1.8	250 °C, air	-	-10	80,000	120
DP (70°C, NaOH, pH 8)	2.2	2.1	300 °C, air	250 °C, H ₂ /He	25	60,000	104
DP (70°C, urea, pH 8)	1.5	4.0	300 °C, air	300 °C, air	175	60,000	114
DP (lysine, NaOH, pH 5-6)	1	4.0	-	200 °C, air	29	15,000	7
DP (60°C, Na ₂ CO ₃ , pH 8-9)	0.53	3.0	-	250 °C, 14 vol% H ₂ /N ₂	~ 20	40,000	121
DP (80°C, urea)	0.96	2.7	-	300 °C, H ₂	n/a	180,000	110
DP (80°C, urea)	0.96	3.8	-	500 °C, 10 vol% O ₂ /He	n/a	180,000	110
CD (pre-formed Au NPs)	2.83	2.5	-	190 °C, CO/O ₂	-28	100,000	122

^a Impregnation = imp, chemical vapour deposition = CVD, ads = adsorption, DP = deposition-precipitation, CD = colloidal deposition.

Au⁰ is widely accepted to be the active oxidation state for CO oxidation but there is evidence to suggest involvement of Au⁺ in the mechanism.¹²³ The exact role of Au⁺ is unclear but its presence has been linked to an increased rate of reaction.¹²⁴ The pre-treatment of supported gold catalysts and thermal treatments is thus an important consideration for maximising catalytic activity as it may alter the desired Au⁰:Au⁺ ratio for a given metal-support combination.^{109,123} Pre-treatment of the catalyst may also result in necessary structural

changes.¹⁰⁹ For example Au/Al₂O₃ is most active after reduction in hydrogen at 200 °C compared to calcination in O₂ at 400 °C, which activates Au/TiO₂.¹²³ Pre-treatment under a mixture of H₂ and O₂ or H₂O at 100 °C has also been reported to enhance Au/Al₂O₃ activity.¹²³ The activity of Au/Al₂O₃ has been reported to be improved by trace water levels from 100 ppm to 5000 ppm as it facilitates O₂ activation at perimeter sites.¹¹ However, the optimum pre-treatment conditions of CO oxidation catalysts are often debated in the literature.

Since the temperature at which Au/Al₂O₃ becomes active for CO oxidation varies greatly between reports as a function of preparation method, pre-treatment conditions and thus particle size, there is not a common, suitable temperature at which to calculate and compare the rate of reaction. As such, the temperature at which 50 % conversion is reached, T₅₀, is used as a catalytic descriptor for CO oxidation for the materials summarised in Table 4. For the reported Au/Al₂O₃ catalysts in the literature, the CO oxidation T₅₀ ranges from -28 to 333 °C. The most active catalyst is produced by colloidal deposition of pre-formed gold nanoparticles and deposition-precipitation at pH 8 is the most common method.¹²²

2.5 Literature review conclusions

Metal nanoparticles offer exciting opportunities, particularly in the field of catalysis. A range of well-established methods varying in complexity are available for their synthesis with different size distribution control. However, the effective stabilisation of metal nanoparticles urgently needs to be addressed. Stabilisation techniques employing electrostatic or steric bulk or encapsulation are unsuitable for some catalytic applications due to the potential of active site blockages and the likelihood of mass transfer limitation. By contrast, stabilisation using bulk solid supports is appropriate for catalysis but are as yet unable to stabilise small metal nanoparticles under reaction conditions, enabling irreversible deactivation by agglomeration.

Based on the commercial interest of Sasol UK, the industrial sponsor of this project, γ - Al_2O_3 is used as the support material. This literature review highlights the advantages of nanostructuring the support by forming different morphologies at the nanoscale. Simple and reproducible hydrothermal methods for the production of nanostructured γ - Al_2O_3 have been summarised. An assessment of the literature suggests that it is possible to obtain a range of different shapes and sizes as a function of the synthesis conditions, however some inconsistencies were observed. As such, a systematic study of the effect of experimental parameters on the resulting product and elucidation of the hydrothermal formation mechanism is presented herein to produce a range of morphologically controlled γ - Al_2O_3 catalyst supports.

NH_3 decomposition and FTS catalytic applications for nanoparticulate cobalt catalysts supported on γ - Al_2O_3 have been reviewed, which are known to be size-sensitive reactions. The review of the current NH_3 decomposition activities with Co/γ - Al_2O_3 suggests that an enhanced activity is possible with particles below 2 nm, which have not yet been reported possibly due to their instability. For FTS, the strength of the interaction with the support and reducibility is an important consideration as it may also contribute to deactivation during testing. All these aspects will be investigated in this thesis, with a focus on stabilisation.

CO oxidation at sub-ambient temperatures has already been achieved using nanoparticulate gold-based catalysts. High activities under these conditions are not expected with Au/γ - Al_2O_3 due to the irreducibility of γ - Al_2O_3 . As this reaction is highly size sensitive, with 2 to 3 nm particles responsible for the majority of the activity, the reaction will provide unequivocal evidence to test the novel stabilisation strategy proposed herein.

Chapter 3 - Experimental methodology

3.1 Hydrothermal synthesis of nanostructured γ - Al_2O_3

Nanostructured alumina (γ - Al_2O_3) materials are synthesised using a hydrothermal method from the procedure reported by Yang.²¹ For a typical hydrothermal synthesis, 20 mL of NaOH solution (NaOH pellets, *Sigma Aldrich*, 98 wt%) is added to a 40 mL aqueous solution containing 0.026 mol of $\text{Al}(\text{NO}_3)_3 \cdot 9\text{H}_2\text{O}$ (*Sigma Aldrich/Honeywell*, 98 wt%) in a PTFE lined stainless steel autoclave. The reactants are stirred and the initial pH is recorded. The sealed autoclave is subsequently placed in an air-circulating oven, ensuring no temperature gradient, and kept there at the desired synthesis temperature for the reaction duration specified in Table 5. After the time has elapsed, the autoclave vessel is left to naturally cool to ambient temperature and the resulting white γ - AlOOH precipitate is separated from the supernatant solution by centrifugation (4000 rpm, 3 minutes). Following this, the solid product (γ - AlOOH) is dried overnight in a vacuum oven at 80 °C and crushed into a fine powder using a mortar and pestle. The γ - AlOOH powder is converted to γ - Al_2O_3 by calcination at 500 °C for 3 hours (3 °C·min⁻¹ rate). The final γ - Al_2O_3 product is washed with distilled water and dried overnight in a vacuum oven at 80 °C. The γ - Al_2O_3 yield (wt%) is calculated using Equation (6):

$$\text{Yield} = \left(1 - \frac{m_{\text{Al},\text{in}} - m_{\text{Al},\text{out}}}{m_{\text{Al},\text{in}}} \right) \times 100 \quad (6)$$

where $m_{\text{Al},\text{in}}$ is the initial amount of Al and $m_{\text{Al},\text{out}}$ is the amount of Al in the final product.

In order to understand the mechanism of formation of these materials, a systematic study of the effect of different parameters is carried out, including the NaOH:Al ratio (by changing the NaOH concentration) and the hydrothermal reaction temperature and time. These parameters are varied within the ranges shown in Table 5.

Table 5. Range of parameters varied during the hydrothermal synthesis of γ -Al₂O₃.

Experimental parameter	Range studied
NaOH:Al reactant ratio	0.77:1 - 6.5:1
Hydrothermal temperature	150 - 200 °C
Hydrothermal time	10 - 80 hours

Furthermore, in order to increase the aluminium yield, a recycle system is designed. In this case, a NaOH:Al ratio of 0.77:1 is used for the series of recycle assays (200 °C, 20 hours) in which the supernatant solution is re-used and depleted reagents are re-added to the autoclave (discussed in Chapter 4). NaOH is completely exhausted after the first batch reaction due to the 3NaOH:1Al reagent stoichiometry. As such, all the NaOH (0.020 mol) must be re-added and 35 % of Al(NO₃)₃·9H₂O (0.007 mol) is re-added in the same autoclave as the supernatant solution containing the existing 0.019 mol of Al³⁺, reproducing the same NaOH:Al molar ratio and pH in each assay. The hydrothermal synthesis and processing steps are subsequently carried out as described above.

3.2 Synthesis of supported nanoparticles

For the synthesis of cobalt nanoparticles, cobalt (II) nitrate hexahydrate (Co(NO₃)₂·(H₂O)₆, *Sigma Aldrich* 99.999 wt%) is used as the cobalt precursor, which contains 20.25 wt% cobalt.

For the synthesis of gold nanoparticles, chloroauric acid (HAuCl₄, *Sigma Aldrich* 99.99%) solution is used as the gold precursor, which contains 17.39 wt% gold. The density of the HAuCl₄ solution is 1.637 g·mL⁻¹.

Cobalt- and gold-catalysts are prepared following methods commonly used in the field, namely incipient wetness impregnation (IWI), wet impregnation (imp), adsorption (ads) and precipitation.¹³ For the precipitation method, some novel precipitants were explored. Full details of the different procedures are described in the following sub-sections.

3.2.1 Incipient wetness impregnation (IWI)

Incipient wetness impregnation consists of impregnation of the support material with a metal solution with a volume equal to the pore volume of the support. The pore volume is determined

by sequentially adding a fixed volume of solvent (H₂O is used herein) dropwise over a known mass of support until the support is completely wet. The H₂O pore volume for the γ -Al₂O₃ supports used to support metal nanoparticles herein are shown in Table 6. A metal precursor solution with a volume equal to the pore volume of the support is added dropwise to the dry support. The resulting material is dried under vacuum overnight at 80 °C. The dried sample is ground with a mortar and pestle. When indicated, the catalysts are calcined under air following the conditions described in Table 10.

Table 6. Pore volume with H₂O solvent for different γ -Al₂O₃ materials.

γ -Al ₂ O ₃ support	Synthesis time, temperature, NaOH:Al molar ratio	H ₂ O pore volume ^a (mL·g ⁻¹)
<i>Plate</i>	20h, 200 °C, 3.91:1	1.6
<i>40hfat</i>	40h, 200 °C, 0.77:1	1.2
<i>180thin</i>	20h, 180 °C, 0.77:1	n/a
<i>10hthin</i>	10h, 200 °C, 0.77:1	1.0
<i>Commercial</i>	n/a	1.0

^a Measured by wetting with H₂O.

3.2.2 Wet impregnation (imp)

Wet impregnation differs from IWI because in this case an excess volume of solvent is used rather than a calculated volume equivalent to the support pore volume. Typically, the support and metal precursor are added to a round-bottomed flask containing 100 mL of de-ionised H₂O. The flask is attached to a rotary evaporator to heat the mixture and remove the H₂O solvent quickly. The flask is positioned in a water bath heated to 60 °C, whilst rotating at 250 rpm under 150 mbar. Once all of the solvent has been removed the flask is placed in the vacuum oven at 80 °C for 30 minutes to remove any drops of water that may have returned back into the flask during removal. When indicated, the dried sample is calcined under air following the conditions in Table 10.

3.2.3 Adsorption/ion exchange (ads)

The distinction between adsorption and ion exchange depends on whether the metal ion in the precursor solution adsorbs electrostatically to a support site (adsorption) or whether they replace ions (e.g protons) on the surface of the support (ion exchange). The type of the method

occurring depends on the nature of the support and the metal precursor, but the experimental procedure is identical in both cases. A beaker containing 100 mL de-ionised H₂O is heated to 60 °C and the desired mass of support is added to the beaker. Once the mixture has reached 60 °C, the required amount of metal salt is added to the beaker under constant stirring. The beaker is heated for three hours, after which it is left to cool down and the contents are centrifuged (4000 rpm, 3 minutes). The solid is dried overnight at 80 °C under vacuum. When indicated, the dried sample is calcined under air following the conditions in Table 10.

3.2.4 Precipitation

The method for precipitation (or deposition-precipitation) is similar to the adsorption method outlined in the previous section, however, a precipitant is added prior to the addition of a metal precursor. Subsequently, the experimental procedure follows the same steps as the adsorption protocol.

For the synthesis of cobalt nanoparticles, the use of various precipitants have been explored including NaOH (NaOH pellets, *Sigma Aldrich*, 98 wt%), a carbonate buffer (*Omega*, 0.26 wt% Na₂CO₃, 0.21 wt% Na(CO₃)₂, 0.01 wt% bromthymol blue and 99.52 wt% H₂O), a borate buffer (*Fisher Chemical*, 0.5 wt% NaOH, 0.5 wt% H₃BO₃, 0.5 wt% KCl and 98.5 wt% H₂O) and urea (*Acros Organics*, 98 wt%).

Table 7. Amount of precipitant used for precipitation of **unsupported** cobalt.

Precipitant	Quantity	Number of moles (mol)
None	n/a	n/a
NaOH	25 mL	0.125
Carbonate buffer	12ml	n/a
Carbonate buffer	50ml	n/a
Borate buffer	12ml	n/a
Borate buffer	50ml	n/a
Urea	5 g	0.083
Urea	25 g	0.416

In order to maximise cobalt precipitation and optimise the quantity of precipitant required, cobalt was first precipitated in the absence of support. A 100 mL aqueous solution of Co(NO₃)₂·6H₂O (0.848 mmol, 0.2469 g) was stirred at 60 °C for 3 hours using different quantities of precipitant as shown in Table 7.

Based on the results of the unsupported precipitation assays, the quantity of the precipitant used with 0.5 g support is shown in Table 8.

Table 8. Amount of precipitant used for the synthesis of **supported** cobalt nanoparticles.

Precipitant	Quantity	Number of moles (mol)
NaOH	25 mL of 5 M solution	0.125
Carbonate buffer	50 mL	n/a
Borate buffer	50 mL	n/a
Urea	25 g	0.416

In addition, the cobalt particles precipitated by NaOH in the absence of a support were characterised and tested for NH₃ decomposition for comparison between the supported and unsupported catalysts.

3.2.5 Methods summary

A brief description of the methods described in this section is provided in Table 9. All the methods discussed are used in Chapter 4 to synthesise Co/ γ -Al₂O₃ catalysts. In Chapter 7, incipient wetness impregnation and adsorption are used to synthesise Au/ γ -Al₂O₃ catalysts.

Table 9. Summary of methods for supported metal nanoparticle synthesis.

Method	Notation	Brief description of method
Incipient wetness impregnation	<i>IWI</i>	Metal salt solution equivalent to support pore volume is pipetted over support.
Wet impregnation	<i>imp</i>	Support and metal salt in excess H ₂ O mixture. Solvent removed by rotary evaporation.
Adsorption	<i>ads</i>	Excess H ₂ O mixture of support and metal salt heated to 60 °C for 3 hours.
Precipitation by NaOH	<i>NaOH</i>	Excess H ₂ O mixture of support, NaOH and metal salt heated to 60 °C for 3 hours.
Precipitation by carbonate buffer	<i>carb</i>	Excess H ₂ O mixture of support, buffer and metal salt heated to 60 °C for 3 hours.
Precipitation by borate buffer	<i>bor</i>	Excess H ₂ O mixture of support, buffer and metal salt heated to 60 °C for 3 hours.
Precipitation by urea	<i>urea</i>	Excess H ₂ O mixture of support, urea and metal salt heated to 60 °C for 3 hours.

3.2.6 Processing conditions

When indicated, catalysts are calcined after the synthesis is complete. The calcination takes place in a static furnace under air atmosphere. The typical calcination conditions are summarised in Table 10 and the choice of conditions will be specified when materials are presented or discussed by the suffix “-calT”, where T is the calcination temperature.

When a catalyst is reduced prior to catalytic testing or characterisation, the suffix “-redT” is used, where T is the reduction temperature. Reduction at the desired temperature is carried out under 20 NmL·min⁻¹ pure H₂ flow for 45 minutes using a 5 °C·min⁻¹ ramp rate.

If the catalyst is not processed, the suffix “-fresh” is used in the catalyst nomenclature. Catalysts may be washed, which is noted by the suffix “-wash”.

Table 10. Calcination conditions used for different catalyst samples.

Material	Target temperature (°C)	Dwell time (hours)	Ramp rate (°C·min ⁻¹)
Co/ γ -Al ₂ O ₃ -cal250	250	5	1
Au/ γ -Al ₂ O ₃ -cal250	250	2	2

3.2.7 Summary of catalysts

The cobalt- and gold-catalysts synthesised with different methods, conditions, metal loadings or supports are summarised in Table 11 and Table 12 respectively. The nature of the γ -Al₂O₃ support morphology is denoted by “plate”, “40hfat” (low curvature nanorods), “180thin” (high curvature nanorods), “10hthin” (high curvature nanorods) and “commercial”. Detailed characterisation of the γ -Al₂O₃ supports can be found in Section 0.

Table 11. Summary of cobalt-based catalysts discussed in Chapters 5 and 6.

Catalyst name	Actual loading^a (wt%)	Method	Catalyst processing
<i>7.7Co/plate-IWI-fresh</i>	7.7	IWI	None
<i>0.9Co/plate-NaOH</i>	0.9	Precipitation by NaOH	None
<i>4.0Co/plate-NaOH</i>	4.0	Precipitation by NaOH	None
<i>6.7Co/plate-NaOH</i>	6.7	Precipitation by NaOH	None
<i>13.0Co/plate-NaOH</i>	13.0	Precipitation by NaOH	None
<i>0.9Co/40hfat-NaOH</i>	0.9	Precipitation by NaOH	None
<i>4.3Co/40hfat-NaOH</i>	4.3	Precipitation by NaOH	None
<i>7.6Co/40hfat-NaOH</i>	7.6	Precipitation by NaOH	None
<i>14.1Co/40hfat-NaOH</i>	14.1	Precipitation by NaOH	None
<i>0.9Co/180thin-NaOH</i>	0.9	Precipitation by NaOH	None
<i>5.2Co/180thin-NaOH</i>	5.2	Precipitation by NaOH	None
<i>9.1Co/180thin-NaOH</i>	9.1	Precipitation by NaOH	None
<i>16.6Co/180thin-NaOH</i>	16.6	Precipitation by NaOH	None
<i>1.1Co/commercial-NaOH</i>	1.1	Precipitation by NaOH	None
<i>4.6Co/commercial-NaOH</i>	4.6	Precipitation by NaOH	None
<i>8.1Co/commercial-NaOH</i>	8.1	Precipitation by NaOH	None
<i>15.1Co/commercial-NaOH</i>	15.1	Precipitation by NaOH	None
<i>7.7Co/plate-imp-cal250</i>	7.7	Wet impregnation	250 °C calcination
<i>1.4Co/plate-ads-cal250</i>	1.4	Adsorption	250 °C calcination
<i>6.8Co/plate-NaOH-cal250</i>	6.8	Precipitation by NaOH	250 °C calcination
<i>7.6Co/plate-carb-cal250</i>	7.6	Precipitation by carbonate buffer	250 °C calcination
<i>7.3Co/plate-bor-cal250</i>	7.3	Precipitation by borate buffer	250 °C calcination
<i>3.8Co/plate-urea-cal250</i>	3.8	Precipitation by urea	250 °C calcination
<i>1.0Co/plate-IWI-cal250</i>	1.0	IWI	250 °C calcination
<i>4.6Co/plate-IWI-cal250</i>	4.6	IWI	250 °C calcination
<i>7.7Co/plate-IWI-cal250</i>	7.7	IWI	250 °C calcination
<i>16.1Co/plate-IWI-cal250</i>	16.1	IWI	250 °C calcination
<i>0.9Co/40hfat-IWI-cal250</i>	0.9	IWI	250 °C calcination
<i>4.9Co/40hfat-IWI-cal250</i>	4.9	IWI	250 °C calcination
<i>9.2Co/40hfat-IWI-cal250</i>	9.2	IWI	250 °C calcination
<i>18.5Co/40hfat-IWI-cal250</i>	18.5	IWI	250 °C calcination
<i>1.3Co/10hthin-IWI-cal250</i>	1.3	IWI	250 °C calcination
<i>4.2Co/10hthin-IWI-cal250</i>	4.2	IWI	250 °C calcination
<i>9.7Co/10hthin-IWI-cal250</i>	9.7	IWI	250 °C calcination
<i>15.1Co/10hthin-IWI-cal250</i>	15.1	IWI	250 °C calcination
<i>5.3Co/commercial-IWI-cal250</i>	5.3	IWI	250 °C calcination
<i>8.8Co/commercial-IWI-cal250</i>	8.8	IWI	250 °C calcination

^a Calculated from ICP of the solid digested in aqua regia at 90 °C.

Table 12. Summary of gold-based catalysts discussed in Chapter 7.

Catalyst name	Theoretical loading (wt%)	Actual loading^a (wt%)	Method	Catalyst processing
<i>1.4Au/plate-IWI</i>	1.4	1.4	IWI	None
<i>0.7Au/plate-IWI-wash</i>	1.4	0.7	IWI	H ₂ O wash
<i>0.7Au/plate-IWI-wash-cal250</i>	1.4	0.7	IWI	H ₂ O wash + 250 °C calcination
<i>0.2Au/40hfat-IWI-wash</i>	1.4	0.2	IWI	H ₂ O wash
<i>0.3Au/10hthin-IWI-wash</i>	1.4	0.3	IWI	H ₂ O wash
<i>0.2Au/commercial-IWI-wash</i>	1.4	0.2	IWI	H ₂ O wash
<i>0.01Au/plate-ads-wash</i>	0.5	0.01	Adsorption	H ₂ O wash
<i>0.1Au/plate-ads-wash</i>	1.4	0.1	Adsorption	H ₂ O wash
<i>1.0Au/plate-ads-wash</i>	3.5	1.0	Adsorption	H ₂ O wash
<i>1.2Au/plate-ads-wash</i>	2.5	1.2	Adsorption	H ₂ O wash
<i>0.02Au/40hfat-ads-wash</i>	0.5	0.02	Adsorption	H ₂ O wash
<i>0.8Au/40hfat-ads-wash</i>	2.5	0.8	Adsorption	H ₂ O wash
<i>1.1Au/40hfat-ads-wash</i>	1.4	1.1	Adsorption	H ₂ O wash
<i>0.01Au/10hthin-ads-wash</i>	0.5	0.01	Adsorption	H ₂ O wash
<i>0.5Au/10hthin-ads-wash</i>	1.4	0.5	Adsorption	H ₂ O wash
<i>1.9Au/10hthin-ads-wash</i>	2.5	1.9	Adsorption	H ₂ O wash
<i>0.4Au/commercial-ads-wash</i>	0.5	0.4	Adsorption	H ₂ O wash
<i>1.2Au/commercial-ads-wash</i>	1.4	1.2	Adsorption	H ₂ O wash
<i>1.9Au/commercial-ads-wash</i>	2.5	1.9	Adsorption	H ₂ O wash

^a Calculated from ICP of the solid digested in aqua regia at 90 °C.

3.3 Materials characterisation

The γ -AlOOH and γ -Al₂O₃ supports and metal/ γ -Al₂O₃ catalysts were extensively characterised in order to gain a comprehensive understanding of their physical and chemical properties. The characterisation methods used and the experimental procedures are outlined in this section.

3.3.1 N₂ sorption

N₂ sorption measurements were carried out at -196 °C using a *Micromeritics ASAP 2020* apparatus. All samples were degassed at 150 °C prior to analysis. The specific surface area was calculated using the Brunauer–Emmett–Teller (BET) theory (Equation (7)) based on multi-layer adsorption, where V_a is the quantity of gas adsorbed at pressure P , P_0 is the saturation pressure of the gas and C is a constant.¹²⁵

$$\frac{P}{V_a(P_0-P)} = \frac{1}{V_m C} + \frac{C-1}{V_m C} \left(\frac{P}{P_0} \right) \quad (7)$$

From this equation, a straight line plot of $\frac{P}{V_a(P_0-P)}$ against $\frac{P}{P_0}$ in the x-axis range of 0.05 to 0.3 enables calculation of the volume of adsorbed gas V_m from the gradient and y-intercept.¹²⁵ The value of V_m is used to calculate the specific surface area s from Equation (8):

$$s = \frac{V_m \sigma N_A}{m V_o} \quad (8)$$

where σ is the area occupied by a single atom of adsorbate (16.2 Å² for nitrogen), N_A is Avogadro's constant (6.023 x 10²³ molecules·mol⁻¹), m is the mass of the sample and V_o is the molar volume, 22,414 cm³. Pore size distributions were obtained from the desorption data using the Barrett-Joyner-Halenda (BJH) method.¹²⁵

3.3.2 Electron microscopy

The specimens are prepared for transmission electron microscopy (TEM) analysis by placing one drop of a sonicated ethanol mixture of the sample onto a carbon-coated 300 mesh copper mesh grid (*C300Cu, EMResolutions*) or a Holey carbon 300 unit mesh copper grid (*Agar Scientific*).

Several different TEM instruments were used throughout the course of this work including *JEOL JEM1200EXII* (University of Bath), *JEOL CX 200* (University of Cambridge), *JEOL ARM200CF* (National University of Singapore) and *FEI Titan Themis* (University of St Andrews) instruments using 200 kV accelerating voltage.

High angle annular dark field scanning transmission electron microscopy (HAADF-STEM) was carried out using a *Tecnai F20* (University of Cambridge) and a *Nion UltraSTEM100* (Oak Ridge National Laboratory) using 200 kV and 100 kV accelerating voltage respectively. In the latter case, electron energy loss spectroscopy (EELS) is used to determine the elemental composition. HAADF-SEM was carried out on a *TESCAN MIRA3* (University of Cambridge) at 30kV accelerating voltage.

Scanning electron microscopy (SEM) was carried out using a *FEI Nova NanoSEM 450* (University of Cambridge) using 5 kV accelerating voltage and 2.5 a.u. spot size at a working distance of 4.8 mm. Samples were sputter coated with approximately 6 nm layer of platinum to minimise charging. Exact platinum coating thickness was not determined and thus SEM is used for qualitative data for size and morphology comparison rather than quantitative analysis.

3.3.3 Powder X-ray diffraction

Crystalline phase identification of the samples was carried out by powder X-ray diffraction (pXRD) analysis using a *Bruker D8 Advance* (University of Bath) and a *Siemens Kristalloflex* (University of Cambridge) diffractometer with Cu K α radiation (1.54 Å), operated at 40 kV and 40 mA. Approximately 50 mg of sample is placed on a silicon wafer disk covered with a thin layer of vacuum grease and secured into the holder. The samples are usually analysed in the 20 to 80° 2 θ range, using a step size of 0.1° and 1 s·step⁻¹.

In addition, pXRD with the capacity for *in situ* reduction was carried out using *PANalytical X'Pert Pro* with a *PIXcel* detector (Sasol UK). The same voltage and current conditions are used (40 kV and 40 mA) as before but a Co K α X-ray source is used. The samples are analysed in the 20 to 80° 2 θ range, using a step size of 0.02626° and 306 s·step⁻¹ under 20 mL·min⁻¹ of pure H₂ flow. A scan is taken at room temperature and every 100 °C until the maximum temperature of 600 °C is reached. The temperature is held constant at the set point while the scan takes place over the complete X-ray angle range (approximately one hour) and then the sample is ramped to the next set point at 5 °C·min⁻¹.

The diffraction pattern of X-rays broadens when crystallites are smaller than 100 nm, which can be exploited to calculate the average crystallite size.¹²⁶ The size d can be calculated from the pXRD diffractogram using the full width at half maximum (FWHM), B , of the dominant peak with the Scherrer equation (Equation (9)):

$$d = \frac{0.9 \cdot \lambda}{B \cos \theta} \quad (9)$$

where λ is the wavelength of the $K\alpha$ source (1.54 Å for Cu and 1.79 Å for Co) and θ is the associated diffraction angle. This calculation technique can typically be applied to metal or metal oxide crystallites in the range 3.5 to 60 nm. Crystallites smaller than 3.5 nm show a broad and diffuse line that may not be detectable and the line broadening is too small for crystallites larger than 60 nm.¹²⁶ The actual values depend on the instrument used.

$$d_{Co^0} = 0.75 \cdot d_{Co_3O_4} \quad (10)$$

The approximate dominant peak positions and JCPDS card number of the relevant compounds are summarised in Table 13. Due to the close proximity of the $\sim 44^\circ$ cubic Co^0 diffraction peak to the 46° γ - Al_2O_3 support peak, the peaks in reduced Co/γ - Al_2O_3 samples were deconvoluted using a Gaussian fitted function in *OriginPro 2015* graphing software to obtain a more accurate FWHM. Conventionally when *in situ* reduction equipment are not available, Co_3O_4 particle size is estimated by converting to Co^0 using the relationship in Equation 10.⁵⁵

Table 13. Approximate **dominant** peak angles and corresponding JCPDS card numbers for relevant compounds.

Compound	Dominant peak position(s) (°)	JCPDS Card No.
γ - Al_2O_3	46 (400) and 67 (440)	10-0425
Cubic Co^0	44	15-806
Co_3O_4	37	43-1003
$CoOOH$	20	14-0673
$NaNO_3$	28	36-1474
$NaAlO_2$	29	33-1200
Au^0	38	04-0784

3.3.4 Temperature programmed reduction

Temperature programmed reduction (TPR) was carried out using a *Micromeritics Autochem 2920* with $20 \text{ mL} \cdot \text{min}^{-1}$ of 5 vol% H_2 in argon from ambient temperature to $900 \text{ }^\circ\text{C}$ at a heating ramp rate of $5 \text{ }^\circ\text{C} \cdot \text{min}^{-1}$. The outlet gas is analysed using a thermal conductivity detector (TCD) using the inlet gas composition as a reference. As the conductivity of hydrogen is higher than for argon, the signal is inverted to obtain positive peaks when reduction takes place. In certain instances, a quadrupole mass spectrometer (*Cirrus 2, MKS*) connected to the outlet of the *Autochem 2920* is used for the detection of ions of interest.

For TPR analysis of the catalysts, the rate of temperature increase is selected to be $5 \text{ }^\circ\text{C} \cdot \text{min}^{-1}$ during reduction as TPR profiles of an example catalyst (*16.1Co/plate-IWI-cal250*) using different temperature ramp rates (2, 5 and $10 \text{ }^\circ\text{C} \cdot \text{min}^{-1}$), demonstrated negligible differences to the peak position and relative shape.

3.3.5 CO pulse chemisorption

The metallic dispersion (number of exposed surface atoms relative to the total number of atoms) and particle size can be estimated using pulse chemisorption of a probe molecule (such as CO) using a *Micromeritics Autochem 2920*.

The specimen is reduced *in situ* for 45 minutes prior to chemisorption analysis using $50 \text{ mL} \cdot \text{min}^{-1}$ 5 vol% H_2/Ar at a heating rate of $5 \text{ }^\circ\text{C} \cdot \text{min}^{-1}$. After reduction is complete, the sample is cooled down to the specific chemisorption temperature depending on the metal and held constantly at this temperature during analysis. The chemisorption temperature depends on the nature of the metal and its interaction with the probe molecule and the determined temperatures are shown in Table 14. A known volume ($\sim 0.5 \text{ cm}^3$) of 5 vol% CO in helium is pulsed through the sample up to ten times and the amount of CO eluted is measured by the TCD.

The known stoichiometry factor (SF) and the volume of gas sorbed V_s calculated from pulse chemisorption are used to estimate the metallic dispersion D and hemispherical metallic particle size d using Equation (11) and Equation (12) respectively, where M_r is the molecular weight, m is the mass of sample, M is the metal loading, N_A is Avogadro's constant, A_g is the cross-sectional area of the metal (see Table 14) and ρ is the metal density.^{125,127}

$$D = \frac{V_s \cdot SF \cdot M_r}{m \cdot M \cdot 22414} \quad (11)$$

$$d = \frac{6 \cdot M \cdot 22414 \cdot 10^{21}}{SF \cdot V_s \cdot N_A \cdot A_g \cdot \rho} \quad (12)$$

The SF of the adsorbate:metal chemisorption interaction depends on the species involved and the values are given in Table 14. The CO:Au chemisorption ratio of 1:1 is commonly accepted. By contrast, the CO:Co ratio is debated and reported to be between 0.4:1 to 2.3:1, depending on the support, metal loading, synthesis method and the prevalence of defects.^{128–131} Due to the difficulty and impracticality of determining the precise CO:Co per sample, it is commonplace for the ratio to be averaged and assumed to be 1:1.⁸²

Table 14. Parameters used for cobalt and gold CO pulse chemisorption.¹³¹

Metal	Adsorbate	Stoichiometric factor, SF	Chemisorption temperature (°C)	Atom cross-sectional area, A_g (nm ²)	Density, ρ (g·cm ⁻³)
Cobalt	CO	1	35	0.0662	8.9
Gold	CO	1	-80	0.0869	19.3

Chemisorption of CO on Co is usually carried out at temperatures slightly higher than ambient.^{57,82} Consequently, 35 °C is used herein for pulse chemisorption of CO on Co.

It is widely practised that pulse chemisorption of CO on Au is carried out at cryogenic conditions, however there is limited information available in the literature about optimum analysis temperatures. As such, a range of temperatures for pulse CO chemisorption were tested with a blank support (γ -Al₂O₃ *plate*, Figure 11) and an example Au/ γ -Al₂O₃ catalyst (*0.5Au/10hrod-IE-WRT*, Figure 12), in order to determine a suitable chemisorption temperature, without CO condensing (i.e. physisorbing) on the analysed sample as a result of the low temperature.

Theoretically the support does not chemisorb CO, which is a realistic assumption for γ -Al₂O₃. Therefore the temperature at which there is CO uptake indicates physisorption. Analysis of the pulse chemisorption trace (Figure 11) and the associated MS data of the γ -Al₂O₃ *plate* support confirms that CO condenses on the support at -120 °C. At -90 °C and -100 °C, the TCD trace also shows CO uptake which may be due to condensation on the support. However, at -80 °C, there is no CO uptake, thus -80 °C is a suitable chemisorption temperature for Au/ γ -Al₂O₃.

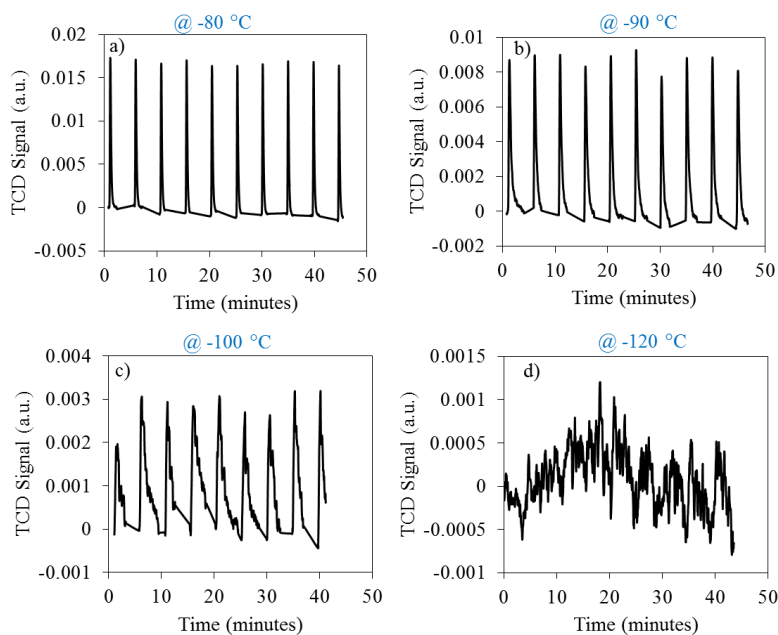


Figure 11. TCD signal during pulse chemisorption of γ -Al₂O₃ plate support. a) -80 °C, b) -90 °C, c) -100 °C and d) -120 °C.

In order to confirm the choice of chemisorption temperature, pulse chemisorption was carried out at -60 °C, -80 °C and -100 °C on *0.5Au/10hrod-IE-WRT* (Au/ γ -Al₂O₃). The TCD traces are shown in Figure 12 and the associated calculated properties are shown in Table 15. Figure 12 shows a noisy trace for the analysis at -100 °C and a deceptively small particle size, probably due to the condensation of CO as discussed earlier. At -60 °C and -80 °C the TCD trace is stable but distinct particle sizes are calculated. The optimum chemisorption temperature of gold can change depending on the type of gold defect sites, such as edges or corners and their concentration.¹³² Thus, as the chemisorption temperature is decreased from -60 °C to -80 °C corner Au sites can now be chemisorbed upon.¹³² Based on this thorough assessment, the chemisorption temperature of -80 °C is used for the characterisation of Au/ γ -Al₂O₃ materials.

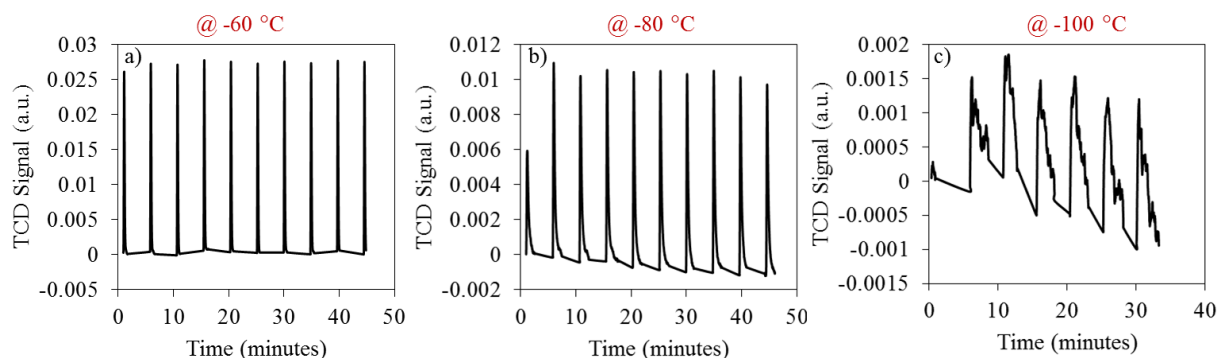


Figure 12. TCD signal during pulse chemisorption of *0.5Au/10hrod-IE-WRT*. a) -60 °C, b) -80 °C and c) -100 °C.

Table 15. Estimated dispersion and particle size of *0.5Au/10hRod-IE-WRT* from pulse CO chemisorption at different cryogenic conditions.

Chemisorption temperature (°C)	Estimated dispersion, D (%)	Estimated particle size, d (nm)
-60	4.8	24.6
-80	15.0	7.8
-100	55.7	2.1

3.3.6 ²⁷Al nuclear magnetic resonance (NMR)

²⁷Al nuclear magnetic resonance (NMR) experiments were run on a 500 MHz Bruker AV500 with 130.32 MHz resonance frequency, using a ca. 90 degree pulse, no proton decoupling (pulse sequence “zg”), spectral width of 500 ppm, acquisition time of 0.12 second, delay time of 1 second and 20 to 1200 scans for each experiment. All solutions were diluted in D₂O prior to analysis.

3.3.7 Thermogravimetric analysis

Thermogravimetric analyses (TGA) on γ -AlOOH were carried out using a TGA-DTA 92 Type 31/1190, Setsoft 2000 instrument from 25 to 600 °C at a heating rate of 10 °C·min⁻¹ using nitrogen as a carrier gas.

TGA on γ -Al₂O₃ was carried out using a Perkin Elmer Pyris 1 TGA using 20 ml·min⁻¹ flow of pure nitrogen. Approximately 2 mg of sample was degassed at 100 °C (rate 10 °C·min⁻¹) for 30 minutes. Subsequently, the sample was heated to 600 °C (rate 10 °C·min⁻¹). The crucible was cooled down to room temperature naturally.

3.3.8 Inductively coupled plasma optical emission spectroscopy

Inductively coupled plasma optical emission spectroscopy (ICP-OES) is used for precise chemical composition determination.¹³³ ICP-OES is carried out on liquid samples, which are usually diluted to give solutions with low ppm concentration (~ 1 ppm). To analyse solids, acid digestion of the sample is carried out using aqua regia (3:1 acid mixture of 36 vol% HCl and 70 vol% HNO₃). The mixtures are added to a water bath at 50 °C, which is gradually heated to 90 °C. When the solutions are cool, the necessary dilutions are carried out. A Perkin Elmer

Optima 2100 DV spectrometer was used for the analysis with argon as the torch gas and nitrogen for purging. The obtained results are calibrated with the appropriate metal standards for cobalt, gold and sodium (1 to 10 mg·L⁻¹).

3.3.9 X-ray photoelectron spectroscopy

X-ray photoelectron spectroscopy (XPS) provides information about the elemental composition, concentration and oxidation states of a sample.¹³⁴

XPS analyses were carried out on a *KRATOS Axis Ultra DLD* instrument. Approximately 10 mg of sample was mounted as a loose powder in a molybdenum sample holder. The measurements were carried out using an achromatic Al $\text{K}\alpha$ source (15 kV, 10 mA). The instrument was operated with the following parameters: hybrid-focussing lens, slot aperture, neutraliser (1.45 A, 2.5 eV). The survey spectrum was collected using a dwell time of 100 ms, a step size of 1 eV and a pass energy of 160 eV. For the individual regions, the dwell time was 1000 ms, the step size was 0.1 eV and the pass energy was 40 eV. The position of aluminium (Al 2p) at 74.0 eV was used for spectral calibration. The XPS analysis and the fitting of the regions was carried out with the software CasaXPS (version 2.3.15). The surface atomic composition (%) was determined using the individual regions. For some samples, *in situ* reduction was carried out in the reaction chamber at 580 °C for 45 minutes at a heating rate of 5 °C·min⁻¹ under 20 mL·min⁻¹ pure H₂ flow.

3.4 CO oxidation catalytic rig design and construction

A catalytic flow rig was designed, built, commissioned and operated as part of this PhD project. A labelled photograph of the catalytic rig is shown in Figure 13 and a P&ID schematic is shown in Figure 14. The purpose of this aspect of the project is to gain rig construction engineering expertise and facilitate the catalytic testing of Au/ γ -Al₂O₃ catalysts in a model reaction. The rig is primarily designed with the intent for the CO oxidation reaction but the design is flexible, in terms of inlet gases and methods of outlet analysis. The catalytic results will be used to assess the stability of Au/ γ -Al₂O₃ catalysts under experimental conditions in order to validate the research hypothesis.

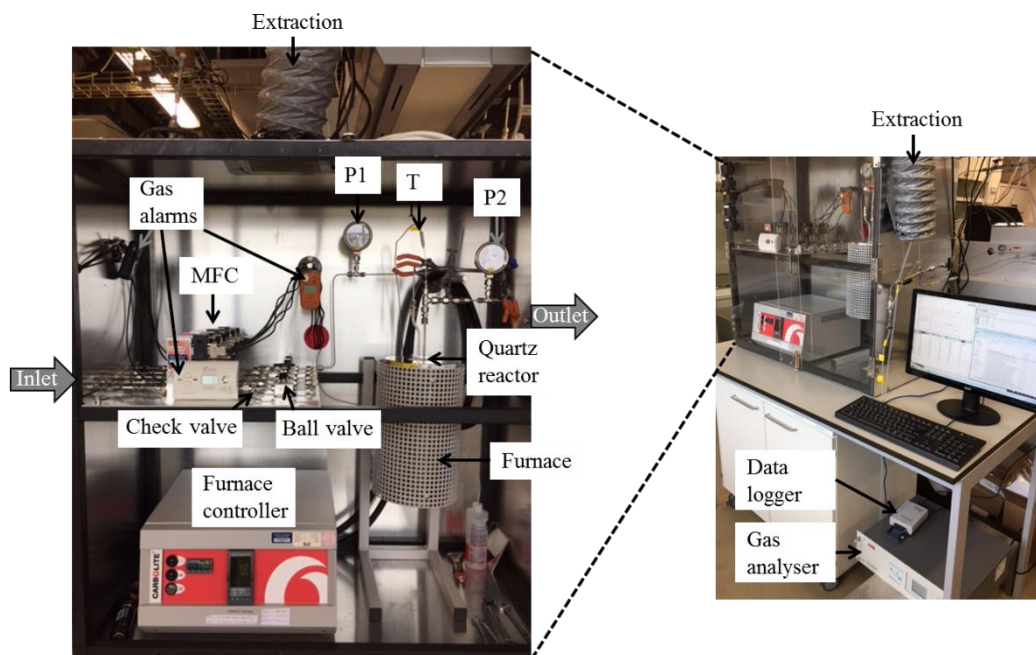


Figure 13. Annotated photograph of the CO oxidation catalytic testing rig.

There are five inlet gas lines for 5 vol% CO/He (99.9 vol % CO & 99.996 vol% He, *BOC*), CO₂ (100.0 %, dry ice), 5 vol% O₂/He (99.6 vol% O₂ & 99.996 vol% He, *BOC*), H₂ (99.999 vol%, *Air Liquide*) and He (99.999 vol%, *Air Liquide*). The inlet flow of each gas is controlled by Bronkhorst® mass flow controllers (MFCs). The inlet flow enters the rig via bulkhead fittings and before the gases are mixed they flow through a filter to the MFC. A check valve prevents mixing of gases by back flow and a ball valve allows manual closure of the gas line. All the stainless steel Swagelok® tubing is 1/8" outer diameter until the flow reaches the quartz reactor, which has 1/4" outer diameter.

The reactor is heated using a Carbolyte™ tube furnace 30 cm in length, with an opening at either end. Quartz U-tube reactors with 0.4 cm internal diameter (ID) have been commissioned to a size specification so the reactor sits vertically in the central 18 cm of the furnace to ensure a constant temperature across the catalyst bed. The use of U-shaped reactors allows the gases to reach the reaction temperature before arriving at the catalyst bed.

At the entrance to the reactor, a PTFE ferrule is used for the stainless steel fitting for the quartz reactor. The catalyst bed is contained in the second half (right hand side) of the reactor. Prior to reaching the catalyst bed, the gas flow passes through 175 mg of fine silicon carbide with 53 µm diameter to ensure conditions of plug flow. The fixed catalyst bed contains 25 mg of catalyst diluted with 600 mg of coarse silicon carbide (average 360 µm diameter), resulting in a catalyst bed of 0.38 cm³ volume. The catalyst bed is held in place with quartz wool, which

also acts to prevent any catalyst particles from being carried through the rig with the flow. On exiting the reactor, a graphite ferrule is used as it can withstand high temperatures. The outlet flow passes out of the rig enclosure by a bulkhead fitting and flows either to vent or through a non-dispersive IR gas analyser (*ABB, EL3020-Uras 26*).

There are two pressure indicators, one before (P_1) and one after (P_2) the reactor, allowing monitoring of the pressure in the system and the pressure drop across the catalytic bed. The temperature is recorded by a type K thermocouple (T in Figure 13) with the tip positioned just above the top of the catalyst bed.

The thermocouple data is acquired using a *PICO® TC-08* data logger and the gas analyser signal is obtained using a *PICO® PICOLOG 1216* logger. Both signals are logged simultaneously every two seconds using the *PicoLog* software (version 5.25.3).

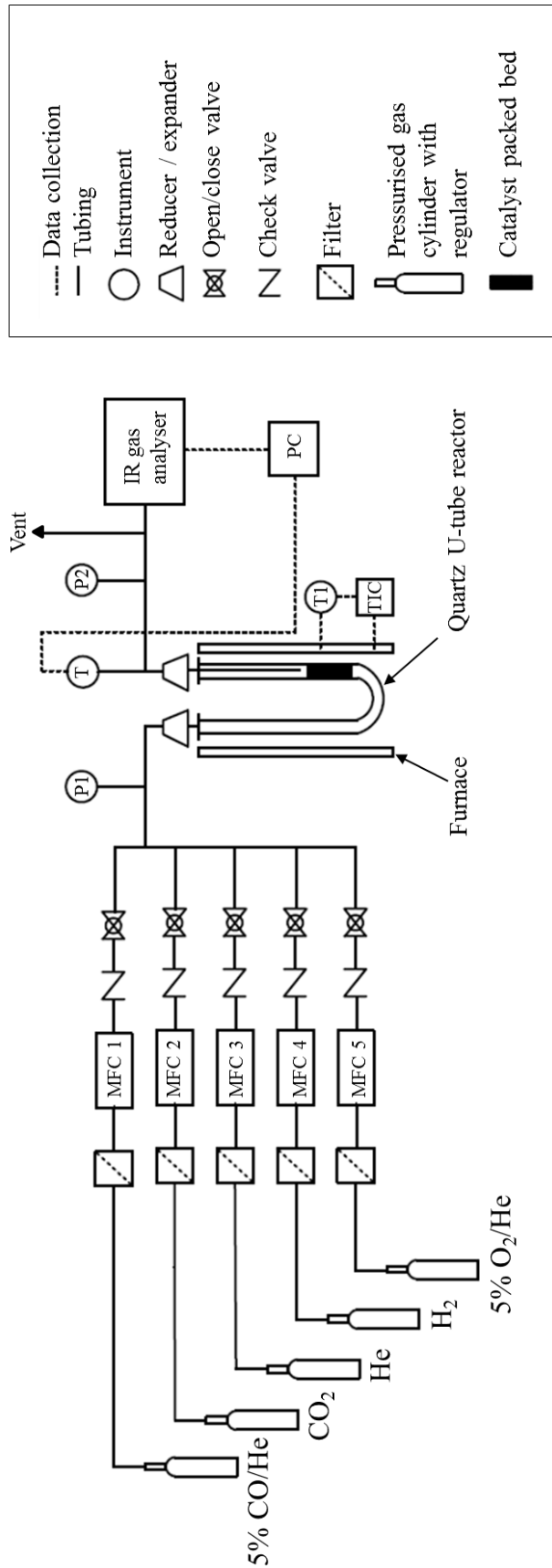


Figure 14. P&ID schematic of the CO oxidation catalytic rig. TIC refers to a digital control instrument.

The rig operates under near plug flow conditions as shown in Figure 15 when $10 \text{ mL}\cdot\text{min}^{-1}$ of 5 vol% CO/He is introduced into the pure helium flow ($290 \text{ mL}\cdot\text{min}^{-1}$) at 1163 s.

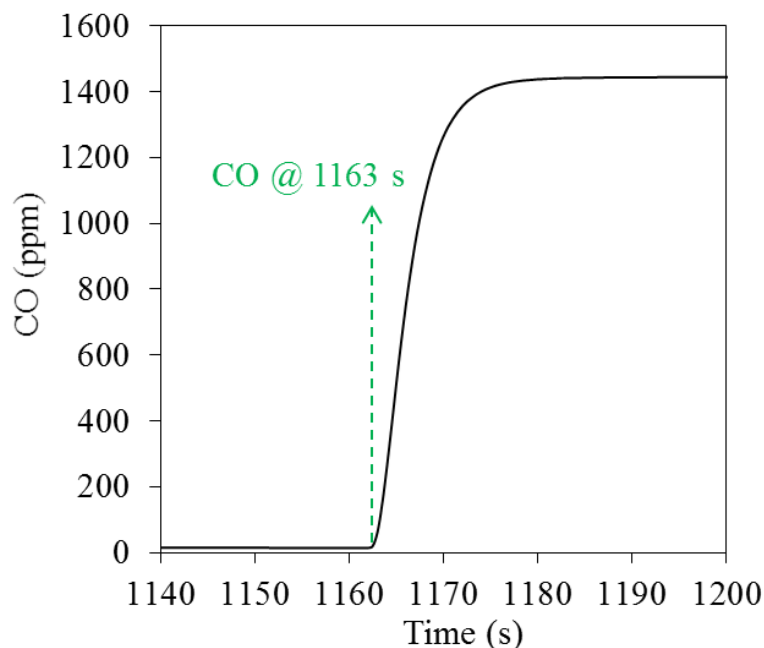


Figure 15. Response of gas analyser upon introduction of CO into the gas stream.

The time delay between the thermocouple and gas analyser arises from two components: the physical time delay for the gas at the thermocouple to reach the gas analyser and the response time of the gas analyser itself. The overall response time and the difference between the two recorded signals is calculated to be 40 s.

3.4.1 Rig safety

As highly toxic and flammable gases are used in this experimental setup, safety is of principal importance. CO is highly toxic with a lower exposure limit of 25 ppm. The non-odorous and colourless nature of CO and H₂ make leaks impossible to detect instinctively by smell or sight. Hydrogen gas is highly flammable in air (4 to 75 vol%) as is carbon monoxide (12.5 to 74 vol%). However, a 5 vol% CO/He cylinder is used, which is not flammable at this concentration.

Handheld CO and H₂ gas alarms are placed within the rig enclosure to alert the rig operator and laboratory users of a gas leak. In addition, the CO line is fitted with a solenoid valve which closes the gas line if the sensor detects greater than 25 ppm CO concentration in the laboratory. The rig is connected to two extraction points (Figure 13) and the laboratory is well ventilated with 3.2 air changes per minute.

All of the gas lines were leak tested and pressure tested overnight during commissioning of the rig and in the case of CO, helium was used for the pressure test. All of the fittings in the rig after the point of gas mixing were pressure tested with helium.

The fittings that are opened and closed to secure the quartz reactor before use are leak tested with helium after every fitting closure before CO or H₂ is introduced to the system.

3.4.2 Calibrations: Furnace, mass flow controller and gas analyser

In order to determine the temperature of the gas flow in the catalyst bed in the reactor, the set point temperature of the tubular furnace was calibrated against the thermocouple reading. The resulting straight line calibration curve is shown in Figure 16. This calibration curve is used to calculate the set point to achieve a desired temperature.

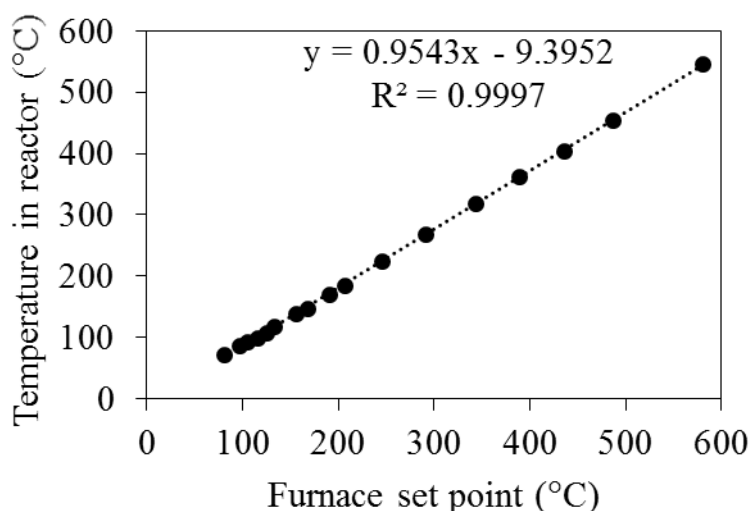


Figure 16. Temperature calibration curve for the furnace.

The MFCs are calibrated with a bubble meter using six flow rate set points with the appropriate gas, e.g. the hydrogen MFC is calibrated with hydrogen gas. The MFCs are calibrated by the supplier for N₂ balance gas but for this set up helium is used, so a 1.41 conversion factor (from the Bronkhorst® manual) is used to convert N₂ to He.

The gas analyser is calibrated weekly to confirm the straight line relationship used to convert to the accurate flow composition. The gas analyser is further calibrated daily before use at two points (0 ppm and 3000 ppm CO) to check the calibration reproducibility in case of any drift.

3.4.3 Data reproducibility

Errors in a gas analyser reading predominantly arise from variations in temperature, pressure or cross-interference. The temperature and pressure are compensated for in the measurement cell of the ABB analyser. In addition, the cross-interference of CO and CO₂, both IR active, is compensated for during the factory assembly of the analyser and should be no higher than 1 % of the measurement range i.e. ± 40 ppm.

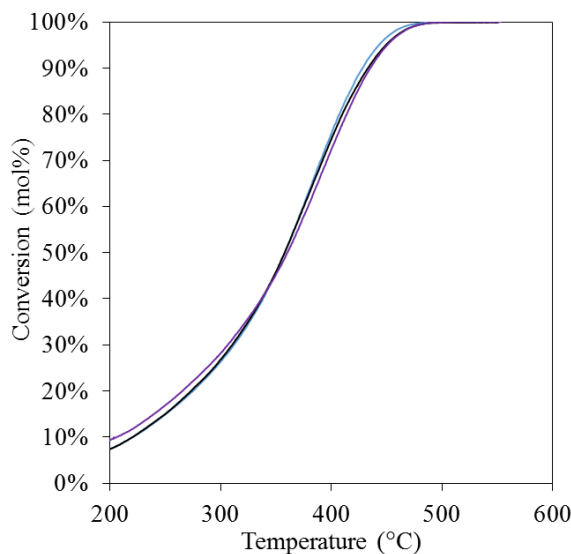


Figure 17. CO oxidation activity of *0.5Au/10hrod-IE-wash-red200* repeated three times. Trial #1 (blue), trial #2 (black) and trial #3 (purple).

A standard catalytic test was repeated three times with the same $\text{Au}/\gamma\text{-Al}_2\text{O}_3$ catalyst (*0.5Au/10hRod-IE-WRT*) under identical reduction and CO oxidation conditions (outlined in Section 3.4.4). The conversion of the first run as a function of temperature for the three trials are shown in Figure 17 and the CO conversion at different temperatures is shown in Table 16.

Table 16. CO conversion at different temperature for three separate catalytic trials of *0.5Au/10hrod-IE-wash-red200*.

Temperature (°C)	CO conversion (%)				Standard deviation
	Trial #1	Trial #2	Trial #3	Average	
200	7.2	7.2	9.1	7.8	1.1
300	25.9	25.6	27.4	26.3	1.0
400	72.8	73.8	70.5	72.3	1.7
500	99.8	100.0	99.9	99.9	0.1

Figure 17 shows a good agreement and reproducibility of the separate catalytic tests of *0.5Au/10hrod-IE-WRT* pre-reduced *in situ* at 200 °C. Considering the values for CO conversion at different temperatures, it seems that at low conversion (< 25 %) the values vary by approximately 1 % but higher conversions (> 70 %) have a standard deviation of ~ 2 %.

3.4.4 Operation of the CO oxidation rig

In the standard operating procedure of the rig, the reactor is set up containing 25 mg of catalyst and SiC diluent (described in Section 3.4). The sample is reduced *in situ* at 200 °C if required and then the CO oxidation reaction takes place.

A 300 mL·min⁻¹ total flow rate is used, composed of 18 NmL·min⁻¹ of 5 vol% CO/He, 18 NmL·min⁻¹ of 5 vol% O₂/He and 264 NmL·min⁻¹ of He. These flow rates result in a concentration of 3000 ppm CO and 3000 ppm O₂, balanced in helium. With this flow rate the residence time in the catalyst bed is equal to 0.075 s at room temperature. The flow conditions results in ~ 0.5 bar pressure drop across the catalyst bed at room temperature, determined by the difference between the P₁ and P₂ pressure indicators. The pressure drop is calculated in Section 3.4.6. The gas hourly space velocity (GHSV) is calculated to be 2160 mL_{CO}·g_{cat}⁻¹·h⁻¹ in terms of the mass of catalyst or 142 h⁻¹ with respect to the volume of the catalyst bed (0.38 cm³).

Based on the stoichiometry of the CO oxidation (Reaction (5)) only half as much oxygen to CO is required but herein a 1:1 reagent ratio is used, representing an excess of oxygen according to the theoretical stoichiometry.

During the reaction, the thermocouple and gas analyser signal are continuously analysed and logged every 2 seconds. The furnace temperature is ramped at 5 °C·min⁻¹ to 550 °C three times for a standard catalytic test. To gain information about the thermal stability of a catalyst, a stress test may be used whereby the furnace is ramped (5 °C·min⁻¹) from a baseline point to consecutively higher temperatures returning to the same initial temperature before each subsequent increase.

3.4.5 Catalytic data processing

The gas analyser data is combined with the corresponding temperature data recorded at the catalyst bed in order to plot conversion against temperature. The mass balance is carried out using the CO ppm signal.

The gas analyser emits a 4-20 mA analogue output, which is converted into a voltage using a 120 Ω resistor (voltage = current \cdot resistance), so the signal can be read by the *PICOLOG 1216* data logger. Given the gas analyser range, 0 to 4000 ppm for CO and CO₂, the maximum voltage range is 480 to 2400 mV. Equation (13) is derived to convert the recorded signal in mV to ppm.

$$\text{Signal (ppm)} = \frac{\text{signal (mV)} - 480 \text{ mV}}{2400 \text{ mV}} \times 4000 \text{ ppm} \quad (13)$$

Negligible conversion is achieved in a blank experiment with an empty reactor or with SiC only. Figure 18 demonstrates that the rig is operating under steady state, differential conditions as the data obtained from continuous ramping at 5 $^{\circ}\text{C}\cdot\text{min}^{-1}$ (black line) and individual holding temperatures (red cross) are equal.

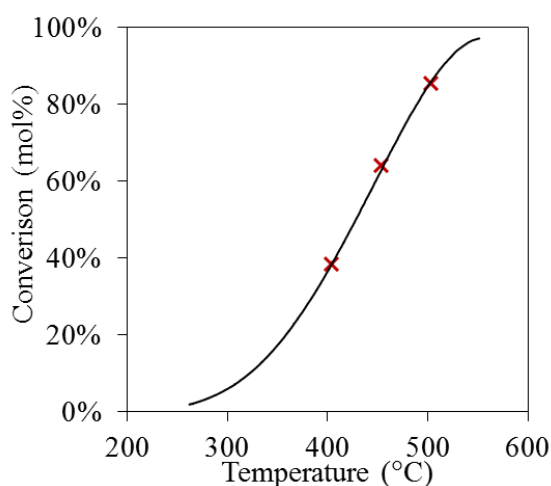


Figure 18. CO conversion data of *0.1Au/plate-ads-wash-red200* analysed by continuous logging (black line) and by averaging the values from holding at three set point (red cross).

3.4.6 Pressure drop

The catalyst bed contains 21.9 wt% fine SiC (53 μm), 75.0 wt% coarse SiC (360 μm) and 3.1 wt% catalyst (average 237 μm), giving rise to a weighted average particle size of 289 μm .

The particle Reynolds number, R_e is 35, assuming pure helium flow (actual He composition is 99.4 vol%) and spherical particles (average diameter 289 μm). R_e is calculated for a packed bed using Equation (14), where ρ is the density, u is the velocity, d is the diameter of the particles, ϵ is the voidage and μ is the viscosity. As such, the interstitial flow between the voids in the catalyst bed is classified as laminar, typical for plug flow through a packed bed.

$$R_e = \frac{\rho \cdot u \cdot d}{\mu \cdot (1 - \epsilon)} \quad (14)$$

$$\Delta p = \frac{150 \cdot \mu \cdot L \cdot v_s \cdot (1 - \epsilon)^2}{D_p^2 \cdot \epsilon^3} + \frac{1.75 \cdot \rho \cdot L \cdot v_s^2 \cdot (1 - \epsilon)}{D_p \cdot \epsilon^3} \quad (15)$$

Consequently, the pressure drop Δp across the packed catalyst bed can be calculated using the Ergun equation (Equation (15)) for a packed bed, where L is the length of the bed, v_s is the superficial velocity (flow rate divided by the bed cross-sectional area) and D_p is the spherical diameter of packing.

Using Equation (15), the average pressure drop across the packed bed is estimated to be 0.7 bar. During operation of the rig with a 300 $\text{mL} \cdot \text{min}^{-1}$ total flow rate, the experimental pressure drop based on P_1 and P_2 pressure indicators is 0.5 bar. This is in good agreement with the pressure drop calculated using the Ergun equation. The small discrepancy may arise from the assumptions and estimations in the calculations.

3.5 Catalyst testing for NH_3 decomposition

A catalytic rig for testing NH_3 decomposition activity was built by a previous member of the group and the complete rig validation can be found elsewhere.¹³⁵ During use of the rig, a number of modifications were made such as the addition of a helium purge set up for the ammonia line to avoid ammonia remaining in the MFC, which could lead to corrosion and damage in the presence of H_2O . In addition, a different method for processing the catalytic data was developed, discussed at the end of this section. Figure 19 shows the P&ID of the rig used to assess the NH_3 decomposition activity and stability of $\text{Co}/\gamma\text{-Al}_2\text{O}_3$ catalysts.

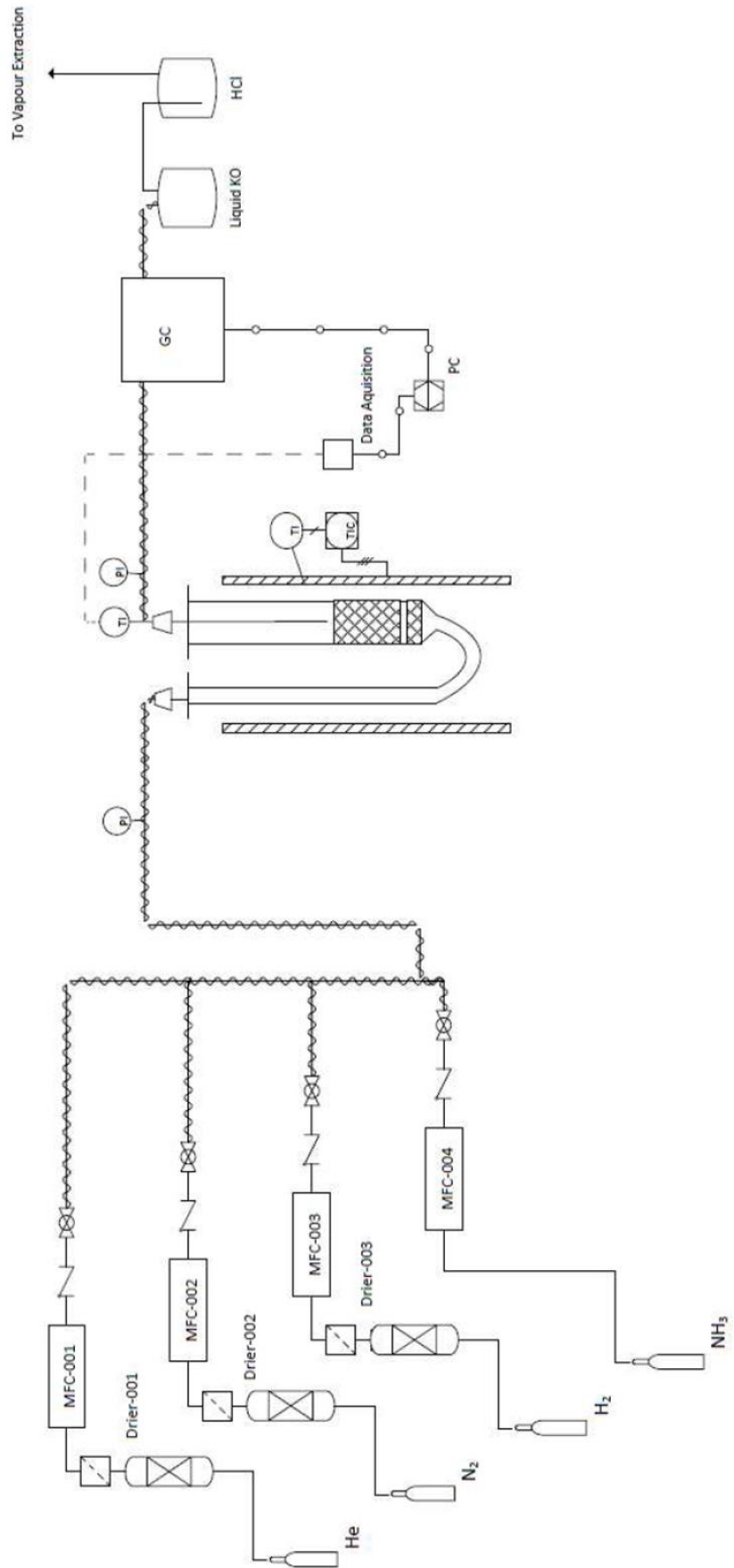


Figure 19. P&ID of the NH_3 decomposition catalytic rig. Directly reproduced from Hill.¹³⁵

The flow rate of the inlet gases (NH₃, H₂, N₂ and He) are controlled by Bronkhorst® MFCs. Due to the corrosive nature of NH₃ in contact with moisture, any line potentially containing NH₃ is heated to 60 °C to prevent condensation of H₂O. As an additional measure, prior to mixing, all of the gases except NH₃ pass through molecular sieves to remove any trace H₂O. The inlet gas stream flows through a packed bed of 25 mg of catalyst in a quartz U-tube reactor, diluted with 450 mg inert coarse SiC (360 μm diameter). The entrance of the bed contains 175 mg fine SiC (53 μm diameter) to ensure conditions of plug flow. The outlet gas stream flows through a gas chromatography (GC) (Agilent 7820A) column (Porapak Q) with an automated sampling 6-way valve and thermal conductivity detector (TCD). The gases are identified by their different elution times, with H₂ eluting first.

The H₂ peak area obtained from the GC is converted to a H₂ mol% composition using a polynomial GC calibration curve, which is obtained weekly. Fitting the calibration curve to a polynomial expression is supported by the reported non-linear H₂ GC response by Snavely and Subramaniam.¹³⁶

The outlet H₂ mol% composition is linked to conversion using the relationship shown in Figure 20. A polynomial equation is appropriate because the total number of moles changes as conversion increases due to the imbalanced stoichiometry of NH₃ decomposition.

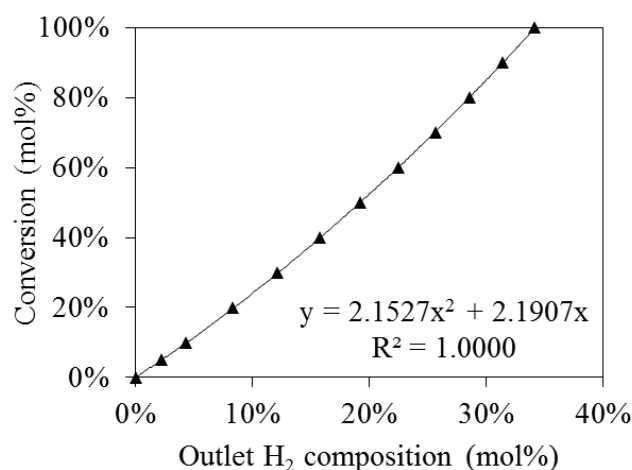


Figure 20. Polynomial relationship between NH₃ conversion and outlet H₂ composition.

The temperature in the reactor is monitored by a type K thermocouple at the exit of catalyst bed, recorded every 5 seconds using LabVIEW™ software (version 11.0). The GC data is aligned with the thermocouple values using their timestamps with the *VLOOKUP* function in *Microsoft Excel 2013*. The GC data has a 45s offset, corresponding to the physical time delay between the thermocouple position and the GC detector.

The cobalt-based catalysts are usually reduced *in situ* prior to the catalytic test at 580 °C. In a typical catalyst test, 2.5 NmL·min⁻¹ NH₃ (99.999 %, *BOC*) and 6 NmL·min⁻¹ He (99.999 vol%, *Air Liquide*) is flowed through the reactor and the furnace is set to increase from 220 °C to 580 °C at 2.6 °C·min⁻¹. Under these flow conditions, the GHSV is calculated to be 6000 mL_{NH₃}·g_{cat}⁻¹·h⁻¹ in terms of the mass of catalyst (0.025 g) or 519.0 h⁻¹ with respect to the volume of the catalyst bed (0.29 cm³).

The furnace is ramped up and down to the set point three times in a standard catalytic test. In some cases, the thermal stability of the Co/ γ -Al₂O₃ catalysts is determined by ramping the furnace temperature up and down from 260 °C to 580 °C but with higher maximum set points on the second and third runs of 650 °C and 740 °C respectively. The change in activity following exposure to higher temperatures is used to determine the thermal stability.

The decomposition of NH₃ is endothermic and the reaction rate is thermally activated above 500 °C as demonstrated by Figure 21 showing the NH₃ decomposition for a reactor containing SiC diluent only and SiC and γ -Al₂O₃.

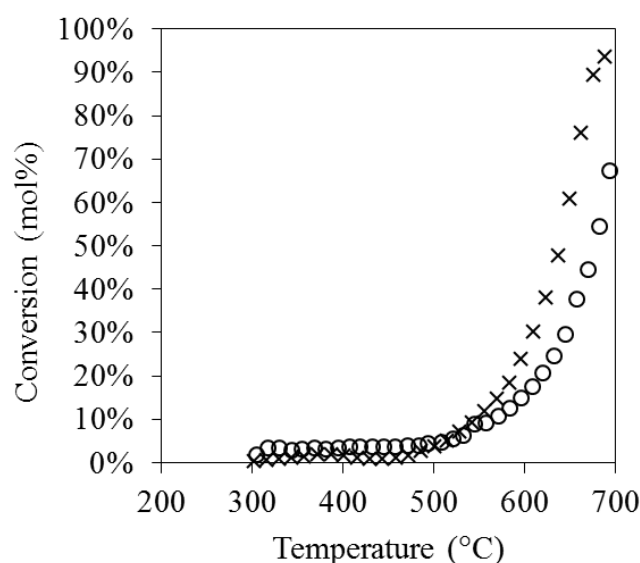


Figure 21. NH₃ decomposition activity for a reactor filled with SiC only (○) and SiC mixed with γ -Al₂O₃ plate support (x).

3.6 Catalyst testing for Fischer-Tropsch synthesis

A selection of Co/ γ -Al₂O₃ catalysts were tested for their activity in Fischer-Tropsch synthesis (FTS) at Sasol UK in St Andrews, Scotland. Prior to testing, the catalysts were reduced using a *Micromeritics Autochem 2920* instrument following the standard industrial Co FTS reduction conditions at 425 °C for 6 hours at 1 °C·min⁻¹ using 40 mL·min⁻¹ H₂.⁵⁹

The FTS testing rig consists of a packed bed reactor designed and built in-house by Sasol UK. The packed bed is ¼" diameter and 5 cm in length, containing 500 to 800 mg catalyst and 3 g of coarse SiC to reduce potential hot spots within the bed. The rig is operated at 16 bar pressure with a H₂:CO ratio of 1.8 to 2 and different temperature conditions to achieve typically 50 mol% conversion. Any waxes (> C₁₈) produced are removed from the gas stream into a hot pot at 180 °C. Subsequently any liquid hydrocarbons (C₅ to C₁₇) are condensed at 15 °C, leaving a gas stream containing only C₁ to C₄ for analysis by gas chromatography (*Agilent RGA*). Any C₅₊ products are not analysed. The GC has three separate detection channels: one flame ionisation detector for hydrocarbons, one TCD for CO₂, Ar and CO analysis and another TCD for H₂. The rate of CO conversion is calculated by comparing the inlet Ar:CO ratio with the outlet composition.

Chapter 4 – Hydrothermal synthesis of nanostructured γ -Al₂O₃

Nanostructured materials as catalytic supports present a range of advantages such as high surface area, as well as the possibility of tailoring the metal-support interaction whilst playing an active role as a nanoparticle stabiliser.

This chapter is focussed on the hydrothermal synthesis of nanostructured γ -Al₂O₃ with a range of different shapes and degrees of curvature, achieved by varying the synthetic parameters. In order to achieve this, a detailed mechanistic understanding of the reaction steps is presented, which facilitates tailoring of the product curvature. These materials are used in subsequent chapters to support metal nanoparticles in order to evaluate the effect of curvature on nanoparticle-support interaction and stability, and to validate the main research hypothesis of this thesis.

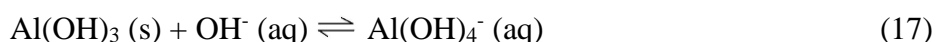
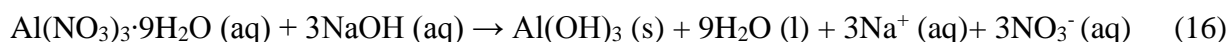
Within this chapter, the aluminium product yield is calculated and correlated to the elucidated mechanism. This understanding reveals the possibility of recycling the supernatant solution to maximise the yield, paving the way to the development of manufacturing routes for large quantities of nanostructured materials with controlled morphologies.

4.1 Mechanism of the hydrothermal synthesis of nanostructured γ -Al₂O₃

The hydrothermal method used herein to produce nanostructured γ -Al₂O₃ materials involves the combination of aqueous solutions of sodium hydroxide and aluminium nitrate nonahydrate in specific molar ratios. The mixture is kept in the oven for a fixed period from 10 to 80 hours at a specific temperature below 200 °C. The effect of NaOH:Al ratio on product yield, synthesis pH and product morphology was systematically studied by varying the NaOH concentration in a 20 hour hydrothermal synthesis at 200 °C.

4.1.1 Effect of NaOH:Al on product yield and overall mechanism

In order to understand the relationship between NaOH:Al ratio and γ -Al₂O₃ product yield, one must first consider the mechanistic steps taking place during the hydrothermal synthesis. Prior to the hydrothermal synthesis of γ -Al₂O₃, aqueous solutions of NaOH and aluminium nitrate nonahydrate (Al(NO₃)₃·9H₂O) are mixed, resulting in a white colloidal suspension of amorphous aluminium hydroxide (Al(OH)₃) as shown in Reaction (16). Due to the amphoteric nature of Al(OH)₃, it forms an equilibrium with OH⁻, as shown in Reaction (17). Based on Reaction (16) and Reaction (17), a deficiency of hydroxide ions decreases the concentration of Al(OH)₃ as the Reaction (16) is incomplete. By contrast when excess OH⁻ is added, soluble Al(OH)₄⁻ forms via Reaction (17) at the expense of the Al(OH)₃. However, Al(OH)₃ is an essential intermediate for the hydrothermal formation of boehmite (γ -AlOOH) in Reaction (18), which has a lamellar structure comprised of crystalline sheets held together by hydrogen bonding. The mechanism of this process is discussed in Section 4.1.2. Boehmite is calcined at 500 °C to yield the final γ -Al₂O₃ product (Reaction (19)).



The stoichiometric dependency of the product yield resulting from the ratio of the reagents (NaOH:Al) can be seen in Figure 22, in which the stoichiometric 3NaOH:1Al molar ratio results in the maximum γ -Al₂O₃ product yield. A NaOH:Al molar ratio below 3:1, results in a

low γ - Al_2O_3 product yield due to the incomplete conversion of $\text{Al}(\text{NO}_3)_3 \cdot 9\text{H}_2\text{O}$ into $\text{Al}(\text{OH})_3$ via Reaction (17) prior to the hydrothermal treatment. By contrast, above the stoichiometric ratio, the low product yield obtained is due to the formation of soluble $\text{Al}(\text{OH})_4^-$ as shown in Reaction (17) at the cost of crucial $\text{Al}(\text{OH})_3$ intermediary. This is confirmed by the absence of solid product resulting from increasing the reagent ratio above 5.2:1 as the equilibrium position of Reaction (17) is far to the right leading to the complete removal of $\text{Al}(\text{OH})_3$.

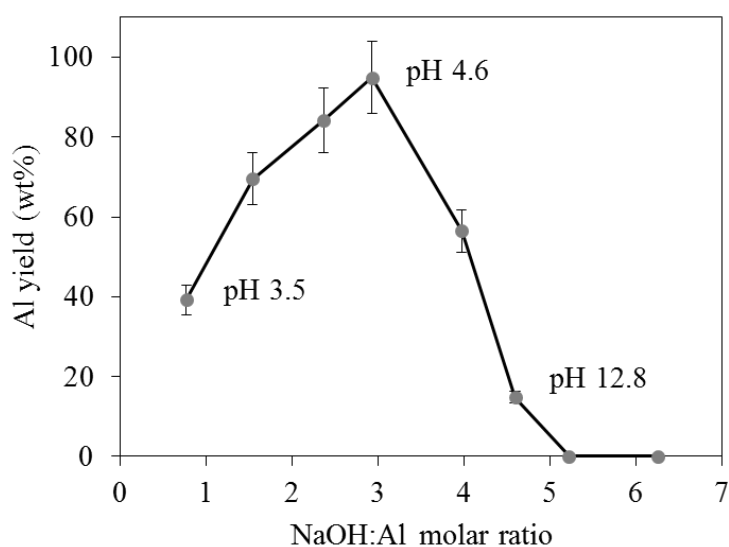
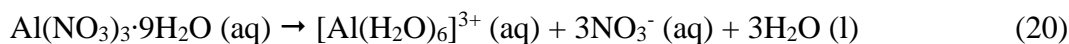


Figure 22. Yield of γ - Al_2O_3 product as a function of NaOH:Al reagent ratio.

4.1.2 Detailed mechanism of AlOOH formation

The chemical nature of the complexes formed after hydrolysis of aluminium salts depends on a delicate balance of the Al^{3+} concentration, base concentration, pH, degree of stirring, temperature, rate of base addition and aging time.¹³⁷ The AlOOH formation mechanism has been probed using a combination of ^{27}Al nuclear magnetic resonance (NMR), transmission electron microscopy (TEM) and scanning electron microscopy (SEM).

The intermediate steps in the conversion of $\text{Al}(\text{NO}_3)_3 \cdot 9\text{H}_2\text{O}$ to $\text{Al}(\text{OH})_3$ (Reaction (17)) have been deduced. Initially, aqueous dissolution of $\text{Al}(\text{NO}_3)_3 \cdot 9\text{H}_2\text{O}$ results in the formation of $[\text{Al}(\text{H}_2\text{O})_6]^{3+}$ cations as shown in Reaction (20). These cations are susceptible to deprotonation as the small, highly charged Al^{3+} polarises and weakens the O-H bonds, facilitating sequential deprotonation to form monomer complexes via Reaction (21) and (22). The extent to which these equilibria proceed, depends on the presence of OH^- , which may be intrinsically present in an aqueous solution due to the auto-ionisation of water, in which case Reaction (21) and (22) do not progress significantly. Alternatively, the addition of base such as NaOH, drives the equilibria towards the precipitation of solid $\text{Al}(\text{OH})_3$ (Reactions (21) - (23)).



The distinctions between the ^{27}Al NMR spectra of the solutions before and after hydrothermal treatment at different temperatures help to deduce the mechanistic pathway. ^{27}Al NMR can be used to unequivocally identify any symmetrical aluminium species in the hydrothermal solutions, such as monomers, dimers/trimers and tridecamers.¹³⁸ The quadrupolar nature of the ^{27}Al isotope permits only symmetrical species to be identified, meaning that other aluminium monomers, oligomers and polymers may be undetected.¹³⁹

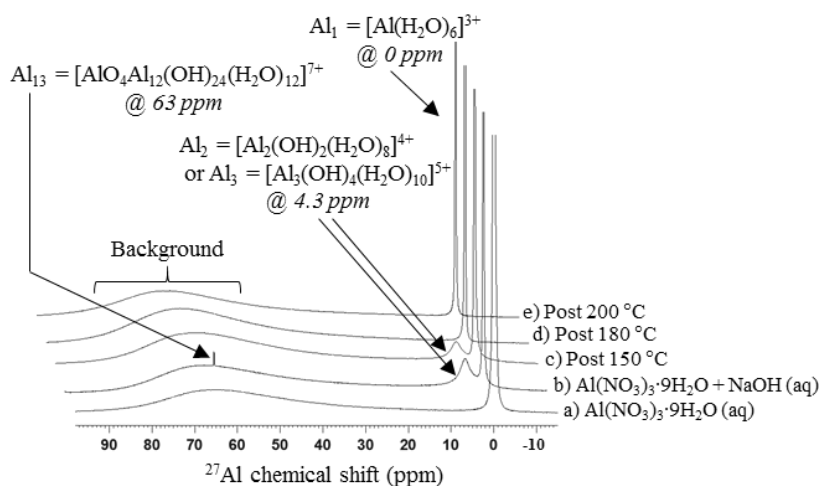
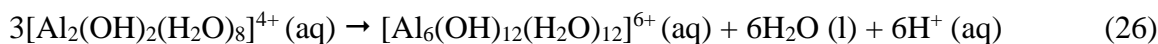
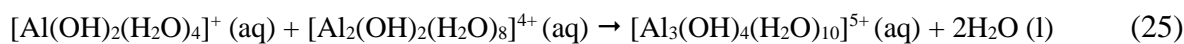


Figure 23. ^{27}Al NMR spectra for Al solutions. a) aqueous solution of $\text{Al}(\text{NO}_3)_3 \cdot 9\text{H}_2\text{O}$, $[\text{Al}] = 1.6 \text{ M}$ b) aqueous solution of NaOH and $\text{Al}(\text{NO}_3)_3 \cdot 9\text{H}_2\text{O}$ (0.77:1), and supernatant solution after hydrothermal treatment of precursors (0.77:1) after 20 hour at c) 150 °C d) 180 °C and e) 200 °C.

The presence of $[\text{Al}(\text{H}_2\text{O})_6]^{3+}$ monomers by aqueous dissolution of $\text{Al}(\text{NO}_3)_3 \cdot 9\text{H}_2\text{O}$ in Reaction (20) is confirmed by the ^{27}Al NMR spectra in Figure 23a. The degree of deprotonation cannot be determined because the reference peak at 0 ppm is due to any symmetric, monomeric, octahedral aluminium species, which includes $[\text{Al}(\text{H}_2\text{O})_6]^{3+}$ as well as $[\text{Al}(\text{OH})(\text{H}_2\text{O})_5]^{2+}$ and $[\text{Al}(\text{OH})_2(\text{H}_2\text{O})_4]^+$.¹³⁷ The aqueous Al^{3+} solution without base does not contain the dimer/trimer/tridecamer complexes as the associated ^{27}Al NMR peaks are not present in Figure 23a, despite the fact that nitrates reportedly facilitate dimerisation.¹⁴⁰

Typically solutions of low $\text{NaOH}:\text{Al}$ ratios (0.77:1, pH 3.5), contain monomeric and dimeric aluminium species.¹⁴¹ It is their basic hydrolysis that leads to the evolution of Al_{13} , provided $\text{NaOH}:\text{Al}$ is between 0.5 and 2.5.^{139,142} This is confirmed by Figure 23b in which room

temperature NaOH addition to an aqueous solution of Al^{3+} forms dimers/trimers (Reactions (24) - (26)) and tridecamers ($[\text{Al}_{13}\text{O}_4(\text{OH})_{24}(\text{H}_2\text{O})_{12}]^{7+}$), evidenced by the ^{27}Al NMR peaks at 4.3 and 63 ppm respectively.^{137,143}



The structure of the Al_{13} 3D tridecamer ($[\text{Al}_{13}\text{O}_4(\text{OH})_{24}(\text{H}_2\text{O})_{12}]^{7+}$) is comprised of a central aluminium tetrahedron (AlO_4) surrounded by four planar trimers ($[\text{Al}_3(\text{OH})_4(\text{H}_2\text{O})_{10}]^{5+}$) analogous to a Keggin Cluster structure.^{142,144} The high local concentration of OH^- during base addition forms the tetrahedral centre of $[\text{Al}(\text{OH})_4]^-$, which becomes surrounded by four planar trimers ($[\text{Al}_3(\text{OH})_4(\text{H}_2\text{O})_{10}]^{5+}$), individually formed in Reaction (25).¹⁴⁵ Al_{13} is more prevalent with slow addition of base, whereas fast base injection leads to $\text{Al}(\text{OH})_3$ precipitation.¹⁴⁵

In addition to the complex combination of soluble aluminium complexes discussed so far, the addition of sufficient NaOH to aqueous Al^{3+} solutions precipitates solid $\text{Al}(\text{OH})_3$ via polymerisation. The formation of $\text{Al}(\text{OH})_3$ by polymerisation of $[\text{Al}(\text{OH})_2(\text{H}_2\text{O})_4]^+$ cations (Reaction (23)) is described in detail by Reactions (24) - (26). The deprotonated monomers dimerise, as shown in Reaction (24) for $[\text{Al}(\text{OH})_2(\text{H}_2\text{O})_4]^+$ and subsequently, monomers and dimers bind to form trimers (Reaction (25)). The dimers consequently aggregate into hexameric rings made up on 6 Al ions ($[\text{Al}_6(\text{OH})_{12}(\text{H}_2\text{O})_{12}]^{6+}$) as shown in Reaction (26). Further aggregation of the hexameric rings leads to the precipitation of $\text{Al}(\text{OH})_3$, limited by the OH^- concentration.

Interestingly, due to the low synthesis pH (3.5), the $\text{Al}(\text{OH})_3$ precipitate undergoes hydrolysis to reform soluble gibbsite fragments, whose size is a function of the $\text{OH}:\text{Al}$ ratio.¹³⁷ Indeed, solid $\text{Al}(\text{OH})_3$ fully dissolves in aqueous solution at pH 3.5 (0.77:1) at room temperature after 48 hours. The dissolution rate is accelerated by heating, confirmed by rapid (< 30 minutes) dissolution of solid $\text{Al}(\text{OH})_3$ at 50 °C. Thus, during acidic hydrothermal synthesis (0.77NaOH:1Al), solid $\text{Al}(\text{OH})_3$ formed at room temperature rapidly dissolves into essential gibbsite fragments shown in Figure 24. With sufficiently high hydrothermal temperature (> 170 °C), deprotonation or hydrolysis of the gibbsite fragments by heating (thermolysis) can take place, confirmed by an observed pH decrease from the liberation of protons, represented

in Figure 24. As deprotonation advances, the formation of relatively stable, uncharged species leads to the crystallisation of solid AlOOH product.

From a mechanistic viewpoint, the importance of $\text{Al}(\text{OH})_3$ intermediate for the formation of AlOOH building blocks is shown to be governed by the amount of gibbsite fragments formed in solution upon dissolution and subsequent thermolysis facilitated by high temperature conditions ($> 170\text{ }^\circ\text{C}$) in Figure 24.

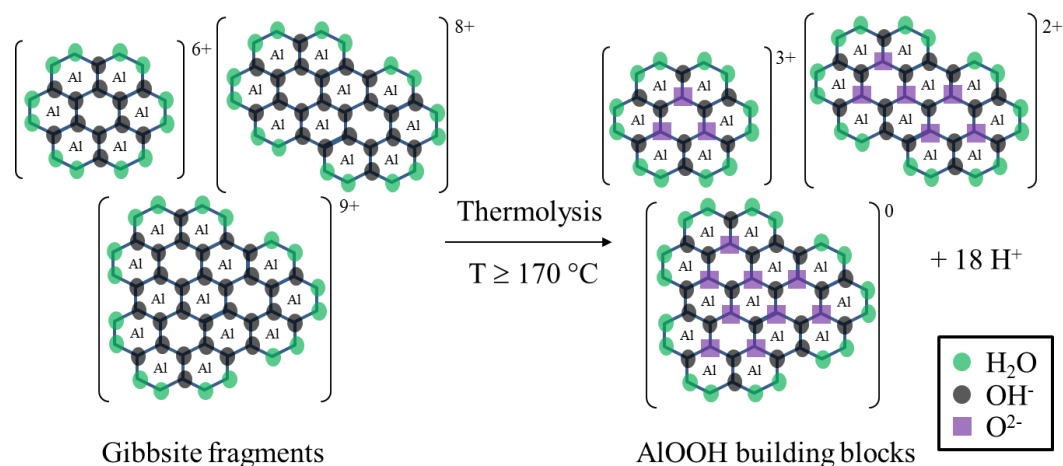


Figure 24. Transformation of planar gibbsite fragments to AlOOH building blocks by thermolysis above $170\text{ }^\circ\text{C}$. Each small hexagon represents an octahedral arrangement of atoms around the Al atom. Ligands are respectively coloured with green, black and purple to represent H_2O , OH^- and O^{2-} .

The aluminium yield (as mass of AlOOH) obtained after hydrothermal synthesis for 20 hours increases as the reaction temperature is raised, as shown in Table 17. Under the studied non-stoichiometric $0.77\text{NaOH}:1\text{Al}$ conditions, the maximum theoretical Al_2O_3 yield is approximately 35 wt% due to the incomplete conversion to the essential $\text{Al}(\text{OH})_3$ precursor (Reaction (20) - (23)). Such maximum conversion is only achieved after 20 hour synthesis at 200°C . The rate of conversion of gibbsite fragments into AlOOH building blocks is kinetically limited at lower temperatures, yielding less product at 170 to $180\text{ }^\circ\text{C}$.

Table 17. Yield of $\gamma\text{-Al}_2\text{O}_3$ after hydrothermal treatment for 20 hours with $0.77\text{NaOH}:1\text{Al}$ molar ratio at different synthesis temperatures. Maximum theoretical Al yield is 35 wt% with this reagent molar ratio.

Synthesis temperature ($^\circ\text{C}$)	Al yield (wt%)
150	0
165	0
170	7
180	11
200	35

By contrast, at hydrothermal temperatures less than or equal to 165 °C, thermolysis of the gibbsite fragments (Figure 24) is not feasible, resulting in no solid product. In this case, $\text{Al}(\text{OH})_3$ is irreversibly dissolved into gibbsite fragments at low pH (3.5) but not deprotonated into AlOOH building blocks by thermolysis. This observation is confirmed by a lack of change in the solution pH after hydrothermal treatment contrasting the decrease from pH 3.5 to 0.9 when the reaction takes place above 170 °C. The pH also remains constant even if the synthesis is carried out for prolonged synthesis times (40 hours), confirming that at temperatures ≤ 165 °C, thermolysis is not kinetically limited but rather it is not feasible. Furthermore, if this supernatant solution is treated at 200 °C for 20 hours, a AlOOH product with the same physical properties as AlOOH synthesised by a single treatment at 200 °C for 20 hours is obtained, in agreement with the conclusions above. There are the several studies in the literature where hydrothermal synthesis of boehmite is reported at temperatures as low as 120 °C.^{143,146} However, such studies use different base and/or aluminium sources, which will affect the equilibria reactions and activation energies of the intermediate steps.

The ^{27}Al NMR spectra of the supernatant after hydrothermal synthesis at different temperatures (Figure 23) highlights that the formation of AlOOH product at ≥ 170 °C is accompanied by an absence of dimer/trimer peak at 4.3 ppm whereas it remains when no solid AlOOH product is formed at ≤ 165 °C. This observation suggests that the dimer/trimer assists in the formation of the final AlOOH solid product. Monomers are observed by ^{27}Al NMR in the post reaction solution in all cases after hydrothermal treatment in the studied temperature range (Figure 23c-e), due to the $\text{NaOH}:\text{Al}$ ratio of 0.77:1 below the stoichiometric value (3:1). In addition, Figure 23c-e shows that in all cases after hydrothermal treatment within the studied temperature range, the Al_{13} Keggin cluster is no longer present, unrelated to the evolution of AlOOH . This suggests that the Al_{13} Keggin cluster may not be involved in the formation of AlOOH . Reportedly, in acidic conditions the concentration of the Al_{13} Keggin cluster decreases over time due to clustering into species undetectable by ^{27}Al NMR.¹⁴³

4.2 Effect of NaOH:Al ratio on synthesis pH and γ - Al_2O_3 morphology

As mentioned earlier, the concentration of hydroxide ions affects the resulting equilibrium position in Reaction (17). This causes a change in synthesis pH prior to hydrothermal treatment. The change in initial pH results in a different morphology for the γ - AlOOH materials obtained after 20 hours hydrothermal synthesis at 200 °C, as shown by TEM in Figure 25. Strongly acidic conditions (pH 3.5) result in the formation of 1D γ - Al_2O_3 nanorods whereas highly basic conditions (pH 12.8) favour the formation of 2D γ - Al_2O_3 nanoplates. Detailed evaluation of the electron micrographs and supplementary SEM of the former sample confirms that the product obtained under strongly acidic conditions (pH 3.5) are solid nanorods and not hollow like nanotubes. The pH resulting from the stoichiometric 3NaOH:1Al ratio synthesis is less acidic (pH 4.6), resulting in a mixture of 1D and 2D morphologies.

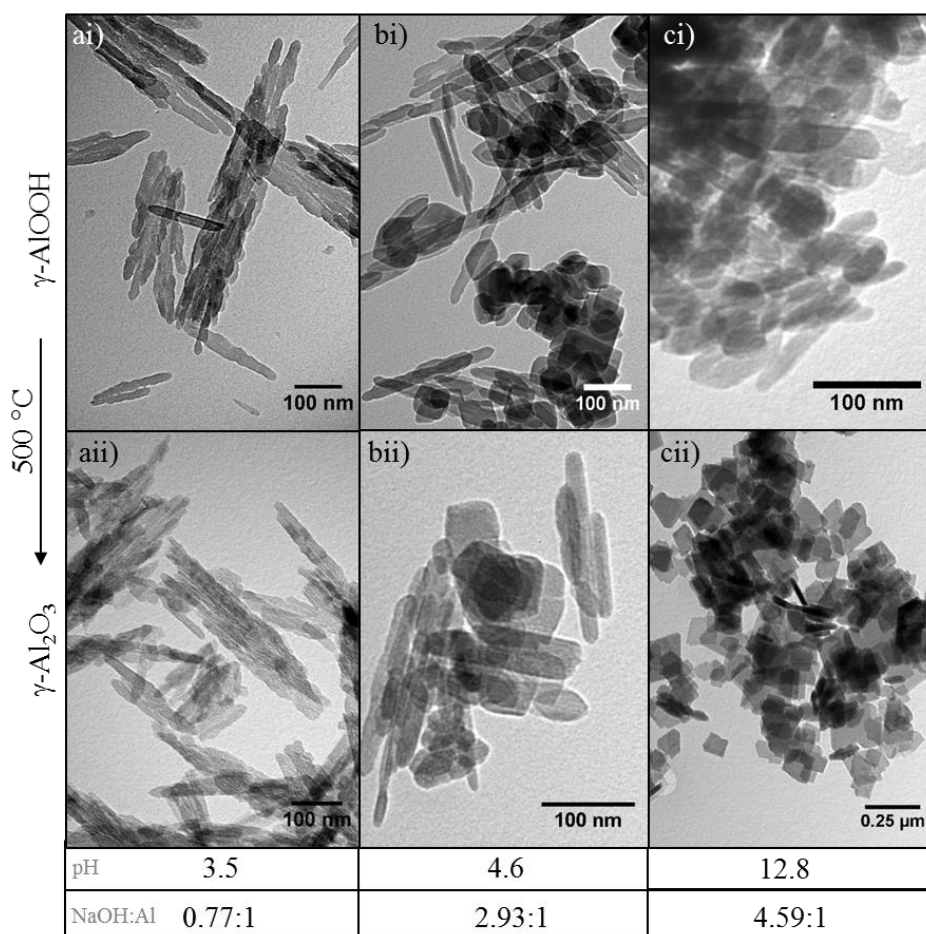


Figure 25. TEM micrographs of γ -AlOOH (i) and γ -Al₂O₃ (ii) after 20 hours hydrothermal synthesis at 200 °C. Different initial NaOH:Al reagent ratios used a) 0.77:1 (pH 3.5) , b) 2.93:1 (pH 4.6) and c) 4.59:1 (pH 12.8).

TEM micrographs before (Figure 25i) and after calcination at 500 °C (Figure 25ii) confirms that the morphology is conserved in the transformation of γ -AlOOH to γ -Al₂O₃.¹⁴⁷ Thermogravimetric analysis (TGA) was used to determine the calcination temperature (Figure 26) of 500 °C, which typically takes place in the range of 300 to 500 °C.³⁰ The decrease in mass at 100 to 120 °C is due to adsorbed water. The high temperature mass loss arises from the loss of interstitial water as γ -AlOOH is converted to γ -Al₂O₃ at 460 °C for nanorods and 507 °C for the nanoplates.

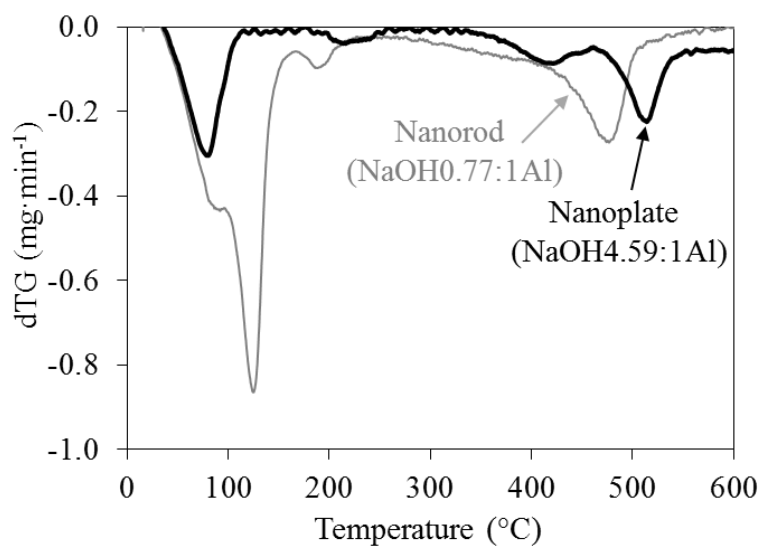


Figure 26. TGA of γ -AlOOH nanorods (grey) and nanoplates (black) synthesised at 200 °C for 20 hours with different NaOH:Al reagent ratios.

The hydrothermal synthesis pH disturbs the hydrogen bonding during the formation of the layered AlOOH. The nature of the disruption is pH-dependent, resulting in the formation of different morphologies.

Below the stoichiometric 3NaOH:1Al molar ratio when small amounts of NaOH are added (e.g. 0.77:1), the hydrothermal synthesis conditions are acidic because the aluminium precursor has an acidic character which has not yet been dominated by the basicity of the NaOH solution. Under such conditions, the excess of protons from the acidic solution disrupts the inter-layer hydrogen bonding, allowing the 2D sheets to separate and subsequently curl up into rods to minimise their surface energy. As shown in Figure 25a, low reagent ratios (0.77:1) result in the formation of morphologically pure nanorods, ~ 130 nm length and ~ 13 nm diameter, due to the acidic synthesis (pH 3.5). The growth of these rods will be discussed in further detail in Section 4.3.2.

Near the stoichiometric reagent ratio (2.97:1), the conditions are acidic (pH 4.6) but not strong enough to fully deprotonate all of the lamellar γ -AlOOH to form pure nanorods, so instead an assortment of 1D and 2D morphologies of heterogeneous sizes are obtained (Figure 25b).

Above the stoichiometric ratio the conditions are strongly basic (e.g. pH 12.8 for 4.59NaOH:1Al) as the equivalence point, where the concentration of acid equals base, is exceeded. Basic conditions stabilise the lamellar γ -AlOOH by hydroxylating under-coordinated surface Al atoms, allowing the product to remain in a 2D sheet-like form called nanoplates, approximately 100 by 100 nm (Figure 25c).

4.2.1 Characterisation of γ -Al₂O₃ nanorods and nanoplates

For the purpose of this thesis, only materials of pure morphology are useful for comparison as a catalyst support. As such, the remainder of this section is focussed on the characterisation of the pure γ -Al₂O₃ nanorods and nanoplates which have been hydrothermally synthesised at 200 °C for 20 hours with 0.77:1 and 4.59:1 NaOH:Al ratio, respectively. The properties of these two materials are summarised in Table 18.

Table 18. The properties of γ -Al₂O₃ obtained from hydrothermal synthesis at 200 °C for 20 hours.

NaOH:Al	Shape	[NaOH] (M)	Initial synthesis pH	S _{ABET} ^a (m ² ·g ⁻¹)	Average size (nm)		
					TEM length	TEM diameter	pXRD ^b
0.77:1	Rods	1.0	3.5	145.6	128	13	8.3
4.59:1	Plates	5.9	12.8	14.9	100	100	4.6

^a S_{ABET} is the specific surface area calculated by the BET approximation using N₂ sorption data at -196 °C.

^b Crystallite size calculated using the (440) γ -Al₂O₃ peak at ~ 67° with the Scherrer equation. JCPDS 10-0425.

The nanorods and nanoplates are confirmed to be γ -Al₂O₃ by powder X-ray diffraction (pXRD) (JCPDS 10-0425) as shown in Figure 27. The crystallite size calculated from the Scherrer equation using the line broadening at half the height of the maximum peak in the pXRD spectra (Figure 27) suggests the nanorods consist of multiple crystals due to the difference in size observed in TEM micrographs. Based on the low energy of the (440) plane, it is likely that the crystallite size estimated in this direction reflects the thickness of the rods, to be 4.6 nm.

The higher sodium content in the hydrothermal synthesis solution under basic conditions (4.59NaOH:1Al) leads to the formation of NaAlO₂, JCPDS Card No. 33-1200, identified by

diffraction peaks at $\sim 29^\circ$, 32° and 48° (Figure 27b), which can be removed by washing as shown in Section 4.4.

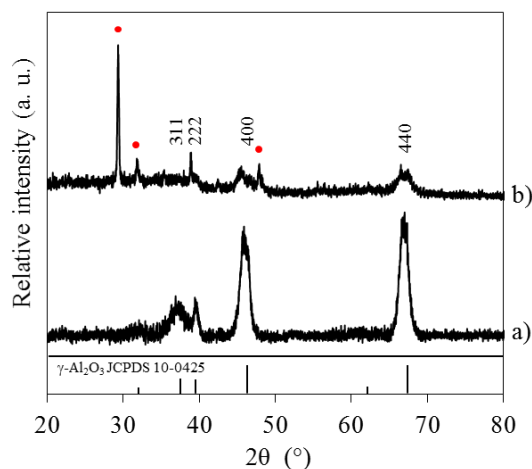


Figure 27. pXRD pattern of **unwashed** $\gamma\text{-Al}_2\text{O}_3$ calcined at 500°C after 20 hours hydrothermal synthesis at 200°C with different initial NaOH:Al reagent ratios. a) 0.77:1 (nanorods) and b) 4.59:1 (nanoplates). $\gamma\text{-Al}_2\text{O}_3$ JCPDS10-0425. Red circle above additional peaks correspond to NaAlO_2 , JCPDS 33-1200.

The specific surface area of the $\gamma\text{-Al}_2\text{O}_3$ nanoplates is significantly lower than the nanorods (Table 18), likely due to their 2D nature, as noted in the literature.¹⁰ The difference in surface area of these materials may have implications on their suitability as a catalyst support material, since a low surface area suggests less capacity to achieve high metal dispersion and loading.

The shape of the N_2 adsorption-desorption isotherms of the $\gamma\text{-Al}_2\text{O}_3$ nanorods and nanoplates shown in Figure 28 corresponds to the IUPAC Type IV, characteristic of mesoporous materials. In addition, the isotherms exhibit a H3 hysteresis loop, common for slit-like pores or aggregation of plate-like particles. The latter could be a valid explanation for the nanoplates produced with 4.59NaOH:1Al ratio based on the morphology observed by TEM (Figure 25).¹⁴⁸

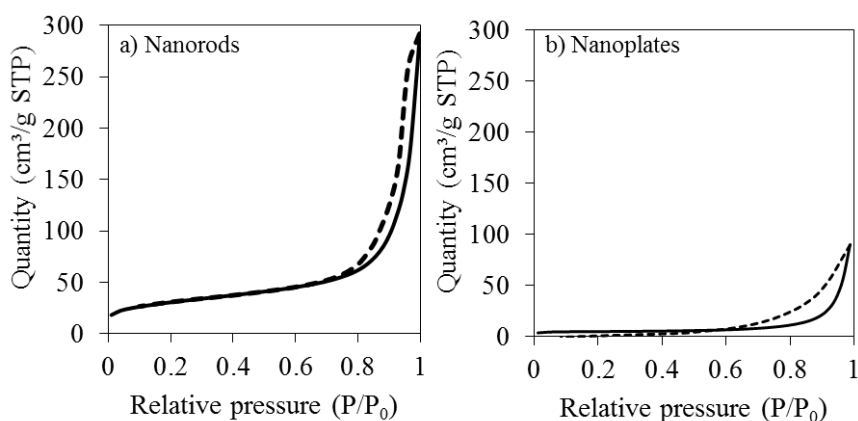


Figure 28. N_2 adsorption-desorption isotherms of $\gamma\text{-Al}_2\text{O}_3$ from 20 hours hydrothermal synthesis at 200°C with different NaOH:Al reagent ratios. a) 0.77:1 (nanorods) and b) 4.59:1 (nanoplates).

4.3 Understanding the nanorod formation mechanism to achieve curvature control

4.3.1 Mechanism of formation of 1D AlOOH nanorods

After the small AlOOH crystallites have scrolled to form nanorods due to the acidic conditions, the crystallites aggregate by the oriented attachment mechanism. This process is assisted by the presence of NO_3^- anions in the solution, which stabilises specific AlOOH crystal surfaces in order to inhibit growth in the direction of the stabilised surface. Specifically, NO_3^- anions are able to bind to the AlOOH surface via the protonated surface hydroxyl groups ($-\text{OH}_2^+$).⁴⁶ This morphology directing effect can be tuned by varying the adsorption strength of the anion and their ability to complex with Al^{3+} , following the order $\text{SO}_4^{2-} > \text{Cl}^- > \text{NO}_3^-$, with NO_3^- anions showing the weakest directing effect.⁴⁶

Characterisation of materials synthesised at different temperatures (170 to 200 °C) over 20 hours hydrothermal synthesis with the same NaOH:Al ratio (0.77:1) provides further insight into the formation mechanism of the AlOOH nanorods. Unless otherwise stated, the characterisation presented is of the obtained AlOOH product calcined at 500 °C, indexed to the γ phase of Al_2O_3 (JCPDS 10-0425), without other crystalline phases present (Figure A92, Appendix).

At temperatures ≥ 180 °C, morphologically pure nanorods are formed (Figure 29b-c). However, lower temperatures (e.g. 170 °C) result in a variety of morphologies, including 2D rectangular nanoplates and nanoparticles (Figure 29a). The difference in morphology observed is due to the lower rate of conversion of the 2D intermediates to the thermodynamically stable nanorods via scrolling followed by oriented attachment. The scrolling step required to form nanorods does not take place at 170 °C.

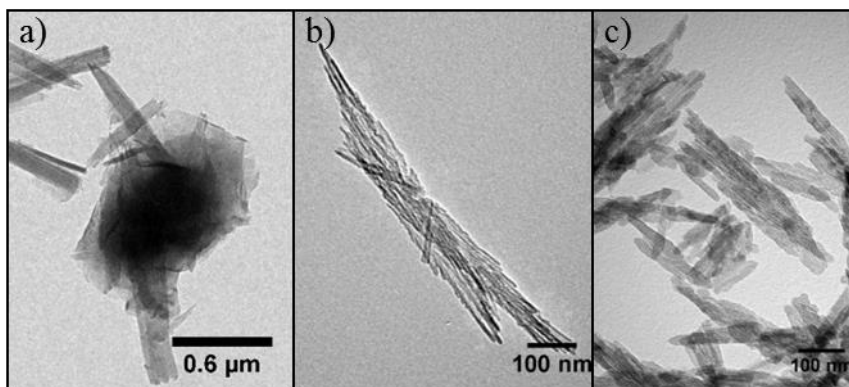


Figure 29. TEM micrographs of γ -Al₂O₃ samples obtained from hydrothermal treatment for 20 hours with NaOH:Al 0.77:1. a) 170 °C b) 180 °C and c) 200 °C.

The materials produced at 180 °C and 200 °C possess similar BET surface areas $\sim 144 \text{ m}^2 \cdot \text{g}^{-1}$ (Table 19), irrespective of the distinct nanorod dimensions calculated from TEM micrographs (Figure 29b-c). By contrast, γ -Al₂O₃ produced at 170 °C has a lower BET surface area of $122 \text{ m}^2 \cdot \text{g}^{-1}$, which may be attributed to the difference in morphology (Figure 29a) and porosity (Figure A93, Appendix).

Table 19. Properties of γ -Al₂O₃ synthesised at 170, 180 and 200 °C for 20 hours with 0.77:1 NaOH:Al ratio.

Synthesis temperature (°C)	Morphology	S _{BET} ^a (m ² ·g ⁻¹)	Average crystallite size (nm)		
			TEM length	TEM diameter	pXRD ^b
170	Rectangular sheets and nanoparticles	122.2	506.1	12.5	5.4
180	Rods	144.3	161.6	7.8	6.4
200	Rods	145.6	127.8	13.3	8.3

^a S_{BET} is the specific surface area calculated using the BET approximation using N₂ sorption data at -196 °C.

^b Calculated from the FWHM of (440) pXRD peak using the Scherrer equation. JCPDS 10-0425.

As shown in Table 19, as the synthesis temperature increases, the average crystallite size calculated from pXRD increases. However, TEM (Figure 29) and SEM (Figure 30) micrographs show that the nanorods synthesised at 180 °C have a higher aspect ratio than those synthesised at 200 °C, due to their smaller diameter and longer length. During SEM preparation, samples were coated with a thin layer of platinum to reduce charging so the SEM micrographs cannot be used for quantitative analysis.

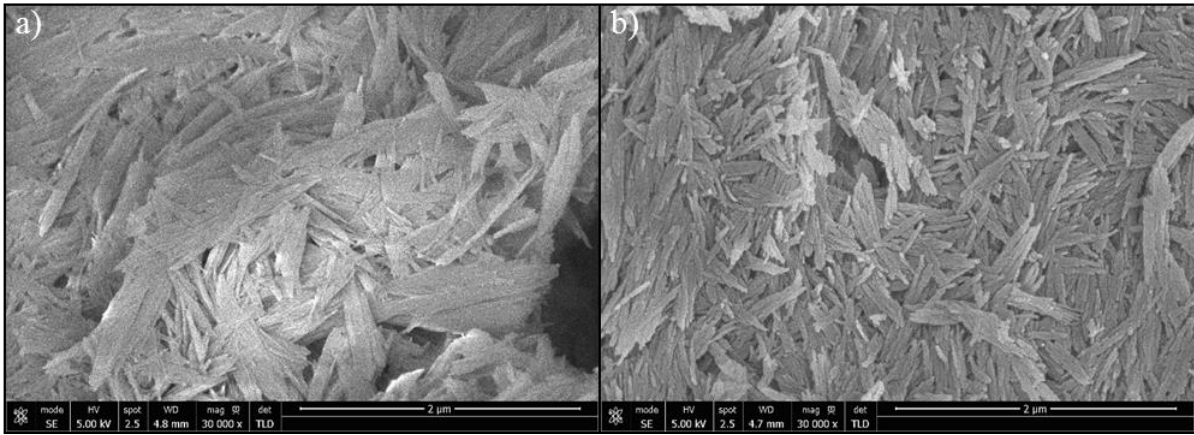


Figure 30. SEM micrographs of γ - Al_2O_3 nanorods synthesised with 0.77:1 NaOH:Al ratio for 20 hours. a) 180 °C and b) 200 °C.

High resolution TEM (HRTEM) of the material synthesised for 20 hours at 200 °C (Figure 31) confirms that the rods consist of attached crystallites, in agreement with the small crystallite size calculated by pXRD (Table 19) and the size observed by TEM (Figure 29). The conclusions drawn from the relevant characterisation methods (pXRD, SEM, TEM and HRTEM) support the oriented attachment mechanism in which individual crystallites aggregate along a preferred axis.

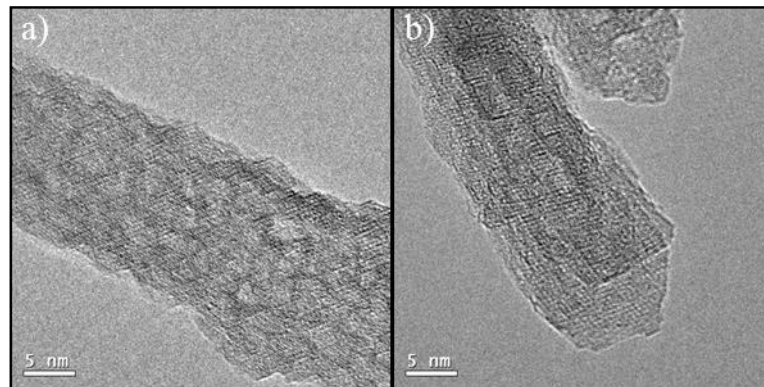


Figure 31. High resolution TEM micrographs of nanorods synthesised with 0.77:1 NaOH:Al molar ratio at 200 °C for 20 hours. a) before and b) after calcination at 500 °C.

4.3.2 Nanorod size control

In order to vary the curvature of the γ -Al₂O₃ rods, synthesis of nanorods with different diameters is required. This section builds upon the previous sections of this chapter where the NaOH:Al ratio conditions required for the selective synthesis of γ -Al₂O₃ rods was revealed to be 0.77:1 as it results in a highly acidic pH (3.5). Further investigations are shown here in which the effect of synthesis time and temperature is studied.

Growth of 1D nanostructures, follows the conventional dissolution-recrystallisation mechanism via Ostwald ripening, as previously reported for other boehmite materials and other ceramic nanostructures, whereby the diameter usually grows at the expense of the length.²⁹ The rate of growth is controlled by the specific hydrothermal synthesis conditions.³⁰

To fully understand the cause of the different nanorod dimensions in Figure 29 and to deduce the effect of temperature on the size of the rods, a series of hydrothermal syntheses were carried out at 180 °C and 200 °C over 10 to 80 hours synthesis duration. The pXRD patterns (Figure A94, Appendix) of all the materials obtained confirm the presence of a single crystalline phase corresponding to γ -Al₂O₃ (JCPDS 10-0425).

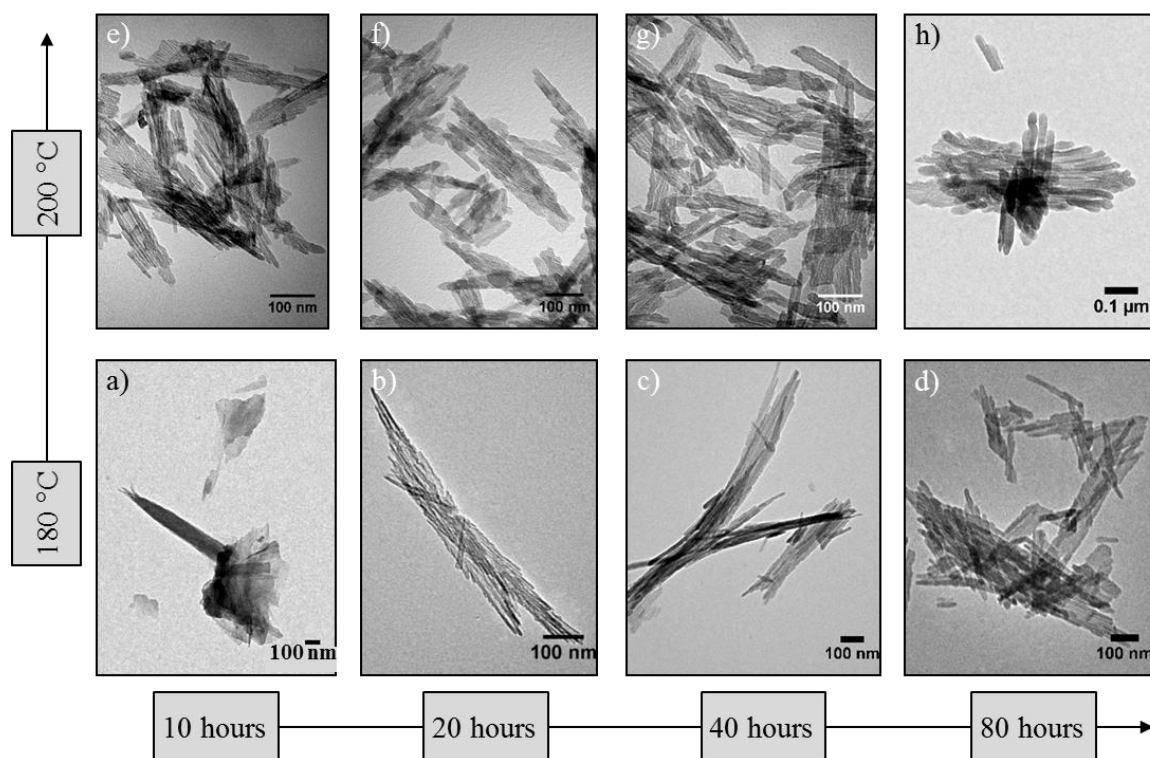


Figure 32. TEM micrographs of γ -Al₂O₃ calcined at 500 °C synthesised with 0.77:1 NaOH:Al ratio. 180 °C a) 10 hours b) 20 hours c) 40 hours d) 80 hours. 200 °C e) 10 hours f) 20 hours g) 40 hours h) 80 hours.

Representative TEM micrographs of the γ -Al₂O₃ materials are shown in Figure 32. All of the γ -Al₂O₃ samples show nanorod morphological purity, except the sample synthesised at 180 °C for 10 hours (Figure 32a) in which nanorods are not formed but rather an assortment of morphologies, including sheets and nanoparticles. Similar observation apply to the sample synthesised at 170 °C for 20 hours (Figure 29a). This observation confirms that under acidic conditions, the scrolling of the AlOOH lamellar sheets is kinetically limited.

Detailed analysis of the TEM micrographs revealed the presence of two distinct products when the synthesis was carried out at 180 °C; rods with a high aspect ratio (> 40) mixed with rods with considerably lower aspect ratio (< 17). These nanorods will be distinguished by the notation “*long/thin NR*” and “*short/thick NR*” respectively. The bimodal length and diameter averages are summarised in Table 20. Size distribution histograms are shown in Figure A95 (Appendix).

Table 20. Properties of γ -Al₂O₃ nanorods hydrothermally synthesised with 0.77:1 NaOH:Al molar ratio at 180 °C and 200 °C for 10 to 80 hours.

Synthesis time (hours)	Yield (wt%)	S _{ABET} ^a (m ² ·g ⁻¹)	Average crystallite size (nm)			pXRD ^c
			TEM NR length	TEM NR diameter	TEM aspect ratio ^b	
180 °C synthesis						
10	11	117	n/a	n/a	n/a	3.9
20	11	144	132	8.3	15.9	6.4
			397	4.8	82.6	
40	28	147	173	10.8	16.0	6.2
			417	6.6	63.2	
80	23	122	213	18.5	11.5	6.9
			518	13.3	38.9	
200 °C synthesis						
10	20	162	80	7.9	10.1	6.4
20	35	146	128	13.3	9.6	8.3
40	25	86	182	19.6	9.3	6.5
80	15	106	290	25.9	11.2	8.5

Data for long/thin nanorods shown in italics.

^a S_{ABET} is the specific surface area calculated using the BET approximation using N₂ sorption data at -196 °C.

^b Length : diameter ratio.

^c Calculated with Scherrer equation using line broadening at half maximum intensity of (440) XRD peak.

All the obtained γ -Al₂O₃ nanorods present similar crystallite sizes (~ 6 to 8 nm) in the (110) direction, independent of the synthesis time. The high resolution TEM in Figure 31 confirms that the rods are indeed formed of aggregated nanorod crystallites.

The N₂ sorption isotherms of γ -Al₂O₃ samples summarised in Table 20 are Type IV with a hysteresis loop, characteristic of mesoporosity (Figure A96, Appendix). The specific surface area of the γ -Al₂O₃ nanorods calculated from N₂ sorption data varies as a function of nanorod synthesis conditions. Interestingly the surface area increases at 180 °C with prolonged synthesis time but decreases at 200 °C, which may be due to differences in porosity. The pore size distributions of γ -Al₂O₃ synthesised at 180 °C indicate some degree of microporosity (< 2 nm) and mesopores 3 to 4 nm in diameter (Figure A97, Appendix). The presence of mesopores decreases as synthesis time increases. By contrast, γ -Al₂O₃ synthesised at 200 °C does not possess the same mesoporosity, although after a short 10 hours synthesis a small number of 3 to 4 nm mesopores are identified. Microporosity starts to become apparent after the 200 °C synthesis for 80 hours.

All the γ -Al₂O₃ materials produced at 200 °C present a similar aspect ratio (~ 10), despite variability of nanorod dimensions with respect to hydrothermal duration, suggesting a multi-directional nature of the dissolution-recrystallisation growth mechanism.

Nanorods with high aspect ratio (*long/thin NR*) are formed by oriented attachment of the scrolled ~ 7 nm crystallites formed as a result of the acidic conditions. After the formation of 1D *long/thin NR* under suitable conditions, they are susceptible to growth via Ostwald ripening¹⁴⁹ in which smaller crystallites dissolve and recrystallise onto larger crystallites, common in other 1D ceramic structures.³⁶ Simultaneous growth and *long/thin NR* rod formation results in a bimodal size distribution, observed for the samples synthesised at 180 °C for at least 20 hours. As a result, the diameter and length size distribution achieved broadens as the hydrothermal time is increased to 80 hours. For hydrothermal synthesis at 200 °C, the rate of both steps is increased, resulting in a monomodal length and diameter size distribution of rods with low aspect ratios (< 16). In addition, growth by dissolution-recrystallisation depends on the solubility of the crystallites,⁴⁹ which increases proportionally with synthesis temperature, facilitating a faster growth rate at 200 °C compared to 180 °C. This is supported by the fact that the average *short/thick NR* is larger when the synthesis is carried out at the higher temperature for a given period.

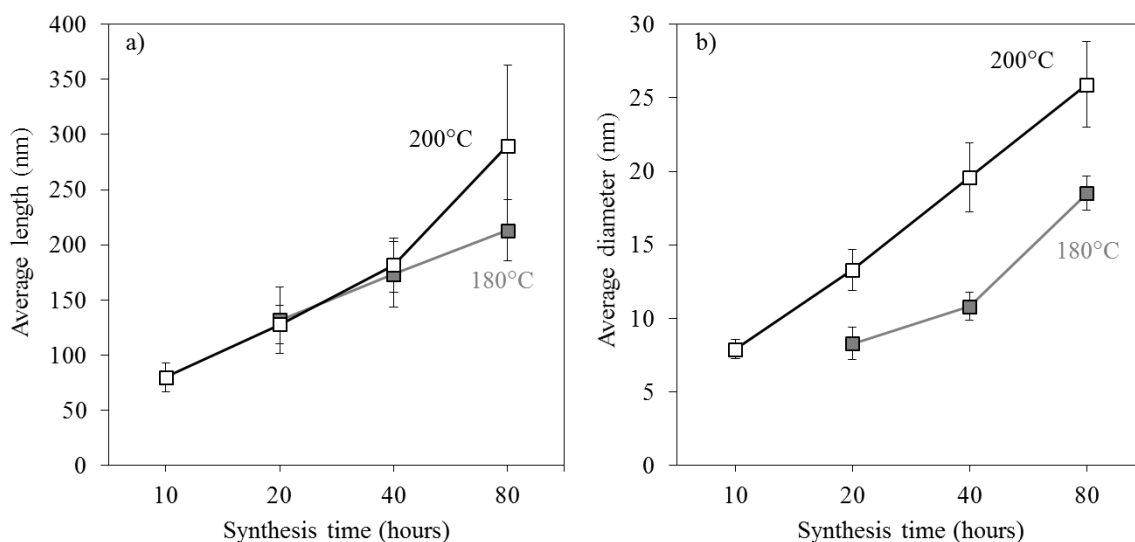


Figure 33. Average sizes of *short/thick NR* γ -Al₂O₃ produced by hydrothermal synthesis for different durations at 180 °C (grey) and 200 °C (black). a) length and b) diameter.

On average, the *short/thick NR* diameter is larger when treated at 200 °C compared to the equivalent material synthesised at 180 °C (Table 20 and Figure 33) due to an increased rate of growth. However, the length of the *short/thick NR* is unaffected by synthesis temperature but the length does increase with synthesis time. This is partially in agreement with Xu *et al.*¹⁴⁶ who reported an increase in the nanorod diameter and length by increasing the temperature from 120 to 180 °C. However, the difference between length trends may be due to the distinction made herein between the high and low aspect ratio rods.

Prolonging the synthesis time increases both the length and the diameter of the *short/thick NR* γ -Al₂O₃ nanorods, as shown in Figure 33. The average diameter of the low aspect ratio rods produced after 20 hours at 180 °C is similar to the product obtained after only 10 hours at 200 °C. Size control of the low aspect ratio γ -Al₂O₃ nanorods synthesised for 80 hours is poor when synthesised at 200 °C compared to 180 °C, as shown by the error bars in Figure 33. In general, the length and diameter distribution widens as the synthesis time increases.

4.3.3 Nanorod formation mechanism overview

Based on the systematic study presented in this chapter in which the NaOH:Al reagent ratio, synthesis time and temperature were varied, the overall mechanism for the hydrothermal synthesis of nanorods in acidic conditions has been determined. A six step mechanism representing this understanding is summarised in Figure 34.

Initially, addition of NaOH to a solution of $\text{Al}(\text{NO}_3)_3 \cdot 9\text{H}_2\text{O}$ precipitates $\text{Al}(\text{OH})_3$ (Step 1), which under acidic conditions is hydrolysed into soluble gibbsite fragments (Step 2). When the hydrothermal temperature is $\geq 170^\circ\text{C}$, thermolysis to AlOOH building blocks takes place (Step 3), which eventually form crystalline sheets of lamellar AlOOH (Step 4), evidenced by TEM of the product obtained after 170°C hydrothermal synthesis. The formation of nanorods (Step 5) only occurs after 20 hours at temperatures greater than or equal to 180°C , whereby the sheets scroll to form nanorod crystallites, which can subsequently attach in an oriented way to form high aspect ratio nanorods. At 200°C , Step 5 can be achieved after only 10 hours hydrothermal time. The high aspect ratio nanorods undergo non-selective, multi-directional growth by Ostwald ripening (Step 6), resulting in low aspect ratio nanorods (< 16). At 200°C , Step 6 is fast so only low aspect ratio nanorods are observed, whereas at 180°C a mixture of low and high aspect ratio nanorods are observed.

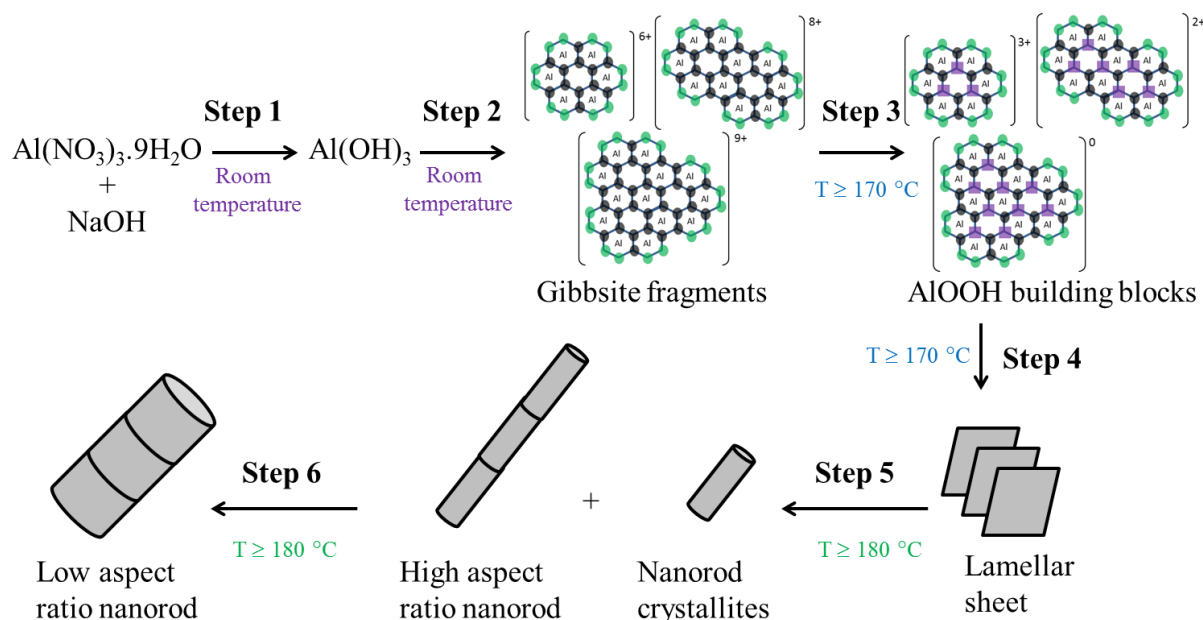


Figure 34. Summary of the six step mechanism determined for $\gamma\text{-Al}_2\text{O}_3$ nanorod formation by hydrothermal synthesis under acidic conditions.

4.4 γ -Al₂O₃ nanorod yield maximisation with morphological control

The previous sections in this chapter achieved the objective of the synthesis of morphologically distinct γ -Al₂O₃ nanostructures. However, the formation of morphologically pure γ -Al₂O₃ nanorods is at the expense of the product yield (< 35 wt%). Higher yields can be achieved by increasing the NaOH:Al ratio, resulting in a higher pH and leading to a variety of morphologies as shown in Figure 25b. By contrast the yield of nanoplates can be increased from 14.9 wt% to 56.5 wt% by decreasing the NaOH:Al reagent ratio from 4.59:1 (characterised in Section 4.2) to 3.91:1 whilst producing the same morphology with a flat surface.

This sub-section investigates recycling of the supernatant solution in a semi-continuous process in order to increase the γ -Al₂O₃ nanorod yield, whilst simultaneously tackling sustainability aspects such as solvent waste and atom efficiency. As proof of concept, the recycle process is carried out sequentially four times and the potential accumulation of spectator ions (Na⁺ and NO₃⁻) is also addressed. The recycle procedure presented in this sub-section investigates the feasibility to shift from a batch hydrothermal synthesis towards a semi-continuous process.

The sample obtained from the first batch synthesis is denoted “*Batch*” and subsequent materials acquired from recycling the supernatant “*x*” times are referred to as “*Recycle_x*”. All materials discussed in this sub-section are washed three times with deionised water unless stated otherwise. The reagent requirements and the differences between a batch and a semi-continuous process are represented in Figure 35. A semi-continuous process combines partial elements of batch and continuous processes, such that a semi-continuous process runs continuously for a discrete length of time until materials need to be periodically replenished.

According to Reaction (16), low NaOH:Al ratios (e.g. 0.77:1) result in a significant amount of unreacted Al³⁺ remaining in the supernatant solution. To keep the initial conditions constant during the recycle of the unreacted Al³⁺ solutions, equivalent amounts of reacted NaOH (0.020 mol) and Al(NO₃)₃·9H₂O precursor (0.007 mol) are added, to reproduce the conditions of the first batch synthesis (e.g. pH 3.5 and NaOH:Al molar ratio of 0.77:1) as shown in Figure 35.

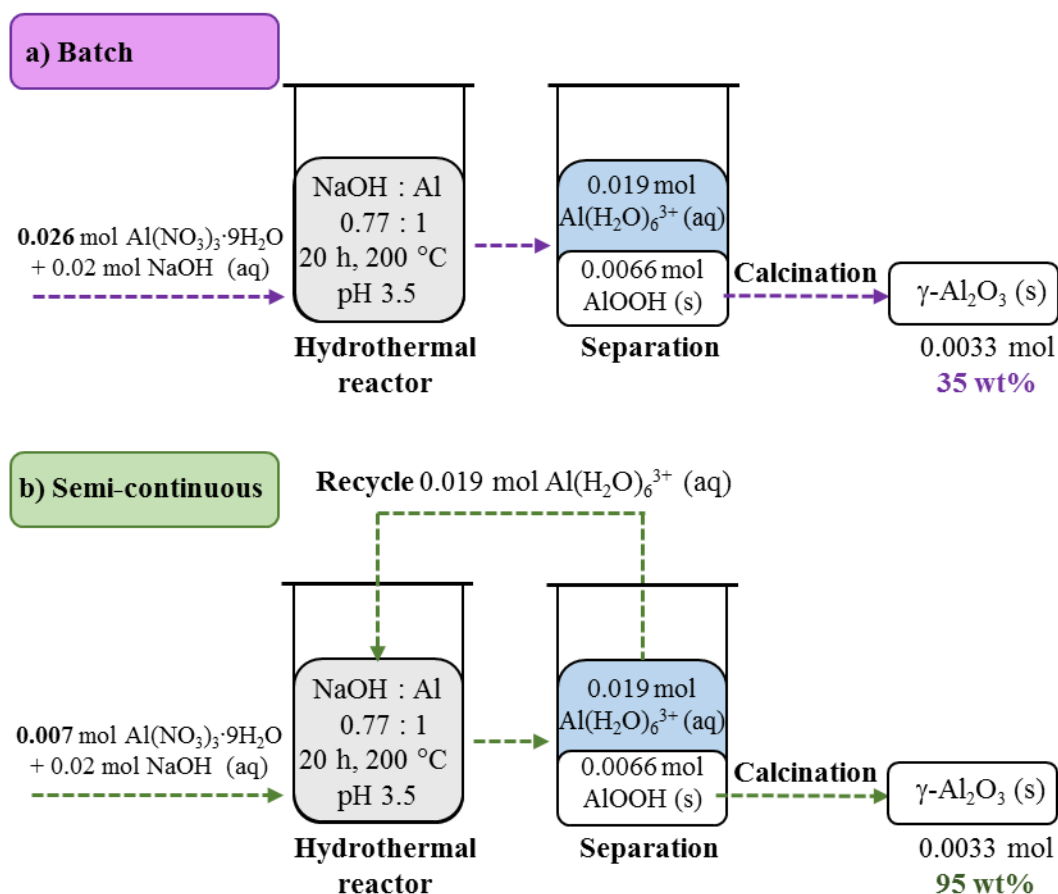


Figure 35. Hydrothermal synthesis of morphologically pure $\gamma\text{-Al}_2\text{O}_3$ nanorods by a) conventional batch process and b) semi-continuous recycle procedure.

The materials obtained after four semi-continuous assays have been characterised by various experimental techniques (pXRD, TEM, N_2 sorption) to demonstrate the feasibility and reproducibility of the recycle semi-continuous process.

The pXRD patterns (Figure 36) of the materials produced by the semi-continuous process show the same crystal structure as $\gamma\text{-Al}_2\text{O}_3$ (JCPDS 10-0425) as well as a similar order of crystallite size and BET specific surface area as the original *Batch* sample (Table 21). The BET specific surface area of the produced materials is similar to the values obtained for $\gamma\text{-Al}_2\text{O}_3$ in the literature.²¹

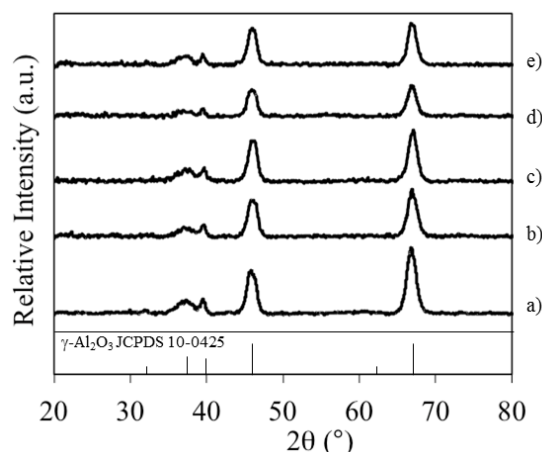


Figure 36. pXRD patterns of γ -Al₂O₃ synthesised at 200 °C with 0.77NaOH:1Al for 20 hours, calcined at 500 °C. a) *Batch*. Following the same experimental conditions but recycling the supernatant solution b) once (*Recycle_1*) c) twice (*Recycle_2*) d) three times (*Recycle_3*) and e) four times (*Recycle_4*). γ -Al₂O₃ (JCPDS 10-0425).

A threefold increase in yield from recycling the reaction solution is reported in Table 21. In the semi-continuous process, the maximum aluminium theoretical yield of 100 % is approached without changing the NaOH:Al ratio. The success of the proposed semi-continuous recycle methodology is further evidenced by the consistency of the γ -Al₂O₃ morphology observed by the TEM micrographs in Figure 37. Morphologically pure γ -Al₂O₃ nanorods with a similar aspect ratio and narrow diameter size distribution are produced from each consecutive recycle. The discrepancy between the sizes determined from TEM (11 to 13 nm diameter and 128 to 179 nm length) and by the Scherrer equation from pXRD pattern (~ 8 nm) indicates a polycrystalline nature.

Table 21. Physical properties of γ -Al₂O₃ produced from recycle syntheses at 200 °C for 20 hours with constant NaOH:Al ratio of 0.77:1 and initial pH values of 3.2 – 3.5. (Error shown in brackets).

Sample	Al yield (wt%)	S _{BET} ^a (m ² ·g ⁻¹)	Average crystallite size (nm)			
			TEM length	TEM diameter	Aspect ratio ^c	pXRD ^b
<i>Batch</i>	35	146 (1.1)	128	13	10	8.3 (0.1)
<i>Recycle_1</i>	95	130 (1.7)	170	13	13	8.2 (0.1)
<i>Recycle_2</i>	95	124 (1.5)	167	11	15	8.6 (0.1)
<i>Recycle_3</i>	95	153 (1.6)	139	13	11	8.6 (0.1)
<i>Recycle_4</i>	95	181 (2.4)	137	11	12	8.8 (0.1)

^a S_{BET} is the specific surface area calculated using the BET approximation using N₂ sorption data at -196 °C.

^b Calculated using the (440) γ -Al₂O₃ peak at ~ 67° with the Scherrer equation. JCPDS 10-0425.

^c Length : diameter.

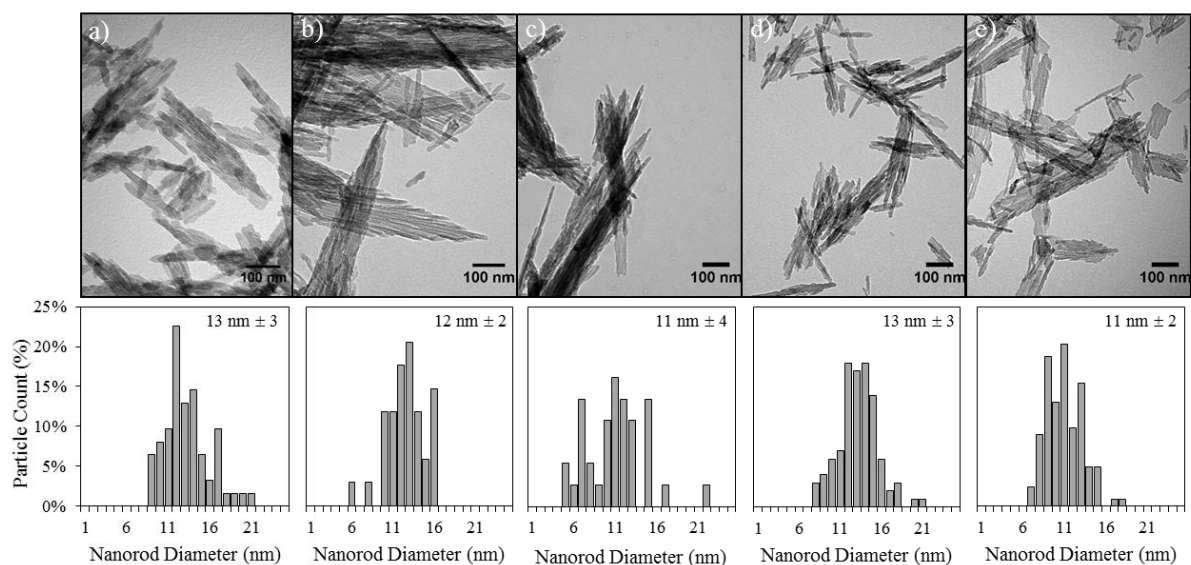


Figure 37. TEM micrographs and distributions of γ - Al_2O_3 synthesised for 20 hours at 200 °C with 0.77NaOH:1Al a) *Batch*. Following the same experimental conditions but recycling the supernatant solution b) once (*Recycle_1*) c) twice (*Recycle_2*) d) three times (*Recycle_3*) and e) four times (*Recycle_4*). Calcined at 500 °C.

The pXRD patterns of γ - Al_2O_3 materials obtained by recycle before (Figure 38) and after (Figure 36) washing with H_2O show diffraction peaks assigned to γ - Al_2O_3 (JCPDS 10-0425). However, after one recycle assay, diffraction peaks at 29.3°, 31.8° and 47.9° appear in the unwashed *Recycle_1* sample (Figure 38b), assigned to NaAlO_2 (JCPDS 33-1200). Similarly, due to the higher sodium concentration, these NaAlO_2 peaks were present in pXRD of the calcined product from the first synthesis with 4.59NaOH:1Al following the synthesis of nanoplates (Section 4.2).

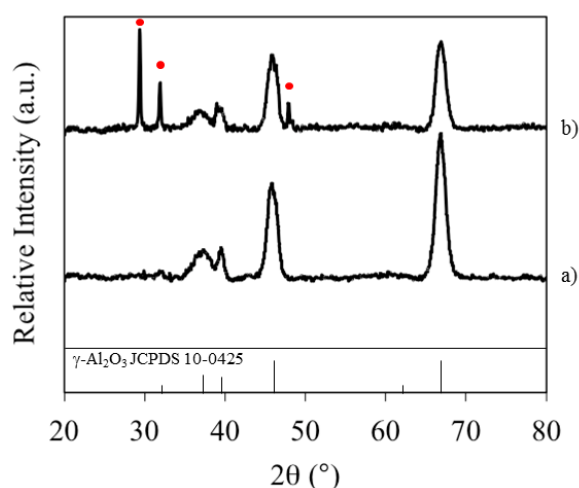


Figure 38. pXRD of **unwashed** γ - Al_2O_3 synthesised with 0.77NaOH:1Al at 200°C for 20 hours. Calcined 500 °C. a) *Batch* and b) *Recycle_1*. γ - Al_2O_3 peaks are assigned to JCPDS 10-0425. Additional peaks marked by a red circle correspond to NaAlO_2 (JCPDS 33-1200).

NaAlO₂ is often employed as a starting precursor for the synthesis of boehmite nanorods and higher NaOH:Al ratios such as 20:1 (0.77:1 used herein) have been used elsewhere to purposely synthesise NaAlO₂.^{41,140,150,151} As such, accumulation of Na⁺ and NO₃⁻ ions upon recycle of the supernatant results in the formation of NaAlO₂ by-product.



NaAlO₂ is believed to form via the reaction of Al(OH)₃ and NaOH as shown in Reaction (27). However, the formation of NaAlO₂ by-product is less than 5 wt% and is inconsequential as it can easily be removed by washing due to its high solubility in water, without affecting the quality of the final γ -Al₂O₃ product. This is confirmed by the absence of NaAlO₂ peaks in the pXRD of the washed product (Figure 36). NaAlO₂ formation resulting from the semi-continuous process equates to only 5 wt% of the total aluminium yield (100 wt%). In this respect, the semi-continuous process is highly atom efficient with a γ -Al₂O₃ nanorod yield of 95 wt% compared to only 35 wt% from the conventional batch synthesis. Additionally, the industrially coveted NaAlO₂ can be recovered by re-crystallisation and used in a range of applications such as waste water treatment.^{140,152}

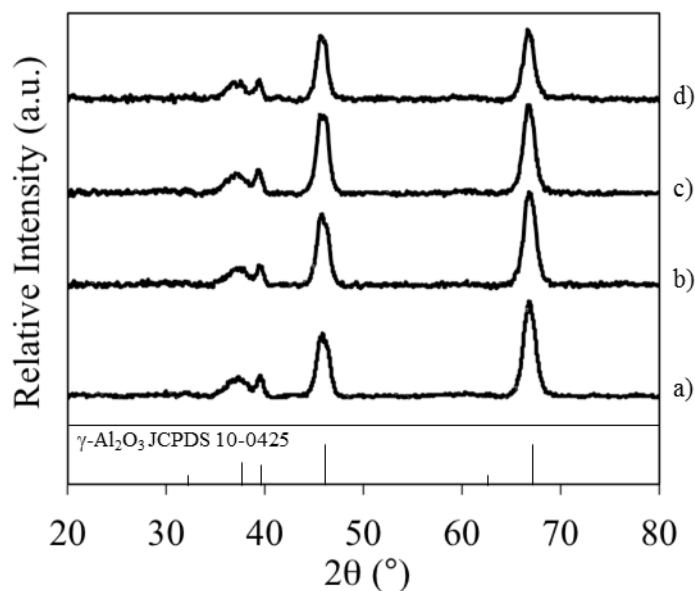


Figure 39. pXRD of γ -Al₂O₃ synthesised with 0.77NaOH:1Al at 200°C for 20 hours. Calcined 500 °C. a) *Batch*, and the number of mol of NaNO₃ that would form after *x* recycles b) *x5_NaNO₃* c) *x10_NaNO₃* and d) *x20_NaNO₃*. Assigned to γ -Al₂O₃ (JCPDS 10-0425).

The formation of NaAlO₂ as a by-product in the hydrothermal synthesis of γ -Al₂O₃ has not been mentioned previously in the literature, possibly because the effect of the ions remaining in solution is often overlooked. Further understanding was achieved by carrying out a series of experiments to determine the potential effect of Na⁺ and NO₃⁻ accumulation in the semi-continuous synthesis from their release via Reaction (16).

Three experiments were carried out using the same batch hydrothermal conditions (20 hours, 200 °C, NaOH:Al 0.77:1) with the addition of equivalent amounts of NaNO₃ that would accumulate if the reaction was carried out for 5, 10 and 20 consecutive recycles. The quantity of NaNO₃ is calculated according to the stoichiometry of Reaction (16), equal to 0.100, 0.200 and 0.400 mol respectively. Samples are denoted “*xn_NaNO₃*”, where “*n*” is the equivalent number of mol of NaNO₃ added.

Table 22. Properties of γ -Al₂O₃ materials calcined at 500 °C produced at 200 °C for 20 hours with 0.77:1 NaOH:Al ratio with 5, 10 and 20 equivalent mol of NaNO₃ including reference *Batch* sample for comparison.

Sample	S _{ABET} ^a (m ² ·g ⁻¹)	Crystallite size ^b (nm)
<i>Batch</i>	146	8.3
<i>x5_NaNO₃</i>	133	7.0
<i>x10_NaNO₃</i>	156	7.4
<i>x20_NaNO₃</i>	151	7.5

^a S_{ABET}: Specific surface area calculated using the BET approximation.

^b Calculated using the (440) γ -Al₂O₃ peak at ~ 67° with the Scherrer equation. JCPDS 10-0425.

The similarity of the pXRD pattern of washed γ -Al₂O₃ without (Figure 36) and with addition of different quantities of NaNO₃ in Figure 39 suggests that Na⁺ and NO₃⁻ are spectator ions in the hydrothermal process and are removed by washing with H₂O. The spectator ions do not affect the mechanism of formation of γ -Al₂O₃ because the NaNO₃ assays produce materials with similar crystallite size and specific surface area (Table 22).

This section demonstrates that a significantly higher yield (95 wt%) of morphologically pure γ -Al₂O₃ nanorods can be achieved by implementing a semi-continuous system of supernatant recycle compared to a conventional batch hydrothermal synthesis (35 wt%). Characterisation of the obtained materials confirms that the physical properties of the γ -Al₂O₃ nanorods obtained from the semi-continuous route are consistent with those of the batch synthesis.

4.5 Materials used as catalyst supports

The versatile hydrothermal method outlined in this chapter has facilitated the synthesis of a range of γ -Al₂O₃ nanostructures. A variety of these materials have been selected for use as a catalyst support in the following research chapters. Two classes of nanorod with different diameters have been chosen to represent a “curved surface” with different degrees of curvature for comparison with the nanoplate “flat surface”. In some cases a commercial γ -Al₂O₃ material acquired from Sasol Ltd is used as a benchmark support for comparison, denoted “*commercial*”. These chosen supports provide curved, flat and bulk surfaces, which will be used to determine the effect of morphology, and more specifically curvature, on the stabilisation of metal nanoparticles.

All of the materials synthesised for use as a catalyst support have been calcined at 500 °C to form γ -Al₂O₃ (Figure 41) and washed three times with deionised water by centrifugation. The *commercial* γ -Al₂O₃ support is used as received. Properties and nomenclature of the selected materials are summarised in Table 23. Some key characterisation results of these supports are summarised in this section to facilitate differentiation of their properties for the subsequent chapters. The *plate* support is synthesised with 3.91:1 reagent ratio (pH 11.2) rather than 4.59:1 (pH 12.8) used in Section 4.2, in order to increase the yield from 14.9 wt% to 56.5 wt% whilst maintaining the same flat, plate-like morphology due to the basic synthesis conditions.

The SEM micrograph and N₂ sorption data of the *commercial* support were obtained from Sasol Ltd. The rest of the characterisation was carried out on the *commercial* support as received. In some instances characterisation of the *commercial* support was not possible.

Table 23. Details of the γ -Al₂O₃ materials selected for use as catalyst supports.

Support nomenclature	Morphology	Synthesis time, temperature, NaOH:Al	SA _{BET} ^a (m ² ·g ⁻¹)	Na ^b (wt%)	Average size (nm)	
					TEM (l x d)	pXRD ^c
<i>180thin</i>	Nanorod	20h, 180 °C, 0.77:1	144	1.9	162 x 7.8	6.4
<i>10hthin</i>	Nanorod	10h, 200 °C, 0.77:1	162	2.1	80 x 7.9	6.4
<i>40hfat</i>	Nanorod	40h, 200 °C, 0.77:1	86	1.7	182 x 19.6	6.5
<i>Plate</i>	Nanoplate	20h, 200 °C, 3.91:1	48	2.7	103*	5.6
<i>Commercial</i>	Micro spheres	n/a	148	0.4	n/a	5.7

^a SA_{BET} is the specific surface area calculated using the BET approximation using N₂ sorption data at -196 °C.

^b Calculated from ICP of the solid digested in aqua regia.

^c Calculated using the (440) γ -Al₂O₃ peak at ~ 67° with the Scherrer equation. JCPDS 10-0425.

* Average of all nanoplate dimensions.

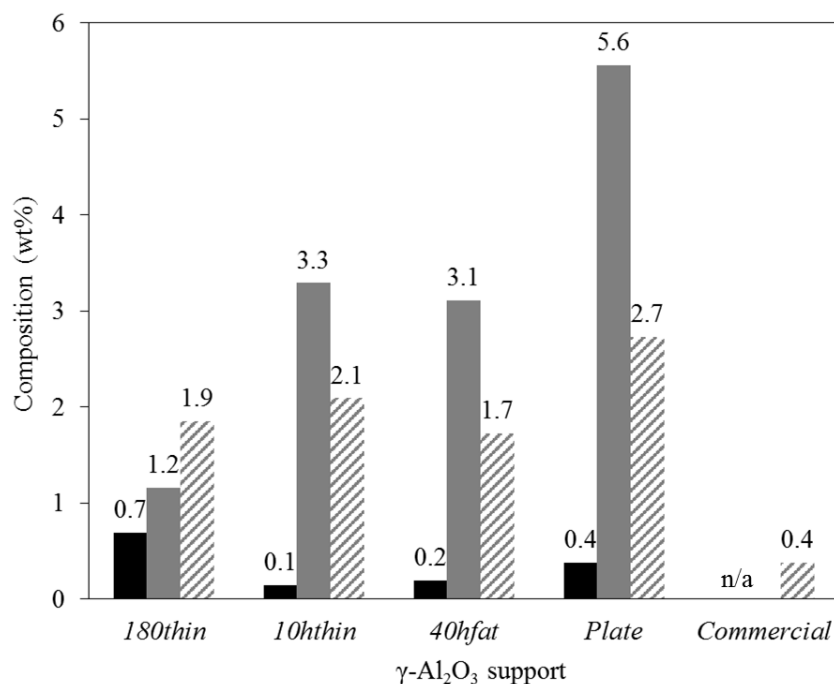


Figure 40. Composition of γ -Al₂O₃ supports determined by different methods. XPS for carbon (black) and sodium (grey), and by ICP for sodium (grey stripes).

XPS data of the *commercial* support was not acquired. For the rest of the supports, XPS shown in Figure 40 highlights the presence of carbon. The remainder of the support is composed of oxygen and aluminium only (not shown in Figure 40). XPS composition data provides information about the top ~ 10 nm of the sample surface, particularly relevant for catalytic application, which may be sensitive to the surface composition. In order to determine the sodium content in the full support, digested solid samples were analysed by ICP.

The *180thin* support synthesised at 180 °C has a higher sodium loading in the bulk than at the surface but the opposite is true for the other supports synthesised at 200 °C in which a considerable amount of sodium is present on the surface (5.6 wt%).

The *plate* support has the highest sodium content, both on the surface and in the bulk. The sodium content is relevant because it may have implications on the catalytic activity and is known to act as a poison in some catalytic application such as Fisher-Tropsch synthesis (FTS)⁹⁸ but may act as a promoter in other cases. The sodium present is amorphous as it is not visible on the pXRD of the washed supports (Figure 41). Prior to washing, the pXRD of *plate* shows the presence of crystalline NaAlO₂, which is removed by washing.

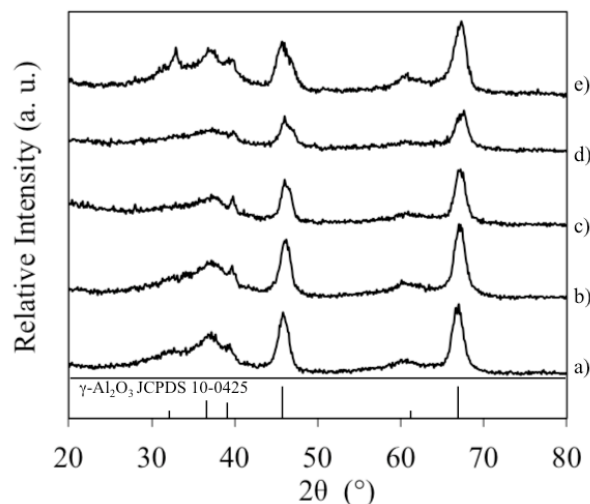


Figure 41. pXRD of washed support materials obtained by hydrothermal synthesis. a) *180thin*, b) *10hthin*, c) *40hfat* and d) *plate*. The pattern of the *commercial* support is shown in e). $\gamma\text{-Al}_2\text{O}_3$ JCPDS 10-0425.

The peaks found in the pXRD pattern of the washed, calcined supports (Figure 41) are assigned to $\gamma\text{-Al}_2\text{O}_3$ (JCPDS10-0425), without any other crystalline phases present.

The specific surface area is lowest for the *plate* support (Table 23). The surface area of the *commercial* support is $148\text{ m}^2\cdot\text{g}^{-1}$, similar to the thin nanorods (*180thin* and *10hthin*) whilst the larger nanorods (*40hfat*) have a lower surface area. The differences in surface area may be linked to their distinct morphology as shown in Figure 42 or the difference in porosity shown in Figure 44.

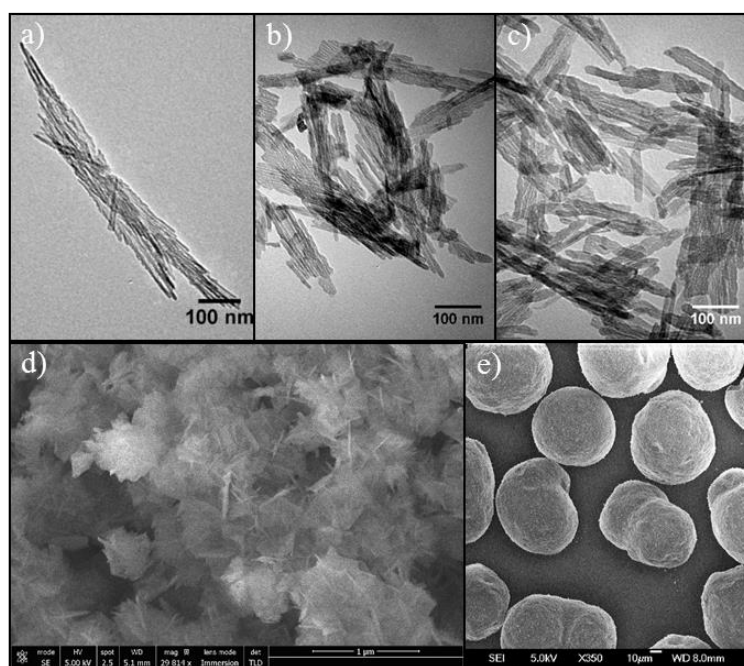


Figure 42. Electron microscopy of $\gamma\text{-Al}_2\text{O}_3$. a) *180thin*, b) *10hthin*, c) *40hfat* d) *plate* and e) *commercial*.

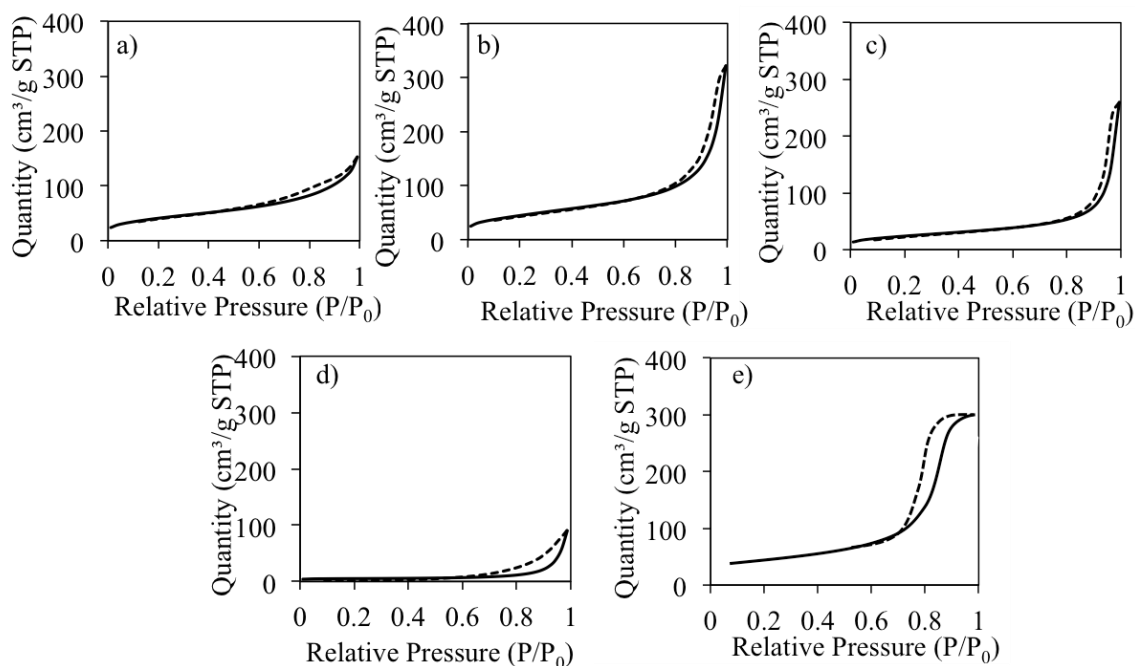


Figure 43. N₂ adsorption-desorption isotherms of γ -Al₂O₃. a) *180thin*, b) *10hthin*, c) *40hfat* d) *plate* and e) *commercial*.

The N₂ adsorption-desorption isotherms for all supports are IUPAC Type IV shape, characteristic of mesoporous materials (Figure 43).

The pore size distributions for *10hthin*, *40hfat* and *plate* in Figure 44 show broad peaks due to the inter-nanostructure voids. By contrast *180thin* exhibits a sharp peak at 3.7 nm due to presence of well-defined pores of this size. The *commercial* support possesses well-defined mesopores of ~ 20 nm in diameter.

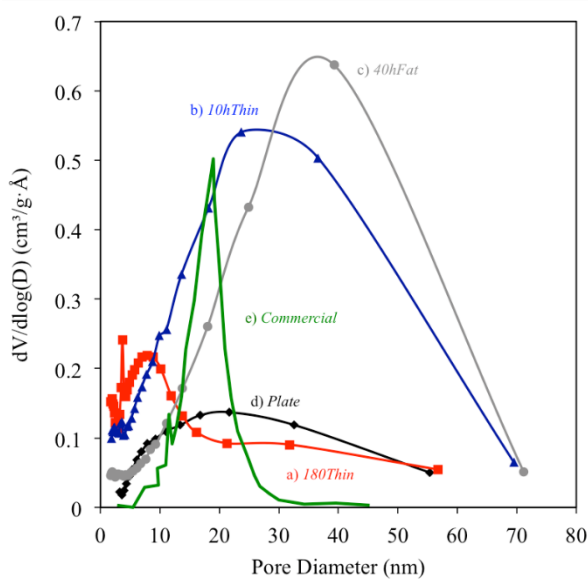


Figure 44. Pore size distributions of γ -Al₂O₃. a) *180thin*, b) *10hthin*, c) *40hfat* d) *plate* and e) *commercial*.

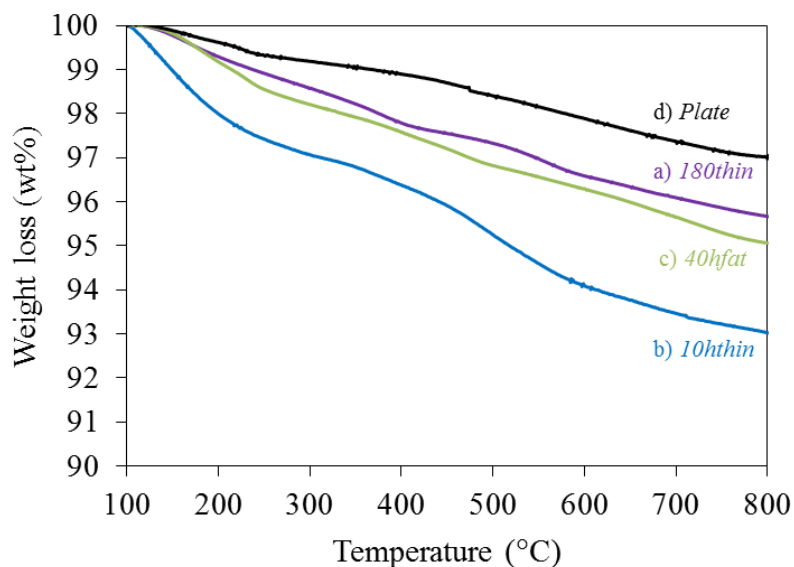


Figure 45. TGA under N₂ of washed γ -Al₂O₃ supports after calcination at 500 °C. a) *180thin*, b) *10hthin*, c) *40hfat* and d) *plate*.

TGA up to 800 °C in an N₂ atmosphere of the synthesised supports shown in Figure 45 demonstrates relative stability with maximum 7 wt% loss observed in the *10hthin* support and only 3 wt% loss in the *plate* support. Thermal decomposition of γ -Al₂O₃ in an inert atmosphere leads to the possible formation of other transition Al₂O₃ phases such as δ at 600 °C and α at 1050 °C.³⁰ For our catalytic applications, 1050 °C is not reached so α is unlikely to form. However in certain instances the reaction temperature may exceed 600 °C potentially inducing a phase transition, which may have little effect on the catalytic activity but it is worth noting in case it affects metal stability.

Chapter 4 conclusions

This chapter presents a systematic study of hydrothermal synthesis conditions (NaOH:Al, pH, temperature and time), which has facilitated the production of a range of morphologically pure γ -Al₂O₃ materials with different curvatures, including nanoplates and nanorods with different diameters. The materials will be used as catalyst supports in the following research chapters.

In the hydrothermal synthesis of γ -Al₂O₃, the NaOH:Al molar ratio governs the product yield. Furthermore, changing the NaOH:Al ratio alters the synthesis pH, which controls the product morphology, with acidic and basic conditions yielding nanorods and nanoplates respectively.

Studying the effect of hydrothermal temperature and time on the formation of γ -Al₂O₃ nanorods reveals a mechanistic understanding of their formation, summarised by an evidence based, six-step mechanism. In Step 1, Al(OH)₃ precipitates from the addition of precursors, which undergoes dissolution due to the acidic conditions into hexameric gibbsite fragments (Step 2). During hydrothermal conditions ≥ 170 °C, the fragments are deprotonated into AlOOH building blocks (Step 3), followed by their crystallisation into lamellar AlOOH (Step 4). Scrolling of lamellar AlOOH followed by oriented attachment into AlOOH nanorods takes place at ≥ 180 °C (Step 5), which consequently undergo growth by Ostwald ripening (Step 6). Manipulation of the relative rate of Steps 4-6 under different synthesis conditions, such as time and temperature, facilitate nanorod dimension control. For example, the diameter is increased after the hydrothermal temperature is raised from 180 to 200 °C or by prolonging the synthesis time. However, after 80 hours synthesis at 200 °C, narrow size control is lost.

The low yield of the pure γ -Al₂O₃ nanorods (35 wt%) by batch synthesis motivated the design of a semi-continuous process in which the supernatant reaction solution is recycled, increasing the product yield to 95 wt% without loss of product quality or morphological purity. The recycle methodology is based upon reproducing the same initial synthesis conditions, such as pH, achieved by controlling the NaOH:Al ratio. The semi-continuous system was demonstrated to be successful for four consecutive recycles and it was shown that Na⁺ and NO₃⁻ ions would not accumulate in the material over 20 recycles. Validation of the recycle procedure highlights the feasibility to shift from conventional batch to semi-continuous manufacturing with reduced waste streams and improved atom efficiency. The recycle methodology could be applied to the manufacturing of other industrially relevant nanostructured metal oxides.

Chapter 5 – Effect of cobalt loading methods on Co/ γ -Al₂O₃ properties and catalytic activity

The objective of Chapter 4 was the synthesis of a range of γ -Al₂O₃ support materials. The following chapter focuses on different methods for the addition of cobalt nanoparticles onto the γ -Al₂O₃ supports. In this chapter, the support material used in all cases is the γ -Al₂O₃ nanoplate, referred to as “plate”. This support is synthesised under hydrothermal conditions at 200 °C for 20 hours with a 3.9NaOH:1Al molar ratio. Full characterisation of *plate* γ -Al₂O₃ can be found in Section 0.

The purpose of this study is to determine the effect of cobalt loading method on cobalt particle size and catalytic activity. The catalytic activity of the materials is determined using ammonia decomposition as a model reaction since this reaction is highly size sensitive when catalysed by cobalt materials, highlighted by previous work using cobalt/carbon catalysts.¹⁵³

Due to the effect of particle size on catalytic activity, the cobalt particle size of the Co/ γ -Al₂O₃ catalysts has been characterised by powder X-ray diffraction (pXRD) and transmission electron microscopy (TEM). Other key properties that may affect the catalytic activity, such as reducibility and composition, are evaluated by temperature programmed reduction (TPR), inductively coupled plasma optical emission spectroscopy (ICP-OES) and X-ray photoelectron spectroscopy (XPS).

The conclusions of the characterisation and catalytic results will be used to choose a set of synthesis parameters and pre-treatment conditions that will be applied to a series of catalysts with different loadings and γ -Al₂O₃ supports in the next chapter (Chapter 6).

5.1 Effect of synthesis methods on Co/ γ -Al₂O₃ properties

The choice of nanoparticle synthesis method is critical as it can result in the formation of distinct particle sizes and can modify the metal-support interaction, both of which have implications on catalytic activity. The methods used herein are based on adsorption, impregnation and precipitation. In the case of impregnation, both incipient wetness impregnation and wet impregnation have been used. For precipitation, a range of precipitants were investigated including NaOH, urea and basic buffer solutions. These synthesis methods have been explained in further detail in the literature review (Section 2.1.1) and experimental section (Section 3.2).

Adsorption is a popular method for obtaining narrow particle size distributions, in which metal ions are adsorbed or exchanged (ion exchange) onto a support surface.¹³ However, initial adsorption assays that should result in 9.1 wt% theoretical loading resulted in only 1.4 wt% loading and the formation of irreducible cobalt aluminates.

The low loading arises from the fact that the ability to load cobalt onto a metal oxide support depends on the pH of the solution, which needs to be greater than or equal to the point of zero charge (PZC) as shown in Figure 46. The PZC is the pH at which all of the surface Al³⁺ ions are coordinated to hydroxyl groups, resulting in a charge neutral surface. For γ -Al₂O₃, the PZC ranges from pH 7 to 10.³⁰ When the solution pH is above the PZC, the surface is comprised of O⁻ and when the pH is below the PZC, the hydroxide groups are protonated as shown in Figure 46. Due to the acidity of Co(NO₃)₂·6H₂O, its addition to an aqueous suspension of γ -Al₂O₃ results in a pH decrease below the PZC. Consequently, the loading takes place in mildly acidic conditions at pH 6.5, making Co²⁺ loading in this environment electrostatically unfavourable.

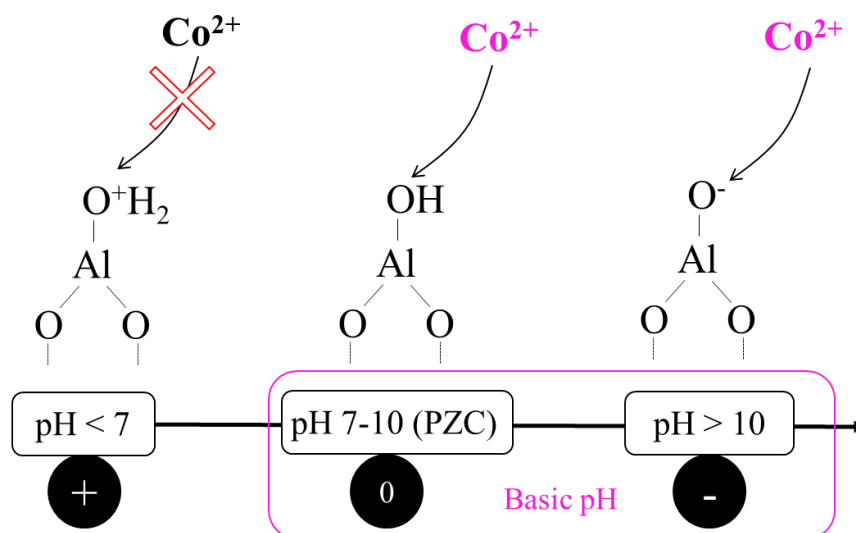


Figure 46. The feasibility of Co^{2+} adsorption in aqueous solution onto Al_2O_3 surface at different pH conditions.

To overcome the pH limitation of the adsorption method, alternative techniques were employed based on precipitation using novel precipitants to increase the synthesis pH above the PZC to induce cobalt precipitation and facilitate higher cobalt loadings.

In order to determine the optimal synthetic conditions, different concentrations of precipitants were added to a 100 mL aqueous solution of cobalt nitrate ($\text{Co}(\text{NO}_3)_2 \cdot 6\text{H}_2\text{O}$) in the absence of the support. The mixture was stirred at $60\text{ }^\circ\text{C}$ for 3 hours. The quantities determined to be sufficient to induce cobalt precipitation are summarised in Table 24.

Some impregnation methods were also used to prepare *Co/plate* catalysts in order to provide a benchmark for comparison between the adsorption and precipitation routes. Both incipient wetness impregnation (IWI) and wet impregnation (impregnation) were used.

The synthesis parameters and properties of catalysts synthesised by different methods with a constant amount of Co precursor are summarised in Table 24. Detailed descriptions of the methods can be found in Section 3.2. The $\text{Co}/\gamma\text{-Al}_2\text{O}_3$ materials will henceforth be referred to using the nomenclature in Table 24, which includes key synthesis parameters such as loading, metal, support, method and processing. The prefix number relates to the actual metal loading. The notation “-cal250” indicates the material has been calcined at $250\text{ }^\circ\text{C}$. All catalysts in this section have been calcined at $250\text{ }^\circ\text{C}$ for 5 hours at a rate of $1\text{ }^\circ\text{C}\cdot\text{min}^{-1}$ in order to remove residual surface species such as nitrates and to form the oxidic cobalt species. For a cobalt catalyst, calcination usually results in the formation of Co_3O_4 crystallites.⁸³

Table 24. Synthesis parameters and properties of calcined *Co/plate-cal250* catalysts synthesised by different methods.

Catalyst	Method	Precipitant quantity	Initial pH (precipitant and Co)	Actual Co loading ^a (wt%)	Catalyst colour
<i>7.7Co/plate-IWI-cal250</i>	IWI	0	n/a	7.7	Black
<i>7.7Co/plate-imp-cal250</i>	Impregnation	0	n/a	7.7	Dark brown
<i>1.4Co/plate-ads-cal250</i>	Adsorption	0	6.5	1.4	Light khaki green
<i>6.8Co/plate-NaOH-cal250</i>	NaOH precipitation	0.125 mol	10.8	6.8	Black / dark green
<i>7.6Co/plate-carb-cal250</i>	Carbonate buffer precipitation	50 mL	9.3	7.6	Black / dark green
<i>7.3Co/plate-bor-cal250</i>	Borate buffer precipitation	50 mL	9.8	7.3	Black / dark green
<i>3.8Co/plate-urea-cal250</i>	Urea precipitation	0.416 mol	5.9	3.8	Violet

^a Calculated from ICP of the digested calcined solid.

Detailed characterisation of the calcined (250 °C) and reduced (580 °C) materials exposes the effect of the synthesis method on the resulting catalyst properties. The characterisation results will first be individually presented and then discussed collectively in order to determine the catalyst properties arising from the choice of synthesis method. The catalytic data will be presented at the end of the Chapter in Section 5.2.

The *3.8Co/plate-urea-cal250* catalyst contains only 42 wt% of the available Co, which may be because 60 °C synthesis temperature was used herein for consistency but higher temperatures (e.g. 80 to 90 °C) are reportedly required to breakdown urea and slowly release OH⁻, inducing precipitation of cobalt.¹³

5.1.1 Characterisation of calcined *Co/plate* catalysts

The reduction process is a significant aspect of cobalt catalyst preparation as Co⁰ is the accepted catalytically active site for NH₃ decomposition.⁵⁶ As such, it is important to thoroughly analyse temperature programmed reduction (TPR) profiles of the catalysts in order to select a suitable reduction temperature. This is crucial because excessive temperatures increase the probability of sintering. The deconvoluted TPR profiles are shown in Figure 47 and the associated temperature of the peaks is summarised in Table 25 for the catalysts synthesised by different methods.

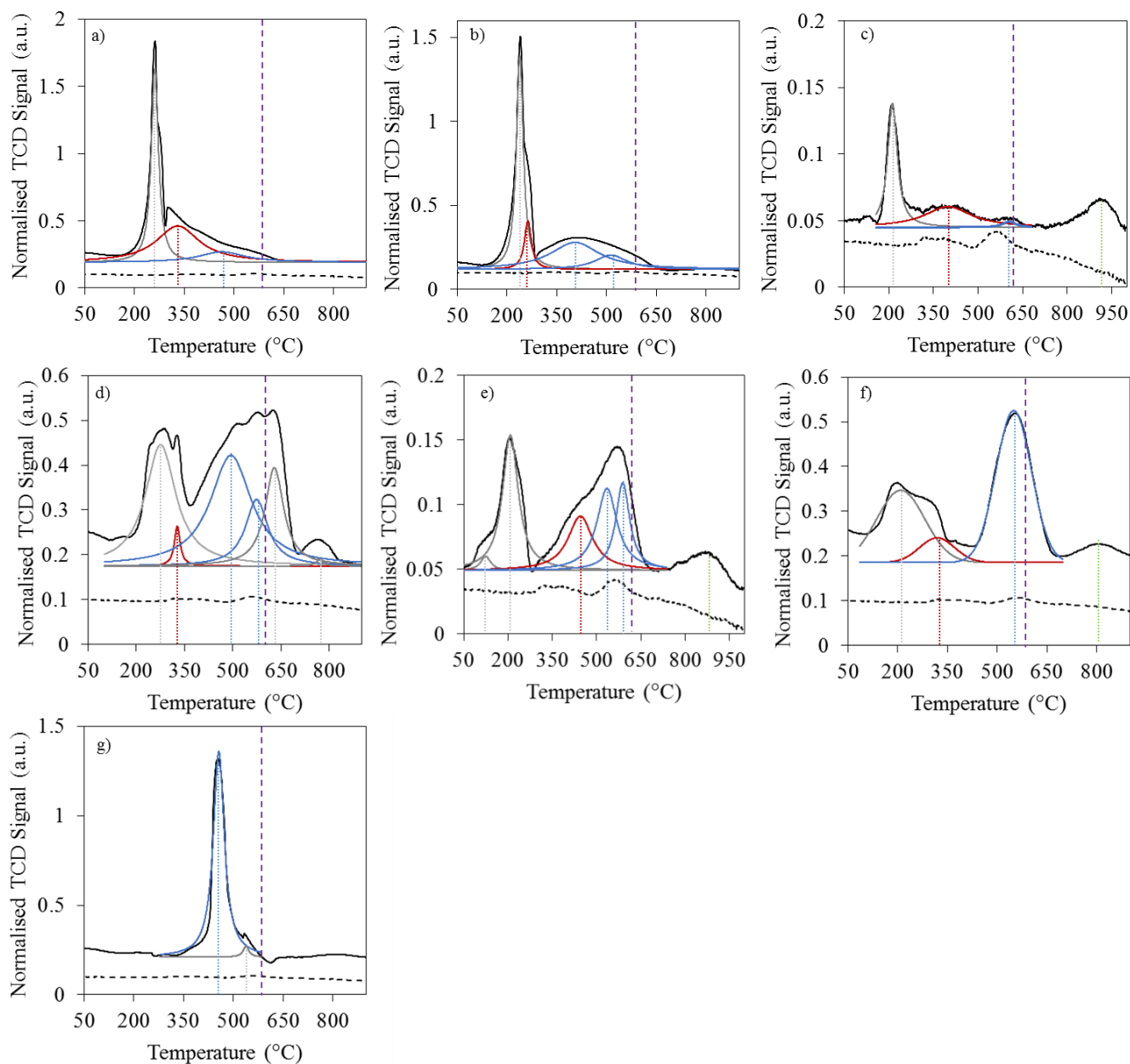


Figure 47. TPR profiles for *Co/plate-cal250* catalysts synthesised by different methods. a) *7.7Co/plate-IWI-cal250*, b) *7.7Co/plate-imp-cal250*, c) *1.4Co/plate-ads-cal250*, d) *6.8Co/plate-NaOH-cal250*, e) *7.6Co/plate-carb-cal250*, f) *7.3Co/plate-bor-cal250* and g) *3.8Co/plate-urea-cal250*. Normalised TCD signal = black line, *plate* support = black dashed line, chosen 580 °C reduction temperature = vertical purple dashed line. Deconvoluted peaks: $\text{Co}^{3+} \rightarrow \text{Co}^{2+}$ = burgundy line and $\text{Co}^{2+} \rightarrow \text{Co}^0$ = blue line $\text{CoAl}_2\text{O}_4 \rightarrow \text{Co}^0$ = green curve and removal of impurities = grey line.

The reduction profile of the $\gamma\text{-Al}_2\text{O}_3$ *plate* support is shown by the dashed black lines in Figure 47. The *plate* support has a negligible overall effect on TCD signal relative to the intensity of the peaks arising from reduction of the cobalt species. The purple dashed line at 580 °C on the graphs in Figure 47 shows the chosen reduction temperature based on analysis of the profiles and NH_3 decomposition catalytic tests in Section 5.2.2.

The typical reduction of cobalt follows a two-step process from Co_3O_4 to CoO to Co^0 .⁵² In addition, the reduction of strongly interacting cobalt aluminates (CoAl_2O_4) reduce to Co^0 typically in the range from 800 to 1000 °C.^{37,53} Peaks in the thermal conductivity (TCD) signal may also be observed from the reduction of impurities such as nitrates which release N_2 or carbon which is gasified to release CH_4 .

In some cases, mass spectrometry (MS) was used to assist with TPR peak identification (Figure A98, Appendix). Specifically, m/z 2, 16, 18 and 28 were recorded in order to investigate the evolution of H_2 , CH_4 , H_2O and N_2 . A m/z peak at 28, anticipated for N_2 evolution, may also arise due to the release of C_2H_4 , the presence of which is unlikely based on the absence of a CH_4 MS peak (m/z 16). A m/z 28 peak could also arise from CO , however it is unlikely in a reductive environment. Note that the MS signal is uncalibrated and as such can only be used for qualitative data analysis. No peaks are observed when H_2O is released (m/z 18) because it is separated in the cold trap in the instrument to protect the detectors.

Table 25. TPR peak temperatures of *Co/plate-cal250* assigned to different reductive chemical processes.

Catalyst	Peak temperature (°C)				Removal impurities e.g. N or C		
	$\text{Co}^{3+} \rightarrow \text{Co}^{2+}$	$\text{Co}^{2+} \rightarrow \text{Co}^0$	$\text{CoAlO}_4 \rightarrow \text{Co}^0$				
<i>7.7Co/plate-IWI-cal250</i>	330.0	463.3	-		261.1		
<i>7.7Co/plate-imp-cal250</i>	405.0	405.0	513.1	-	238.9		263.1
<i>1.4Co/plate-ads-cal250</i>	398.4	604.5	911.4				211.9
<i>6.8Co/plate-NaOH-cal250</i>	327.4	494.0	574.0	-	275.6	629.0	770.0
<i>7.6Co/plate-carb-cal250</i>	445.0	535.1	588.6	877.8	124.5		208.3
<i>7.3Co/plate-bor-cal250</i>	318.7	549.5	807.8				209.4
<i>3.8Co/plate-urea-cal250</i>	-	456.3	-				537.8

Figure 47 shows that the catalysts prepared by impregnation (*7.7Co/plate-IWI-cal250* and *7.7Co/plate-imp-cal250*) have similar reduction profiles. The *3.8Co/plate-urea-cal250* catalyst contrasts the rest of the catalyst series because it lacks a Co^{3+} reduction peak. For the rest of the catalysts, reduction of Co^{3+} takes place within the range of 275 to 450 °C, in agreement with expectations from the literature.^{53,56,58,59}

Often Co^{2+} reduction is difficult with an Al_2O_3 support due to their strong interaction, as evidenced by a broad reduction peak.^{56,80} For the catalysts herein, Co^{2+} reduction takes place from 400 °C to 600 °C, which is fairly low within the reported range of 400 °C to 800 °C.⁵⁶

For the *6.8Co/plate-NaOH-cal250* and *7.6Co/plate-carb-cal250* catalysts, reduction of Co^{2+} in the TPR profiles (Figure 47) is multi-step as the broad peak can be deconvoluted into two peaks.

In all cases, there is peak assigned to the removal of an impurity. In the majority of catalysts, this removal takes place at low temperatures ($< 260\text{ }^\circ\text{C}$) but for *6.8Co/plate-NaOH-cal250* and *3.8Co/plate-urea-cal250* the required temperature higher, 500 to $700\text{ }^\circ\text{C}$. MS suggests the latter peak to be due to gasification of the carbon in the support.

For some of the catalysts (*1.4Co/plate-ads-cal250*, *7.6Co/plate-carb-cal250*, *7.3Co/plate-bor-cal250* and *3.8Co/plate-urea-cal250*) there are high temperature peaks ($> 800\text{ }^\circ\text{C}$) due to the reduction of cobalt aluminate.

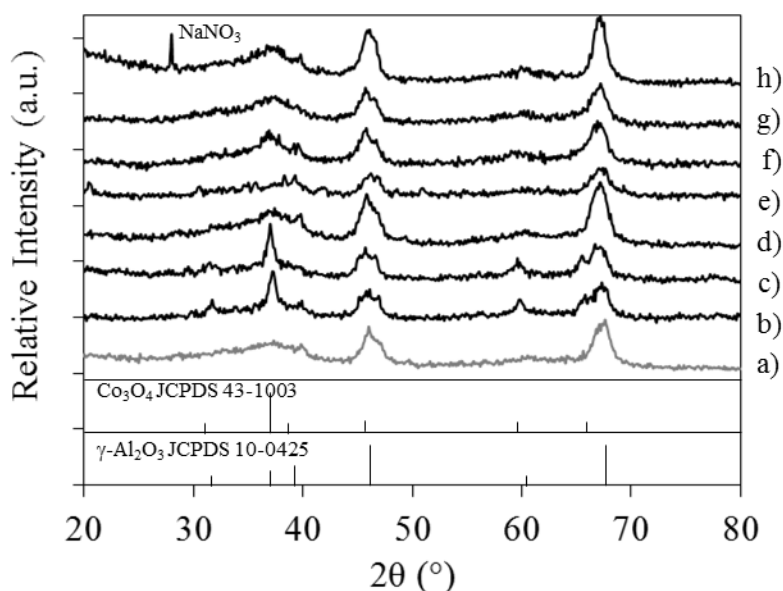


Figure 48. pXRD spectra of fresh *Co/plate-cal250* samples synthesised by different methods. a) nanoplate $\gamma\text{-Al}_2\text{O}_3$ support (JCPDS Card No. 10-0425) (grey), b) *7.7Co/plate-IWI-cal250*, c) *7.7Co/plate-imp-cal250*, d) *1.4Co/plate-ads-cal250*, e) *6.8Co/plate-NaOH-cal250*, f) *7.6Co/plate-carb-cal250*, g) *7.3Co/plate-bor-cal250* and h) *3.8Co/plate-urea-cal250*. All calcined at $250\text{ }^\circ\text{C}$.

pXRD patterns in Figure 48 of all the calcined catalysts show diffraction peaks at 40° , 46° and 67° , attributed to the $\gamma\text{-Al}_2\text{O}_3$ plate support (JCPDS Card No. 10-0425). Cobalt aluminates, CoO and $\gamma\text{-Al}_2\text{O}_3$ diffraction peaks overlap in pXRD.^{59,154} As such, pXRD of the fresh catalyst is mainly useful for identifying crystalline Co_3O_4 , which should exhibit a distinct peak at $\sim 37^\circ$, as well as smaller peaks at 32° , 60° and 65° . However, well-defined Co_3O_4 peaks in Figure 48 are only clearly visible for the samples synthesised by impregnation (*7.7Co/plate-IWI-cal250*

and *7.7Co/plate-imp-cal250*). The pXRD pattern of *3.8Co/plate-urea-cal250* shows an additional peak at $\sim 28^\circ$, which is assigned to NaNO_3 (JCPDS 36-1474¹⁵⁵).

In the case of *1.4Co/plate-ads-cal250*, the absence of cobalt pXRD may be due to the low loading of 1.4 wt%, below the detection capabilities of pXRD, or due to the formation of cobalt aluminates which is common at low Co loading (< 6 wt%).⁵³

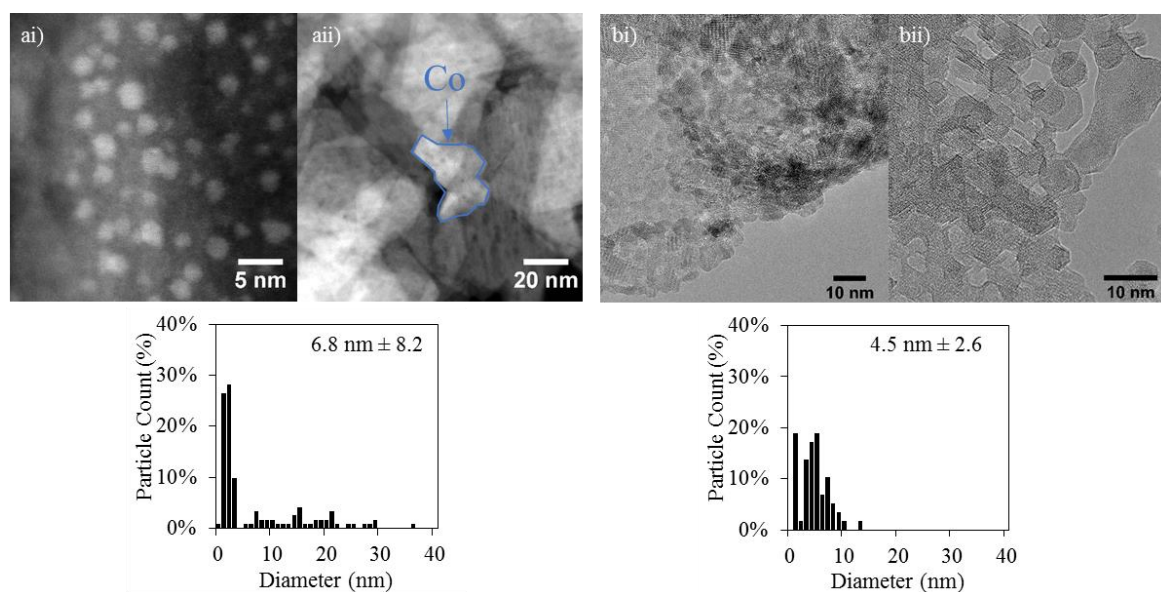


Figure 49b. Representative TEM micrographs and particle size distributions of *Co/plate-cal250* catalysts. a) *7.7Co/plate-IWI-cal250* and b) *7.6Co/plate-carb-cal250*.

Transmission electron microscopy (TEM) of Co_3O_4 supported on $\gamma\text{-Al}_2\text{O}_3$ is challenging due to their similar contrast, evident in Figure 49a. The plate-like nanomorphology of the $\gamma\text{-Al}_2\text{O}_3$ makes distinction possible but nevertheless complicated. As such, the particle size distribution from TEM micrographs of *7.6Co/plate-carb-cal250* (Figure 49b) is subject to interpretation as it was carried out in bright field, but generally shows particles of < 10 nm.

In the case of *7.7Co/plate-IWI-cal250*, the imaging was carried out both in bright field and high angle annular dark field scanning transmission electron microscopy (HAADF-STEM) using elemental mapping to confirm the location of cobalt by electron energy loss spectroscopy (EELS) (Figure A99, Appendix). Combined analysis of both sets of results show a bi-modal size distribution with a high proportion of 1-3 nm particles with also some larger < 30 nm particles. In Figure 49a, the blue line outlines an area of a few cobalt particles 25 to 28 nm in diameter confirmed by EELS elemental mapping (Figure A99, Appendix).

TEM micrographs for the *7.7Co/plate-IWI-cal250* catalyst (Figure 49a) show that the initial support nano-architecture remains intact after Co impregnation. By contrast, TEM micrographs of *7.6Co/plate-carb-cal250* (Figure 49b), suggest that the carbonate precipitation synthesis method may have modified the nanoplate morphology yielding a honey-comb like structure.

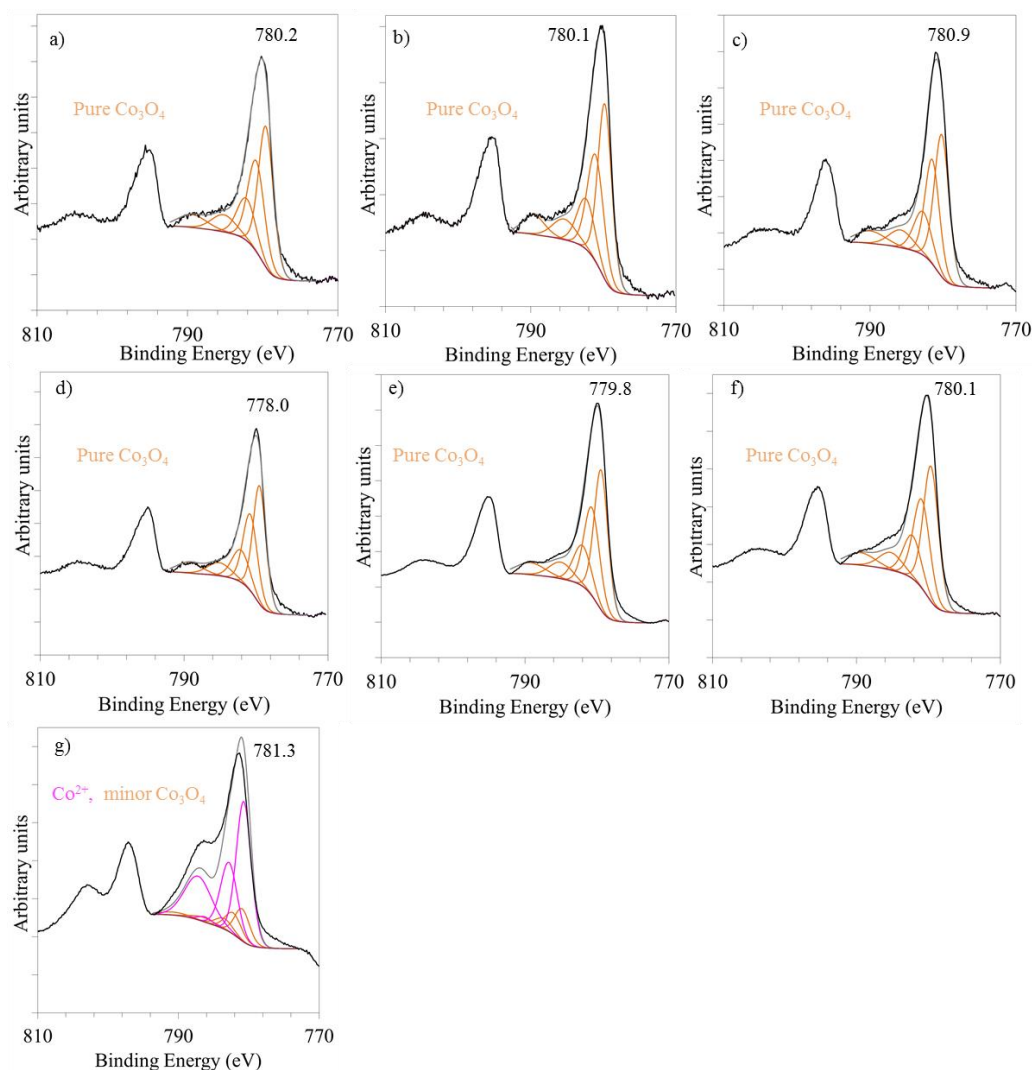


Figure 50. Co 2p XPS spectra for *Co/plate-cal250* catalysts synthesised by different methods. a) *7.7Co/plate-IWI-cal250*, b) *7.7Co/plate-imp-cal250*, c) *1.4Co/plate-ads-cal250*, d) *6.8Co/plate-NaOH-cal250*, e) *7.6Co/plate-carb-cal250*, f) *7.3Co/plate-bor-cal250* and g) *3.8Co/plate-urea-cal250*. Black lines = raw data, orange lines = fitting to Co_3O_4 and pink line = Co^{2+} .

X-ray photoelectron spectroscopy (XPS) provides information about the elements and their oxidation state in the top ~ 10 nm of a sample.¹⁵⁶ The common oxidation states of cobalt (Co^0 , Co^{2+} and Co^{3+}) all have unpaired d electrons meaning that they exhibit multiplet XPS spectra, often making peak fitting and data interpretation challenging.¹⁵⁷ Nevertheless, the shape of the envelope and the 2p peaks enable the identification of the cobalt oxidation state, which have

been precisely fitted by Biesinger *et al.*¹⁵⁷ for Co_3O_4 , $\text{Co}(\text{OH})_2$, CoO and Co^0 . The XPS spectra of the calcined catalysts in Figure 50 confirms the surface cobalt species to be Co_3O_4 in all cases except *3.8Co/plate-urea-cal250* which only has a minor set of Co_3O_4 peaks but predominantly exhibits pure Co^{2+} .

5.1.2 Characterisation of reduced catalysts

As the metallic Co^0 form is believed to be the active species for NH_3 decomposition,⁵⁶ it is imperative to select a suitable reduction temperature that maximises the proportion of Co^0 whilst minimising the potential effect of sintering at high temperatures. The TPR data (Figure 47) and catalytic tests in Section 5.2.2. suggests 580 °C to be a suitable reduction temperature. It is, therefore, important to characterise the reduced form of the catalysts in order to understand the properties of the catalysts in their pre-testing state. The characterisation results of the materials reduced at 580 °C are the focus of this section. The reduced samples are labelled with the suffix “-red580”. Due to equipment limitations, the reduced samples were exposed to air prior to pXRD and TEM characterisation so the materials are subject to re-oxidation. For the XPS analysis and catalytic tests, however, samples were reduced *in situ* at 580 °C.

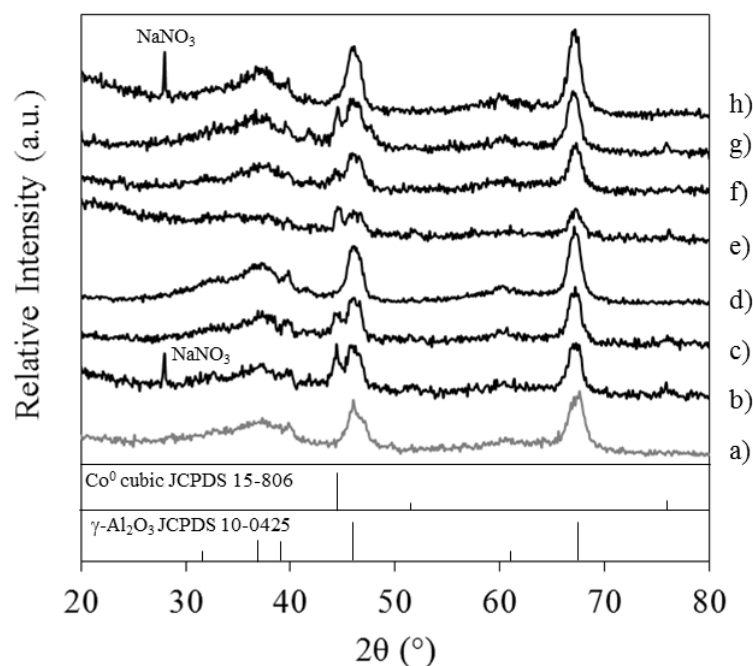


Figure 51. pXRD patterns of *Co/plate-cal250* catalysts **reduced** at 580 °C synthesised by different methods. a) $\gamma\text{-Al}_2\text{O}_3$ plate support (grey), b) *7.7Co/plate-IWI-cal250-red580*, c) *7.7Co/plate-imp-cal250-red580*, d) *1.4Co/plate-ads-cal250-red580*, e) *6.8Co/plate-NaOH-cal250-red580*, f) *7.6Co/plate-carb-cal250-red580*, g) *7.3Co/plate-bor-cal250-red580* and h) *3.8Co/plate-urea-cal250-red580*.

The pXRD patterns of all the catalysts in Figure 51 show diffraction peaks at 40°, 46° and 67°, attributed to the γ -Al₂O₃ plate support (JCPDS 10-0425). The dominant peak for cobalt species expected after reduction, cubic Co⁰, exhibits a strong peak at ~ 44° (JCPDS 15-806⁸²) with a smaller peak at 76°. However, these peaks are only seen in four of the diffractograms in Figure 51 (7.7Co/plate-IWI-cal250-red580, 7.7Co/plate-imp-cal250-red580, 6.8Co/plate-NaOH-cal250-red580 and 7.3Co/plate-bor-cal250-red580). No diffraction peaks for Co₃O₄ are visible after reduction at 580 °C, despite the exposure to air prior to characterisation. In the 7.7Co/plate-IWI-cal250-red580 and 3.8Co/plate-urea-cal250-red580 samples, an additional peak at ~ 28° is present which is assigned to NaNO₃ (JCPDS 36-1474¹⁵⁵).

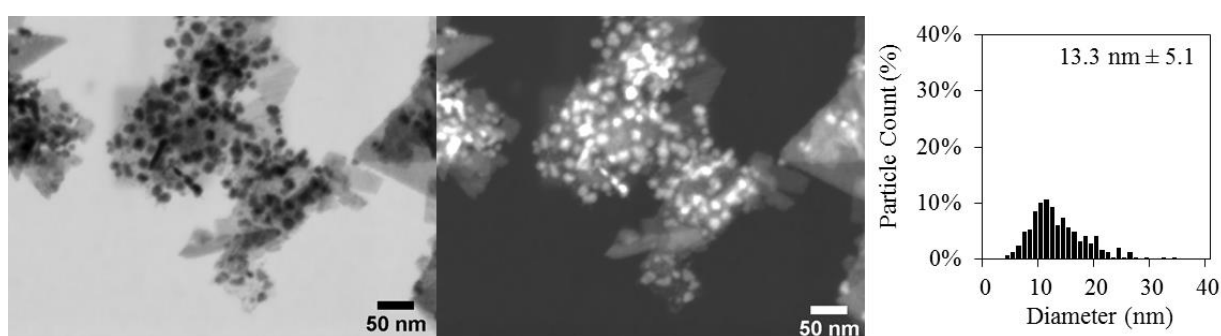


Figure 52. Representative bright (LHS) and dark (centre) field SEM micrographs with associated Co⁰ particle size distribution (RHS) of 7.6Co/plate-carb-cal250-red580.

Many cobalt particles in close proximity are visible from the EM micrographs of 7.6Co/plate-carb-cal250-red580 in Figure 52. The average size determined from the EM size distribution (13.3 nm) is larger than the size estimated from pXRD (7.7 nm). The morphology of the support was not observably affected after reduction unlike in the unreduced sample (Figure 49bii).

The XPS of all the reduced catalysts in Figure 53 show predominantly the characteristic peak for Co⁰ with minor contributions from Co²⁺ (fitted to the peak fitting of Biesinger *et al.*¹⁵⁷ for CoO). In some cases (Figure 53c, Figure 53f and Figure 53g) where the fitting of the left shoulder of the peak is not exact, the pink line is labelled in the figure as Co²⁺ rather than CoO as the difficulty in fitting CoO suggests the presence of another Co²⁺ species. The proportion of unreduced Co²⁺ varies between catalysts as quantified later in Figure 54. The reducibility is significant as it affects the proportion of Co⁰ available to catalyse a reaction, which is discussed in Section 5.1.4.

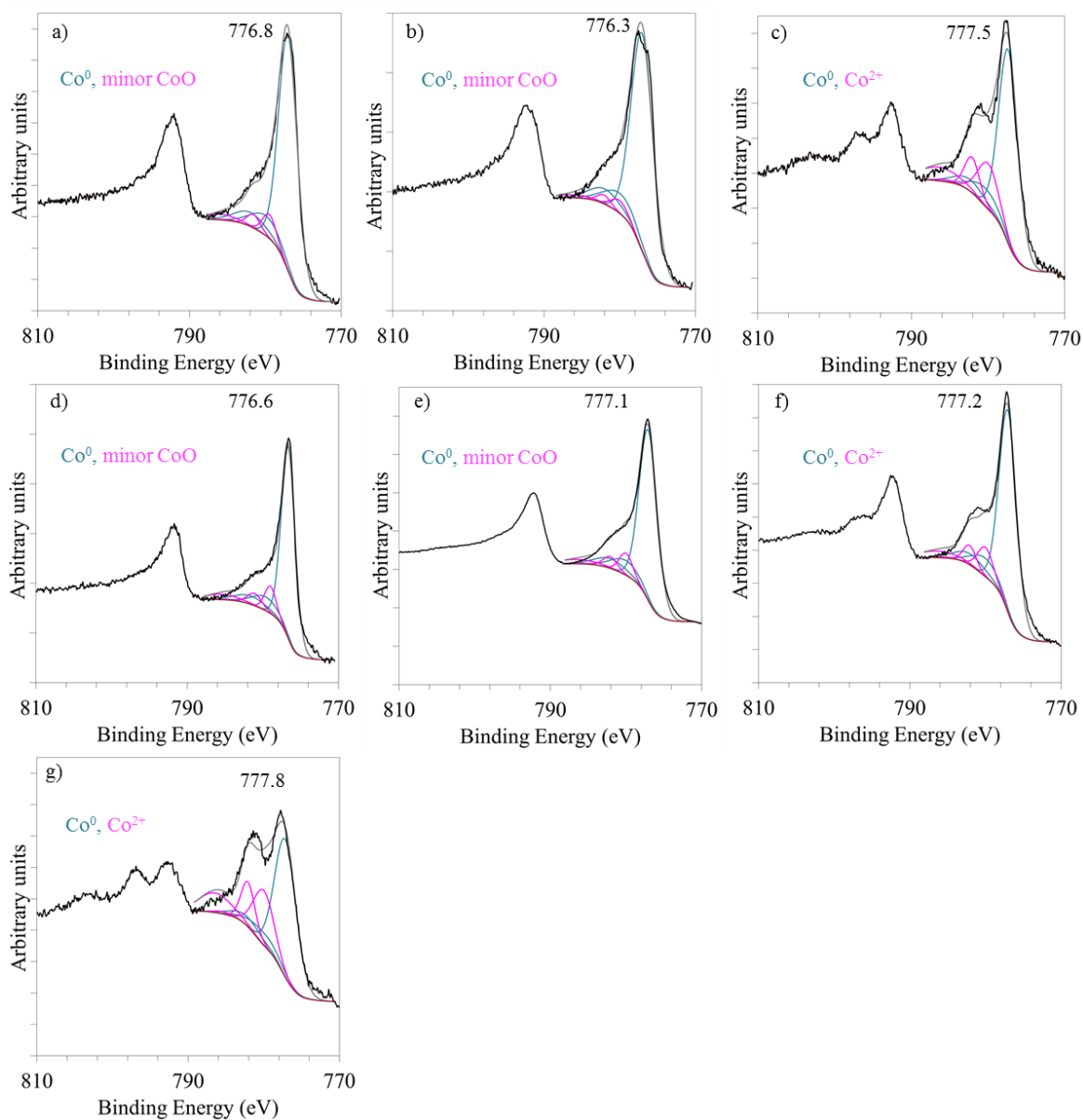


Figure 53. Co 2p XPS spectra for *Co/plate-cal250* catalysts reduced *in situ* at 580 °C synthesised by different methods. a) *7.7Co/plate-IWI-cal250-red580*, b) *7.7Co/plate-imp-cal250-red580*, c) *1.4Co/plate-ads-cal250-red580*, d) *6.8Co/plate-NaOH-cal250-red580*, e) *7.6Co/plate-carb-cal250-red580*, f) *7.3Co/plate-bor-cal250-red580* and g) *3.8Co/plate-urea-cal250-red580*. Black lines = raw trace, blue lines are fitted to Co^0 and pink lines are fitted to CoO .

5.1.3 Discussion of chemical composition of catalysts

The chemical composition and oxidation state of a catalyst can have significant implications on the catalytic activity. As such, the XPS, pXRD and ICP results are discussed in this section to determine the effect of the method on the chemical nature of the catalyst.

For all catalysts, the same amount of $\text{Co}(\text{NO}_3)_2 \cdot 6\text{H}_2\text{O}$ is used in the synthesis but the accurate loading is determined by inductively coupled plasma optical emission spectroscopy (ICP-OES) analysis of the solid catalyst. The cobalt and sodium content are summarised in Table 24.

Table 26. ICP results for *Co/plate-cal250* catalyst synthesised by different methods with 0.848 mmol of $\text{Co}(\text{NO}_3)_2 \cdot 6\text{H}_2\text{O}$ (0.2469 g).

Catalyst	ICP of solid ^a	
	Na content (wt%)	Co loading (wt%)
<i>7.7Co/plate-IWI-cal250</i>	2.7	7.7
<i>7.7Co/plate-imp-cal250</i>	2.6	7.7
<i>1.4Co/plate-ads-cal250</i>	1.5	1.4
<i>6.8Co/plate-NaOH-cal250</i>	8.4	6.8
<i>7.6Co/plate-carb-cal250</i>	3.0	7.6
<i>7.3Co/plate-bor-cal250</i>	2.2	7.3
<i>3.8Co/plate-urea-cal250</i>	1.8	3.8

^a Calculated from ICP of the digested solid (calcined catalyst).

After calcination of cobalt complexes in air the crystalline mixed oxide Co_3O_4 typically forms, which is confirmed by pXRD and XPS techniques. However, only the two catalysts produced by impregnation (*7.7Co/plate-IWI-cal250* and *7.7Co/plate-imp-cal250*) exhibit well-defined Co_3O_4 pXRD peaks (Figure 48), confirming the presence of the $\text{Co}^{3+/2+}$ oxide crystallite. The rest of the calcined catalysts, do not show a clear Co_3O_4 pXRD peak (Figure 48) but there is a degree of broadening at $\sim 37^\circ$, suggesting the presence of small or poorly crystalline Co_3O_4 . The shape of the Co_3O_4 XPS envelope confirms the presence of Co_3O_4 (Figure 50) in all the calcined catalysts except *3.8Co/plate-urea-cal250*.¹⁵⁷ The XPS results provide alternative information about the catalyst as the technique is not dependent on crystallinity, however, XPS can only probe ~ 10 nm into the sample.¹⁵⁶

It is possible that a higher calcination temperature ($> 250^\circ\text{C}$) is needed for the series produced by precipitation to form a highly crystalline Co_3O_4 phase.¹⁴ This is in agreement with pXRD of

an analogous catalyst (*6.8Co/plate-NaOH-cal500*) prepared by the NaOH precipitation method but calcined at 500 °C, in which a sharp peak at ~ 37° is visible, corresponding to crystalline Co₃O₄ (JCPDS 43-1003) with 12 nm average diameter (Figure A100, Appendix).

The Co²⁺ set of XPS peaks in *3.8Co/plate-urea-cal250* (pink line in Figure 50g) have a similar envelope shape as the fitted curves for CoO or Co(OH)₂ from the fitting parameters by Biesinger *et al.*¹⁵⁷. The presence of the Co 2p_{1/2} peak at 786 eV (Figure 50g) confirms the Co²⁺ oxidation state. However, the binding energy values more closely agree with the spectra of Yang *et al.*¹⁵⁸ for cobalt hydroxide carbonate (Co₂CO₃(OH)₂). The interpretation of the XPS fitting to cobalt hydroxide carbonate is in agreement with the violet catalyst colour and the absence of Co₃O₄ pXRD peaks (Figure 48h). The minor Co^{3+/2+} set of peaks in *3.8Co/plate-urea-cal250* are likely due to the partial formation of Co₃O₄ from calcination.¹⁵⁷

The colour of the fresh, calcined catalysts provides some further information about the cobalt species present. Pure Co₃O₄ is black or grey in colour¹⁵⁹ so only *7.7Co/plate-IWI-cal250* appears to be pure Co₃O₄, in strong agreement with the XPS data and the pXRD pattern (Figure 48). CoO, by contrast, can be olive-green or red depending on the particle size,¹⁵⁹ suggesting the presence of some CoO in *6.8Co/plate-NaOH-cal250*, *7.6Co/plate-carb-cal250* and *7.3Co/plate-bor-cal250* due to the dark green colour of the fresh catalysts (Table 24). However, XPS (Figure 53) shows that the particle surface is oxidised to Co₃O₄.

The larger Co²⁺ peaks and the poor fitting of the reduced Co 2p XPS (Figure 53) spectra of *1.4Co/plate-ads-cal250*, *7.3Co/plate-bor-cal250* and *3.8Co/plate-urea-cal250* may be due to the presence of a high proportion of irreducible CoAl₂O₄, in agreement with the TPR profiles (Figure 47) of the first two materials.

XPS also provides information about contaminants present on the sample surface and their persistence after reduction at 580 °C. As expected, all of the Co/γ-Al₂O₃ catalysts contain cobalt, aluminium and oxygen, however sodium and carbon were also identified as contaminants in the entire series. Two catalysts also contained additional elements such as nitrogen, boron, chlorine and potassium.

The XPS composition data reveals that carbon is present before and after reduction in all the catalysts, but usually in low quantities (< 0.5 wt%). It is likely that the carbon content is derived from the *plate* support as the XPS (Figure 40, Chapter 4) reveals a similar carbon content. The carbon source may arise from the laboratory reagent grade used to produce the *plate* support

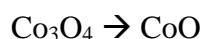
(NaOH and $\text{Al}(\text{NO}_3)_3 \cdot 9\text{H}_2\text{O}$) which are ≥ 98 wt% pure. In *6.8Co/plate-NaOH-cal250* and *3.8Co/plate-urea-cal250* the carbon content is noticeably higher in the fresh catalyst (1.8 and 3.2 wt% respectively), the majority of which is removed by reduction (< 0.4 wt% remaining). The source of carbon in *6.8Co/plate-NaOH-cal250* is likely the NaOH laboratory reagent grade (≥ 98 wt%). In *3.8Co/plate-urea-cal250*, carbon may arise from residual urea ($\text{CO}(\text{NH}_2)_2$) in agreement with the presence of nitrogen, or from the existence of Co^{2+} as cobalt hydroxide carbonate, in agreement with XPS data (Figure 50g) discussed earlier.

Sodium is a ubiquitous, persistent element in this series of catalysts, with all of the catalysts containing at least 1.5 wt% sodium according to the solid ICP results in Table 26. The XPS composition also confirms the presence of sodium but at a higher concentration of at least 3.5 wt%. This discrepancy suggests the sodium is primarily found on the catalyst surface (top 10 nm) of the cobalt or support. A significant proportion of sodium may arise from the *plate* support, which is synthesised using NaOH and consequently has a high sodium content based on XPS (5.6 wt%) and ICP (2.7 wt%) despite washing with deionised water. In the *7.6Co/plate-carb-cal250* catalyst, the source of sodium is probably the buffer solution as it is composed of sodium carbonate and sodium bicarbonate. The NaOH precipitation method results in a catalyst containing the highest sodium content (8.4 Co wt% by ICP or 10.7 wt% by XPS). The NaNO_3 formation in some of the catalysts (*3.8Co/plate-urea-cal250*, *3.8Co/plate-urea-cal250-red580* and *7.7Co/plate-IWI-cal250-red580*) identified by pXRD is likely due to the sodium content and the introduction of nitrogen from the precipitant or the use of a cobalt nitrate precursor.

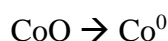
In the *7.3Co/plate-bor-cal250* catalyst, boron, potassium and chlorine elements arise from the borate buffer precipitant, which is composed of 0.5 wt% of each of NaOH, H_3BO_3 and KCl. The high sodium content in *6.8Co/plate-NaOH-cal250* and the persistent contaminants such as chlorine in *7.3Co/plate-bor-cal250* may have significant implications on the catalytic activity.

5.1.4 Discussion of cobalt reducibility

The reducibility of a catalyst is significant in determining its activity as it controls the proportion of metal in the active oxidation state, metallic Co^0 in this case.⁵⁶ The reduction temperature depends on the strength of the metal-support interaction, which may be linked to the particle size as smaller particles tend to have a stronger interaction.^{53,56-59} The reductive processes in $\text{Co}/\text{Al}_2\text{O}_3$ catalysts can be categorised into the following steps:



The first cobalt reduction step usually takes place from 260 to 450 °C.^{53,56,58,59} Table 25 shows that this step takes place towards the top of this range (444 °C) for *7.6Co/plate-carb-cal250*, suggesting a strong metal-support interaction which may be due to a small particle size in agreement with TEM. The rest of the catalysts are reduced from $\text{Co}^{3+/2+}$ to Co^{2+} within this range, except *3.8Co/plate-urea-cal250*, which exhibits no peak due to the existence of this catalyst primarily as Co^{2+} in the form of cobalt hydroxide carbonate, in agreement with earlier conclusions from XPS (Figure 50g).



The reduction of CoO depends on the support type and porosity, as well as crystallite size, with particles less than 6 nm in diameter significantly harder to reduce.^{53,55} As a result, this transformation can take place up to 800 °C, often accompanied with a broad peak.^{56,57} The broadness of the Co^{2+} reduction peak in the TPR profile of *7.7Co/plate-imp-cal250*, *6.8Co/plate-NaOH-cal250* and *7.6Co/plate-carb-cal250* (Figure 47) arises from a broad particle size distribution with different metal-support interaction strengths.

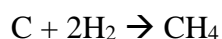


Cobalt aluminate formation is undesirable in $\text{Co}/\text{Al}_2\text{O}_3$ catalysts because it requires high reduction temperatures from 800 to 1000 °C, giving rise to their description as “irreducible”.^{37,53} Reportedly, the formation of CoAl_2O_4 is more likely with low metal loadings (1.5 to 6 wt%).⁵³ As such, CoAl_2O_4 is likely in *1.4Co/plate-ads-cal250* and *3.8Co/plate-urea-cal250*. A peak at > 800 °C is clearly observed in the TPR profile (Figure 47) for *1.4Co/plate-ads-cal250* and *7.3Co/plate-bor-cal250*. Using 580 °C as the reduction temperature leads to a higher proportion of Co^{2+} , as shown in their XPS spectra (Figure 53c and Figure 53g respectively) as CoAl_2O_4 remains unreduced. The

proposed presence of CoAl_2O_4 is in agreement with poor CoO fitting in the XPS spectra of these two catalysts. A small peak at 877.8 eV for $7.6\text{Co/plate-carb-cal250}$ (Figure 47f) is indicative of CoAl_2O_4 reduction. The peak centred at 770 eV in the TPR of $6.8\text{Co/plate-NaOH-cal250}$ (Figure 47d) is present in the TPR of unsupported cobalt nanoparticles precipitated by NaOH (Figure A101, Appendix) and as such cannot be assigned to reduction of CoAl_2O_4 . Instead, mass spectrometry (MS) of the TPR outlet of $6.8\text{Co/plate-NaOH-cal250}$ (Figure A98, Appendix) shows a peak at m/z 28 which could be due to the release of N_2 or C_2H_4 , the latter agreeing with the decrease in carbon after reduction according to XPS.



Removal of residual nitrates takes place below $225 \text{ }^\circ\text{C}$.⁸² Nitrate reduction is evident from the TPR profile (Figure 47) for the catalysts synthesised by impregnation, adsorption and precipitation by borate buffer. For the adsorption catalyst, the evolution of nitrates is confirmed by a peak of m/z 28 in the MS signal at $\sim 200 \text{ }^\circ\text{C}$. High temperature evolution of N_2 (based on a m/z based at 28) is observed for $6.8\text{Co/plate-NaOH-cal250}$ at $629.0 \text{ }^\circ\text{C}$ (Figure 47d).



Removal of residual carbon by methanation occurs at $200\text{-}500 \text{ }^\circ\text{C}$.⁵⁹ Methanation is observed in the reduction profile of $7.6\text{Co/plate-carb-cal250}$ at $208.3 \text{ }^\circ\text{C}$ (Figure 47e) confirmed by a m/z 16 MS peak. In addition, $3.8\text{Co/plate-urea-cal250}$ exhibits a methanation peak at $535.5 \text{ }^\circ\text{C}$ (Figure 47g), in agreement with XPS, which indicates a reduction in carbon content from $3.2 \text{ wt}\%$ to $0.4 \text{ wt}\%$ after reduction at $580 \text{ }^\circ\text{C}$.

The proportion of Co^0 after reduction at $580 \text{ }^\circ\text{C}$ relative to the total cobalt content can be extracted from the XPS spectra of the reduced samples (Figure 53) and the TPR profiles (Figure 47), as summarised in Figure 54. The reducibility based on XPS is calculated by comparing the cumulative area of the Co^0 peaks to the total cobalt peaks area. The reducibility based on the TPR profile is calculated by comparing the area assigned to cobalt species reduced up to $580 \text{ }^\circ\text{C}$ with the total area of all the cobalt reduction peaks.

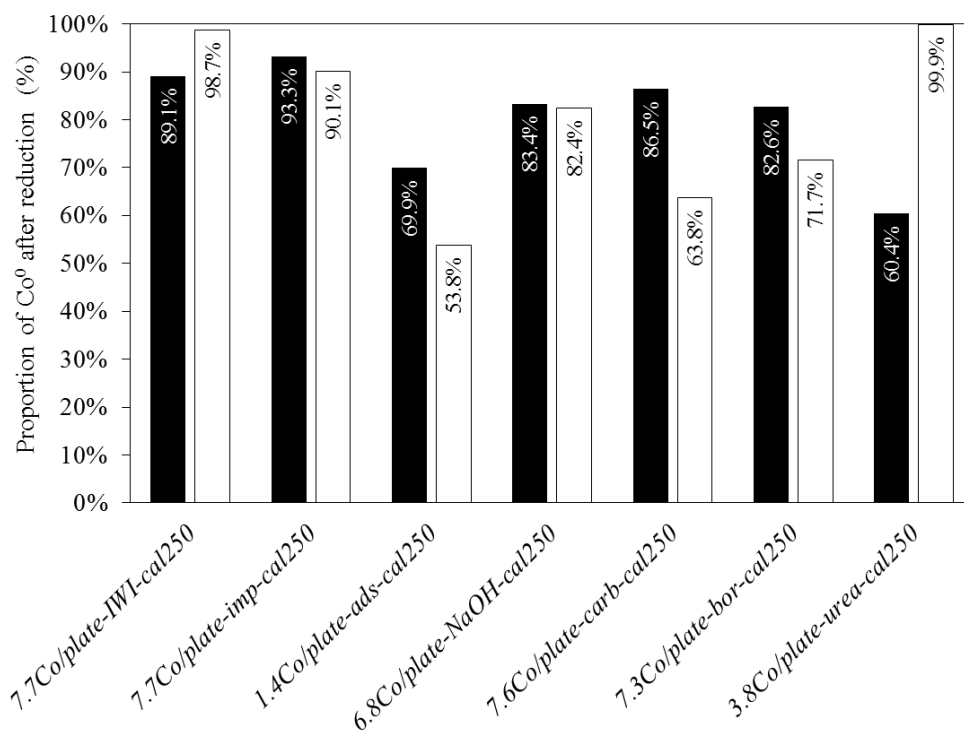


Figure 54. Proportion of Co^0 in *Co/plate-cal250* catalysts synthesised by different methods after reduction at 580 °C calculated from XPS spectra of the reduced samples (black bar) and from the TPR profiles (white bar).

The reducibility of the catalysts reduced at 580 °C calculated from XPS and TPR (Figure 54) varies significantly with the choice of cobalt loading method, ranging from 53.8 % to 99.9 %. In the case of *7.7Co/plate-imp-cal250* and *6.8Co/plate-NaOH-cal250*, the reducibility calculated by both characterisation techniques is similar but the rest of the series are not in agreement.

It is surprising for the catalysts that are expected to be fully or predominantly reduced at 580 °C based on the TPR profiles (Figure 47) such as *7.7Co/plate-IWI-cal250* and *3.8Co/plate-urea-cal250*, which show minor unreduced CoO components by XPS (Figure 53). Since the XPS analysis was carried out after reduction *in situ* and remains under vacuum during analysis, there is no possibility for sample re-oxidation. For example, the *3.8Co/plate-urea-cal250* catalyst shows no CoAl_2O_4 TPR reduction peak and the TPR reduction profile suggests complete reduction by 580 °C but nevertheless based on XPS the catalyst possesses only 60.4 % Co^0 , which is not currently understood.

The difference in reducibility between samples may be due to the choice of method resulting in different loading, changing the proportion of “irreducible” cobalt aluminates formed. Since the catalysts in this chapter contain relatively low Co loadings less than 12 wt% (1.4 to 7.7

wt%), the presence of cobalt aluminates is feasible.^{53,56} Unfortunately the formation of cobalt aluminates cannot be confirmed with pXRD as the peaks overlap with Al₂O₃.⁵⁹ However, a CoAl₂O₄ reduction peak at > 800 °C can clearly be seen in the TPR profiles of *1.4Co/plate-ads-cal250*, *7.6Co/plate-carb-cal250* and *7.3Co/plate-bor-cal250* (Figure 47), resulting in their low reducibility calculated from TPR (53.8 to 71.7 %). For these samples, the CoAl₂O₄ reduction peak accounts for 43.3 %, 14.1 % and 7.6 % respectively of the total H₂ consumption from all the Co reduction processes (i.e. excluding removal of nitrates and methanation).

Based on the reducibility data, it seems that the adsorption method results in the lowest loading and the most irreducible catalyst, decreasing the catalytically available Co⁰. Both of the impregnation methods results in catalysts with fairly high reducibility, greater than ~ 90 %, suggesting a weaker metal-support interaction than in the catalysts produced by other methods, in agreement with literature criticism of impregnation methods.¹⁵

5.1.5 Discussion of particle size

Metal nanoparticles often exhibit size dependent catalytic activity within a narrow particle size range, which is known to be the case for NH₃ decomposition but the optimum size is not yet clear.^{92,132,160} As such, the particle size of the different *Co/plate* catalysts has been investigated by pXRD and in some cases TEM. The particle size calculated by these methods, for both fresh (calcined at 250 °C) and reduced (at 580 °C) catalysts in the series are shown in Table 27.

As the reduced samples were exposed to air prior to pXRD and TEM analysis, there could be a quantitative limitation of the calculated Co⁰ size. Re-oxidation of cobalt particles upon exposure to air is size dependent with primarily only cobalt particles less than 4 nm thermodynamically capable of re-oxidising.⁵³ Any re-oxidised cobalt will not be detected by pXRD because this size is below the detection capabilities and CoO peaks overlap with γ -Al₂O₃. This explains why Co⁰ is the only cobalt species detected by pXRD of the reduced samples (Figure 51) even if partial re-oxidation has occurred.

For the calcined materials presented in this section only *7.7Co/plate-IWI-cal250* and *7.7Co/plate-imp-cal250* show a Co₃O₄ pXRD diffraction peak (Figure 48), yet all the catalysts show Co²⁺ TPR reduction peaks (Figure 47) and XPS identifies Co₃O₄ in all except *3.8Co/plate-urea-cal250*, suggesting the formation of amorphous cobalt after calcination.

Table 27. Average cobalt particle size of calcined *Co/plate-cal250* catalysts synthesised by different methods.

Catalyst	Average particle size (nm)			
	Co ₃ O ₄ - Calcined at 250 °C		Co ⁰ - Reduced at 580 °C	
	pXRD ^a	TEM	pXRD ^b	TEM
<i>7.7Co/plate-IWI-cal250</i>	10.5	6.8	11.1	n/a
<i>7.7Co/plate-imp-cal250</i>	14.5	n/a	9.3	n/a
<i>1.4Co/plate-ads-cal250</i>	No peak	n/a	No peak	n/a
<i>6.8Co/plate-NaOH-cal250</i>	No peak	n/a	14.8	n/a
<i>7.6Co/plate-carb-cal250</i>	No peak	4.5	7.7	13.3
<i>7.3Co/plate-bor-cal250</i>	No peak	n/a	17.0	n/a
<i>3.8Co/plate-urea-cal250</i>	No peak	n/a	No peak	n/a

^a Calculated using the FWHM of the Co₃O₄ peak at ~ 37° (JCPDS 43-1003⁸²) with the Scherrer equation.

^b Calculated using the FWHM of the deconvoluted cubic Co peak at ~ 44° (JCPDS 15-806⁸²) with the Scherrer equation.

For the catalysts reduced at 580 °C, the majority of the catalysts exhibit crystalline cubic Co⁰ diffraction peaks at ~ 44° (Figure 51). No other crystalline cobalt species in the reduced samples are detected, making pXRD size comparison across the complete series limited. The absence of cubic Co⁰ diffraction peaks in *1.4Co/plate-ads-cal250-red580* and *3.8Co/plate-urea-cal250-red580* may be due to low loading or the presence of small crystallites (< 3.5 nm).¹²⁶ For the reduced catalysts displaying a Co⁰ pXRD diffraction peak, the average particle sizes ranges considerably from 8 to 17 nm, with *7.6Co/plate-carb-cal250-red580* containing the smallest crystallites on average. Based on TEM analysis, *7.6Co/plate-carb-cal250* contains cobalt particles below 10 nm (Figure 49). There is an increase in breadth of particle size distribution and average particle size of *7.6Co/plate-carb-cal250* following reduction at 580 °C, suggesting some degree of sintering has taken place.

Combined bright field and dark field analysis of *7.7Co/plate-IWI-cal250* revealed nearly 30 % of particles analysed were ~ 1-2 nm in size but the sample also contains a wide range of large particles up to 30 nm, suggesting a bi-modal size distribution. Upon reduction, a ¾ decrease in particle size is expected from the transformation of Co₃O₄ to Co⁰ due to the contraction of the crystal lattice.⁵⁵ This behaviour is followed by *7.7Co/plate-imp-cal250* (14.5 to 9.3 nm), suggesting good thermal stability with minimal agglomeration taking place after reduction at 580 °C. However, the inverse is observed for the *7.7Co/plate-IWI-cal250* catalyst, which is similar in size after reduction (10.5 to 11.1 nm), suggesting a degree of sintering.

5.2 NH₃ decomposition catalytic activity

The ammonia (NH₃) decomposition reaction provides a useful model reaction to compare the catalytic activity of the catalysts. Catalysts are tested as described in Section 3.5. In essence the catalysts are pre-reduced *in situ* at 580 °C (based on TPR analysis in Figure 47) and then a 2.4:1 mixture of He:NH₃ is flowed through the packed bed reactor whilst the furnace temperature is ramped up to 580 °C and down to 200 °C in three consecutive runs. In all cases the data of the first catalyst run during temperature increase is presented unless the activity changes in subsequent runs, in which case the third run is used.

Prior to catalytic testing the processing conditions, such as calcination and reduction, need to be optimised. These conditions are determined by considering the effect of calcination and reduction on the ammonia decomposition activity for selected catalysts prepared by impregnation (IWI) and precipitation by NaOH. Finally, the ammonia decomposition catalytic activity of the Co/ γ -Al₂O₃ series of catalysts produced by seven different methods supported on *plate* γ -Al₂O₃ are presented at the end of this section.

5.2.1 Effect of calcination on NH₃ decomposition activity

Calcination is a thermal treatment in air at a temperature higher than the drying temperature aimed at removing impurities.¹³ In this chapter, all the materials presented so far have been calcined at 250 °C, since industrial cobalt catalysts are typically calcined at those conditions.⁵⁹ Two materials are tested for NH₃ decomposition in this sub-section (*7.7Co/plate-IWI* and *6.8Co/plate-NaOH*) both fresh (*-fresh*) and calcined at 250 °C (*-cal250*). The aim is to determine the effect of calcination on catalyst properties such as particle size that may influence the catalytic activity. The catalytic activity of these materials are summarised in Figure 55 and Table 28.

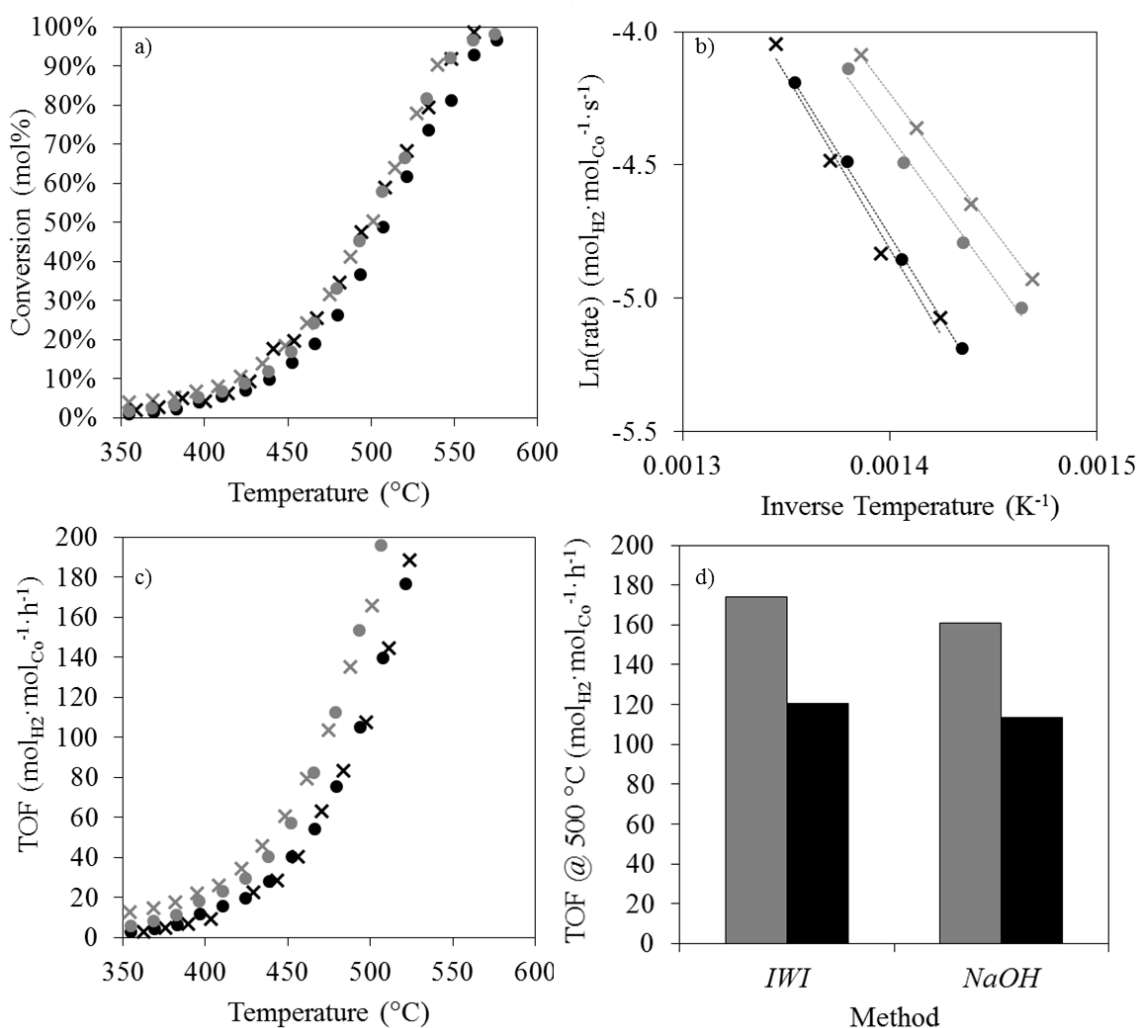


Figure 55. NH₃ decomposition catalytic data (pre-reduced *in situ* at 580 °C under H₂) for Co/plate catalysts synthesised by IWI (●) and NaOH precipitation (x) calcined at 250 °C (black) and uncalcined (grey). a) activity as a function of temperature, b) Arrhenius plot, c) apparent rate (TOF) as a function of temperature and d) TOF at 500 °C. 6.5Co/plate-IWI- fresh-red580 (●), 7.7Co/plate-IWI-cal250-red580 (●), 6.7Co/plate-NaOH-fresh-red580 (x) and 6.8Co/plate-NaOH-cal250-red580 (x).

The purpose of calcination is to form the active phase and to remove any residual chemically bonded compounds in the catalysts such as H₂O or nitrates if a nitrate precursor has been used.¹³ Nitrate removal is particularly important in large scale operations as the release of nitrates can lead to the formation of nitric acid and potential equipment corrosion.

Since the process of calcination removes species from the catalyst, a small increase in loading is observed. This is reflected by the change in the catalyst nomenclature prefix in Table 28 and the effect is larger for the catalyst synthesised by IWI. As a result, when the catalytic activity is considered per mol of cobalt in Figure 55c, the effect of calcination on catalytic activity becomes apparent.

Table 28. Catalytic activity and particle size of *Co/plate* catalysts produced by IWI and NaOH precipitation either fresh (uncalcined) or calcined at 250 °C.

Catalyst	Catalytic activity ^a			Average Co ⁰ size by pXRD ^{a, c} (nm)
	E _a (kJ·mol ⁻¹)	TOF @ 500 °C (mol _{H₂} ·mol _{Co} ⁻¹ ·h ⁻¹)	Stability over 3 runs ^b	
<i>6.5Co/plate-IWI-fresh-red580</i>	88.7	173.9	Stable	9.9
<i>7.7Co/plate-IWI-cal250-red580</i>	103.9	120.3	Stable	11.1
<i>6.7Co/plate-NaOH-fresh-red580</i>	85.3	152.5	Stable	15.0
<i>6.8Co/plate-NaOH-cal250-red580</i>	108.6	113.4	-16.9 % TOF	14.8

^a Pre-reduced at 580 °C (5 °C·min⁻¹, 45 min).

^b (-) indicates deactivation.

^c Calculated using the FWHM of the deconvoluted cubic Co⁰ peak at ~ 44° (JCPDS 15-806 ⁸²) with the Scherrer equation. Samples were exposed to air prior to analysis.

For the catalysts produced by both methods (IWI and NaOH precipitation), the fresh catalysts are more active for NH₃ decomposition per mol of cobalt than the calcined ones (Figure 55c), which are aligned with lower activation energies (Table 28). In addition, *6.8Co/plate-NaOH-cal250-red580* is catalytically unstable and decreases in activity on subsequent runs from 167 to 119 to 117 mol_{H₂}·mol_{Co}⁻¹·h⁻¹ TOF at 500 °C, but this is not observed in the fresh equivalent.

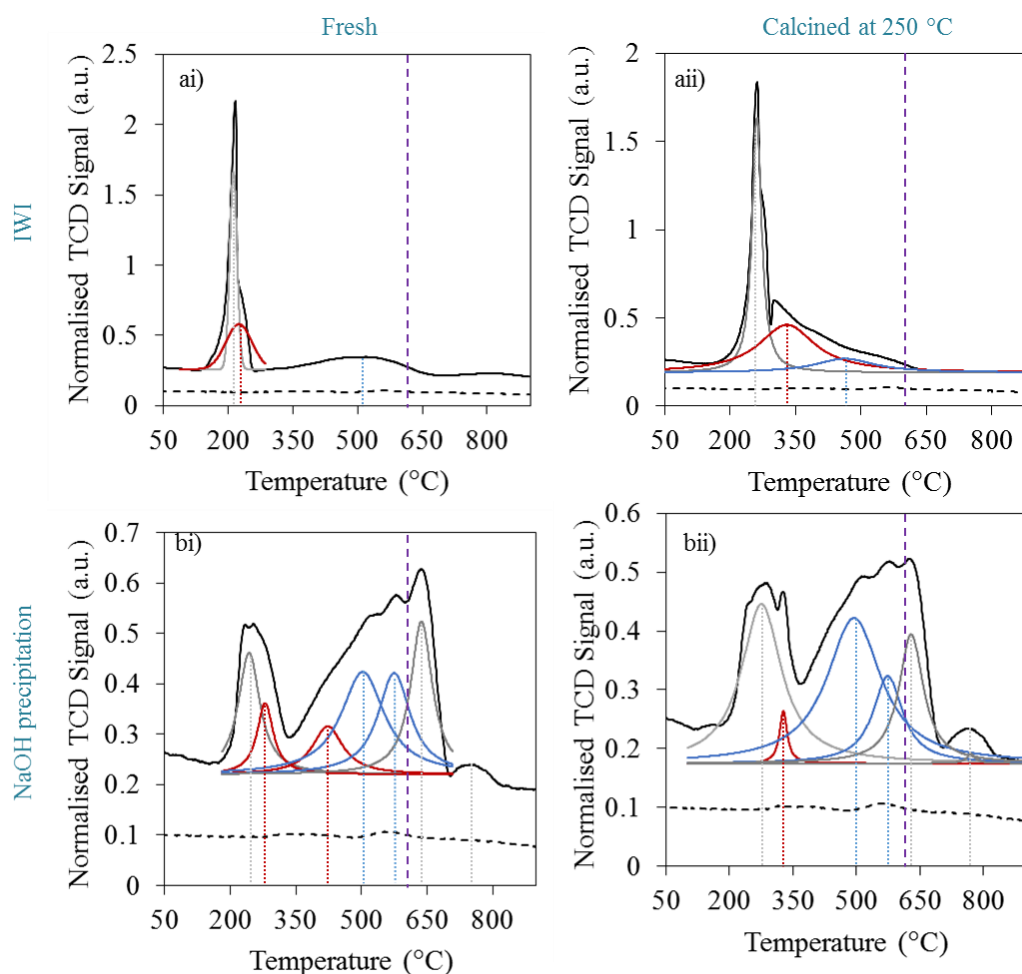


Figure 56. Deconvoluted TPR profile of *Co/plate* catalysts synthesised by a) IWI and b) NaOH precipitation methods with different calcination pre-treatments. ai) *6.5Co/plate-IWI- fresh-red580*, aii) *7.7Co/plate-IWI-cal250-red580*, bi) *6.7Co/plate-NaOH-fresh-red580* and bii) *6.8Co/plate-NaOH-cal250-red580*. Normalised TCD signal = black line, *plate* support = black dashed line, 580 °C, reduction temperature = vertical purple dashed line. Deconvoluted peaks: $\text{Co}^{3+} \rightarrow \text{Co}^{2+}$ = burgundy line and $\text{Co}^{2+} \rightarrow \text{Co}^0$ = blue line, removal of impurities = grey line.

Distinct TPR patterns profiles are obtained for the catalysts produced by different methods (Figure 56a cf Figure 56b). However, the profile is similar before and after calcination (Figure 56i cf Figure 56ii). Based on the blue peak maxima ($\text{Co}^{2+} \rightarrow \text{Co}^0$) of the TPR patterns, all four catalysts are reduced by 580 °C, maximising the presence of Co^0 . TPR indicates that reducibility is not significantly affected by calcination and is unlikely to cause the difference in activity from calcination observed in Figure 55.

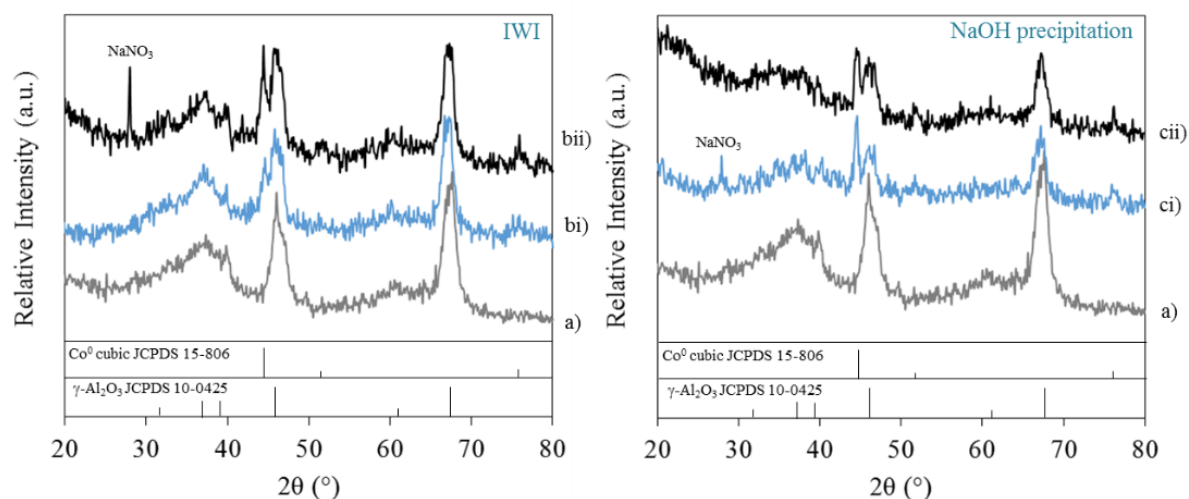


Figure 57. pXRD pattern of *Co/plate* catalysts reduced at 580 °C under H₂ synthesised by IWI (b) and NaOH precipitation (c) methods with different calcination pre-treatments. a) γ -Al₂O₃ plate support (grey line) (JCPDS Card No. 10-0425) bi) *6.5Co/plate-IWI-fresh-red580* (blue), bii) *7.7Co/plate-IWI-cal250-red580* (black), ci) *6.7Co/plate-NaOH-fresh-red580* (blue) and cii) *6.8Co/plate-NaOH-cal250-red580* (black).

All of the four reduced cobalt materials exhibit γ -Al₂O₃ peaks and a peak at ~ 44 ° (Figure 57), assigned to cubic Co⁰ (Figure 57). Despite exposure to air prior to pXRD analysis, no cobalt oxide phases are identified. The peak at 28° in Figure 57bii and Figure 57ci is assigned to NaNO₃ (JCPDS 36-1474),¹⁵⁵ which arises from the use of nitrate precursors and NaOH in the synthesis. The crystallite particle size predicted by pXRD for the materials produced by IWI and NaOH precipitation is unchanged following calcination at 250 °C.

This sub-section demonstrates that calcination at 250 °C results in a small decrease in activity for catalysts produced by IWI and NaOH precipitation. The decrease in activity cannot be attributed to a change in crystallinity, particle size or reducibility.

Calcination must be consistent across a catalyst series and the choice to calcine a material or not can be made based on practical requirements. A calcination protocol (250 °C) will be employed throughout to remove nitrates to align with standard industry procedure. Materials produced by NaOH precipitation in Chapter 6 are uncalcined due to the catalytic instability of *6.8Co/plate-NaOH-cal250-red580* observed in the results in this sub-section.

5.2.2 Effect of reduction temperature on NH₃ decomposition activity

The optimum reduction temperature is a compromise between the proportion of active metallic species present and the particle size, as the particles are more susceptible to sintering at higher temperatures. To determine the optimum conditions, two Co/ γ -Al₂O₃ catalysts using the *plate* support synthesised by IWI (7.7Co/*plate*-IWI-cal250) and by NaOH precipitation (6.7Co/*plate*-NaOH) were tested for NH₃ decomposition with different reduction pre-treatments. Prior to testing, the catalysts are reduced *in situ* at different temperatures (400 °C and 580 °C) in order to determine the effect of reduction temperature. Additionally, the catalysts were tested without a reduction step and in this case the sample was purged with helium at room temperature prior to the experiment.

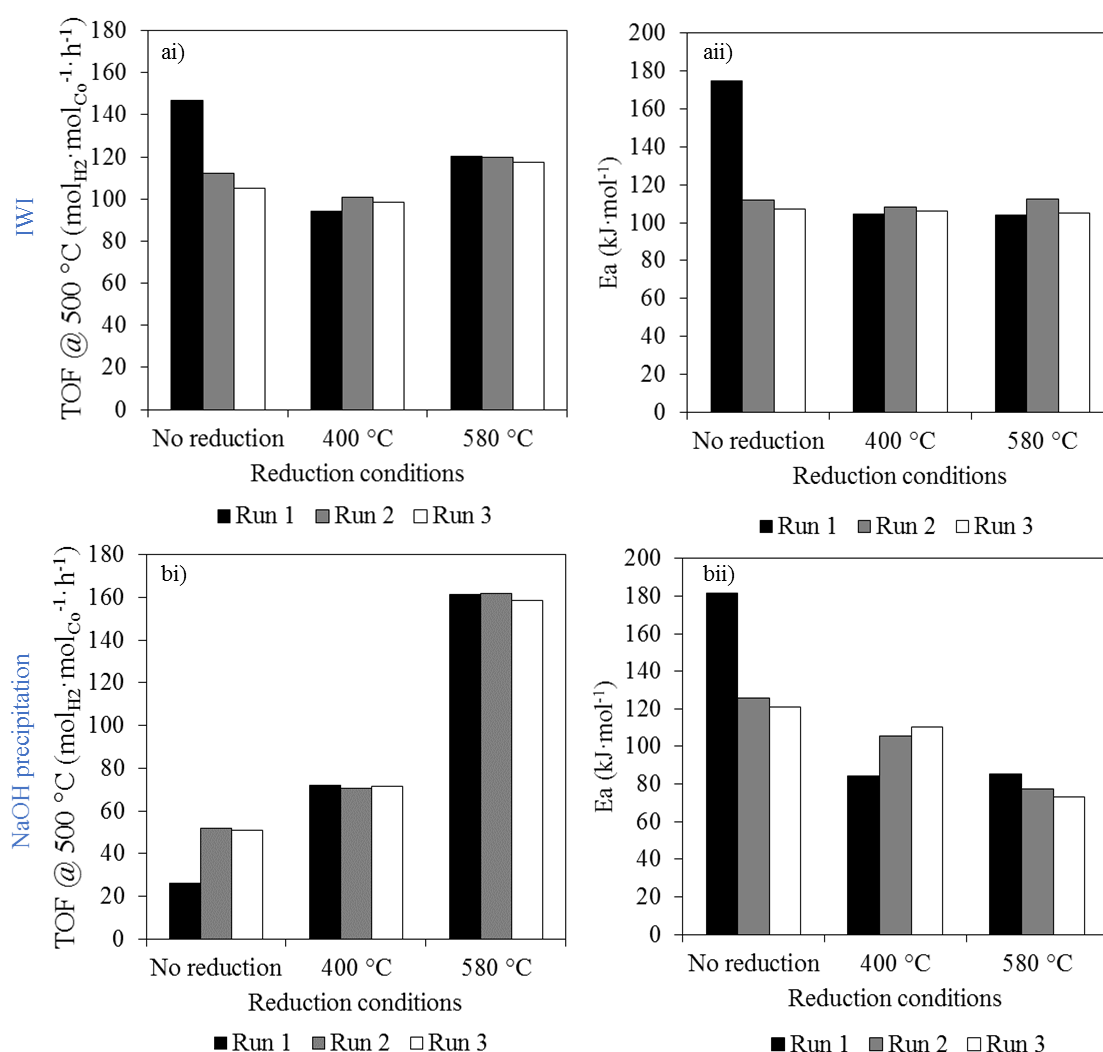


Figure 58. NH₃ decomposition TOF at 500 °C (i) and E_a (ii) for Co/*plate* catalysts reduced under H₂ at different temperatures synthesised by a) IWI and b) NaOH precipitation. Run 1 (black), run 2 (grey) and run 3 (white).

Table 29. Third run NH₃ decomposition activation energy (E_a) and turnover frequency (TOF) of *Co/plate* catalysts prepared by IWI and NaOH precipitation with different *in situ* reduction procedures.

Catalyst	E _a (kJ·mol ⁻¹)	TOF @ 500 °C (mol _{H2} ·mol _{Co} ⁻¹ ·h ⁻¹)	Stability over 3 runs ^a
<i>7.7Co/plate-IWI-cal250-nored</i>	106.9	105.0	-28.5 % TOF
<i>7.7Co/plate-IWI-cal250-red400</i>	106.0	98.5	Stable
<i>7.7Co/plate-IWI-cal250-red580</i>	105.1	117.3	Stable
<i>6.7Co/plate-NaOH-nored</i>	120.9	51.0	+6.8 % TOF
<i>6.7Co/plate-NaOH-red400</i>	110.5	71.7	Stable
<i>6.7Co/plate-NaOH-red580</i>	73.3	158.4	Stable

Reduction conditions: 5 °C·min⁻¹ ramp, 20 mL·min⁻¹ H₂ flow, 45 mins at different maximum temperature.

^a (-) indicates deactivation and (+) activation.

The reduction temperature of the sample is denoted by the suffix “-redT” where T is the reduction temperature and in the case of no reduction, “-nored” notation is used. The TOF at 500 °C and E_a for both catalysts pre-treated at different reduction temperatures is shown in Figure 58 and Table 29 summarises the third run catalytic data. Note that *6.7Co/plate-NaOH* has not been calcined because the fresh *6.7Co/plate-NaOH* catalyst was found to be more stable based on the results in Section 5.2.1. By contrast, *7.7Co/plate-IWI-cal250* has been calcined at 250 °C identified by the “-cal250” suffix.

Interestingly, the materials obtained from the two methods demonstrate contrasting catalytic behaviour (Figure 58) after consecutive runs when the different reduction conditions are used. The *6.7Co/plate-NaOH* catalyst exhibits a significant difference in activity from the choice of reduction pre-treatment, with the maximal activity resulting from the highest temperature. The *6.7Co/plate-NaOH* catalyst is harder to reduce than *7.7Co/plate-IWI-cal250*, as shown by the TPR profiles (Figure 47). As such, *6.7Co/plate-NaOH* exhibits an increase in catalytic activity when pre-treated in hydrogen at higher temperatures, reflected by the significant increase in TOF at 500 °C from 51.0 to 158.4 mol_{H2}·mol_{Co}⁻¹·h⁻¹. By contrast, the third run activities of *7.7Co/plate-IWI-cal250* reduced under different conditions increase slightly with higher reduction temperature from 95.8 to 117.3 mol_{H2}·mol_{Co}⁻¹·h⁻¹ TOF at 500 °C when the reduction temperature is increased from 400 to 580 °C.

After the first run, the unreduced *6.7Co/plate-NaOH-nored* catalyst increases in activity, possibly due to *in situ* reduction from the H₂ produced in the reaction and the elevated temperature. Conversely, the unreduced *7.7Co/plate-IWI-cal250* deactivates. The reason for

this deactivation is probably due to deactivation during the reaction and not sintering during reduction as confirmed by pXRD with *in situ* reduction (Table 27).

Figure 58 shows that the E_a for both catalysts decreases when a reduction pre-treatment is employed as more Co^0 active sites are available. Furthermore, reduction leads to stable catalyst activity across consecutive runs, reflected by the TOF at 500 °C and the activation energy (Figure 58).

The difference in catalytic behaviour following different reductive pre-treatments can be understood from the differences in the TPR profiles shown in Figure 47. The TPR profiles show that a higher Co^{2+} to Co^0 reduction temperature is needed for the NaOH catalyst (574.0 °C) compared to the IWI catalyst (463.2 °C). This is in agreement with the observed increase in catalytic activity of the NaOH catalyst when reduced at higher temperatures. Interestingly, industrial cobalt FTS catalysts are typically reduced at 425 °C, closer to the lower temperature tested here but these conditions achieve only 10 to 45 wt% Co^0 .^{56,59}

This sub-section highlights the importance of the choice of reduction temperature. For consistency and to maximise the proportion of Co^0 , 580 °C pre-reduction conditions will be used in all subsequent catalysis and characterisation. The choice of 580 °C reduction is supported by the TPR data presented earlier (Figure 47). In addition, this study confirms that Co^0 has a higher catalytic activity than other oxidation states of cobalt, in agreement with the accepted active species.⁵⁶

5.2.3 Effect of synthesis method on NH₃ decomposition activity

The materials characterised in Section 5.1 synthesised by different methods were tested for catalytic activity in the NH₃ decomposition reaction. All materials are calcined at 250 °C prior to testing and reduced *in situ* at 580 °C (5 °C·min⁻¹, 45 min). The NH₃ decomposition catalytic activity of the materials is shown in Figure 59 and several catalytic activity indicators are summarised Table 30.

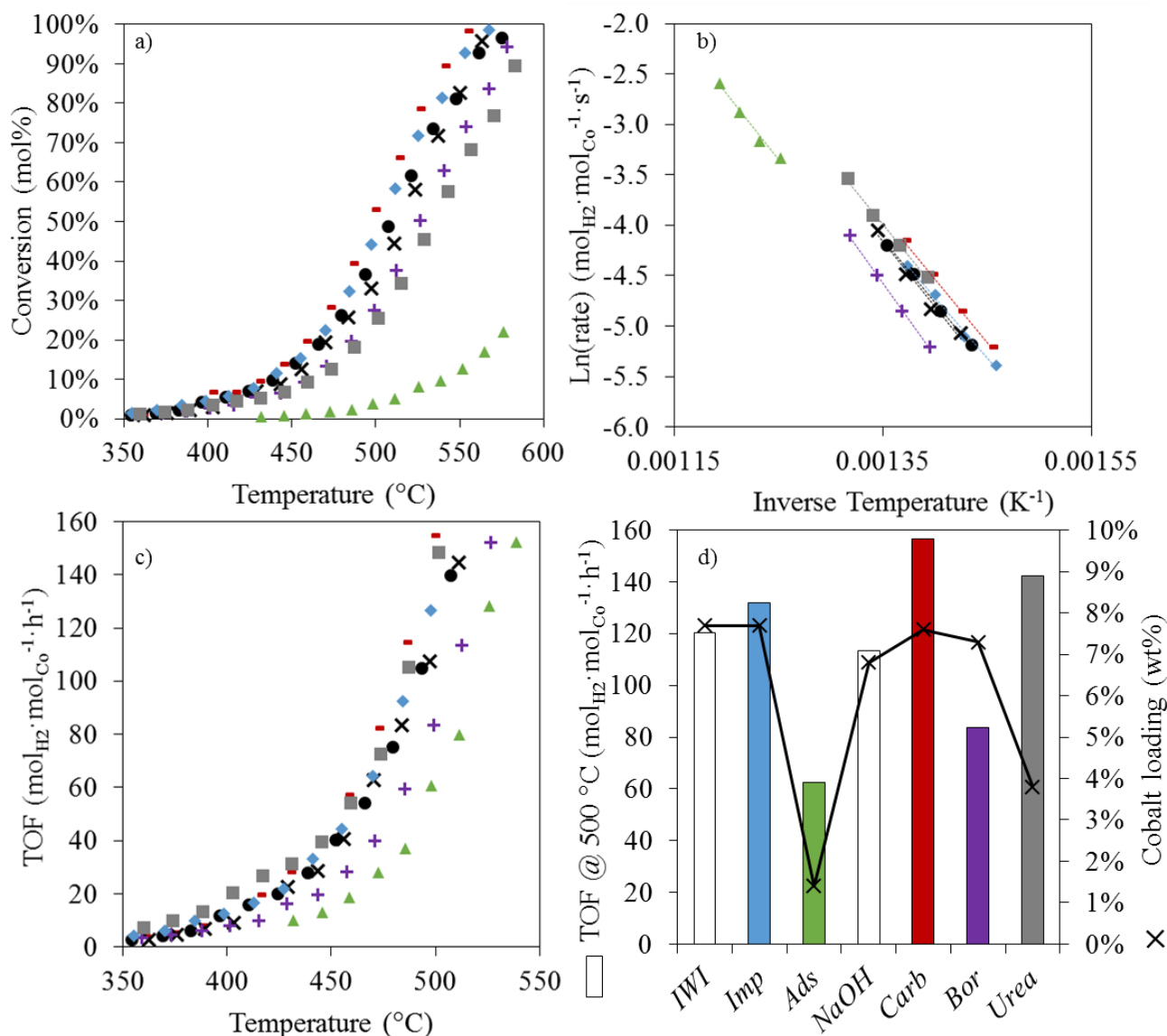


Figure 59. NH₃ decomposition catalytic data for the calcined *Co/plate-cal250* catalysts synthesised by different methods. Pre-reduced *in situ* at 580 °C a) activity as a function of temperature b) Arrhenius plot c) TOF as a function of temperature and d) TOF at 500 °C (LHS) and actual Co loading (RHS). 7.7Co/plate-IWI-cal250-red580 (●), 7.7Co/plate-imp-cal250-red580 (◆), 1.4Co/plate-ads-cal250-red580 (▲), 6.8Co/plate-NaOH-cal250-red580 (x), 7.6Co/plate-carb-cal250-red580 (-), 7.3Co/plate-bor-cal250-red580 (+) and 3.8Co/plate-urea-cal250-red580 (■).

Table 30. Catalytic data and actual loading of *Co/plate-cal250* catalysts synthesised by different methods.

Catalyst	E_a ($\text{kJ}\cdot\text{mol}^{-1}$)	TOF @ 500 °C ($\text{mol}_{\text{H}_2}\cdot\text{mol}_{\text{Co}}^{-1}\cdot\text{h}^{-1}$)	Stability over 3 runs ^a
<i>7.7Co/plate-IWI-cal250-red580</i>	103.9	120.3	Stable
<i>7.7Co/plate-imp-cal250-red580</i>	99.1	131.8	Stable
<i>1.4Co/plate-ads-cal250-red580</i>	120.7	62.6	-50.0 % TOF
<i>6.8Co/plate-NaOH-cal250-red580</i>	108.6	113.4	-32.3% TOF
<i>7.6Co/plate-carb-cal250-red580</i>	105.3	156.4	Stable
<i>7.3Co/plate-bor-cal250-red580</i>	120.0	83.6	Stable
<i>3.8Co/plate-urea-cal250-red580</i>	104.2	142.3	Stable

^a (-) indicates deactivation and (+) activation.

Figure 59d shows that the catalytic activity at 500 °C depends on the choice of cobalt loading methods, with the TOF at 500 °C varying from 62.6 to 156.4 $\text{mol}_{\text{H}_2}\cdot\text{mol}_{\text{Co}}^{-1}\cdot\text{h}^{-1}$. The corresponding activation energies (Table 30) are within the range 99.1 to 120.7 $\text{kJ}\cdot\text{mol}^{-1}$. The TOF at 500 °C (Table 30) increases across the series in the order *1.4Co/plate-ads-cal250-red580* < *7.3Co/plate-bor-cal250-red580* < *6.8Co/plate-NaOH-cal250-red580* < *7.7Co/plate-IWI-cal250-red580* < *7.7Co/plate-imp-cal250-red580* < *3.8Co/plate-urea-cal250-red580* < *7.6Co/plate-carb-cal250-red580*. The two least active catalysts (*7.3Co/plate-bor-cal250-red580* and *1.4Co/plate-ads-cal250-red580*) have the highest activation energies $\sim 120 \text{ kJ}\cdot\text{mol}^{-1}$. The catalytic activity in terms of TOF of *6.8Co/plate-NaOH-cal250-red580* and *1.4Co/plate-ads-cal250-red580* deactivate by 32 % and 50 % over the three consecutive runs.

The trend in activity at 500 °C follows the order of crystallite size calculated from pXRD peak broadening with the smallest size (7.7 nm) associated to the most active catalyst (*7.6Co/plate-carb-cal250-red580*). However, as a Co^0 pXRD peak was not observed for *1.4Co/plate-ads-cal250-red580* and *3.8Co/plate-urea-cal250-red580* it is not possible to extend the size-activity dependency across the complete series. The reason for the high activity of the *3.8Co/plate-urea-cal250-red580* is therefore less obvious, however, it may be due to the low Co^{2+} reduction temperature (456.3 °C) and associated high reducibility or the relatively low loading favouring the formation of small cobalt nanoparticles. The latter explanation is supported by the absence of a Co^0 pXRD peak, suggesting the presence of 2 to 3 nm particles.

In the middle range of activity at 500 °C, *7.7Co/plate-IWI-cal250-red580* and *7.7Co/plate-imp-cal250-red580* all have low reduction temperatures (< 513 °C), fairly small crystallites (< 11.1 nm from pXRD) and contain no unexpected elements such as boron, chlorine or

potassium. However, impregnation methods are often criticized for a poor metal-support interaction strength, which may result in sintering during reduction or catalytic testing. Sintering during reduction of *7.7Co/plate-IWI-cal250* is plausible as the pXRD crystallite size increases from 10.5 to 11.1 nm after reduction, despite a $\frac{3}{4}$ size decrease expected from the contraction of the crystal lattice.⁵⁵

Closely following in the activity sequence, *6.8Co/plate-NaOH-cal250-red580* has a quite high reduction temperature (574 °C) and lower reducibility than the impregnation catalysts. In addition, the high sodium content (8.4 wt%) may alter the activity as it is an electron rich element. The cause for instability and deactivation of this catalyst after three consecutive catalytic runs is not clear. Section 5.2.1 demonstrates that the deactivation takes place only in the calcined version of the NaOH precipitated catalyst, thus the deactivation cannot be due to the high sodium content as it is ~ 8 wt% in both catalysts.

The borate catalyst (*7.3Co/plate-bor-cal250-red580*), has the largest particle size estimated by pXRD, low reducibility from the formation of CoAl_2O_4 and contains additional numerous contaminants (B, Cl and K) that could contribute to a lower activity by blocking active sites.

The catalyst synthesised by adsorption (*1.4Co/plate-ads-cal250-red580*) exhibits the worst activity likely due to the very low loading leading to a high proportion of CoAl_2O_4 formation or “irreducible” Co^{2+} , supported by the absence of a Co^0 pXRD peak, low reducibility estimated by XPS with *in situ* reduction and the blue catalyst colour after reduction. Additionally, this catalyst deactivates by 50 % over three consecutive runs.

Catalytic testing of the *Co/plate* series of catalysts synthesised by different methods highlights the importance of method selection as it affects significant factors such as the particle size, reducibility and chemical composition. Undoubtedly, the particle size plays an important role due to the known size-sensitivity. However it is difficult to directly correlate size and activity across the complete series as pXRD peaks are not observed in two of the catalysts. The adsorption and precipitation by the borate buffer methods are found to produce the least active $\text{Co}/\gamma\text{-Al}_2\text{O}_3$ catalysts for NH_3 decomposition.

Chapter 5 conclusions

This chapter presents detailed characterisation and catalytic testing of a series of Co/ γ -Al₂O₃ catalysts synthesised by different methods including impregnation, adsorption and precipitation. The purpose of this study is to determine a suitable method of cobalt nanoparticle synthesis for use with a range of γ -Al₂O₃ morphologies and different loadings in the subsequent chapter.

The results herein reveal the dependence of the choice of method on the resulting catalyst properties, notably the particle size, strength of metal-support interaction, reducibility, tendency to form of CoAl₂O₄, metallic loading and chemical composition. The experimental work up steps, such as calcination and reduction, have also been determined to significantly affect the catalyst properties and the NH₃ decomposition kinetics and activity. The use of a calcination step must be consistent across a series. Higher temperature reduction conditions (580 °C) will be used to increase the proportion of Co⁰, which has been confirmed as the catalytic active site by the study herein.

The catalysts that exhibit the lowest activity per mol of cobalt are produced by adsorption (*1.4Co/plate-ads-cal250-red580*) and by precipitation with a borate buffer (*7.3Co/plate-bor-cal250-red580*). The poor activity of the *1.4Co/plate-ads-cal250-red580* catalyst is likely due to the low loading resulting in the formation of a significant proportion of CoAl₂O₄, which remains unreduced at 580 °C. For *7.3Co/plate-bor-cal250-red580*, the low activity may be due to the larger crystallite size (17.0 nm estimated by pXRD) or the presence of contaminants such as boron, potassium or chlorine.

When considering the rate of NH₃ decomposition at 500 °C, the catalyst synthesised by precipitation using a carbonate buffer (*7.6Co/plate-carb-cal250-red580*) is the most active, likely due to the small Co⁰ particle size (7.7 nm estimated by pXRD) and high reducibility. However, TEM analysis of the sample revealed some honeycomb structures which may appear from attrition of the γ -Al₂O₃ support under the basic synthesis conditions. These structures could affect the support surface roughness, introducing an additional experimental variable. As such, the carbonate precipitation method is not selected as the method for the following chapter, despite the high activity of the resulting catalyst.

At lower temperatures, a few methods produce catalysts with similar activity such as IWI, impregnation and precipitation by NaOH and urea. The urea precipitation method produces a catalyst with a loading far below the theoretical value and as such will not be used in the next chapter. By contrast, precipitation by NaOH results in a catalyst with a loading closer to the theoretical value with an average Co⁰ crystallite size of 14.8 nm. The preliminary results suggest that the high sodium content in *6.8Co/plate-NaOH-cal250-red580* does not have detrimental effects on the catalytic activity. Based on these observations, precipitation by NaOH will be used in the next chapter. The IWI and impregnation methods produce similar catalysts but IWI is easier to scale up and can be used to produce multiple materials simultaneously. Based on these practicalities, IWI will also be used to synthesise materials in the next chapter.

Chapter 6 – Effect of support morphology on Co/ γ -Al₂O₃ catalytic activity and stability

This chapter presents two methods of cobalt nanoparticle synthesis, based on conclusions derived from the previous chapter, namely NaOH precipitation and incipient wetness impregnation (IWI). These two methods are used to synthesise a range of catalysts with different loadings and different support morphologies.

In order to determine the effect of curvature on nanoparticle stabilisation, three different nanostructured support morphologies were used as well as a bulk support for comparison. Characterisation of these materials can be found in Section 0 and the materials are referred to by the following terms:

- “*Plate*”: γ -Al₂O₃ nanoplates synthesised by hydrothermal treatment for 20 hours at 200 °C with 3.91:1 NaOH:Al ratio.
- “*40hfat*”: γ -Al₂O₃ nanorods with low aspect ratio synthesised by hydrothermal treatment for 40 hours at 200 °C with 0.77:1 NaOH:Al ratio.
- “*180thin*”: γ -Al₂O₃ nanorods with high aspect ratio synthesised by hydrothermal treatment for 20 hours at 180 °C with 0.77:1 NaOH:Al ratio.
- “*10hthin*”: γ -Al₂O₃ nanorods with high aspect ratio synthesised by hydrothermal treatment for 10 hours at 200 °C with 0.77:1 NaOH:Al ratio.
- “*Commercial*”: Bulk commercial γ -Al₂O₃ from Sasol Ltd without well-defined nanostructured morphology.

The materials are fully characterised in order to determine the effect of the change in support morphology on the catalytic activity owing to differences in particle size, catalyst composition or reducibility. All of the materials are tested for NH₃ decomposition and based on these results, a selection of materials are tested for Fischer-Tropsch synthesis (FTS) under industrially relevant conditions.

6.1 NH₃ decomposition

NH₃ decomposition presents an exciting opportunity to support the H₂ economy by providing a safe and efficient means of H₂ storage. In order for NH₃ to be used as a H₂ vector, heterogeneous catalysts need to be developed to facilitate H₂ release on demand at low temperatures (< 150 °C). Catalysts capable of operating at these low temperature conditions have not yet been discovered.

The most active catalyst for NH₃ decomposition is ruthenium supported on carbon nanotubes and recent efforts in the research group have further enhanced the activity by introducing electron donating promoters and increasing the support conductivity.^{62,71} The cost of ruthenium limits its wide scale use and as such the scientific community have recently explored alternatives such as cobalt, which to date have been limited by fairly poor activity at low temperatures.¹⁶¹ We were able to demonstrate, however, that the NH₃ decomposition activity for cobalt catalysts is highly dependent on the cobalt particle size and is not necessarily enhanced by the addition of electron donating promoters.¹⁵³

NH₃ decomposition by cobalt catalysts is size-sensitive so it can be used to probe the degree of stabilisation resulting from the choice of support in order to validate the research hypothesis. As such, this chapter focuses on the effect of metal loading and γ -Al₂O₃ support morphology on the cobalt particle size and consequently the catalytic activity and stability.

6.1.1 Catalysts synthesised by NaOH precipitation

A series of cobalt catalysts were synthesised by the NaOH precipitation method in which the metal loading and the γ -Al₂O₃ support morphology was varied (γ -Al₂O₃ characterisation in Section 0). Based on conclusions from the previous chapter, the catalysts in this series were not calcined but were reduced at 580 °C prior to catalytic testing and characterisation (unless stated otherwise).

6.1.1.1 Characterisation of fresh Co/ γ -Al₂O₃-NaOH catalysts

For each nanostructured support, Co/ γ -Al₂O₃ with four different metal loadings were synthesised in the range of 1 to 17 wt% cobalt. To compare the effect of the support morphology on particle size, a commercial support (“*commercial*”) was used to synthesise

comparable cobalt catalysts. The maximum theoretical cobalt contents are 1.0, 4.8, 9.1 and 16.7 wt% Co. The nomenclature used throughout to refer to the materials is found in Table 31 as well as the loading and colour of the obtained samples. The actual cobalt loading achieved is at least 70 % of the theoretical loading in all cases. Interestingly, *5.2Co/180thin-NaOH* and *1.1Co/commercial-NaOH* achieve loadings slightly greater than the theoretical maximum by 0.1 to 0.3 wt%, possibly due to loss or dissolution of the support during cobalt loading and processing.

In addition, cobalt particles were also obtained from precipitation of 0.848 mmol of $\text{Co}(\text{NO}_3)_2 \cdot 6\text{H}_2\text{O}$ using 0.125 mol NaOH in the absence of support, referred to as “*42.6Co-unsupported*” since the material contains 42.6 wt% Co determined by ICP. The amount of cobalt precursor used is the same as for the synthesis of $\text{Co}/\gamma\text{-Al}_2\text{O}_3$ with 9.1 wt% theoretical Co content.

Table 31. Content and colour of fresh *Co*/ $\gamma\text{-Al}_2\text{O}_3$ -*NaOH* catalysts (unreduced) with different loadings on $\gamma\text{-Al}_2\text{O}_3$ supports with different morphologies.

Catalyst	Co loading ^a (wt%)	Na content ^a (wt%)	Colour	CoOOH size ^b (nm)
<i>0.9Co/plate-NaOH</i>	0.9	6.1	Beige	No peak
<i>4.0Co/plate-NaOH</i>	4.0	6.9	Light brown	22.4
<i>6.7Co/plate-NaOH</i>	6.7	6.8	Brown	15.2
<i>13.0Co/plate-NaOH</i>	13.0	8.0	Dark brown	10.0
<i>0.9Co/40hfat-NaOH</i>	0.9	8.4	Beige	No peak
<i>4.3Co/40hfat-NaOH</i>	4.3	6.5	Light brown	13.7
<i>7.6Co/40hfat-NaOH</i>	7.6	6.7	Dark grey	11.5
<i>14.1Co/40hfat-NaOH</i>	14.1	7.6	Dark grey	10.1
<i>0.9Co/180thin-NaOH</i>	0.9	10.1	Beige	13.2
<i>5.2Co/180thin-NaOH</i>	5.2	8.2	Khaki/brown	17.9
<i>9.1Co/180thin-NaOH</i>	9.1	18.7	Dark khaki/brown	22.4
<i>16.6Co/180thin-NaOH</i>	16.6	5.8	Dark brown	15.2
<i>1.1Co/commercial-NaOH</i>	1.1	6.1	Beige	-
<i>4.6Co/commercial-NaOH</i>	4.6	4.8	Khaki/brown	No peak
<i>8.1Co/commercial-NaOH</i>	8.1	6.1	Dark brown	No peak
<i>15.1Co/commercial-NaOH</i>	15.1	5.5	Black	-
<i>42.6Co-unsupported</i>	42.6	8.3	Dark brown	16.8

^a Calculated from ICP of the digested solid (fresh catalyst).

^b Calculated using the FWHM of the CoOOH peak at $\sim 20^\circ$ (JCPDS 14-0673) with the Scherrer equation.

The fresh catalysts are generally brown in colour, which increases in intensity as the cobalt loading is increased. A high sodium content for all the catalysts, greater than 5 wt% is determined by ICP.

pXRD (Figure 60) of the fresh samples identifies CoOOH (JCPDS 14-0673) to be the only cobalt species present in the samples, and the γ phase of Al_2O_3 support is also identified (JCPDS 10-0425). Due to the low loading, no cobalt peaks can be seen for the ~ 1 wt% series. Additionally, no CoOOH or other cobalt species pXRD peaks are observed for the catalysts supported on *commercial* $\gamma\text{-Al}_2\text{O}_3$, however patterns were not obtained for 1.1 and 15.1 wt% Co. The CoOOH particle size calculated using the Scherrer equation is shown in Table 31. Interestingly, the CoOOH particle size calculated from pXRD decreases as the loading is increased.

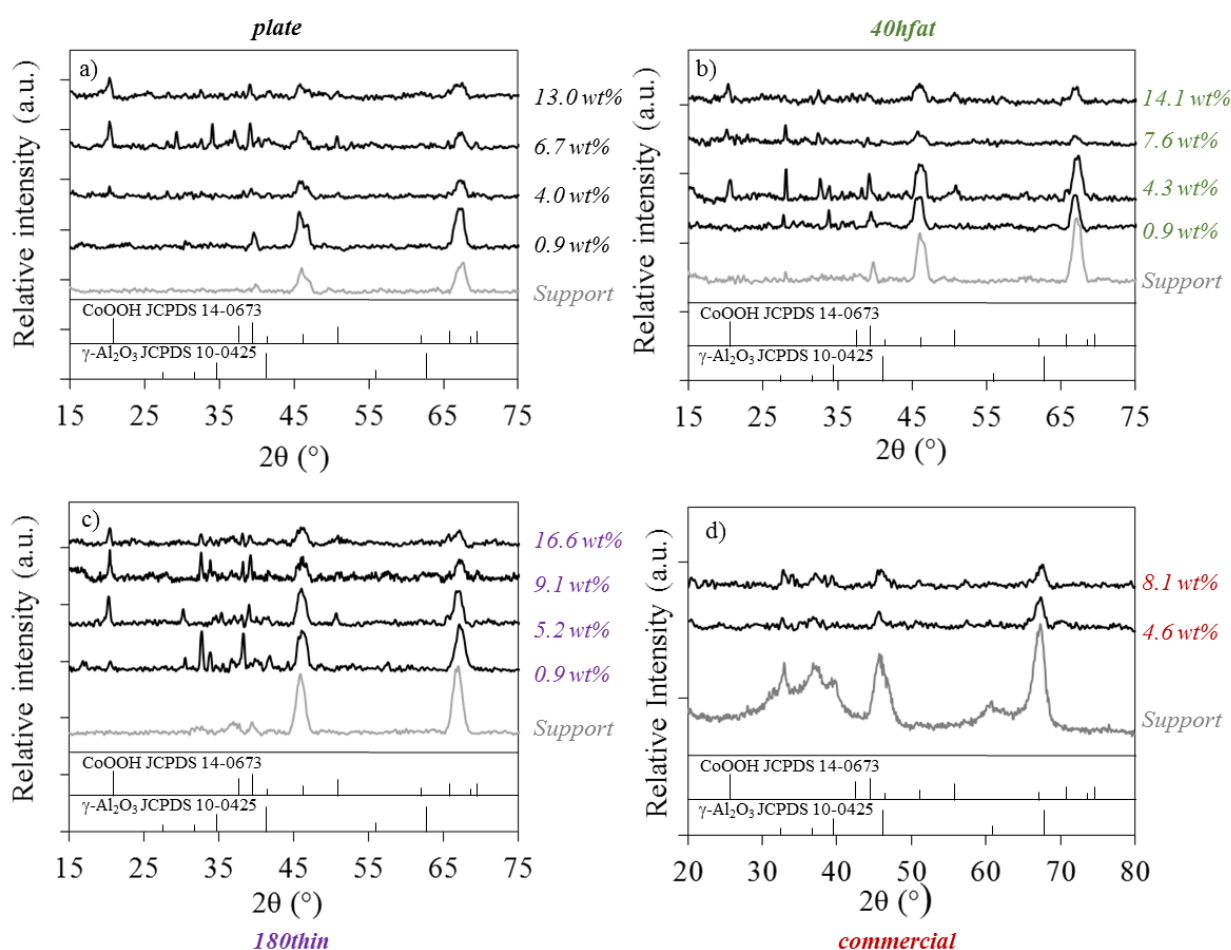


Figure 60. pXRD patterns of $\text{Co}/\gamma\text{-Al}_2\text{O}_3\text{-NaOH}$ catalysts synthesised by NaOH precipitation with different loadings on $\gamma\text{-Al}_2\text{O}_3$ supports with different morphologies. a) *plate*, b) *40hfat*, c) *10hthin* and d) *commercial*.

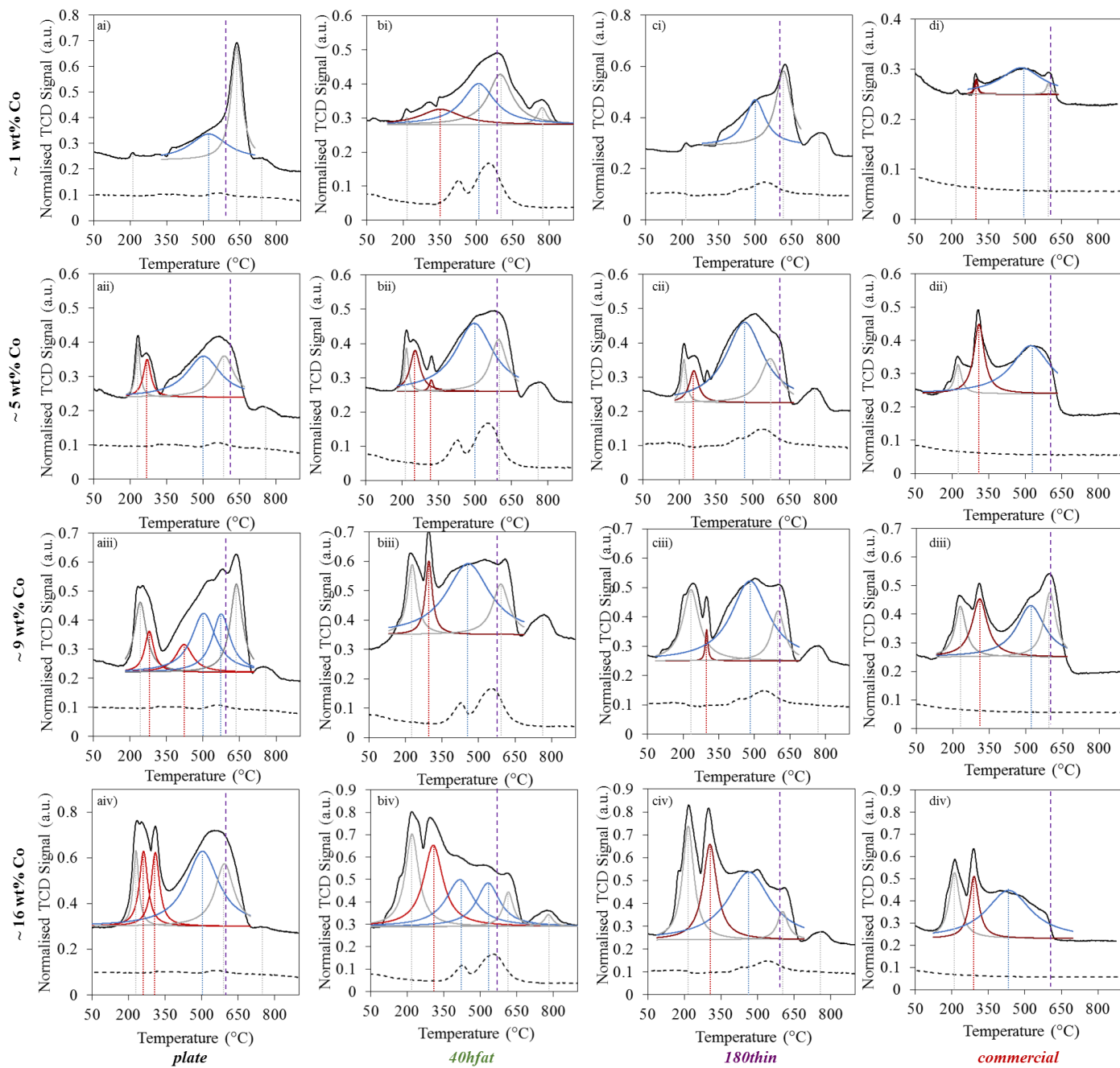


Figure 61. Deconvoluted temperature programmed reduction profiles of $Co/\gamma-Al_2O_3-NaOH$ catalysts with different loadings on $\gamma-Al_2O_3$ supports with different morphologies. a) *plate*, b) *40hfat*, c) *10thin* and d) *commercial*. Normalised TCD signal = black line, support = black dashed line, 580 °C employed reduction temperature = vertical purple dashed line, $Co^{3+} \rightarrow Co^{2+}$ = burgundy curve and $Co^{2+} \rightarrow Co^0$ = blue curve, $CoAl_2O_4 \rightarrow Co^0$ = green curve, removal of impurities = grey curve.

Table 32. TPR peak temperatures of *Co/γ-Al₂O₃-NaOH* catalysts assigned to different chemical processes.

Catalyst	Peak temperature (°C)					
	$\text{Co}^{3+} \rightarrow \text{Co}^{2+}$		$\text{Co}^{2+} \rightarrow \text{Co}^0$		$\text{CoAl}_2\text{O}_4 \rightarrow \text{Co}^0$	Removal impurities e.g. N or C
<i>0.9Co/plate-NaOH</i>	-	-	522.3	-	-	192.9 636.2 742.0
<i>4.0Co/plate-NaOH</i>	270.0	-	502.4	-	-	231.9 588.2 745.5
<i>6.7Co/plate-NaOH</i>	279.7	422.6	502.8	574.6	-	242.9 637.0 758.1
<i>13.0Co/plate-NaOH</i>	262.1	310.3	503.8	-	-	231.3 594.3 765.3
<i>0.9Co/40hfat-NaOH</i>	352.7	-	509.6	-	-	215.0 597.9 770.0
<i>4.3Co/40hfat-NaOH</i>	253.7	320.4	496.6	-	-	218.1 596.5 771.3
<i>7.6Co/40hfat-NaOH</i>	295.6	-	456.8	-	-	227.0 591.0 769.7
<i>14.1Co/40hfat-NaOH</i>	307.2	-	416.5	532.2	-	220.0 614.9 780.1
<i>0.9Co/180thin-NaOH</i>	-	-	500.7	-	-	216.6 616.1 773.8
<i>5.2Co/180thin-NaOH</i>	259.0	-	467.2	-	-	218.7 572.1 765.1
<i>9.1Co/180thin-NaOH</i>	299.2	-	481.4	-	-	232.7 599.8 772.0
<i>16.6Co/180thin-NaOH</i>	305.2	-	464.8	-	-	216.1 603.0 767.5
<i>1.1Co/commercial-NaOH</i>	300.2	-	484.5	-	-	219.8 596.7
<i>4.6Co/commercial-NaOH</i>	310.7	-	523.4	-	-	225.0
<i>8.1Co/commercial-NaOH</i>	310.0	-	519.5	-	-	230.7 598.1
<i>15.1Co/commercial-NaOH</i>	291.4	-	433.2	-	-	211.3
<i>42.6Co-unsupported</i>	244.0	-	332.9	-	-	197.9 448.2 815.1

- Indicates no peak.

The deconvoluted TPR profiles (Figure 61) of the samples prepared by NaOH precipitation show multiple reduction peaks, which have been assigned to a reductive process in Table 32. The peaks are assigned based on numerous factors including the peak temperature, intensity and broadness. Assignment of the peaks was assisted by TPR with MS for the *6.7Co/plate-NaOH* sample (Figure A98, Appendix) and TPR of the unsupported cobalt sample *42.6Co-unsupported* (Figure A101, Appendix).

CoOOH is usually reduced in a two-step process from Co^{3+} to Co^{2+} to Co^0 .⁵⁸ Co^{3+} reduction peaks are evident around ~ 300 °C in all the samples except *0.9Co/plate-NaOH* and *0.9Co/180thin-NaOH* in which no peak is observed, which may be due to the low loading.

The temperature of the $\text{Co}^{2+} \rightarrow \text{Co}^0$ reduction indicates the strength of metal-support interaction and/or particle size. This transformation takes place in the range of 410 to 580 °C for the supported samples. By contrast, the unsupported CoOOH particles (*42.6Co-unsupported*) reduce at a much lower temperature, 332.9 °C.

The reduction peaks above 700 °C cannot be assigned to cobalt aluminate reduction as this usually takes place at temperatures higher than 800 °C and there is a similar peak present in the unsupported CoOOH reduction profile (Figure A101, Appendix). These peaks are not present in the samples supported with *commercial* γ -Al₂O₃. Thus, the TPR peaks above 700 °C are assigned in Table 32 to the removal of an impurity which releases N₂ according to the MS peak for m/z 28 at this temperature for *6.8Co/plate-NaOH* (Figure A98, Appendix).

TEM micrographs of these samples have poor contrast between cobalt and γ -Al₂O₃, making size analysis challenging. However *16.6Co/180thin-NaOH* contains some very large (100 to 340 nm), unsupported hexagonal cobalt compounds structures (Figure A102, Appendix), which are not visible in *13.0Co/plate-NaOH* or in micrographs of the supports (Figure 42).

6.1.1.2 Characterisation of reduced *Co/ γ -Al₂O₃-NaOH* catalysts

All the catalysts were reduced at 580 °C following analysis of the TPR profiles (Figure 61) since the maximum temperature of the blue curves (Co²⁺ → Co⁰) is 575 °C. The pXRD patterns of the reduced samples (Figure 62) show a distinct peak at ~ 44°, assigned to cubic Co⁰ (JCPDS 15-806), as well as the characteristic peaks of the γ -Al₂O₃ support (JCPDS 10-0425). No cobalt peaks are observed for the 1 wt% loaded series as the cobalt content may be below detection limit. Note that the reduced samples are exposed to air prior to pXRD and are thus subject to re-oxidation, particularly particles smaller than 4 nm.⁵³ Upon reduction, the catalyst colour changes to shades of grey, typical for Co⁰, which increase in intensity with loading.

The average Co⁰ crystallite size determined from pXRD ranges from 15 to 30 nm (Table 33). For materials supported on nanostructured γ -Al₂O₃, the particle size generally increases as the loading is increased. However, the opposite is true for the series supported on *commercial* γ -Al₂O₃, which decrease in size from 30.5 to 19.2 nm with increased cobalt loading.

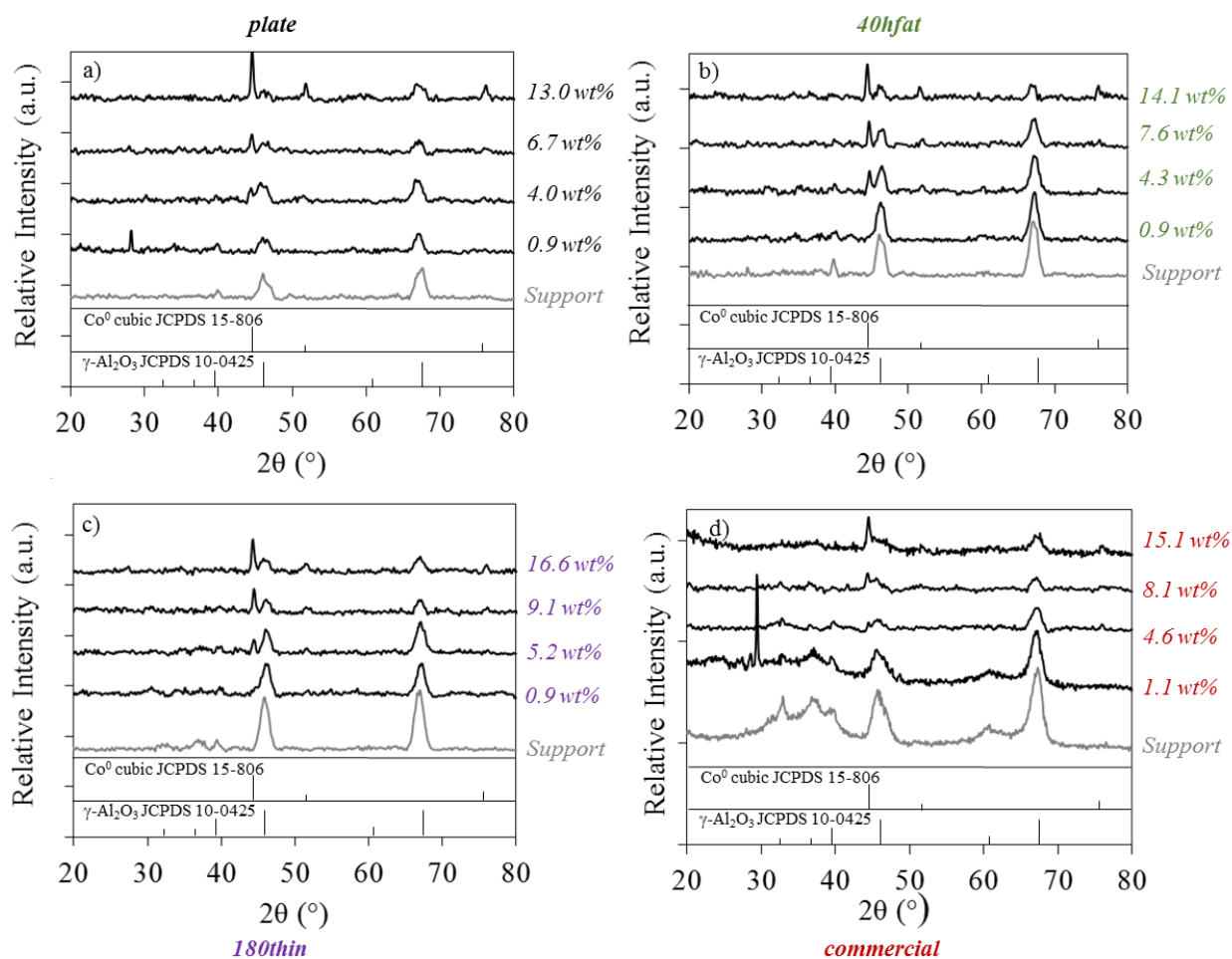


Figure 62. pXRD of $Co/\gamma-Al_2O_3-NaOH$ catalysts reduced *ex situ* (580 °C) synthesised by NaOH precipitation with different loadings on $\gamma-Al_2O_3$ supports with different morphologies. a) *plate*, b) *40hfat*, c) *180thin* and d) *commercial*.

6.1.1.3 Catalytic activity of $Co/\gamma-Al_2O_3-NaOH-red580$ catalysts

The NH_3 decomposition catalytic data of the $Co/\gamma-Al_2O_3$ catalysts prepared by NaOH precipitation is shown in Figure 63 and key data is summarised in Table 33. The data is quoted for the first run if the activity is constant after three consecutive runs. Alternatively, the third run data is presented if the catalyst deactivates. The deactivation degree is shown in Table 33.

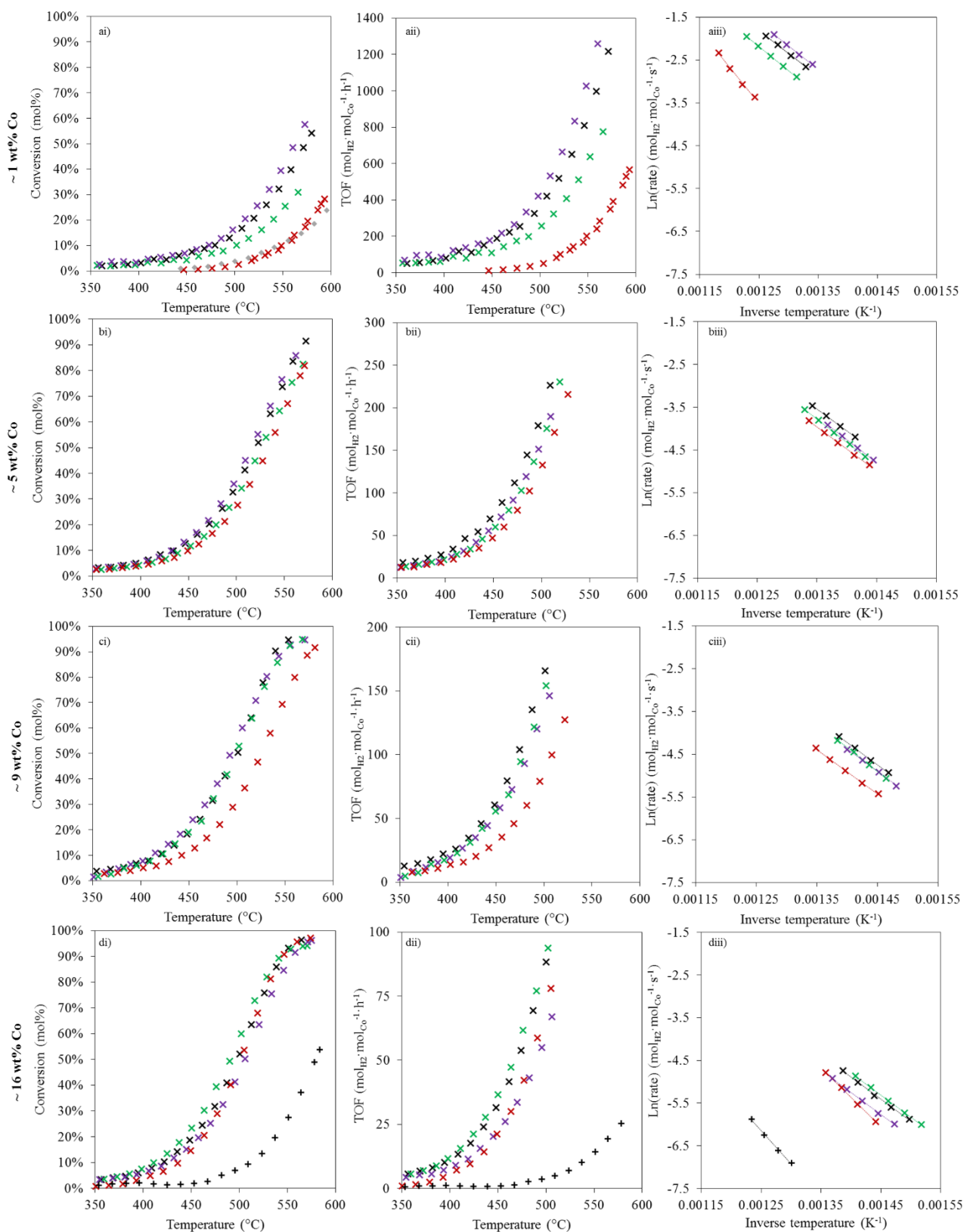


Figure 63. NH_3 decomposition activity of $\text{Co}/\gamma\text{-Al}_2\text{O}_3\text{-NaOH}$ catalysts with different target cobalt loadings on different $\gamma\text{-Al}_2\text{O}_3$ supports. *plate* = black, *40hrod* = green, *180thin* = purple, *commercial* = red. i) conversion as a function of temperature, ii) rate of reaction (TOF) relative to reaction temperature up to 50 % conversion and iii) Arrhenius plot. a) 1 wt%, b) 5 wt%, c) 9 wt% and d) 16 wt% Co. *42.6Co-unsupported-red580* (+) and *plate* (◆) data are shown for reference.

Table 33. NH₃ decomposition data and Co⁰ size of Co/ γ -Al₂O₃-NaOH catalysts with different loadings supported on γ -Al₂O₃ with distinct morphologies. Reduced at 580 °C under H₂ flow.

Catalyst	E _a (kJ·mol ⁻¹)	TOF @ 500 °C (mol _{H₂} ·mol _{Co} ⁻¹ ·h ⁻¹)	Stability over 3 runs ^b	Average Co ⁰ size ^{a, c} (nm)
0.9Co/plate-NaOH-red580	82.5	364.2	Stable	No peak
4.0Co/plate-NaOH-red580	84.6	189.7	Stable	15.3
6.7Co/plate-NaOH-red580	85.3	161.1	Stable	15.0
13.0Co/plate-NaOH-red580	85.9	86.7	Stable	20.9
0.9Co/40hfat-NaOH-red580	92.8	245.3	Stable	No peak
4.3Co/40hfat-NaOH-red580	90.5	157.4	Stable	13.7
7.6Co/40hfat-NaOH-red580	88.7	146.4	Stable	19.1
14.1Co/40hfat-NaOH-red580	86.3	89.7	Stable	19.6
0.9Co/180thin-NaOH-red580	81.6	432.6	Stable	No peak
5.2Co/180thin-NaOH-red580	88.9	158.1	Stable	17.3
9.1Co/180thin-NaOH-red580	87.2	132.8	Stable	18.1
16.6Co/180thin-NaOH-red580	86.2	59.3	Stable	19.0
1.1Co/commercial-NaOH-red580	139.7	45.8	-70.1 % TOF	No peak
4.6Co/commercial-NaOH-red580	85.6	128.5	-12.2 % TOF	30.5
8.1Co/commercial-NaOH-red580	86.8	77.3	-5.3 % TOF	19.3
15.1Co/commercial-NaOH-red580	115.2	69.9	-22.3 % TOF	19.2
42.6Co-unsupported-red580	129.1	3.9	Stable	n/a

^a All materials are pre-reduced at 580 °C (5 °C·min⁻¹, 45 min). Samples are exposed to air prior to pXRD.

^b (-) indicates deactivation and (+) activation.

^c Calculated with the FWHM of the deconvoluted cubic Co peak at ~ 44° (JCPDS 15-806⁸²) with the Scherrer equation.

All catalysts supported on nanostructured γ -Al₂O₃ are stable following three consecutive runs to 580 °C but the catalysts supported on *commercial* support deactivate following the same number of runs (Table 33). Out of the *commercial* supported series, *1.1Co/commercial-NaOH-red580* deactivates the most significantly; the apparent rate of reaction (TOF) at 500 °C decreases from 152.9 to 45.8 mol_{H₂}·mol_{Co}⁻¹·h⁻¹. Grey diamonds in Figure 63ai show the NH₃ decomposition curve for the *plate* support without cobalt, highlighting that the deactivated *1.1Co/commercial-NaOH-red58* catalyst has similar activity to the *plate* support.

The catalytic data of *42.6Co-unsupported-red580* in Figure 63d highlights the benefit of dispersing the catalyst on a solid support as it decreases the activation energy and exposes more

cobalt active sites on the surface due to the difference in particle size, leading to higher catalytic activity and TOFs.

In general, the catalytic activity of the catalysts supported on nanostructured γ -Al₂O₃ are more active than the analogous catalyst supported on *commercial* γ -Al₂O₃ except for the ~ 16 wt% series which has similar activity.

The most significant variation in activity is observed from the use of different support morphology in the ~ 1 wt% series. The activity of the series follows the order *0.9Co/180thin-NaOH-red580* > *0.9Co/plate-NaOH-red580* > *0.9Co/40hfat-NaOH-red580* >> *1.1Co/commercial-NaOH-red580*. The most active catalyst per mole of cobalt is *0.9Co/180thin-NaOH-red580* (432.6 mol_{H₂}·mol_{Co}⁻¹·h⁻¹ at 500 °C), which also has the lowest activation energy (81.6 kJ·mol⁻¹). The activation energy of the 1 wt% series supported on nanostructured γ -Al₂O₃ is much lower than for the catalyst supported on *commercial* (*1.1Co/commercial-NaOH-red580*). Furthermore, the activity starts at a lower temperature (350 °C) for the 1 wt% catalysts supported on nanostructured γ -Al₂O₃ compared to *commercial* γ -Al₂O₃ (450 °C).

Based on the pXRD pattern (Figure 60), the nature of cobalt formed in the fresh catalysts is cobalt oxy hydroxide (CoOOH), which is in agreement with the brown colour of the catalysts. However, the fresh catalysts supported on the *commercial* γ -Al₂O₃ support do not exhibit CoOOH peaks. This may be due to the tendency of CoOOH to form another Co³⁺ species such as Co(OH)₃, which is likely based on the presence of Co³⁺ TPR reduction peaks of these materials. However the absence of Co(OH)₃ pXRD in these catalysts suggests the presence of amorphous cobalt species.

Based on the blue deconvoluted TPR curves of all the samples (Figure 61), 580 °C is a suitable reduction temperature to form Co⁰. This is confirmed by the presence of Co⁰ diffraction peaks in pXRD (Figure 62). In both the fresh and reduced sets of pXRD data, no cobalt peaks are detected for the 1 wt% series, possibly because the loading is below the detection limit or the resulting particles are too small to produce a distinct peak at 44° from the adjacent dominant γ -Al₂O₃ peak at 46°. Small particles are also likely to undergo re-oxidation to form CoO which overlaps with γ -Al₂O₃ in pXRD and are thus not visible.⁵³

There is no evidence of cobalt aluminate formation in the TPR profiles (Figure 61) as there are no peaks higher than 800 °C. This is unusual for cobalt catalysts supported on γ -Al₂O₃ as their strong interaction strength encourages the formation of cobalt aluminate during heat treatment, particularly for low cobalt loading.⁵³ The absence of irreducible mixed oxides results in higher reducibility and Co⁰ content in the reduced catalyst, in turn enhancing the catalytic activity.

The 1 wt% series supported on nanostructured γ -Al₂O₃ are the most active. In fact, these catalysts enable the decomposition of NH₃ at 100 °C lower than when the *commercial* support is used, possibly due to the presence of difference active sites exposed by difference particle sizes. The absence of a pXRD Co⁰ peak and cobalt particles by dark field TEM suggest the presence of small cobalt particles. This is in agreement with the high Co²⁺ reduction temperature of the 1 wt% Co series observed from the TPR profiles (Figure 61).

The catalytic data and characterisation of the 1 wt% series suggests that the nanostructured γ -Al₂O₃ are capable of stabilising smaller particles than the bulk *commercial* support. This is in agreement with the fact that all the catalysts supported on nanostructured γ -Al₂O₃ do not deactivate over the three consecutive runs to 580 °C, whereas all the catalysts supported on the *commercial* support deactivate. Particularly, *1.1Co/commercial-NaOH-red580*, which deactivates by 70 % after three runs, rendering the cobalt content in the catalyst effectively inactive, as shown in Figure 63ai. By contrast, for the same loading, the *180thin* nanorod support effectively stabilises highly active nanoparticles in *0.9Co/180thin-NaOH*, resulting in a catalytic activity per mole of metal of 432.6 mol_{H₂}·mol_{Co}⁻¹·h⁻¹. This activity is highly superior to the best cobalt catalyst reported to date in the literature for this application, which is supported on MWCNT and contains 4.3 nm particles resulting in an activity of 159 mol_{H₂}·mol_{Co}⁻¹·h⁻¹ at 500 °C.^{55,81} In fact, all of the 1 wt% and 4.8 wt% Co catalysts supported on nanostructured γ -Al₂O₃ are more active than this catalyst reported in the literature, but none of the catalysts supported on the *commercial* support exceed the literature benchmark. Interestingly, *0.9Co/plate-NaOH* and *0.9Co/180thin-NaOH* do not exhibit Co³⁺ reduction peaks, which may influence their exceptionally high catalytic activity per mole of metal.

The high sodium content (~ 6 wt%) of all the catalysts, arising from the use of NaOH as a precipitant, could have implications on catalytic activity or inhibiting CoAl₂O₄ formation. Sodium, potassium and caesium have been reported to increase NH₃ decomposition rate for ruthenium catalysts due to the formation of active Ru^δ.^{62,162,163} However, we have previously

observed that caesium does not have an electron-donating promotion effect on cobalt catalysts for NH₃ decomposition as Co⁰ is the active species.¹⁵³ As such, the key aspect to enhancing catalytic activity for this application is optimising cobalt particle size.¹⁵³ Furthermore, the order of sodium content does not follow the activity trend of the 1 wt% series, highlighting that sodium does not play an activity-enhancing role.

The formation of large, 100 to 340 nm, unsupported hexagonal cobalt particles, evidenced by TEM micrographs of *16.6Co/180thin-NaOH* (Figure A102, Appendix), may be the cause of the lower activity per mole of metal of the samples with higher cobalt loading, however the other samples were not imaged by TEM. Cobalt in a hcp arrangement is reported to form after reduction without calcination in air, however no hcp pXRD peaks (JCPDS 05-0727) are visible in the spectra in Figure 62.⁹¹

6.1.2 Catalysts synthesised by incipient wetness impregnation

A series of cobalt catalysts were synthesised following the standard industrial procedure of IWI followed by calcination at 250 °C. The cobalt loading and the γ -Al₂O₃ support morphology were varied in order to determine the extent of cobalt nanoparticle stabilisation arising from the choice of support morphology. The materials were characterised and tested for NH₃ decomposition.

In this section, the high aspect ratio nanorod support used is *10thin*, which differs from *180thin* (used in the previous section) by the synthesis conditions, however, both have the same average rod diameter of 8 nm and thus the same curvature.

6.1.2.1 Characterisation of calcined *Co/γ-Al₂O₃-IWI-cal250* catalysts

The loading, colour and crystallite size of the unreduced calcined catalysts produced by IWI are summarised in Table 34. The colour of the samples increases in darkness as the loading increases. The use of different supports for the same loading, does not affect the colour observed. The sodium content of the catalysts is generally highest when the *plate* support is used (2 to 4 wt%) and lowest with the *commercial* support (< 0.5 wt%).

pXRD patterns of all the calcined samples (Figure 64) confirms the presence of crystalline γ -Al₂O₃ and Co₃O₄ as the only cobalt species when the cobalt loading is 4.8 wt% or above, in

agreement with Co XPS (Figure 65). The smaller peak on the left side of the Co 2p_{3/2} XPS peak (Figure 65) at ~ 796 eV is the 2p_{1/2} peak.

For the ~ 1 wt% Co loaded samples, no distinct pXRD peak is observed but rather a very broad bump is present, which is most likely due to the γ -Al₂O₃ support. The average Co₃O₄ crystallite size estimated from pXRD for all the samples, except 1 wt%, is within the range ~ 9 to 20 nm. The use of a nanostructured support results in a change in Co₃O₄ particle size due to different loadings but when the *commercial* support is used the particle size is unaffected. The particle size dependency on loading varies for each support. Interestingly the use of *40hfat* support results in the smallest and largest average Co₃O₄ size with 4.9 and 18.5 wt% Co loading respectively.

Dark field TEM of *7.7Co/plate-IWI-cal250* in the previous chapter (Figure 49) shows a broad, bi-modal particle size distribution with many particles less than 5 nm and also a range of larger particles 6 to 30 nm in diameter. A similar distribution may be true for other samples in Table 34 to account for the inconsistent average particle size trends.

Table 34. Content and colour of *Co/ γ -Al₂O₃-IWI-cal250* catalysts synthesised by IWI with different loadings on γ -Al₂O₃ supports with different morphologies.

Catalyst	Co loading ^a (wt%)	Na content ^a (wt%)	Colour	Co ₃ O ₄ size ^b (nm)
<i>1.0Co/plate-IWI-cal250</i>	1.0	4.1	White & khaki	No peak
<i>4.6Co/plate-IWI-cal250</i>	4.6	2.3	Dark brown	14.0
<i>7.7Co/plate-IWI-cal250</i>	7.7	2.7	Black	10.5
<i>16.1Co/plate-IWI-cal250</i>	16.1	2.1	Black	15.5
<i>0.9Co/40hfat-IWI-cal250</i>	0.9	1.4	White & khaki	No peak
<i>4.9Co/40hfat-IWI-cal250</i>	4.9	0.9	Dark brown	8.6
<i>9.2Co/40hfat-IWI-cal250</i>	9.2	1.3	Black	15.3
<i>18.5Co/40hfat-IWI-cal250</i>	18.5	1.0	Black	19.5
<i>1.3Co/10hthin-IWI-cal250</i>	1.3	2.3	White & khaki	No peak
<i>4.2Co/10hthin-IWI-cal250</i>	4.2	2.0	Dark brown	12.3
<i>9.7Co/10hthin-IWI-cal250</i>	9.7	1.2	Black	11.2
<i>15.1Co/10hthin-IWI-cal250</i>	15.1	1.9	Black	16.8
<i>5.3Co/commercial-IWI-cal250</i>	5.3	0.6	Black	10.1
<i>8.8Co/commercial-IWI-cal250</i>	8.8	0.3	Black	10.5

^a Calculated from ICP of the digested solid (fresh catalyst).

^b Calculated using the FWHM of the Co₃O₄ peak at ~ 37° (JCPDS 43-1003⁸²) with the Scherrer equation.

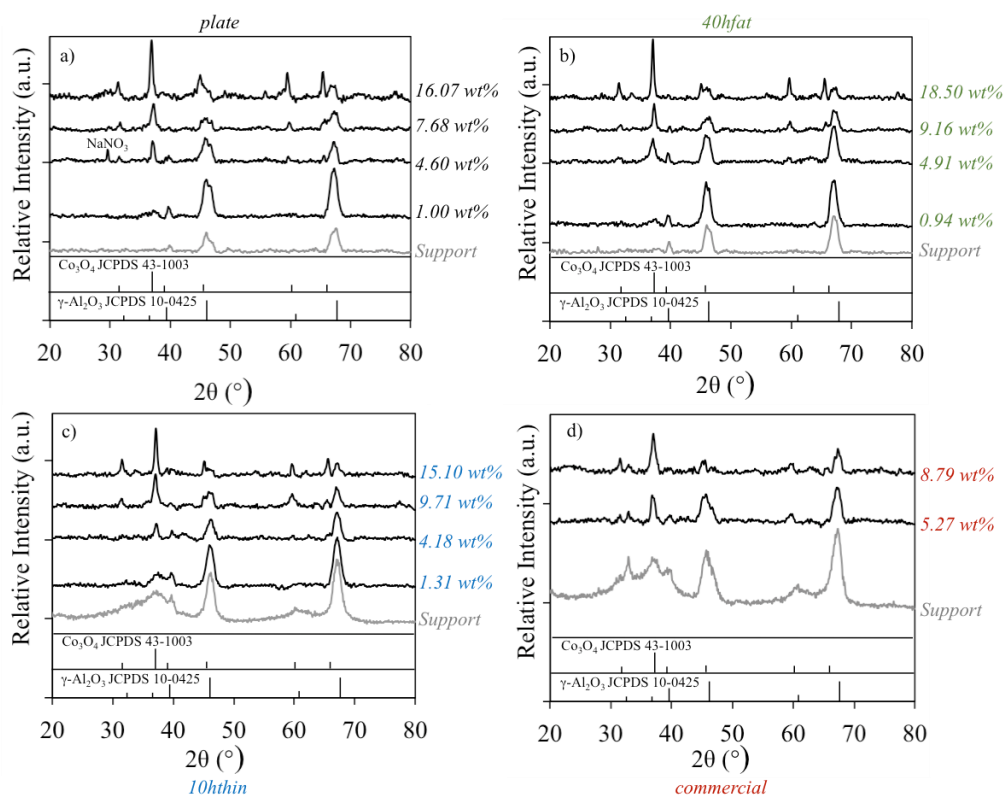


Figure 64. pXRD patterns of $Co/\gamma-Al_2O_3$ -IWI-cal250 catalysts (unreduced) with different loadings on $\gamma-Al_2O_3$ supports with different morphologies. a) *plate*, b) *40hfat*, c) *10hthin* and d) *commercial*. Supports shown in grey.

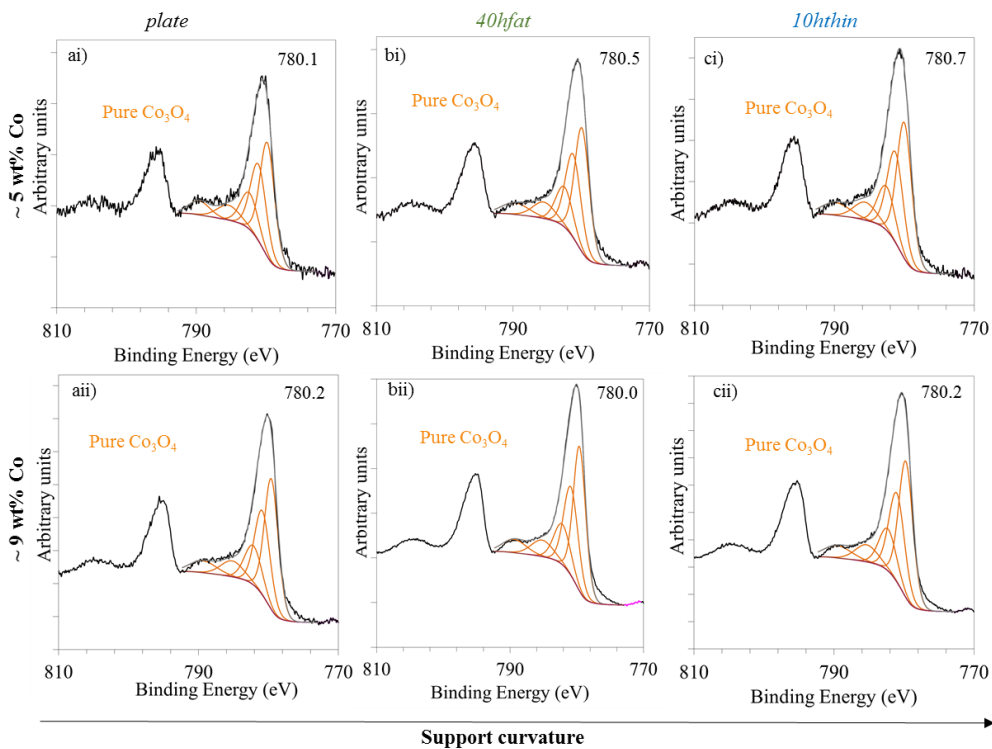


Figure 65. Co 2p XPS spectra for $Co/\gamma-Al_2O_3$ -IWI-cal250 catalysts (unreduced) with different loadings on $\gamma-Al_2O_3$ supports with different morphologies. a) *plate*, b) *40hfat* and c) *10hthin*. Black line = raw trace and orange lines = fitting to Co_3O_4 .

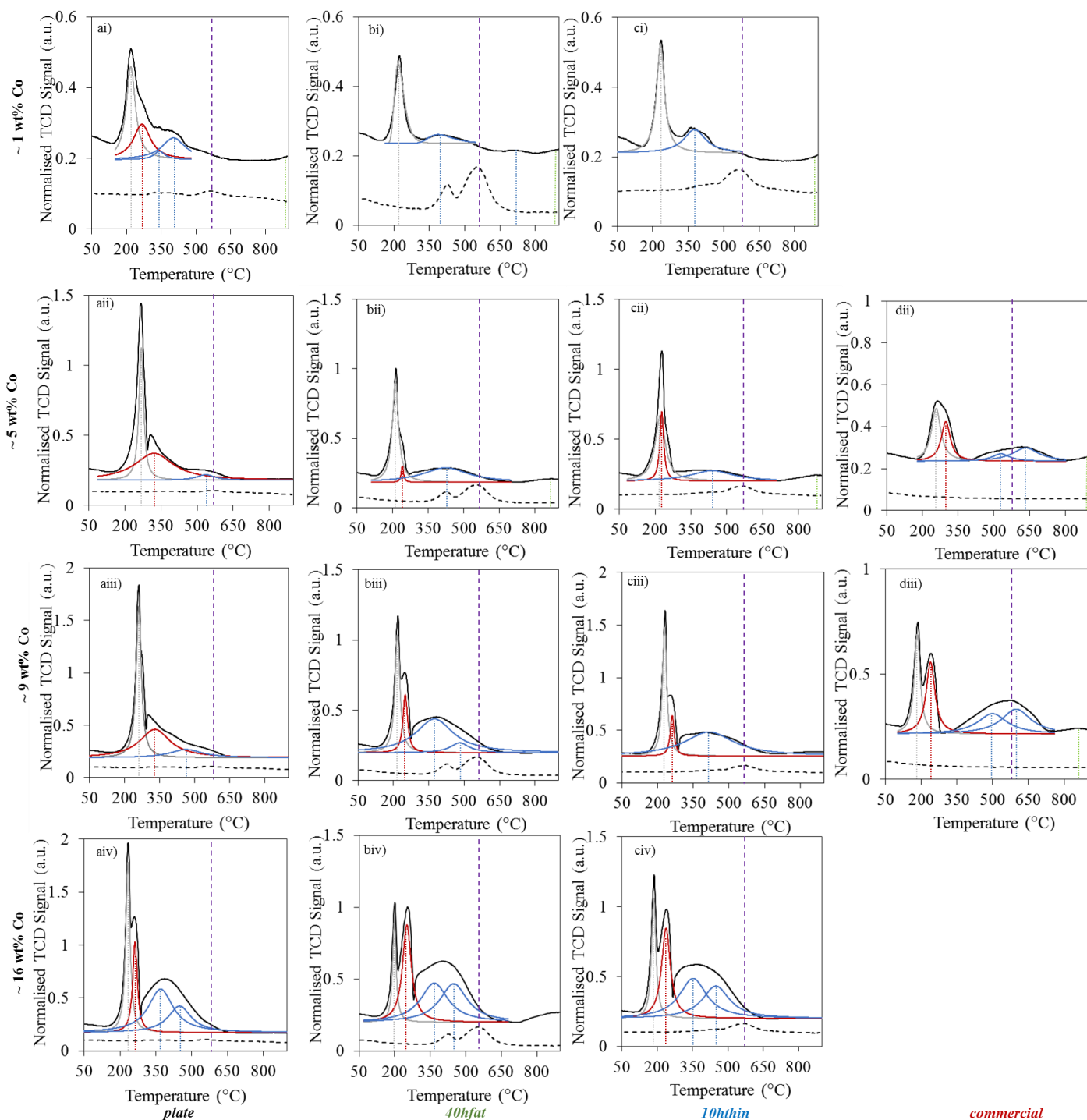


Figure 66. Deconvoluted TPR profiles of *Co/γ-Al₂O₃-IWI-cal250* catalysts with different loadings on γ -Al₂O₃ with different morphologies. a) *plate*, b) *40hfat*, c) *10hthin* and d) *commercial*. Normalised TCD signal = black line, support = black dashed line, 580 °C reduction temperature = vertical purple dashed line, Co³⁺ → Co²⁺ = burgundy curve and Co²⁺ → Co⁰ = blue curve, CoAl₂O₄ → Co⁰ = green curve and removal of impurities = grey curve.

Table 35. TPR peak temperatures of *Co/γ-Al₂O₃-IWI-cal250* catalysts assigned to different chemical processes.

Catalyst	Peak temperature (°C)				Removal of impurities e.g. N or C
	Co ³⁺ → Co ²⁺	Co ²⁺ → Co ⁰		CoAl ₂ O ₄ → Co ⁰	
<i>1.0Co/plate-IWI-cal250</i>	266.9	342.1	403	892.6	218.6
<i>4.6Co/plate-IWI-cal250</i>	321.0	535.8		-	267.7
<i>7.7Co/plate-IWI-cal250</i>	330.0	463.3		-	261.1
<i>16.1Co/plate-IWI-cal250</i>	263.1	370.2	449.7	-	233.4
<i>0.9Co/40hfat-IWI-cal250</i>	-	387.8	723.4	894.8	218.4
<i>4.9Co/40hfat-IWI-cal250</i>	241.4	423.9		868.9	212.0
<i>9.2Co/40hfat-IWI-cal250</i>	250.6	374.1	481.3	-	217.4
<i>18.5Co/40hfat-IWI-cal250</i>	252.0	367.4	449.2	-	198.9
<i>1.3Co/10hthin-IWI-cal250</i>	-	376.9		896.3	233.2
<i>4.2Co/10hthin-IWI-cal250</i>	227.9	438.7		873.0	221.3
<i>9.7Co/10hthin-IWI-cal250</i>	260.9	416.5		-	229.1
<i>15.1Co/10hthin-IWI-cal250</i>	237.4	352.2	449.0	-	185.4
<i>5.3Co/commercial-IWI-cal250</i>	298.7	529.3	633.1	896.6	258.2
<i>8.8Co/commercial-IWI-cal250</i>	239.1	499.0	598.7	864.3	183.0

- Indicates no peak.

The TPR peaks in Figure 66 are colour categorised by the reductive transformation taking place and the peak maxima are shown in Table 35. In some cases, the Co²⁺ → Co⁰ (blue) transformation can be deconvoluted into two peaks, possibly due to the presence of a range of particle sizes with different metal-support interaction strengths. It is interesting that for the lowest loading samples supported on nanorods (*0.9Co/40hfat-IWI-cal250* and *1.3Co/10hthin-IWI-cal250*), no Co³⁺ reduction peaks are identified and thus it is likely that calcination encourages the formation of CoO and CoAl₂O₄ rather than Co₃O₄. An unusually high temperature (723.4 °C) for the second Co²⁺ reduction peak is observed for the *0.9Co/40hfat-IWI-cal250*, which is indicative of the presence of small, strongly interacting particles.

In general, higher cobalt loading is expected to increase the reducibility due to the larger crystallite size,⁵³ which is true for the IWI series if the Co²⁺ reduction temperature is considered as an average of both Co²⁺ reductive processes (CoO and CoAl₂O₄). The formation of CoAl₂O₄ is only observed by TPR for the 1 and 4.8 wt% loading samples when the nanostructured supports are used and with 9.1 wt% loading with the *commercial* support. The observed

CoAl₂O₄ TPR peaks are relatively small, suggesting a low tendency towards CoAl₂O₄ formation.

6.1.2.2 Characterisation of reduced Co/ γ -Al₂O₃-IWI-cal250 catalysts

Reduction of the Co/ γ -Al₂O₃ samples to obtain the active site Co⁰ is carried out at 580 °C, as the TPR profiles suggests Co²⁺ reduction to Co⁰ (blue curves in Figure 66) predominantly takes places below this temperature. However, XPS with *in situ* reduction capabilities (Figure 67) of some of the samples demonstrates that despite the suitable choice of temperature based on TPR, a small proportion of cobalt remains unreduced in the Co²⁺ oxidation state.

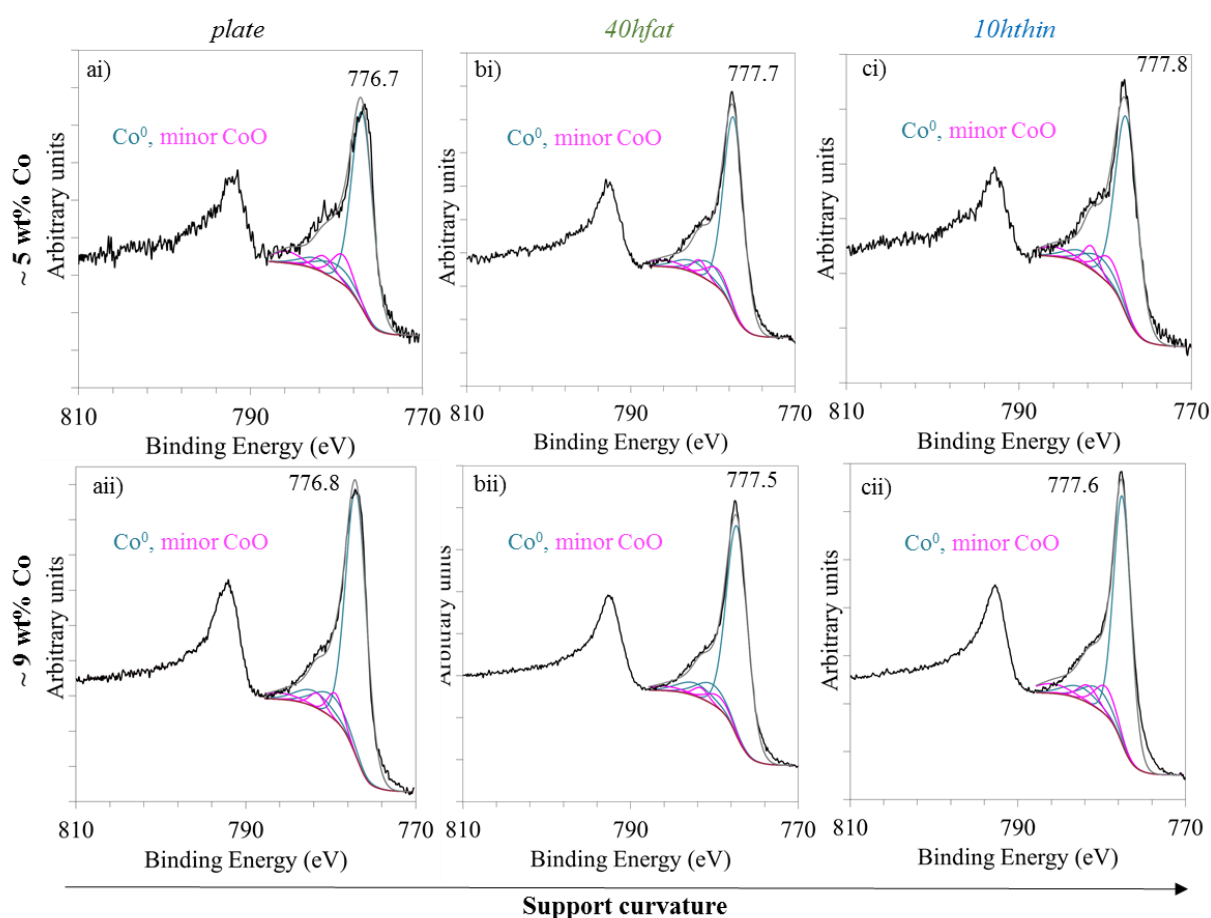


Figure 67. Co 2p XPS spectra for Co/ γ -Al₂O₃-IWI-cal250 reduced in situ at 580 °C on γ -Al₂O₃ supports with different morphologies. a) *plate*, b) *40hfat* and c) *10hthin*. Black lines = raw trace blue lines are fitted to Co⁰ and pink lines are fitted to CoO.

The reducibility, reflected by the proportion of Co⁰ following *in situ* reduction, according to XPS is quantified in Figure 68. For the samples supported on *plate* and *40hfat*, an increase in loading improves the reducibility, contrary to the use of *10hthin* as the support which is unaffected by loading. In general, the reducibility is greater with the *40hfat* support.

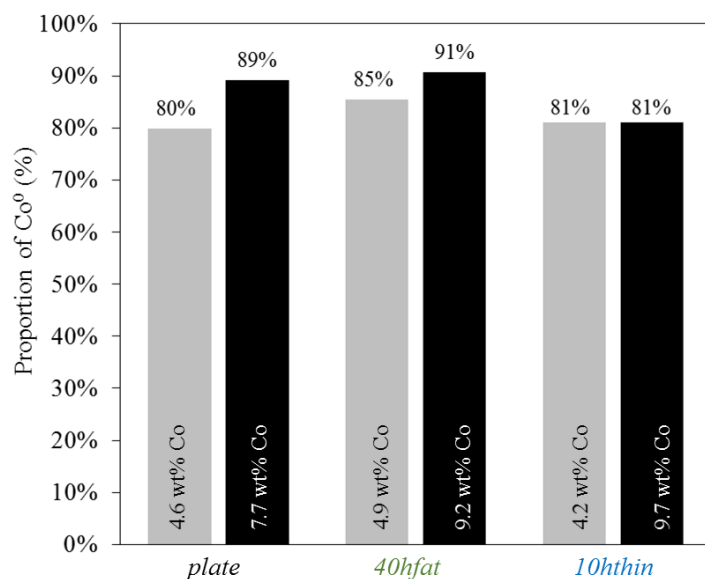


Figure 68. Proportion of Co⁰ from XPS of Co/ γ -Al₂O₃-IWI-cal250 supported on γ -Al₂O₃ with different morphologies (*plate*, *40hfat* and *10hthin*). Reduced *in situ* at 580 °C under H₂ for 4.8 wt% (grey) and 9.1 wt% Co (black) content.

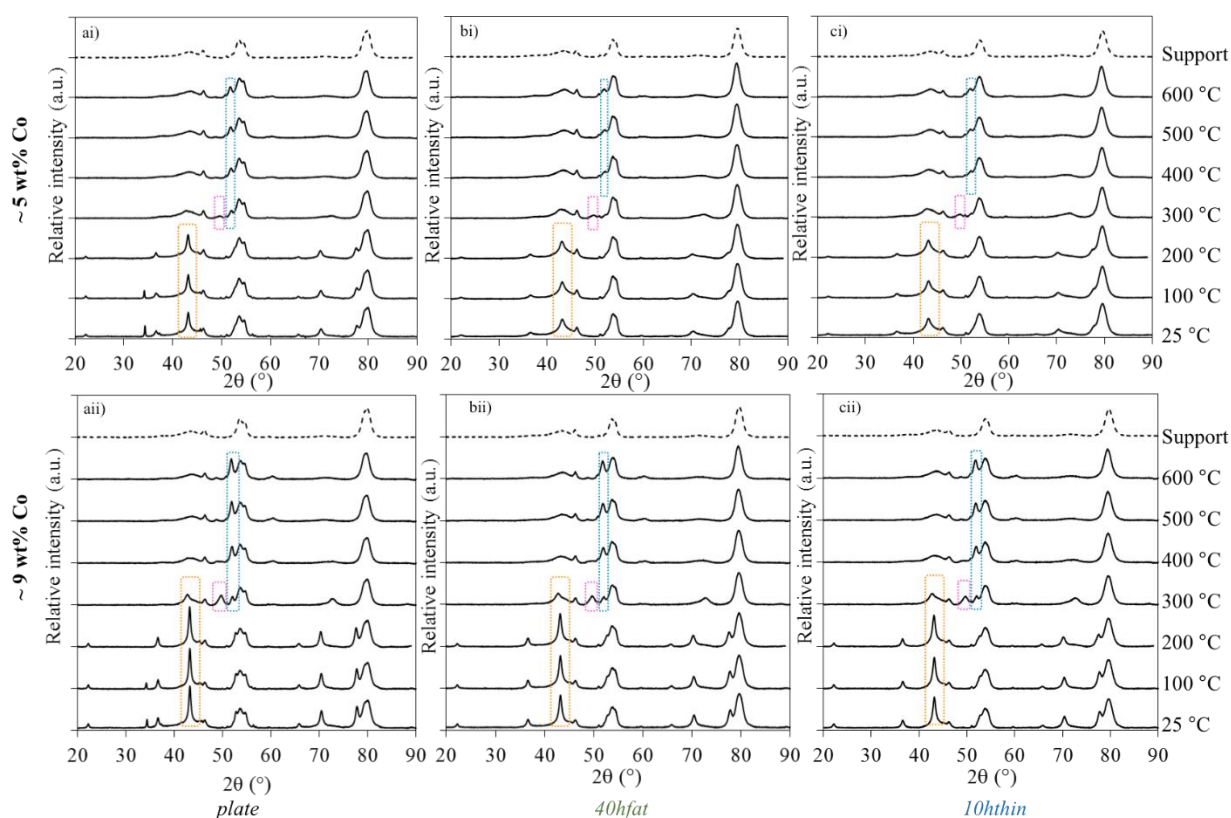


Figure 69. pXRD of Co/ γ -Al₂O₃-IWI-cal250 catalysts (4.8 wt% and 9.1 wt%) reduced *in situ* from room temperature to 600 °C. Supported on nanostructured γ -Al₂O₃ with different morphologies a) *plate*, b) *40hfat* and c) *10hthin*. Peaks selected in orange are Co₃O₄ (43.2°), peaks selected in pink are CoO (49.5°) and peaks selected in blue are Co⁰ (51.8°). The pXRD pattern of the support is shown by the dashed black line. Co X-ray source.

pXRD with *in situ* reduction capability (Figure 69) of these samples highlights the temperature at which Co^{3+} and Co^{2+} reduction takes place. Reduction starts at 300 °C in all samples, which is confirmed by CoO and Co^0 reflections at this temperature. The appearance of CoO and Co^0 takes place simultaneously, in agreement with the deconvoluted TPR peaks (Figure 66). Pure Co^0 is observed at temperatures greater than 400 °C for all supports. For the ~ 5 wt% series, Co^0 appears at 300 °C with the *plate* support but a higher temperature of 400 °C is needed when either of the nanorod supports are used. This suggests a strong interaction of CoO with the nanorod supports at lower cobalt loading. A NaNO_3 pXRD peak is visible at 34.4° in the catalysts supported by *plate* only, which is reduced at 200 °C.

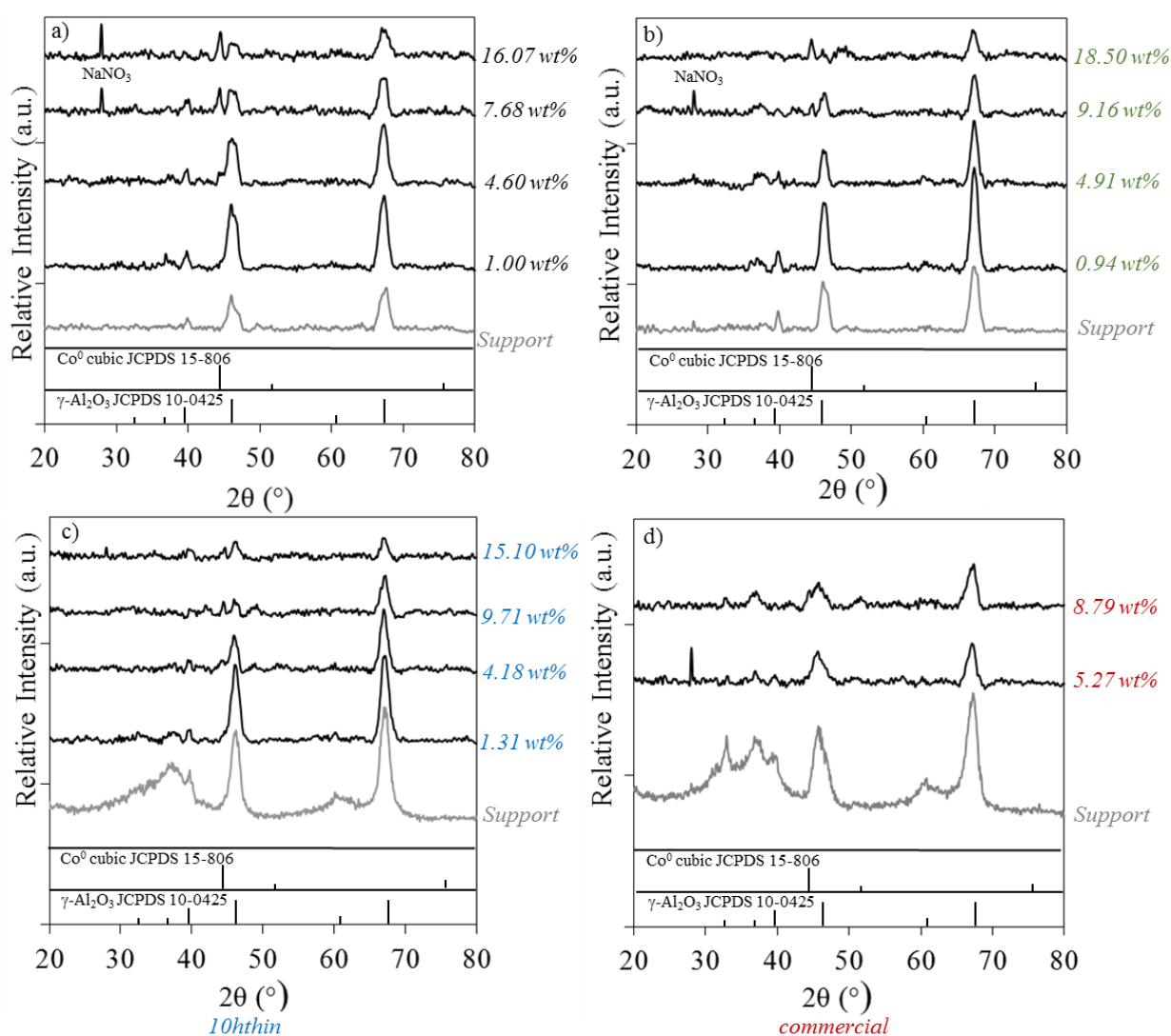


Figure 70. pXRD $\text{Co}/\gamma\text{-Al}_2\text{O}_3\text{-IWI-cal250}$ reduced *ex situ* (580 °C under H_2) with different loadings on $\gamma\text{-Al}_2\text{O}_3$ supports with different morphologies. a) *plate*, b) *40hfat*, c) *10hthin* and d) *commercial*.

As pXRD with *in situ* reduction was not possible for the full set of catalysts, pXRD of the full series was carried on the reduced samples after exposure to air (Figure 70). No Co⁰ peaks for the ~ 1 wt% series are observed, likely due to the low loading or re-oxidation. The pattern for 4.9Co/40hfat-IWI-cal250-red580 and 5.3Co/commercial-IWI-cal250-red580 were repeated in the 40 to 50 2 θ range using a smaller step size but still no Co⁰ peak was visible. The rest of the samples exhibit a peak at ~ 44.4 ° (JCPDS 15-806) assigned to cubic Co⁰.

The particle size calculated by various methods are summarised in Table 36. In order to calculate the particle size from the pXRD data, the peaks at ~ 44 and 46 ° were deconvoluted to obtain a more accurate FWHM value.

Table 36. Average Co⁰ particle size for Co/ γ -Al₂O₃-IWI-cal250 catalysts with different loadings on γ -Al₂O₃ supports with different morphologies

Catalyst	Average Co ⁰ size (nm)		
	pXRD ^{a, b}	pXRD ^{b, c}	TEM ^c
1.0Co/plate-IWI-cal250-red580	n/a	No peak	n/a
4.6Co/plate-IWI-cal250-red580	13.5	12.5	16.0
7.9Co/plate-IWI-cal250-red580	14.4	11.1	n/a
16.1Co/plate-IWI-cal250-red580	n/a	14.5	n/a
0.9Co/40hfat-IWI-cal250-red580	n/a	No peak	n/a
4.9Co/40hfat-IWI-cal250-red580	9.1	No peak	6.1
9.2Co/40hfat-IWI-cal250-red580	11.7	16.5	n/a
18.5Co/40hfat-IWI-cal250-red580	n/a	13.9	n/a
1.3Co/10hthin-IWI-cal250-red580	n/a	No peak	n/a
4.2Co/10hthin-IWI-cal250-red580	9.6	4.4	5.7
9.7Co/10hthin-IWI-cal250-red580	12.4	18.6	n/a
15.1Co/10hthin-IWI-cal250-red580	n/a	13.3	n/a
5.3Co/commercial-IWI-cal250-red580	n/a	No peak	n/a
8.8Co/commercial-IWI-cal250-red580	n/a	17.2	n/a

^a Reduced *in situ* at 580 °C, 45 minutes, 20 NmL·mL⁻¹ pure H₂, 5 °C·min⁻¹.

^b Calculated using the FWHM of the deconvoluted cubic Co peak at ~ 44° (JCPDS 15-806⁸²) with the Scherrer equation.

^c Reduced at 580 °C (45 minutes, 20 NmL·mL⁻¹ pure H₂, 5 °C·min⁻¹) and exposed to air prior to analysis.

In general the average cobalt crystallite size calculated from pXRD is less than 20 nm for all the catalysts synthesised by IWI. The cobalt size calculated from pXRD with *in situ* reduction and by TEM is smaller for the ~ 5 and 9.1 wt% samples supported on nanorods, compared to the *plate* support.

The particle size calculated from the pXRD patterns with *in situ* reduction (Figure 69) are shown in Figure 71 for the 4.8 and 9.1 wt% Co samples supported on nanostructured γ -Al₂O₃. The particle size is usually expected to decrease by 75 % upon reduction of Co₃O₄ to Co⁰ due to the contraction of the crystal lattice.⁵⁵ This rule is only followed by the catalysts supported on *plate* and 4.9Co/40hf_{at}-IWI-cal250-red580, suggesting a degree of sintering may be taking place in the other samples. After reduction, the Co⁰ particle size is constant for all samples within the 300 to 600 °C range analysed, which demonstrates good thermal stability across the studied temperature range.

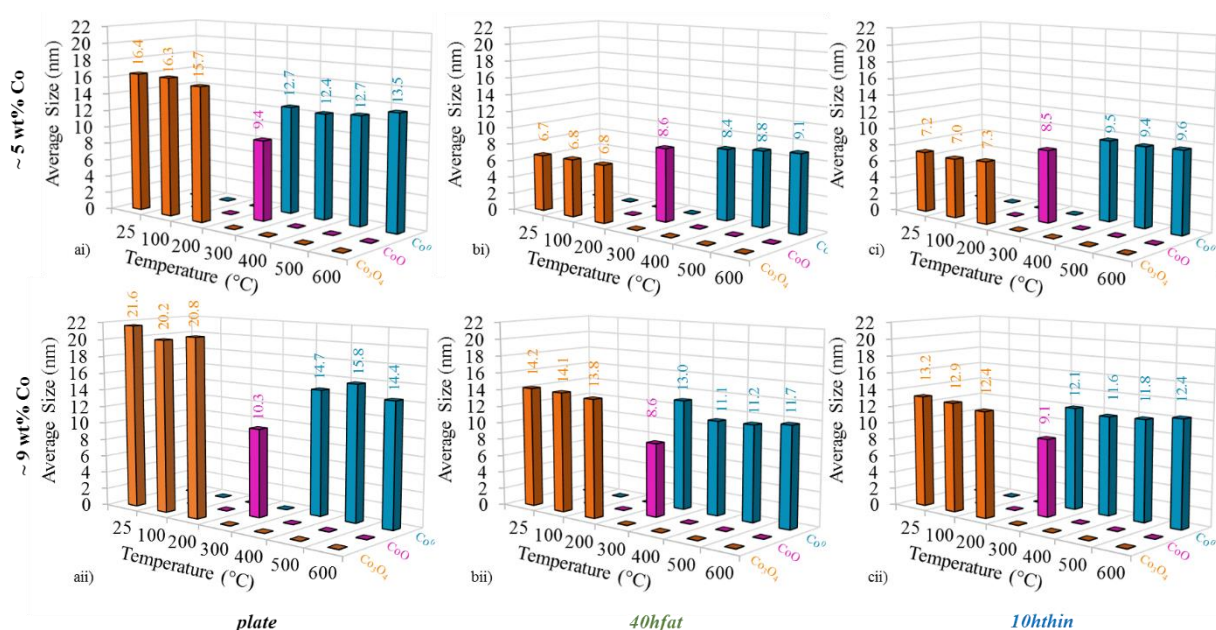


Figure 71. Average particle size for different cobalt species calculated from pXRD with sequential *in situ* reduction up to 600 °C for Co/ γ -Al₂O₃-IWI catalysts. 4.8 wt% and 9.1 wt% Co supported on nanostructured γ -Al₂O₃ with different morphologies a) *plate*, b) *40hf_{at}* and c) *10h_{thin}*. Co₃O₄ (orange), CoO (pink) and Co⁰ (blue).

XPS confirms that the catalysts synthesised by IWI are comprised solely of aluminium, oxygen, cobalt, sodium and carbon without additional contaminants. The sodium is believed to be derived from the use of NaOH in the synthesis of the γ -Al₂O₃ support and carbon arises from the use of reagent grade quality precursors.

Representative TEM micrographs and size distributions of the 4.8 wt% series are shown in Figure 72. When the nanostructured support is used, it is possible to distinguish between Co^0 and the $\gamma\text{-Al}_2\text{O}_3$ support due to its distinct shape. This is not the case with the *commercial* support so bright field TEM of *5.3Co/commercial-IWI-cal250-red580* was not carried out. In agreement with the other particle size estimations summarised in Table 36, the average particle size is smaller when the nanorod supports are used compared to the *plate* morphology.

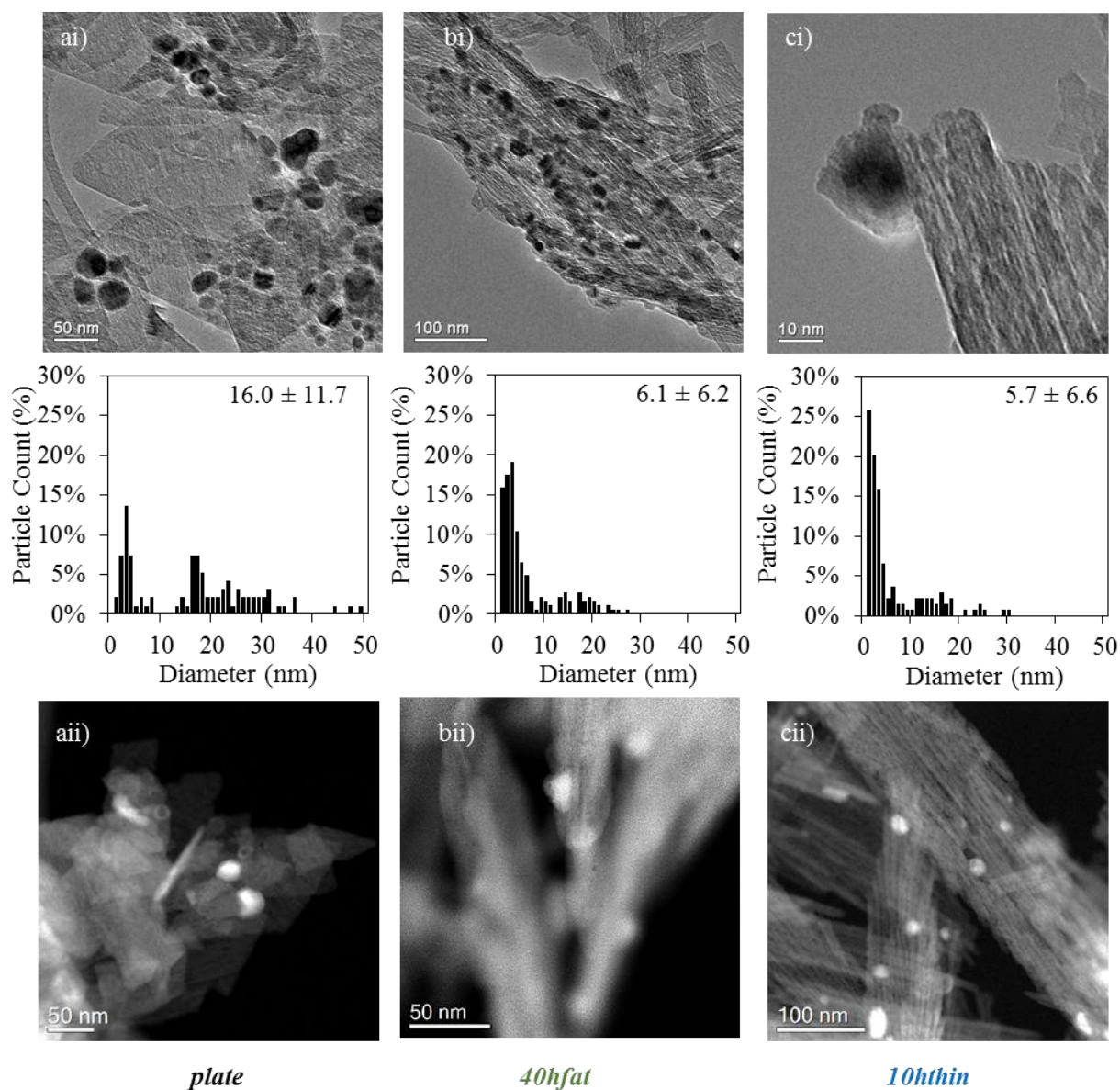


Figure 72. Bright field TEM (i) and HAADF-STEM (ii) micrographs of $\text{Co}/\gamma\text{-Al}_2\text{O}_3\text{-IWI-red580}$. a) *4.6Co/plate-IWI-cal250-red580*, b) *4.9Co/40hfat-IWI-cal250-red580* and c) *4.2Co/10hthin-IWI-cal250-red580*.

6.1.2.3 Catalytic activity of *Co/γ-Al₂O₃-IWI-cal250-red580* catalysts

The NH₃ decomposition catalytic of the *Co/γ-Al₂O₃* catalysts with different loadings synthesised by IWI is shown in Figure 73 and some data is summarised in Table 37. Since all catalysts are stable during three consecutive catalytic runs, the first run data is shown in all cases.

The largest difference in catalytic activity with respect to choice of support is in the ~ 5 wt% loading series. No ~ 1 or 16 wt% Co catalysts were produced on the *commercial* support due to the lack of differences when different nanostructures were used with these loadings.

For the ~ 1 wt% series the activity is the same as the *plate* support without any cobalt present, which is shown by grey diamonds in Figure 73ai, demonstrating the inactivity of these catalysts.

For the catalysts supported on nanostructured γ -Al₂O₃ there is an optimum loading resulting in a maximum apparent rate at 500 °C of 151.1 mol_{H₂}·mol_{Co}⁻¹·h⁻¹ (represented by the TOF at 500 °C value in Table 37) in *4.6Co/plate-IWI-cal250-red580*. However, when the *commercial* support is employed there is no difference in rate when the loading is increased from 5.3 to 8.8 wt% Co. The ~ 5 wt% series is the most interesting, with the *plate* support resulting in the most active catalyst followed by *10hthin*. The activity of the ~ 5 wt% catalysts supported on *40hfat* and *commercial* is significantly lower than the other catalysts in the series but only a small difference in activity is observed between them.

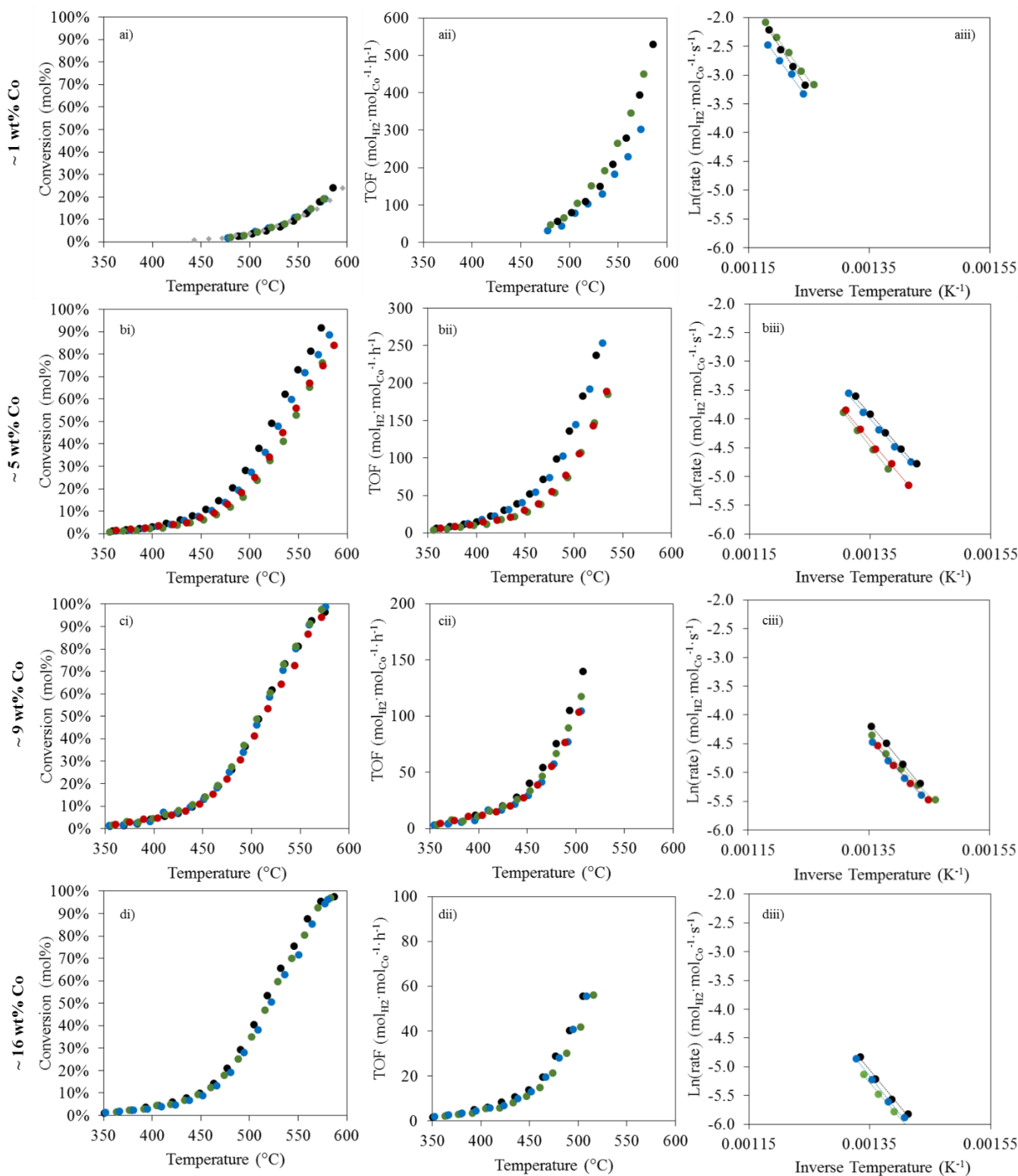


Figure 73. NH_3 decomposition activity of $\text{Co}/\gamma\text{-Al}_2\text{O}_3\text{-IWI-cal250}$ catalysts. Reduced *in situ* at 580 °C under H_2 flow) with different Co loadings supported on different morphologies of $\gamma\text{-Al}_2\text{O}_3$. Plate (◆) shown for reference. i) conversion as a function of temperature, ii) rate of reaction (TOF) relative to reaction temperature up to 50 % conversion and iii) Arrhenius plot. The colour indicates the $\gamma\text{-Al}_2\text{O}_3$ support used: *plate* (black), *40hfat* (green), *10hthin* (blue) and *commercial* (red). a) 1 wt%, b) 5 wt%, c) 9 wt% and d) 16 wt% Co.

Table 37. NH₃ decomposition catalytic data of Co/ γ -Al₂O₃-IWI-cal250 catalysts with different loadings supported on γ -Al₂O₃ with different morphologies (*plate*, *40hfat* and *10hthin*) reduced *in situ* at 580 °C.

Catalyst	E _a (kJ·mol ⁻¹)	TOF @ 500 °C (mol _{H₂} ·mol _{Co} ⁻¹ ·h ⁻¹)	Stability over 3 runs
1.0Co/ <i>plate</i> -IWI-cal250-red580	108.7	76.3	Stable
4.6Co/ <i>plate</i> -IWI-cal250-red580	96.8	151.1	Stable
7.7Co/ <i>plate</i> -IWI-cal250-red580	103.9	120.3	Stable
16.1Co/ <i>plate</i> -IWI-cal250-red580	104.5	50.2	Stable
0.9Co/ <i>40hfat</i> -IWI-cal250-red580	114.5	82.6	Stable
4.9Co/ <i>40hfat</i> -IWI-cal250-red580	110.0	89.3	Stable
9.2Co/ <i>40hfat</i> -IWI-cal250-red580	87.8	104.2	Stable
18.5Co/ <i>40hfat</i> -IWI-cal250-red580	101.7	39.8	Stable
1.3Co/ <i>10hthin</i> -IWI-cal250-red580	117.5	86.8	Stable
4.2Co/ <i>10hthin</i> -IWI-cal250-red580	95.4	138.6	Stable
9.7Co/ <i>10hthin</i> -IWI-cal250-red580	94.8	93.7	Stable
15.1Co/ <i>10hthin</i> -IWI-cal250-red580	108.5	46.5	Stable
5.3Co/ <i>commercial</i> -IWI-cal250-red580	102.2	94.1	Stable
8.8Co/ <i>commercial</i> -IWI-cal250-red580	93.2	97.6	Stable

Characterisation by pXRD and XPS of the fresh catalysts confirms the presence of Co₃O₄ in all the catalysts except the ~ 1 wt% series. These materials likely contain predominantly CoAl₂O₄ based on the absence of Co₃O₄ pXRD peak, TPR peak at > 800 °C and negligible catalytic activity associated to the cobalt species when compared to the *plate* support only. This observation is supported by the fact that these materials do not chemisorb CO after *in situ* reduction at 580 °C and their blue colour after reduction. For the rest of the catalysts, 580 °C is believed to be a suitable reduction temperature based on TPR profiles. However, XPS with *in situ* reduction of the sample highlights that these reduction conditions result in only 80 % reducibility.

A large proportion of the sodium composition is believed to be found on the surface based on comparisons of the composition from ICP and XPS. The sodium content may have implications on the catalytic activity as discussed earlier. Despite extensive attempts to optimise the chemisorption parameters, large cobalt sizes for the catalysts are estimated by CO chemisorption. The discrepancy of the cobalt size calculated from pXRD with and without *in situ* reduction may be due to the thermodynamic re-oxidation of small particles less than 4 nm.⁵³

The largest difference in catalytic activity is observed from the use of different nanostructured support morphologies is within the ~ 5 wt% series. The *in situ* reduction pXRD study (Figure 71) of ~ 5 and 9 wt% series suggests that smaller particles sizes are obtained when nanorod supports are used. However the highest activity at 500 °C in these catalysts of 151.1 mol_{H₂}·mol_{Co}⁻¹·h⁻¹ is reported for 4.6Co/plate-IWI-cal250-red580, not the nanorod supported catalysts in this series. TEM micrographs in Figure 72ai highlight that the *plate* support does not inhibit the mobility of nanoparticles as the average particle size is larger compared to when the nanorod supports are used. By contrast the nanorod support seems to play an important stabilising role by restricting mobility to only permit the mobility along the rod axis to form elongated particles visible in Figure 72bi and Figure 72cii. It may be that the particles initially formed from 5 wt% loading are too large to exploit the stabilisation capability of nanorod as the diameter of the nanoparticle exceeds that of the nanorod support.

The activity of the superior catalyst (4.6Co/plate-IWI-cal250-red580) in this set of catalysts is comparable to the highest reported activity for a cobalt NH₃ decomposition catalyst of 159.1 mol_{H₂}·mol_{Co}⁻¹·h⁻¹.^{55,81}

6.1.3 Discussion of the effect of synthesis method on catalytic activity of Co/γ-Al₂O₃

As discovered in the previous chapter, the choice of synthesis method significantly affects the catalytic activity. This chapter builds upon this understanding by demonstrating that the loading and choice of support γ-Al₂O₃ morphology also plays a significant role in governing the ability to decompose NH₃ at lower temperatures. This observation is clearly highlighted by Figure 74 in which the apparent rate at 500 °C with respect to the cobalt loading is shown for all the Co/γ-Al₂O₃ materials synthesised by NaOH precipitation and IWI. Figure 74 also shows that the cobalt loading varies from the use of different γ-Al₂O₃ supports, particularly at higher loading as shown by the variation in loading along the x-axis.

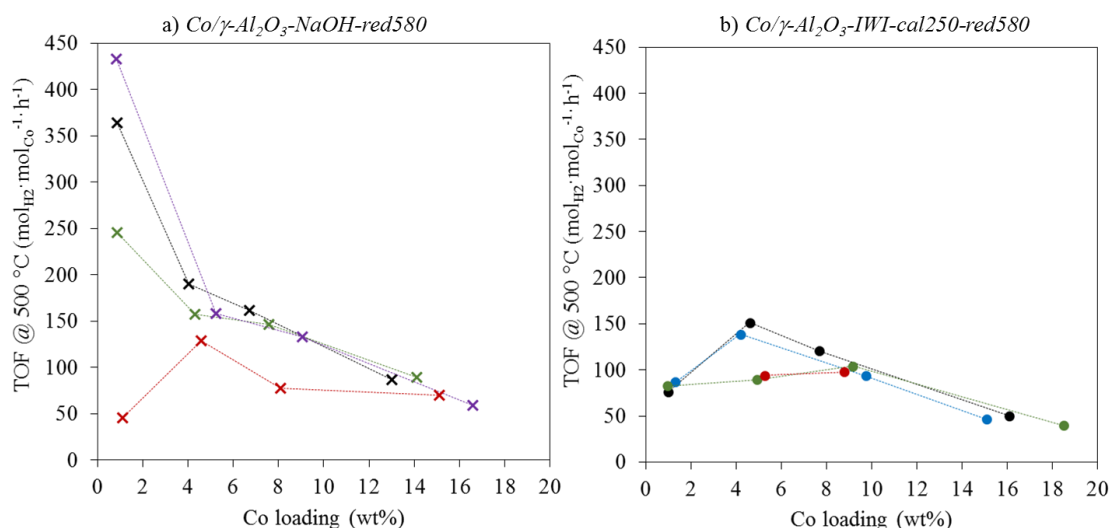


Figure 74. Apparent NH₃ rate of reaction (TOF) at 500 °C with respect to Co loading for Co/γ-Al₂O₃ catalysts synthesised by a) NaOH precipitation (x) and b) IWI (●). The colour indicates the γ-Al₂O₃ support used: *plate* (black), *40hfat* (green), *10hthin* (blue) and *commercial* (red). Reduced *in situ* at 580 °C under H₂ flow.

One of the most significant differences between the two methods is the reducibility. This may be due to the formation of irreducible cobalt aluminate species with the IWI method, as confirmed by TPR and XPS. Cobalt aluminate formation in the IWI series may form as a result of the method itself, the low loading, the 250 °C calcination process or a combination of these factors. By contrast, the 1 wt% series produced by NaOH precipitation does not produce any observable cobalt aluminate based on the TPR profile and the grey catalyst colour after reduction. As such these catalysts exhibit high activities (Figure 74a).

The ~ 1 wt% series synthesised by NaOH precipitation highlights the effect of support morphology on catalytic activity because the samples are expected to contain small particles but no cobalt aluminate. The activity of these materials supported on nanostructured γ-Al₂O₃ significantly exceeds the activity of the best cobalt NH₃ decomposition catalyst in the literature of 159.0 mol_{H₂}·mol_{Co}⁻¹·h⁻¹, which is 5 wt% Co supported on carbon nanotubes containing 4.3 nm cobalt particles.^{55,81} The difference in activity with respect to cobalt loading is shown in Figure 75 with only the catalysts superior to the literature materials and *1.1Co/commercial-NaOH-red580* for comparison. By contrast, the 1 wt% series synthesised herein by the IWI method is considered inactive as they exhibit the same activity as the *plate* support without cobalt. The *1.1Co/commercial-NaOH* catalyst behaves in the same way, exhibiting minimal enhancement of NH₃ decomposition capability. As a result, a typical volcano-type relationship is observed for the series synthesised by IWI and the *commercial* supported NaOH precipitation catalysts, with the optimum activity obtained with ~ 5 wt% activity.

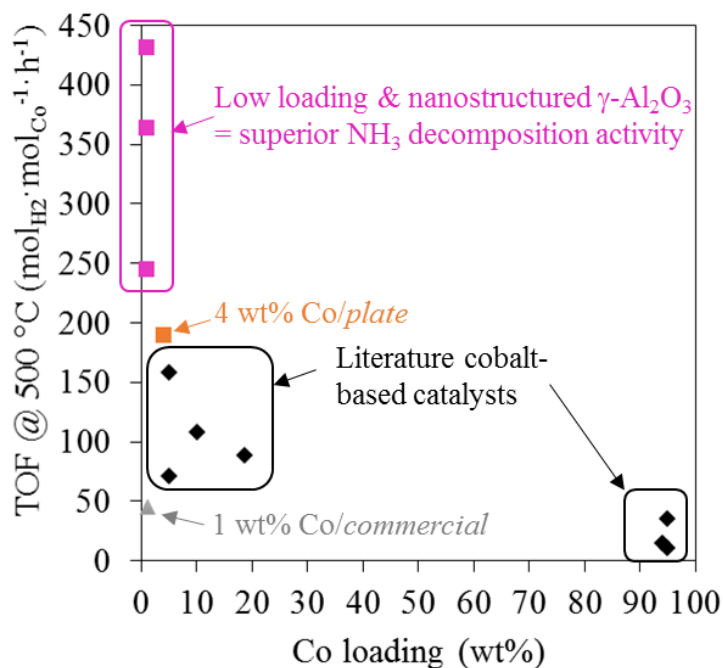


Figure 75. NH₃ decomposition activity of Co/γ-Al₂O₃-NaOH catalysts tested herein compared to the literature. 1.1Co/commercial-NaOH-red580 (grey triangle), 4.0Co/plate-NaOH-red580 (orange square) and pink squares in increasing activity: 0.9Co/180thin-NaOH-red580, 0.9Co/plate-NaOH-red580 and 0.9Co/40hfat-NaOH-red580.

The catalytically active cobalt site for NH₃ decomposition has not been addressed nor elucidated in the literature. The results herein suggest that the active site for cobalt-catalysed NH₃ decomposition is the B3 site on fcc Co (111) since the concentration of these sites drastically increase when the particle size is decreased below 2 nm according to theoretical calculations.⁹⁴ This is supported by the significant enhancement of activity of the 1 wt% Co/γ-Al₂O₃-NaOH catalysts when the support is nanostructured due to the presence of fcc Co particles believed to be very small size based on the fact that they cannot be detected by pXRD or dark field TEM.

Undoubtedly, the effect of sodium must be considered, as sodium has been reported to enhance ruthenium NH₃ decomposition catalysts activity by forming active Ru^{δ-} 163 and the sodium concentration is higher in the NaOH precipitation series (> 6 wt%) compared to the IWI catalysts (< 4 wt%). However, for loadings greater than 5 wt% when nanostructured γ-Al₂O₃ is employed as the support there is only a small difference in catalytic activity between the two methods, which may be due to the difference in calcination procedures. In addition, unlike for Ru^{δ-}, there is no information in the literature confirming or denying the enhanced catalytic activity of Co^{δ-} for NH₃ decomposition and the results in Section 5.2.2 confirm Co⁰ to be the active species.

The biggest difference in catalytic activity of all the materials is seen across the 1 wt% series synthesised by NaOH decomposition but the activity trend does not follow the sodium content order. For example, *0.9Co/plate-NaOH* contains 6.1 wt% Na, equivalent to 6.1 wt% sodium in *1.1Co/commercial-NaOH*, yet these two catalysts exhibit very different NH₃ decomposition activities. Thus, there must be other factors responsible for the observed difference, which are probably size and the degree of stabilisation provided by the support.

For the 1 wt% series synthesised by NaOH decomposition series, the absence of cobalt pXRD peaks and particles by dark field TEM makes particle size evaluation challenging. However, it is likely that the low loading permits the formation of small particles, which are effectively stabilised as a function of support morphology. The difference in activity of the 1 wt% series synthesised by NaOH precipitation highlights that not only is the support morphology significant for nanoparticles stabilisation, but also that the nanorod diameter plays an important role. This effect is represented in Figure 76 for increasing nanorod support diameter and nanoparticle diameter. For example, *0.9Co/180thin-NaOH* is visualised as the case where ratio of the nanoparticle diameter (P) to the nanorod diameter (R) is $P:R < 1$ in the bottom left corner of Figure 76, whereas *0.9Co/40hfat-NaOH* is the case $P:R \lll 1$ in the bottom right corner. The difference in support curvature delivers a different degree of stabilisation, resulting in superior catalytic activity in *0.9Co/180thin-NaOH*. In fact, γ -Al₂O₃ nanorods contain inter-crystallite pores¹⁰⁰, which may provide some stabilisation for *0.9Co/40hfat-NaOH* since $P:R \lll 1$ (bottom right in Figure 76) and thus the curved surface is unlikely to play an important role in this particular case.

The difference in activity observed in the 5 wt% series synthesised by IWI is not as exaggerated as that of the 1 wt% NaOH precipitation materials as the higher loading in the former encourages the formation of larger particles. Consequently, the high aspect ratio nanorod diameter of 8 nm is less capable of stabilising the nanoparticles during reduction and catalyst testing in *4.2Co/10hthin-IWI-cal250*. This is depicted in the top right image in Figure 76, resulting in a similar catalytic activity as the use of *plate* support (*4.6Co/plate-IWI-cal250*). A difference in activity in the 1 wt% IWI series is not observed due to the formation of inactive cobalt aluminate.

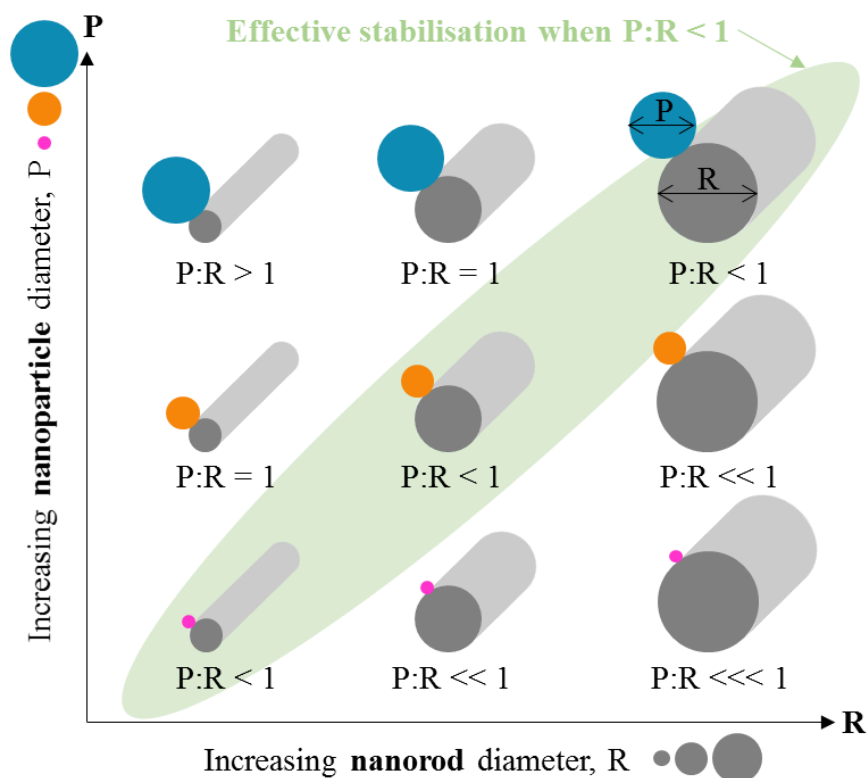


Figure 76. Stabilisation by nanorods related to their diameter (R) and the size of the nanoparticle (P).

With higher cobalt loadings (> 4 wt%) there are less observable differences in activity resulting from the choice of support morphology. In these cases, pXRD predicts average particle sizes less than 20 nm from IWI synthesis or 15 to 30 nm from the NaOH precipitation method. These findings are in agreement with Bezemer *et al.*⁹² who report larger cobalt particles with precipitation (~ 30 nm) method compared to IWI (8 to 16 nm). The higher loadings used herein also suffer from the formation of unsupported, hexagonal cobalt compounds by NaOH precipitation (Figure A102, Appendix), possibly because the rate of precipitation is too high at these solution concentrations, which leads to bulk precipitation rather than local precipitation at the support surface.

The most active catalyst tested herein is produced by the NaOH precipitation method with 1 wt% Co. The unprecedented superior catalyst activity of *0.9Co/180thin-NaOH* is attributed to the expected small cobalt particles formed by this method that are small enough to be effectively stabilised by the curved nanorod support. By contrast, the other supports are less effective at stabilising the small nanoparticles due to their morphology. When the loading is increased above 4.8 wt% Co, the resulting nanoparticle that forms may be too large for the nanorod supports to stabilise relative to their diameter, which is 8 nm (*180thin* or *10hthin*) or 20 nm (*40hfat*) on average. Thus the relative nanoparticle to nanorod diameter ratio is crucial

and needs to be optimised in order to observe the benefits of the nanorod support. The results herein suggest that larger nanorods are needed to stabilise cobalt loadings greater than or equal to 4.8 wt%. Appropriate selection of rod diameter, method and loading can lead to the formation of small particles which can be effectively stabilised by the curvature of the nanorod.

6.1.4 Thermal stability of Co/ γ -Al₂O₃ catalysts

The NaOH precipitated catalysts supported on nanostructured γ -Al₂O₃ and all the IWI catalysts are stable on three consecutive catalyst runs up to 580 °C. By contrast, the NaOH precipitation catalysts supported on *commercial* γ -Al₂O₃ deactivate during testing. Thus, a series of NH₃ decomposition experiments were carried out in which the maximum temperature was increased for each successive run from 580 to 670 to 750 °C, in order to further probe the thermal stability of the catalysts.

The 9.1 wt% catalysts (theoretical content) synthesised by IWI (calcined at 250 °C) and NaOH precipitation with each of the four classes of support morphology (flat, high curvature nanorod, low curvature nanorod and bulk) were studied for their thermal stability. In addition, pXRD spectra of the catalysts after exposure to 750 °C temperature conditions were recorded in order to determine the final size. The results are summarised in Table 38.

In general, all the catalysts tested for their high temperature thermal stability exhibit a relatively small degree of deactivation after 670 °C. However, a larger degree of deactivation is observed after 750 °C reaction temperature, particularly for the catalysts synthesised by NaOH precipitation. Specifically, *8.1Co/commercial-NaOH-red580* deactivates by 44.7 % after 750 °C exposure. By contrast, most of the catalysts synthesised by IWI deactivate by only 13 to 17 % but *9.2Co/40hfat-IWI-cal250-red580* is less stable, deactivating by 30 %.

Table 38. Change in NH₃ decomposition activity and Co⁰ crystallite size of Co/ γ -Al₂O₃ after exposure to 750 °C.

Catalyst	Change in TOF @ 500 °C ^{a, b} (%)		Average Co ⁰ size ^{a, c} (nm)	
	After 670 °C	After 750 °C	580 °C	750 °C
<i>6.7Co/plate-NaOH-red580</i>	-8.0	-31.3	15.0	16.8
<i>7.6Co/40hfat-NaOH-red580</i>	-10.7	-37.1	19.1	15.9
<i>9.1Co/180thin-NaOH-red580</i>	-9.6	-36.2	18.1	18.3
<i>8.1Co/commercial-NaOH-red580</i>	-16.7	-44.7	19.3	20.4
<i>7.9Co/plate-IWI-cal250-red580</i>	-8.1	-13.7	11.1	13.6
<i>9.2Co/40hfat-IWI-cal250-red580</i>	-15.4	-30.4	16.5	17.6
<i>9.7Co/10hthin-IWI-cal250-red580</i>	-1.3	-16.8	18.6	9.5
<i>8.8Co/commercial-IWI-cal250-red580</i>	-1.0	-17.4	17.2	15.2

^a All materials are pre-reduced at 580 °C (5 °C·min⁻¹, 45 min) under H₂ flow.

^b (-) indicates deactivation.

^c Calculated using the FWHM of the deconvoluted cubic Co peak at ~ 44° (JCPDS 15-806) with the Scherrer equation. Samples are exposed to air prior to pXRD.

There is no significant observable increase in crystallite size according to pXRD spectra when comparing sizes of samples reduced at 580 or 750 °C. In some cases, such as *7.6Co/40hfat-NaOH-red580*, *9.7Co/10hthin-IWI-cal250-red580* and *8.8Co/commercial-IWI-cal250-red580* the crystallite size determined by pXRD decreases.

In sections 6.1.1 and 6.1.2, the only catalysts that were found to be unstable during the consecutive catalytic tests up to 580 °C were the series synthesised by NaOH precipitation supported on *commercial*. The high temperature stability tests show that all the ~ 9 wt% catalysts deactivate to some extent after 670 °C and 750 °C reaction conditions, with a negligible deactivation after 670 °C in some catalysts such as *9.7Co/10hthin-IWI-cal250-red580* and *8.8Co/commercial-IWI-cal250-red580*. Following the same observation as the 580 °C tests, in general the NaOH precipitation synthesised catalysts deactivate to a greater extent than those by IWI. This may be due to the absence of a calcination step with NaOH precipitation to enhance the metal-support interaction. However, for this particular catalyst (*6.8Co/plate-NaOH-cal250-red580*), Section 5.2.1 highlighted that calcination led to poor stability with the TOF at 500 °C decreasing by 17 % after a standard three-run catalytic test.

For both synthesis methods, the most stable catalyst after high temperature thermal stability tests (Table 38) are those supported on nanostructured *plate* γ -Al₂O₃. It is likely that the 16 to 20 nm particle (P) sizes formed at high loading (9 wt%) are too large to be effectively stabilised

by the nanorod supports whose average diameters (D) are 8 or 20 nm for *10hthin/180thin* (P:R > 1) and *40hfat* (P:R = 1), respectively, in relation to the nanorod stabilisation theory proposed in Figure 76. The size of these cobalt particles supported on the nanorods is similar to those supported on *commercial* γ -Al₂O₃ (17 to 19 nm), suggesting that minimal additional stability is added by using a nanostructured support when the loading is high (9 wt%). The function of the *plate* support, on the other hand, is not limited by the size of the particle formed and it can appear to offer some stabilisation to large particles 11 to 15 nm in diameter, with only ~ 2 nm increase in size after 750 °C exposure.

Another key difference between using nanostructured supports with different morphology is the exposure of different crystal planes, which may be more or less effective at providing an anchoring site for cobalt nanoparticles. For example computational studies by Digne *et al.*^{42,164} shows the difference in vacant, available sites for the low energy (110), (100) and (111) γ -Al₂O₃ surfaces. The lowest energy γ -Al₂O₃ plane is (110), which therefore dominates the surface of 2D structures such as the *plate* support.⁴² By contrast, γ -Al₂O₃ is made up of a combination of different surfaces including the lowest energy surfaces (110), (100) and (111) as well as possible small contributions from higher energy surfaces.⁴²

6.2 Fisher-Tropsch synthesis

Based on the NH_3 decomposition catalytic data of the $\text{Co}/\gamma\text{-Al}_2\text{O}_3$ catalysts produced by IWI, 4.8 and 9.1 wt% Co support on nanostructured $\gamma\text{-Al}_2\text{O}_3$ were tested for FTS activity as they contain sufficient cobalt content to show activity for FTS. The $\text{Co}/\gamma\text{-Al}_2\text{O}_3$ series produced by NaOH precipitation were not tested for FTS due to their high sodium content (Table 31), which has been reported to poison FTS catalysts.^{90,98,165}

FTS selectivity, however, is not believed to be related to sodium content, but rather support pore size.¹⁶⁵ Catalysts for FTS are often described by their CH_4 selectivity as its formation is undesirable but regrettably common. An effective FTS catalyst produces ~ 4 mol% CH_4 .

Industrial cobalt catalysts for FTS are reduced at 425 °C because this temperature is reportedly effective for the high metal loadings (15 to 30 wt%) usually employed in industrial catalysts.⁶⁰ As such the $\text{Co}/\gamma\text{-Al}_2\text{O}_3$ catalysts were reduced at 425 °C, which is lower than the 580 °C reduction temperature used prior to NH_3 decomposition.⁵⁹

6.2.1 Effect of sodium on FTS activity of $\text{Co}/\gamma\text{-Al}_2\text{O}_3$ -IWI-cal250

The sodium content of 4.6Co/plate-IWI-cal250 and 7.7Co/plate-IWI-cal250 (2.3 and 2.7 wt% respectively) is sufficient to result in a poor FTS activity as shown in Figure 77. Here the sodium content is three times lower than the analogous NaOH precipitation catalysts, highlighting the unsuitability of $\text{Co}/\gamma\text{-Al}_2\text{O}_3$ synthesised by NaOH precipitation for FTS.

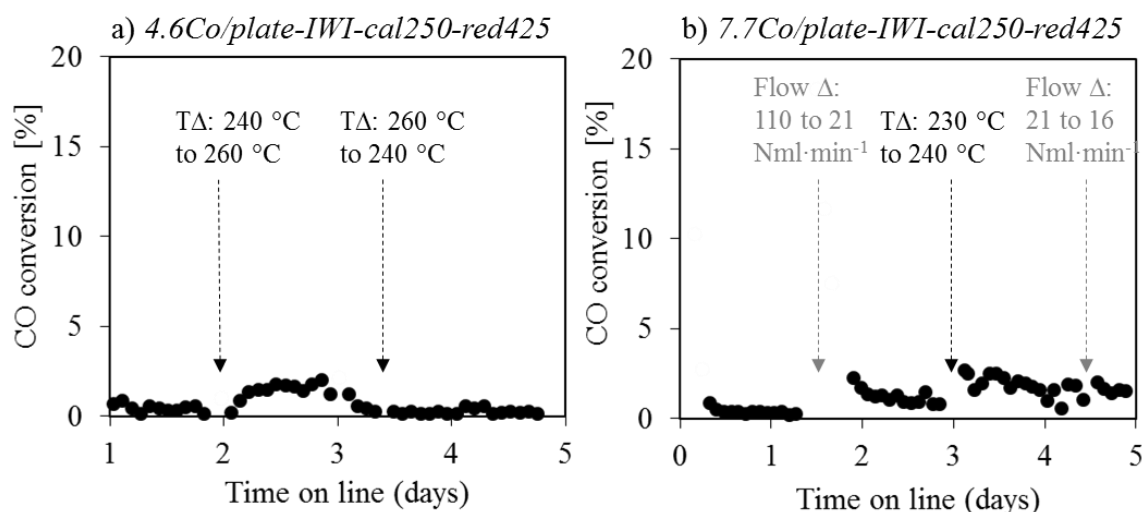


Figure 77. FTS activity of $\text{Co}/\gamma\text{-Al}_2\text{O}_3$ -IWI-cal250. a) 4.6Co/plate-IWI-cal250-red425 and b) 7.7Co/plate-IWI-cal250-red425. Samples were pre-reduced *in situ* at 425 °C, 1 °C·min⁻¹, for 6 hours at 40 mL·min⁻¹ H_2 .

As shown in Figure 77, increase in synthesis temperature or decrease in flow rate does not significantly affect the catalytic activity of *4.6Co/plate-IWI-cal250* and *7.7Co/plate-IWI-cal250*. The activity remains below 3 mol% conversion under all the tested conditions. As the activity of *4.6Co/plate-IWI-cal250* and *7.7Co/plate-IWI-cal250* is so low, the selectivity data of these catalysts is not evaluated in the following sub-sections.

XPS of *4.6Co/plate-IWI-cal250* and *7.7Co/plate-IWI-cal250* highlights a very high concentration of sodium present on the surface, higher than ICP calculation. Sodium on the surface may lead to possible blockage of the active Co^0 site.

6.2.2 Activity and selectivity of *Co/ γ -Al₂O₃-IWI-cal250* catalysts

The FTS activity and selectivity of *4.9Co/40hfat-IWI-cal250-red425* and *4.2Co/10hthin-IWI-cal250-red425* are summarised in Figure 78. After 24 hours of testing, the reaction temperature was increased from 240 °C to 260 °C and then returned to 240 °C after 48 hours of testing, as annotated in Figure 78. All other reaction parameters remained constant throughout the test: 30 $\text{Nml}\cdot\text{min}^{-1}$ inlet flow rate, 17 bar pressure and 1.7 H_2 :1CO molar ratio.

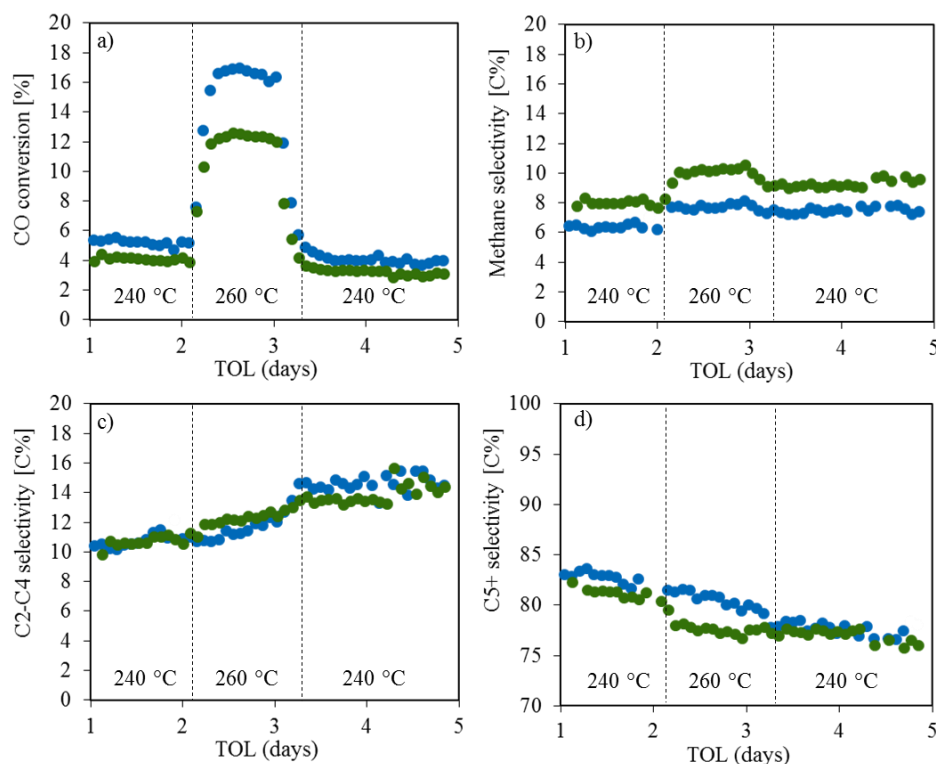


Figure 78. FTS activity and selectivity of *4.9Co/40hfat-IWI-cal250-red425* (green) and *4.2Co/10hthin-IWI-cal250-red425* (blue). a) CO conversion, b) CH₄ selectivity, c) C₂-C₄ selectivity and d) C₅₊ selectivity. Constant conditions: 30 $\text{Nml}\cdot\text{min}^{-1}$ inlet flow rate, 17 bar pressure and 1.7 H_2 :1CO molar ratio. Samples were pre-reduced *in situ* at 425 °C, 1 °C $\cdot\text{min}^{-1}$, for 6 hours at 40 $\text{mL}\cdot\text{min}^{-1}$ H_2 . TOL = time on line.

The rate of CO conversion in Figure 78 is constant during the periods of consistent conditions. The activity of *4.2Co/10hthin-IWI-cal250-red425* increases from 5.5 % to 17 % when the temperature is increased to 260 °C and then decreases to 4.5 % when the temperature is returned to 240 °C. After 48 additional hours of testing, the activity decreases to 4 %, stable within the experimental error.

A smaller improvement in FTS activity is observed for *4.9Co/40hfat-IWI-cal250-red425* following the increase in temperature during the catalytic test from 4 to 12.5 %. After the temperature is returned to 240 °C, activity is decreased slightly to 3.5 % and after two more days on line at constant temperature the activity decreases to 3 %.

The methane selectivity for both catalysts is below ~ 11 % under the conditions tested, but an effective FTS catalyst usually produces less than 4 % CH₄. Note that when the temperature is increased, the methane selectivity increases for *4.9Co/40hfat-IWI-cal250-red425* from 10 to 12 % compared to 6 to 7.5 % for the more active catalyst, *4.2Co/10hthin-IWI-cal250-red425*. A similar increase in C₂-C₄ selectivity is also observed from exposure to higher reaction temperature conditions. The increase in temperature results in a 4 % associated decrease in C₅₊ selectivity for *4.2Co/10hthin-IWI-cal250-red425* and a 5 % decrease for *4.9Co/40hfat-IWI-cal250-red425*. Overall, *4.2Co/10hthin-IWI-cal250-red425* is more active and selective than *4.9Co/40hfat-IWI-cal250-red425*.

The FTS testing results of higher cobalt loaded samples (*9.16Co/40hfat-IWI-cal250-red425* and *9.71Co/10hthin-IWI-cal250-red425*) are shown in Figure 79. After 60 hours of testing, the flow rate was decreased from 110 to 21 Nml·min⁻¹ and at the beginning of the second day the reaction temperature was increased from 230 °C to 240 °C. After 96 hours (beginning of day 4), the flow rate was decreased again to 16 Nml·min⁻¹ whilst maintaining the other initial reaction parameters: 17 bar pressure and 1.7H₂:1CO.

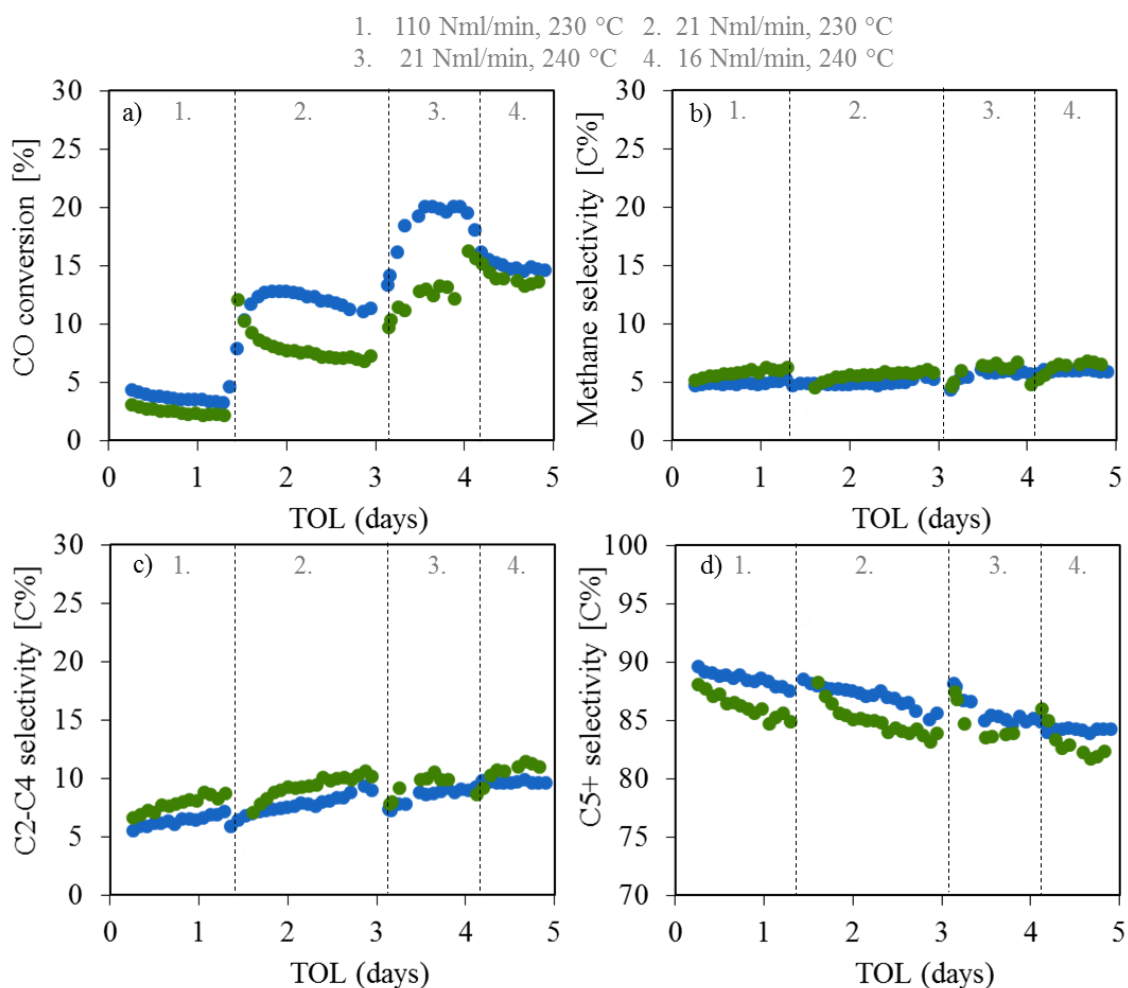


Figure 79. FTS activity and selectivity of *9.2Co/40hfat-IWI-cal250-red425* (green) and *9.7Co/10hthin-IWI-cal250-red425* (blue). a) CO conversion, b) CH₄ selectivity, c) C₂-C₄ selectivity and d) C₅₊ selectivity. Constant conditions: 17 bar pressure and 1.7H₂:1CO. Samples were pre-reduced *in situ* at 425 °C, 1 °C·min⁻¹, for 6 hours with 40 mL·min⁻¹ H₂. Variable conditions during testing are segmented as follows: 1 = 110 Nml/min, 230 °C; 2 = 21 Nml/min, 230 °C; 3 = 21 Nml/min, 240 °C and 4 = 16 Nml/min, 240 °C. TOL = time on line.

The FTS activity in Figure 79a demonstrates that the efficiency of both catalysts is enhanced by decreasing the flow rate to 21 Nml·min⁻¹ and increasing the reaction temperature to 240 °C. The extent of the increase in activity is higher with *9.7Co/10hthin-IWI-cal250-red425* than *9.2Co/40hfat-IWI-cal250-red425*, which exhibit maximum 20 mol% and 12.5 mol% conversion respectively.

In terms of selectivity, both catalysts show excellent low methane selectivity ~ 5 % (Figure 79b). In general, selectivity is independent of reactor temperature here and thus conversion. However, during time on line FTS testing, the C₂-C₄ selectivity increases as C₅ selectivity decreases by the same amount, ~ 5 %, suggesting some form of deactivation is taking place during testing.

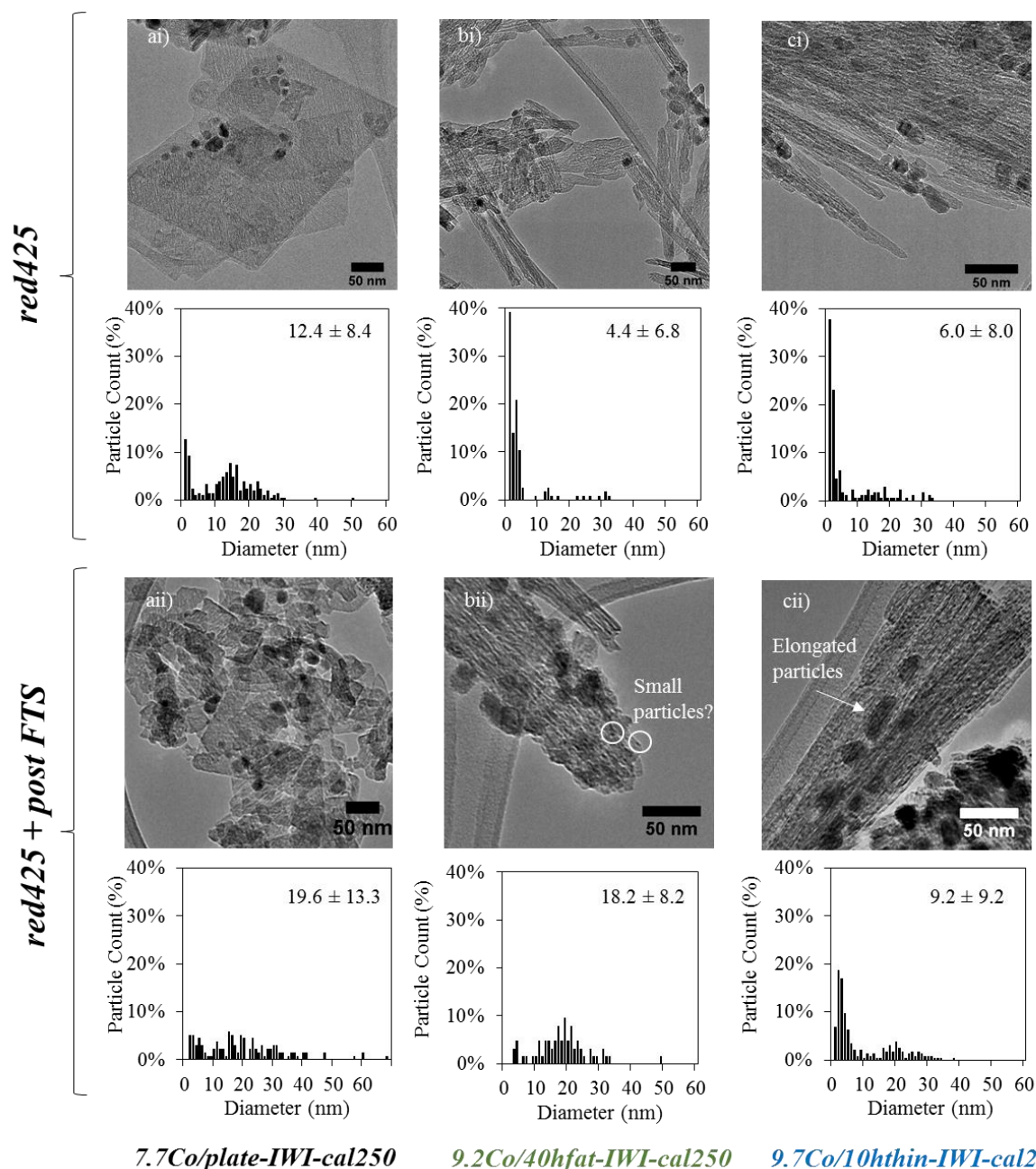


Figure 80. TEM micrographs of Co/ γ -Al₂O₃-IWI catalysts after i) reduction *ex situ* at 425 °C and ii) FTS testing. a) 7.7Co/plate-IWI-cal250, b) 9.2Co/40hfat-IWI-cal250-red425 and c) 9.7Co/10hthin-IWI-cal250-red425.

TEM micrographs of the ~ 9 wt% Co catalysts supported on nanostructured γ -Al₂O₃ after reduction at 425 °C (Figure 80i) and after a five day FTS test (Figure 80ii) were acquired. After reduction, all the catalysts show a fairly broad particle size distribution with particles from 1 to 30 nm in diameter. However, the use of the *plate* support results in a lower proportion of small 1 to 2 nm cobalt particles of ~ 22 % compared to at least 53 % when a nanorod support is used.

After FTS, the spent catalyst supported on *plate* shows a broadening of particle size distribution up to 30 nm whereas the catalysts supported on nanorods do not. The latter do, however, decrease their proportion of small particles in exchange for larger 20 nm particles. Based on the average particle size and the size distribution, *10hthin* support is the most effective at stabilising small cobalt nanoparticles during FTS catalytic testing. The presence of cobalt nanoparticles predominantly less than 7 nm (P) in *9.7Co/10hthin-IWI-cal250-red425* (Figure 80cii) after FTS highlights the stabilisation effect offered by the highly curved nanorod surface (R) as P:R < 1. Furthermore, TEM imaging of this sample shows the presence of particles elongated along the length of the nanorod (Figure 80i), confirming that the mobility of the particles have been restricted in all directions except along the rod length. The elongated particles may play a part in the enhanced activity observed for this sample (Figure 79a) as these strained particles are believed to exhibit superior activity, as reported for CO oxidation.¹⁶⁶

It is likely that the catalysts are predominantly reduced by 425 °C based on the TPR profiles (Figure 66) and the pXRD study with *in situ* reduction (Figure 69). All the catalysts tested for FTS exhibit similar TPR profiles. However, the 5 wt% series exhibit small high temperature cobalt aluminate TPR peaks with a similar ratio.

6.2.3 Discussion of the effect of loading and support morphology on FTS activity, selectivity and stability

For the ~ 5 wt% catalysts, *4.2Co/10hthin-IWI-cal250-red425* is more active than *4.9Co/40hfat-IWI-cal250-red425* despite slightly lower loading. The same trend is also observed in the NH₃ decomposition activity (Figure 74). In fact, 5 wt% is fairly low metal loading for a FTS catalyst, with most FTS catalysts containing 15 to 30 wt% Co as the resulting materials are easier to reduce.⁶⁰

In *9.7Co/10hthin-IWI-cal250* and *9.2Co/40hfat-IWI-cal250* the overall sodium content by ICP is very similar (1.2 to 1.3 wt%) but higher in the latter based on XPS, suggesting more sodium on the surface. Sodium acts as a poison to FTS catalyst by blocking Co⁰ sites, with as little as 2 wt% content in the catalyst.⁹⁸ Interestingly the sodium content is higher in the lower loaded samples, with 2.0 wt% in *4.2Co/10hthin-IWI-cal250* compared to 0.9 wt% in *4.9Co/40hfat-IWI-cal250* yet the former is more active for FTS. The high sodium content in *7.7Co/plate-IWI-cal250* of 2.7 wt% is the most likely cause for the low FTS activity (Figure 77b) as XPS suggests a high proportion of the sodium is on the surface in this case.

It is hard to compare the FTS catalytic results herein with the literature as different conditions are used. However, the most comparable reported Co/ γ -Al₂O₃-IWI catalyst exhibited 12.5 mol% CO conversion⁹⁹, which is the same as *9.2Co/40hfat-IWI-cal250-red425*. However, changing the γ -Al₂O₃ support morphology significantly enhances the activity to 20 mol% with *9.7Co/10hthin-IWI-cal250-red425*.

The most likely cause for the difference in activity between the catalysts supported on *10hthin* and *40hfat* is the particle size and the ability of the support to stabilise the optimum particle size during reduction and FTS testing. The TEM study of the ~ 9 wt% samples pre- and post-FTS highlights that *10hthin* is most effective at maximising 6 to 10 nm particles, known to be the most active particle size for FTS.⁹⁴

For both loadings, the more active catalysts are supported on *10hthin* and are also the most selective to C₅₊. The catalysts supported on nanorods exhibit superior CH₄ selectivity in comparison with the selected materials presented in the literature review (Table 3). Specifically, the ~ 9 wt% catalysts have the better CH₄ selectivity (~ 5 %) compared to the ~ 5 wt% catalysts (8 to 11 %) which may be due to the presence of smaller cobalt particles in the latter as particles smaller than 3 nm have been reported to enhance CH₄ selectivity.⁹²

A high degree of stabilisation resulting from the *10hthin* support is evidenced by TEM of spent catalyst (Figure 80), in agreement with high catalytic activity and stability. The *9.7Co/10hthin-IWI-cal250* catalyst is the most active for FTS as shown in Figure 79. Particle size stability during FTS testing is not observed with the *plate* supported sample compared to the *10hthin* supported sample reduced under the same conditions. This indicates that the difference in support morphology enhances the cobalt nanoparticles stability against sintering. Furthermore, TEM of *9.7Co/10hthin-IWI-cal250* reveals the presence of elongated particles. The presence of these elongated particles demonstrates that the *10hthin* nanorod support is capable of inhibiting motion of cobalt particles in all directions except along the length of the nanorod, thus providing more stabilisation than a flat or bulk support. It is also possible that the elongated particles may be partly responsible for the enhanced catalytic activity of this sample.

Overall the *10hthin* supported Co/ γ -Al₂O₃-IWI catalysts for FTS are better than using the *40hfat* support, quantified in terms of the higher FTS activity, selectivity and nanoparticle stability.

Chapter 6 conclusions

The evaluation of the characterisation and catalytic data, both for NH₃ decomposition and FTS, of a series of Co/ γ -Al₂O₃ catalysts with different loadings and support morphologies synthesised by NaOH precipitation and IWI has been carried out in this chapter.

In general, the NaOH precipitation method results in the most active NH₃ decomposition catalysts when the loading is very low (~ 1 wt%) and when supported on γ -Al₂O₃ nanorods with a thin 8 nm diameter. This is due to successful stabilisation by the curved surface when the ratio of the nanoparticle diameter (P) and the nanorod diameter (R) is less than one (P:R < 1). In this series, a significant difference in catalytic activity is observed from changing the morphology of the γ -Al₂O₃ support relative to the *commercial* support. These results highlight the importance of support morphology and curvature for the stabilisation of small cobalt nanoparticles. The high catalytic activity of the catalysts containing small, stabilised nanoparticles suggests that the B3 arrangement acts as the active site for NH₃ decomposition by (111) fcc Co. The same catalytic improvement is not seen for the 1 wt% catalysts synthesised by IWI due to the preferential formation of irreducible cobalt aluminate with such low cobalt loading.

For the 4.8 wt% Co/ γ -Al₂O₃-IWI-cal250 series the highest NH₃ decomposition activity is observed with the *plate* support because the higher loading leads to the formation of larger particles which cannot be effectively stabilised by nanorods as the resulting particles (P) are too large relative to the rod diameter (R), thus P:R > 1. This is true for the other catalysts with higher cobalt content, resulting in a fairly similar activity for these series, despite using different support morphologies. Thus, the *plate* support proves to be the most effective for 9.1 wt% Co catalysts compared to the nanorods. For FTS, the 8 nm diameter nanorod (*10hthin*) supported catalyst leads to the highest activity, selectivity and stability compared to the use of a larger diameter nanorod (*40hfat*). The high sodium content poisons the analogous *plate* supported catalysts.

In summary, low cobalt loading results in the formation of smaller cobalt nanoparticles, which are more effectively stabilised by γ -Al₂O₃ nanorods. This stabilisation effect is most noticeable with thin nanorods due to their high surface curvature and because the ratio of the nanoparticle diameter (P) and the nanorod diameter (R) is less than one (P:R < 1). This is evidenced by

catalytic data for both NH_3 decomposition and FTS and supported by the formation of elongated particles in these samples. The presence of elongated particles indicates that the motion of the nanoparticle on the curved surface has been successfully restricted in all directions, except along the length of the rod as the surface tension vectors in this direction are effectively analogous to the case of the flat surface (Figure 2a) so mobility is unrestricted. Nanoplate morphologies are more effective at stabilising larger cobalt nanoparticles than nanorods when the diameter of the particle exceeds the diameter of the rod support ($P:R > 1$). These observations justify the use of nanostructured supports over *commercial* supports due to the enhanced stabilisation, even for higher loading (> 4 wt% Co).

Chapter 7 – Effect of support morphology on Au/ γ -Al₂O₃ catalytic activity and stability

The previous two research chapters were focussed on Co/ γ -Al₂O₃ catalysts. The final research chapter is devoted to the synthesis, characterisation and catalytic testing of Au/ γ -Al₂O₃ to investigate the research hypothesis of nanoparticle stabilisation using curved supports in another catalytic system, in which particle size determination is easier.

The synthesis method is first optimised and subsequently used to produce a range of Au/ γ -Al₂O₃ catalysts with different loadings and support morphologies. The same supports as those in Section 6.1.2 are used (*plate*, *10hthin*, *40hfat* and *commercial*) but the metal loading is much lower, less than 2 wt% Au typical for gold-based CO oxidation catalysts. The purpose of using different morphologies is to determine if small gold nanoparticles can be stabilised by the curvature of the nanorod compared to the flat (*plate*) or conventional (*commercial*) supports. The materials are tested for a model reaction, CO oxidation in this case. The final part of this chapter is focussed on the thermal stability of some of the materials, which is determined by carrying out high temperature catalytic stability tests.

7.1 Optimisation of Au/ γ -Al₂O₃ synthesis procedure

Prior to the synthesis of a series of materials, the experimental conditions were optimised in order to select appropriate washing, calcination and reduction procedures for catalyst preparation. A test material was synthesised by incipient wetness impregnation (IWI) using the *plate* γ -Al₂O₃ support with 1.4 wt% theoretical gold loading. This catalyst was tested for CO oxidation in five assays: as synthesised (*1.4Au/plate-IWI-fresh*), washed (*0.7Au/plate-IWI-wash*), washed and calcined (*0.7Au/plate-IWI-wash-cal250*), washed and calcined and reduced (*0.7Au/plate-IWI-wash-cal250-red200*), or washed and reduced (*0.7Au/plate-IWI-wash-*

red200). Calcination was carried out at 250 °C (2 hours, 2 °C·min⁻¹) in a static furnace. Calcined samples are denoted with “-cal250”.

The catalyst was washed with 200 mL of cold deionised water (for ~ 0.5 g scale catalyst synthesis) by Büchner filtration under vacuum and dried at 80 °C. Washed catalysts are denoted with the suffix “-wash”. A simple silver nitrate test of the washed liquid was carried out to ensure 200 mL of water is sufficient to remove all the chloride ions. Approximately 0.5 g of *1.4Au/plate-IWI* was washed with four portions of 50 mL deionised water. To each portion, 100 µL of 0.1 M AgNO₃ solution was added. In the first portion the formation of a white precipitate (AgCl) was clearly visible; the second portion contained visibly less precipitate while the third and fourth portions contained no visible precipitate. This test suggests that 100 mL is sufficient volume to wash ~ 0.5 g of *1.4Au/plate-IWI*. However, 200 mL will be used in order to ensure complete chloride removal for higher loadings. Note that the gold loading of the catalyst decreases from 1.4 to 0.7 wt% as a result of the washing procedure.

pXRD of *1.4Au/plate-IWI-fresh*, *0.7Au/plate-IWI-wash* and *0.7Au/plate-IWI-wash-red200* did not show any Au⁰ peaks. However, an Au⁰ pXRD peak (JCPDS 04-0784) is visible in the washed and calcined sample, *0.7Au/plate-IWI-wash-cal250*. pXRD is not used for the characterisation of the rest of the uncalcined Au/γ-Al₂O₃ catalysts.

The colour, reduction temperature and gold size of the Au/*plate-IWI* catalysts after washing and washing/calcination without reduction are summarised in Table 39. The colour of the Au/γ-Al₂O₃ material is derived from Au 5d orbitals overlapping with Al³⁺ orbitals.¹¹²

Table 39. Properties and third run CO oxidation catalytic data for Au/γ-Al₂O₃-*IWI* catalysts with different treatment conditions.

Catalyst	Colour	Au reduction temperature ^a (°C)	E _a (kJ·mol ⁻¹)	TOF @ 450 °C (mol _{CO2} ·mol _{Au} ⁻¹ ·h ⁻¹)
<i>1.4Au/plate-IWI</i>	Pale yellow	168.1	88.8	348
<i>0.7Au/plate-IWI-wash</i>	Pale pink	149.8	61.7	2080
<i>0.7Au/plate-IWI-wash-cal250</i>	Mauve	114.4	72.7	253
<i>0.7Au/plate-IWI-wash-cal250-red200</i>	Pink/purple	n/a	62.4	1454
<i>0.7Au/plate-IWI-wash-red200</i>	Grey/purple	n/a	57.6	2106

^a Determined from TPR profiles.

The gold active site for CO oxidation is usually accepted to be Au⁰ but studies suggest that Au⁺ may also be involved at the metal-support interface.^{112,124} Nevertheless, the catalyst needs to be reduced to modify the precursor oxidation state from the as-formed Au³⁺ to Au⁰/Au⁺ active state. Based on the gold reduction temperature in Table 39 obtained from TPR profiles of the fresh, washed and washed/calcined materials (Figure 81), 200 °C was chosen as a suitable reduction temperature, within the commonly used range for gold from 120 to 250 °C.¹¹² Reduction is carried out using the following protocol: 5 °C·min⁻¹ ramp to 200 °C held for 45 minutes under 20 mL·min⁻¹ pure H₂ flow. Samples are reduced *in situ* prior to catalyst testing as denoted by the suffix “-red200”.

TPR (Figure 81d) profiles suggest that the calcination process may partially reduce 0.7Au/*plate-IWI-wash-cal250* to Au⁰ because there is no well-defined TPR peak and Au⁰ peaks were visible by pXRD (JCPDS 04-0784) estimating a particle size of 23.4 nm. The TPR profiles (Figure 81) also suggest that the *plate* support undergoes a thermal change at ~ 500 °C and the use of MS suggests this may be due to the release of N₂ from nitrate decomposition (based on a peak at m/z 28). This behaviour for γ-Al₂O₃ has been reported by Busca *et al.*²⁵.

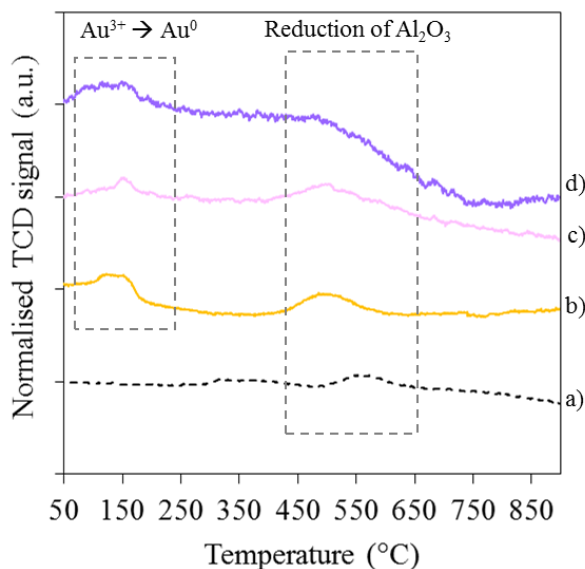


Figure 81. TPR profiles of a) γ-Al₂O₃ *plate* support, b) 1.4Au/*plate-IWI*, c) 0.7Au/*plate-IWI-wash* and d) 0.7Au/*plate-IWI-wash-cal250*.

The catalysts were subjected to a standard three run CO oxidation catalytic test. The third run CO oxidation catalytic data for the Au/*plate* materials with different washing, calcination and reduction combinations are shown in Figure 82. The associated third run activation energy and turnover frequency (TOF) values are summarised in Table 39 with the colour and reduction temperature.

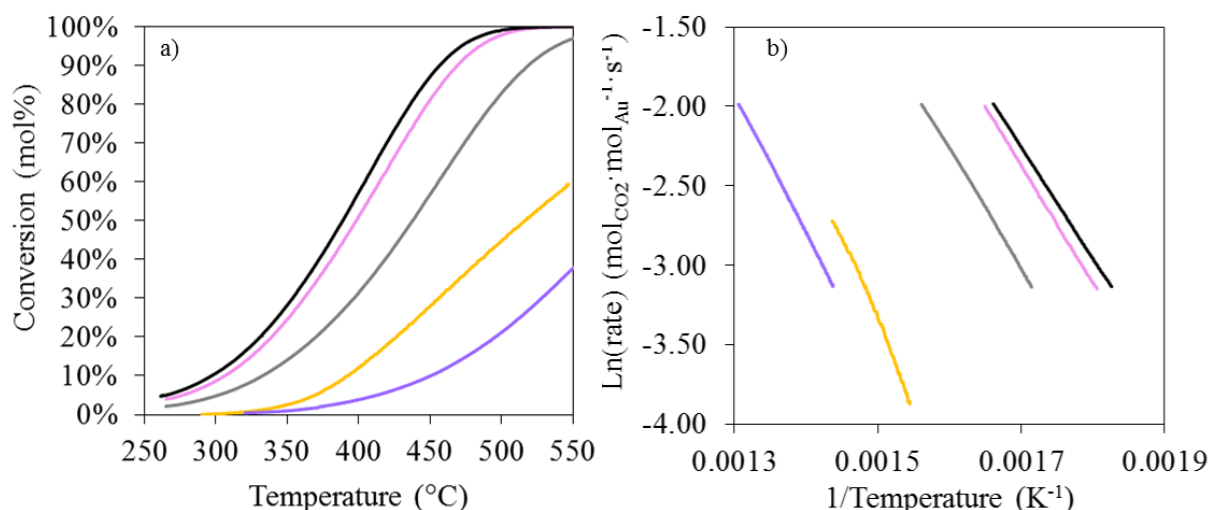


Figure 82. CO oxidation catalytic activity of $Au/\gamma-Al_2O_3-IWI-wash$. a) conversion as a function of temperature and b) Arrhenius plot. $1.42Au/plate-IWI$ (yellow), $0.69Au/plate-IWI-wash$ (pink), $0.69Au/plate-IWI-wash-cal250$ (blue), $0.69Au/plate-IWI-wash-cal250-red200$ (grey) and $0.69Au/plate-IWI-wash-red200$ (black).

Calcination of the washed catalyst ($0.7Au/plate-IWI-wash-cal250$) results in a significant decrease in activity (Figure 82), probably due to agglomeration indicated by pXRD. The Arrhenius plot (Figure 82b) highlights the poor activity of $1.4Au/plate-IWI$. Washing is therefore confirmed to be a necessary step to remove chloride ions derived from the gold precursor ($HAuCl_4$), which is a known poison for CO oxidation catalysts as it is reported to encourage sintering.¹⁷ Figure 82 demonstrates that the activity of the washed catalyst ($0.7Au/plate-IWI-wash$) is slightly improved by reduction of this material at 200 °C ($0.7Au/plate-IWI-wash-red200$), in agreement with a reduction in activation energy (61.7 to 57.6 kJ·mol⁻¹).

The aim of this section is to determine a suitable experimental work up protocol for the synthesis of $Au/\gamma-Al_2O_3$ catalysts. The catalytic results demonstrate that washing is essential to remove unwanted chloride ions. Furthermore, calcination of the washed catalyst appears to increase the gold particle size, indicated by pXRD and the colour change, leading to a lower catalytic activity. Reduction at 200 °C is deemed a suitable reduction temperature based on TPR profiles and catalytic data. The H_2 pre-reduction does not significantly enhance the catalytic activity of $0.7Au/plate-IWI-wash$ because CO in the reaction feed can also act as a reducing agent.¹²⁴ However, it is important to apply a thermal treatment to all the catalysts for consistency, particularly since Au^{3+} is thermally unstable and capable of reducing during drying procedures.¹¹² Thus, the $Au/\gamma-Al_2O_3$ catalysts produced in the following sections are washed with cold deionised water and pre-reduced at 200 °C.

7.2 Effect of support morphology on Au/ γ -Al₂O₃ catalysts synthesised by IWI and adsorption

Using the experimental protocol determined in the previous section, a series of theoretical 1.4 wt% Au catalysts supported on γ -Al₂O₃ with different morphologies (*plate*, *40hfat*, *10hthin* and *commercial*) were synthesised by IWI, denoted by “-IWI”. As the support nomenclature suggests, the shape of the supports are nanoplates, fat low curvature nanorods (diameter ~ 20 nm), thin high curvature nanorods (diameter ~ 8 nm) respectively and the commercial support has no defined morphology at the nanoscale but exists rather as bulk γ -Al₂O₃. Using the same supports, three series of Au/ γ -Al₂O₃-ads catalysts, denoted by “-ads”, were also prepared with 0.5 to 3.5 wt% theoretical gold loadings. In order to determine if the synthesis method and support morphology have an effect on the resulting catalyst, the materials have been fully characterised and tested for CO oxidation. First, the results are presented for each method and then the results are discussed in Section 7.2.5. The adsorption synthesis process and washing of the catalyst results in different gold loadings so the exact loading (measured by ICP) is always quoted in the catalyst nomenclature.

7.2.1 Characterisation of Au/ γ -Al₂O₃-IWI catalysts

The physical properties of the Au/ γ -Al₂O₃-IWI-wash catalysts are summarised in Table 40. As shown in Table 40, the obtained gold loading is much lower than the theoretical 1.4 wt% loading due to the washing process. The loading varies throughout the catalyst series.

The sodium content (Table 40) is believed to be derived from the support, based on the support sodium loadings presented in Table 23 (Chapter 4) and the purity of the gold precursor (99.99 wt%). Thus, as expected, the sodium content is highest in *0.7Au/plate-IWI-wash* with the rest of the catalysts containing less than 1 wt% sodium. Sodium is not expected to have an effect on CO oxidation activity.¹²

Table 40. Physical properties of washed $Au/\gamma-Al_2O_3$ -IWI-wash catalysts.

Catalyst	Au content ^a (wt%)	Na content ^a (wt%)	Colour after 200 °C reduction	Au reduction temperature ^b (°C)	Au ⁰ size (nm)	
					CO chemi ^c	TEM ^d
<i>0.7Au/plate-IWI-wash</i>	0.7 [1.4]	3.0	Grey/purple	149.8	17.7	4.7
<i>0.2Au/40hfat-IWI-wash</i>	0.2 [1.4]	0.6	Grey/purple	161.8	2.9	-
<i>0.3Au/10hthin-IWI-wash</i>	0.3 [1.4]	1.0	Grey/purple	136.6	10.1	5.4
<i>0.2Au/commercial-IWI-wash</i>	0.2 [1.4]	0.3	Burgundy	169.1	2.1	-

^a Calculated from ICP of the digested solid (fresh washed catalyst), [theoretical loading].

^b Determined from TPR profiles.

^c Calculated by pulse CO chemisorption at -80 °C with *in situ* pre-reduction at 200 °C.

^d Calculated by TEM size distributions with *ex situ* pre-reduction at 200 °C.

The *0.2Au/commercial-IWI-wash* catalyst produces a distinct, bright burgundy colour after reduction at 200 °C, unlike the other reduced catalysts in the series which are purple/grey.

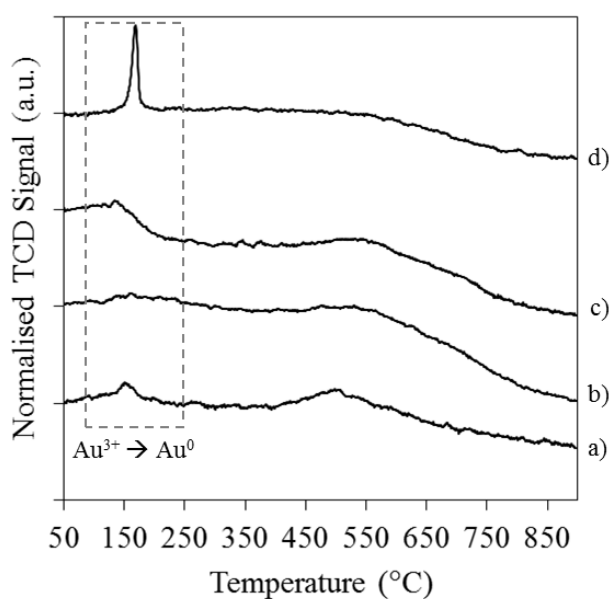


Figure 83. TPR profile of $Au/\gamma-Al_2O_3$ -IWI-wash catalysts. a) *0.7Au/plate-IWI-wash*, b) *0.2Au/40hfat-IWI-wash*, c) *0.3Au/10hthin-IWI-wash* and d) *0.2Au/commercial-IWI-wash*.

The TPR profiles (Figure 83) of all the IWI catalysts show an Au^{3+} reduction peak below 200 °C and the synthesised supports (*plate*, *10hthin* and *40hfat*) show an additional broad peak at ~ 500 °C related to the support.

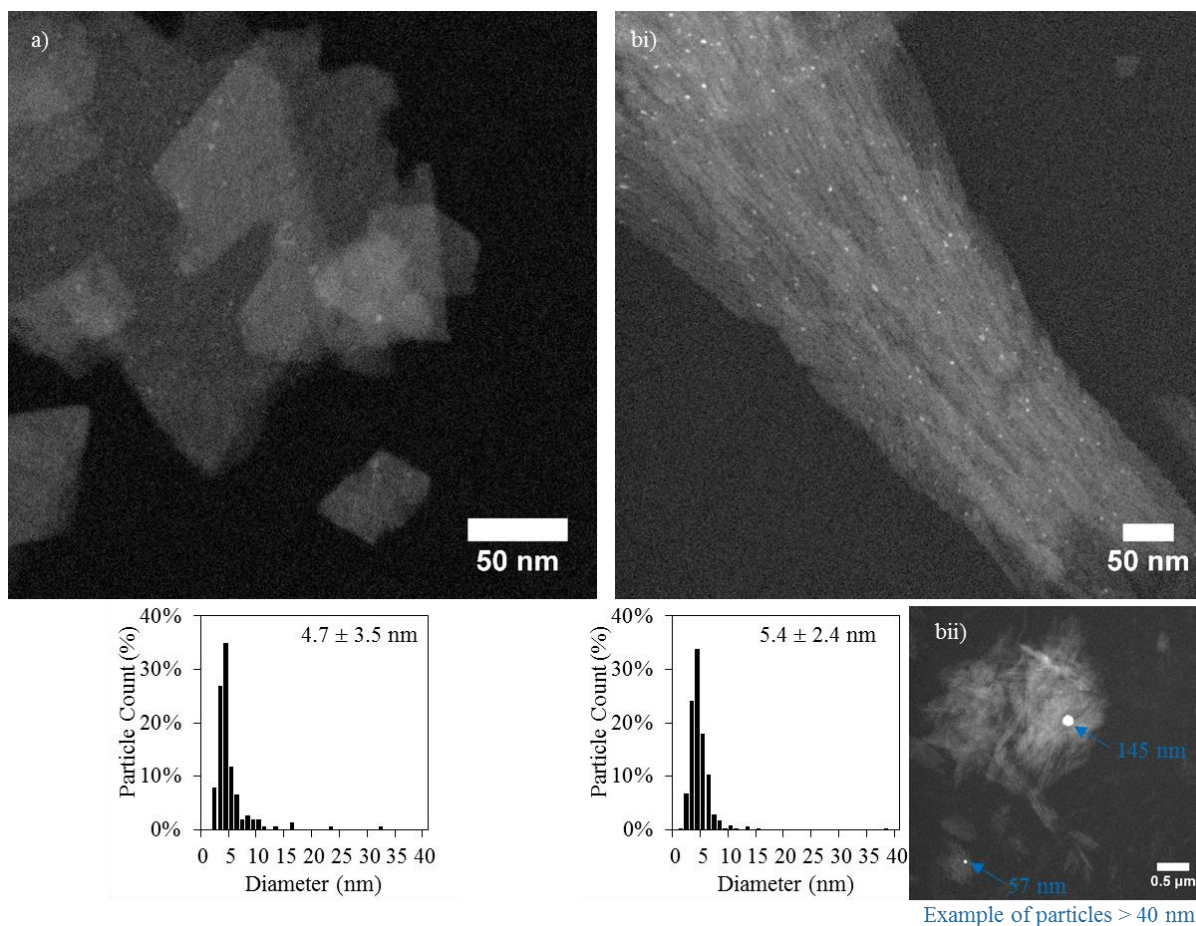


Figure 84. Representative HAADF-STEM micrographs and Au particle size distributions for a) *0.7Au/plate-IWI-wash-red200* and b) *0.3Au/10hthin-IWI-wash-red200*.

Based on CO pulse chemisorption, the smallest average particle size in the IWI series is calculated for *0.2Au/40hfat-IWI-wash* (2.9 nm) and *0.2Au/commercial-IWI-wash* (2.1 nm), in agreement with the higher gold reduction temperature observed in the TPR profiles in Figure 83. The average size of gold in *0.3Au/10hthin-IWI-wash* is estimated to be 10.1 nm and the use of the plate support (*0.7Au/plate-IWI-wash*) results in the largest average sized particles in the series (17.7 nm).

However, the average Au⁰ particle size of *0.7Au/plate-IWI-wash* (4.7 nm, Figure 84a) and *0.3Au/10hthin-IWI-wash* (5.4 nm, Figure 84b) based on HAADF-STEM imaging is smaller than from CO chemisorption calculations, 17.7 nm and 10.1 nm respectively. The differences arise from the fact that electron microscopy imaging samples only a small fraction of particles whereas chemisorption considers all of the particles. In addition, the chemisorption calculations assume the shape of the particle to be hemispherical, which could lead to errors.¹²⁷ The concurrent use of the two techniques provides an overall idea about the particle size, shape and

size distribution of the sample. For example, a few particles larger than 40 nm (not shown in the size distribution but included in the average size) were observed in *0.3Au/10hthin-IWI-wash* (Figure 84bii) with sizes including 45, 48, 51, 57 and 145 nm. As only a few of these large particles were imaged relative to hundreds of particles less than 10 nm in diameter, the larger ones have a negligible effect on the average size. Thus, it is likely that *0.7Au/plate-IWI-wash* contains a higher proportion of particles greater than 40 nm in diameter resulting in the 17.7 nm average size calculated by pulse chemisorption.

7.2.2 Catalytic testing of $Au/\gamma-Al_2O_3$ -IWI catalysts

The gold catalysts synthesised by IWI were tested for CO oxidation activity in a standard three consecutive run with *in situ* reduction at 200 °C. The third run catalytic data is presented in Figure 85 and Table 41 summarises some catalytic activity descriptors.

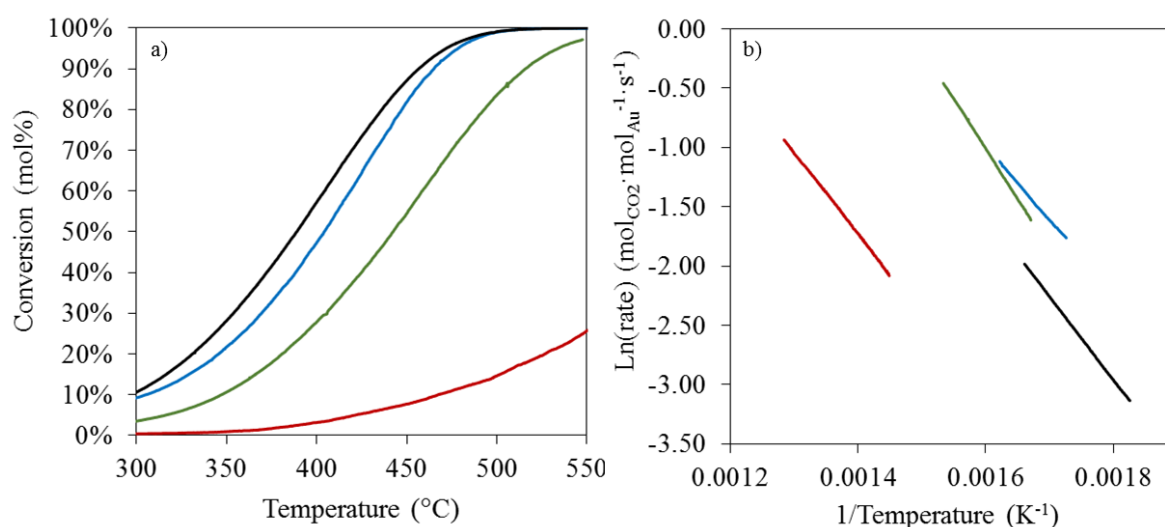


Figure 85. CO oxidation activity for $Au/\gamma-Al_2O_3$ -IWI catalysts a) conversion-temperature and b) Arrhenius plot. *0.7Au/plate-IWI-wash* (black), *0.2Au/40hfat-IWI-wash* (green), *0.3Au/10hthin-IWI-wash* (blue) and *0.2Au/commercial-IWI-wash* (burgundy). GHSV = 2160 mL_{CO}·g_{cat}⁻¹·h⁻¹. Pre-reduced at 200 °C under H₂ flow.

As shown in Figure 85, the catalytic activity varies significantly within the series of catalysts. The *0.7Au/plate-IWI-wash-red200* catalyst has the highest conversion at a given temperature but due to its higher gold content, the TOF is lower compared to the two catalysts supported on nanorods (*0.2Au/40hfat-IWI-wash-red200* and *0.3Au/10hthin-IWI-wash-red200*). The catalyst supported on the *commercial* support (*0.2Au/commercial-IWI-wash-red200*) exhibits poor activity in Figure 85, highlighted by the relatively low TOF (713.5 mol_{CO2}·mol_{Au}⁻¹·h⁻¹). Given the low loading of *0.2Au/40hfat-IWI-wash-red200*, the activity per mol of gold is

remarkably high, $6377.2 \text{ mol}_{\text{CO}_2} \cdot \text{mol}_{\text{Au}}^{-1} \cdot \text{h}^{-1}$, almost ten times higher than for *0.2Au/commercial-IWI-wash-red200*. The temperature at 50 % conversion, T_{50} ranges by 50 °C, with the lowest temperature achieved using the *plate* support whereas the use of *commercial* does not reach 50 % conversion within the studied temperature range.

Within the series, the catalyst supported on the thin nanorod, *0.3Au/10hthin-IWI-wash-red200*, is the most stable over the three consecutive runs, with the TOF decreasing only by 5.5 % between the first and third run.

The *0.2Au/commercial-IWI-wash-red200* catalyst exhibits a distinct burgundy colour (Table 41) after reduction or catalytic testing compared to the other catalysts which are grey or purple.

Table 41. CO oxidation catalytic data for *Au/γ-Al₂O₃-IWI-wash* catalysts supported on $\gamma\text{-Al}_2\text{O}_3$ with different morphologies.

Catalyst	E_a ($\text{kJ} \cdot \text{mol}^{-1}$)	T_{50} ^a (°C)	TOF @ 450 °C ($\text{mol}_{\text{CO}_2} \cdot \text{mol}_{\text{Au}}^{-1} \cdot \text{h}^{-1}$)	Stability over 3 runs ^b	Catalyst colour after test
<i>0.7Au/plate-IWI-wash-red200</i>	57.6	389.2	2105.5	-16.0 % TOF	Grey/purple
<i>0.2Au/40hfat-IWI-wash-red200</i>	70.2	442.4	6377.2	-13.2 % TOF	Grey/purple
<i>0.3Au/10hthin-IWI-wash-red200</i>	51.6	404.4	4986.2	-5.5 % TOF	Light grey
<i>0.2Au/commercial-IWI-wash-red200</i>	57.1	> 550	713.5	-8.5 % TOF	Burgundy

^aTemperature at which 50 mol% conversion is achieved.

^b(-) indicates deactivation and (+) activation.

7.2.3 Characterisation of *Au/γ-Al₂O₃-adsorption* catalysts

Since the IWI method is often criticised for poor gold particle size control, a series of three catalysts with each support were synthesised by adsorption. The physical properties of the *Au/γ-Al₂O₃-ads-wash* catalysts are summarised in Table 42.

The nature of the adsorption method means only a proportion of the metal in the synthesis solution can adsorb onto the support surface. Furthermore, the inclusion of a washing step means that the actual gold loading (Table 42) determined by ICP is significantly lower than the theoretical content. The sodium content (Table 42) of the catalysts is fairly low, less than 2 wt%, believed to be derived from the use of NaOH in the synthesis of the support.

Table 42. Physical properties of $Au/\gamma-Al_2O_3$ -ads-wash catalysts synthesised by adsorption with different support morphologies and loadings.

Catalyst	Au content ^a (wt%)	Na content ^a (wt%)	Au reduction temperature ^b (°C)	Au ⁰ size (nm)	
				CO chemi ^c	TEM ^d
<i>0.01Au/plate-ads-wash</i>	0.01 [0.5]	1.4	-	0.3	n/a
<i>0.1Au/plate-ads-wash</i>	0.1 [1.4]	2.1	189.3	4.3	n/a
<i>1.0Au/plate-ads-wash</i>	1.0 [3.5]	1.8	153.9	11.4	11.6
<i>1.2Au/plate-ads-wash</i>	1.2 [2.5]	1.8	131.3	19.2	n/a
<i>0.02Au/40hfat-ads-wash</i>	0.02 [0.5]	0.4	-	1.1	Not visible
<i>0.8Au/40hfat-ads-wash</i>	0.8 [2.5]	0.7	147.4	9.5	n/a
<i>1.2Au/40hfat-ads-wash</i>	1.2 [1.4]	1.3	142.3	4.6	n/a
<i>0.01Au/10hthin-ads-wash</i>	0.01 [0.5]	0.5	-	0.3	n/a
<i>0.5Au/10hthin-ads-wash</i>	0.5 [1.4]	1.2	158.1	7.8	5.2 & 13.1
<i>1.9Au/10hthin-ads-wash</i>	1.9 [2.5]	0.9	157.3	19.1	n/a
<i>0.4Au/commercial-ads-wash</i>	0.4 [0.5]	0.2	-	4.0	n/a
<i>1.2Au/commercial-ads-wash</i>	1.2 [1.4]	0.9	151.0	37.5	n/a
<i>1.9Au/commercial-ads-wash</i>	1.9 [2.5]	0.2	154.5	24.7	n/a

^a Calculated from ICP of the digested solid (fresh washed catalyst). The theoretical loading is in square brackets.

^b Determined from TPR profiles. – indicates no peak.

^c Calculated by pulse CO chemisorption at -80 °C with *in situ* pre-reduction at 200 °C.

^d Calculated by TEM size distributions with *ex situ* pre-reduction at 200 °C.

In the TPR profiles shown in Figure 86, no Au³⁺ reduction peak is visible for the lowest loaded catalyst in each series with different supports, possibly due to their low gold loading. The latter is feasible because *0.02Au/40hfat-ads-wash* remained the same pale pink colour after reduction at 200 °C. For the rest of the catalysts, a Au³⁺ reduction peak is visible around 140 to 160 °C in Figure 86. An exception is *0.1Au/plate-ads-wash*, which despite the low loading (0.08 wt%) exhibits a clear Au³⁺ reduction peak at a higher temperature (189.3 °C) than the other catalysts.

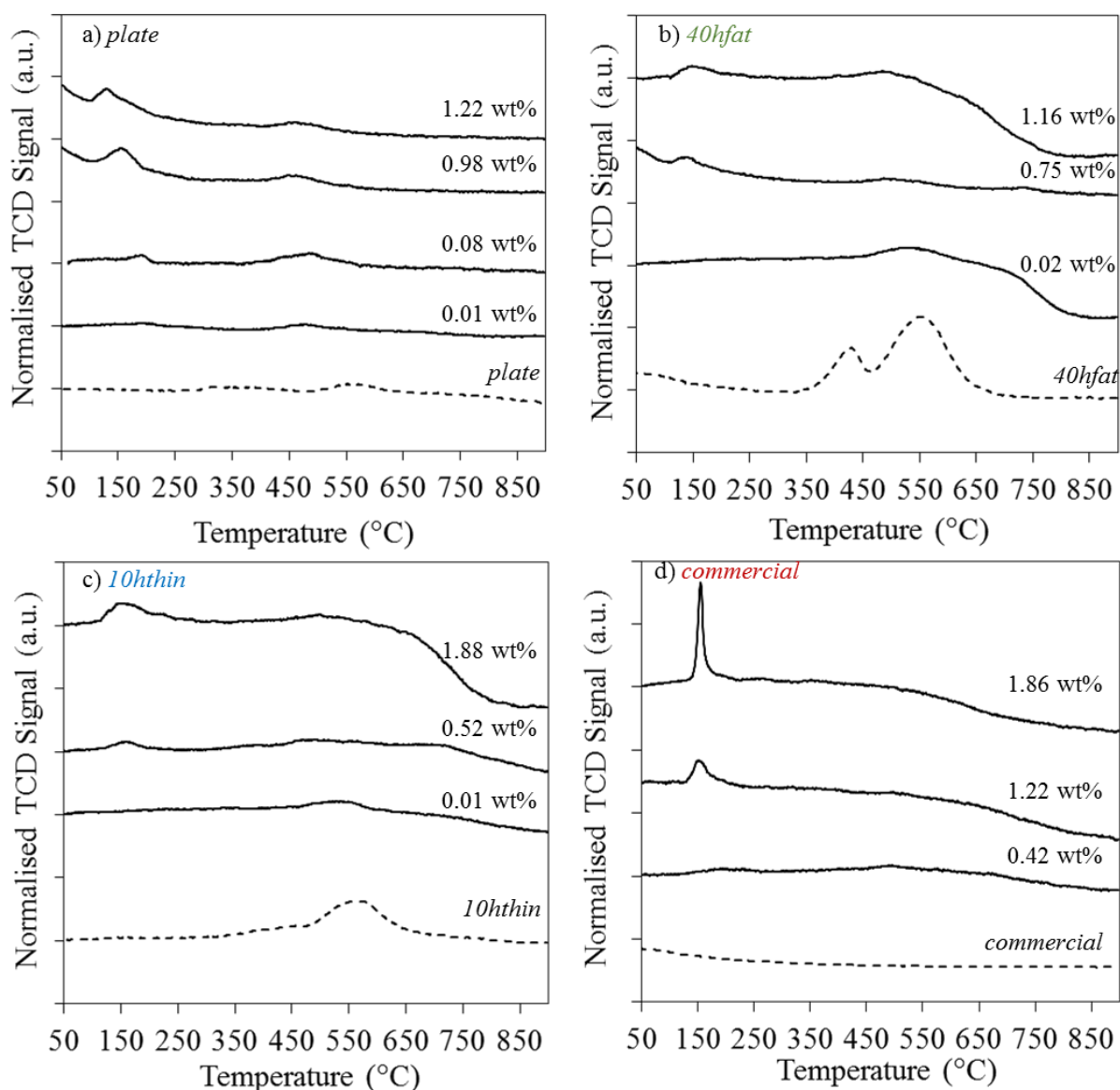


Figure 86. TPR profile of washed $Au/\gamma-Al_2O_3-ads-wash$ catalysts prepared by adsorption with different loadings. Supported on a) *plate*, b) *40hfat* c) *10hthin* and d) *commercial*. $Au/\gamma-Al_2O_3-ads$ catalysts are shown by a solid black line and the relevant supports are shown by a dashed black line.

Often the ease of reducibility is related to the particle size, with smaller particles harder to reduce. However, for the catalysts reduced within the range of 140 to 160 °C, the particle size estimated by pulse CO chemisorption ranges significantly from 4.6 to 37.5 nm.

In general, the particle sizes summarised in Table 42 increase with higher theoretical loadings. gold loadings greater than 1 wt% result in large average gold particles greater than 25 nm when the *commercial* support is used, compared to the analogous catalysts using the nanostructured supports which results in the formation of particle less than 20 nm average and less than 10 nm with the *40hfat* support.

HAADF-STEM micrographs of *0.5Au/10hthin-ads-wash-red200* (Figure 87b) show a bi-modal distribution of spherical particles less than 10 nm and elongated particles greater than 10 nm in length. The sample was comprised of approximately 18 % elongated particles. Note that the size of the elongated particles in the size distribution in Figure 87b is the maximum dimension, i.e. the length. The overall average size of all the particles analysed is 6.5 nm, in good agreement with the average size estimated by pulse chemisorption of 7.8 nm.

By contrast, *1.0Au/plate-ads-wash-red200* contains a bi-modal size distribution of only spherical particles containing small 2 to 5 nm particles and large 5 to 40 nm particles (Figure 87a). The average particle size of this distribution (11.6 nm) is equivalent to the average size estimated by pulse chemisorption (11.4 nm).

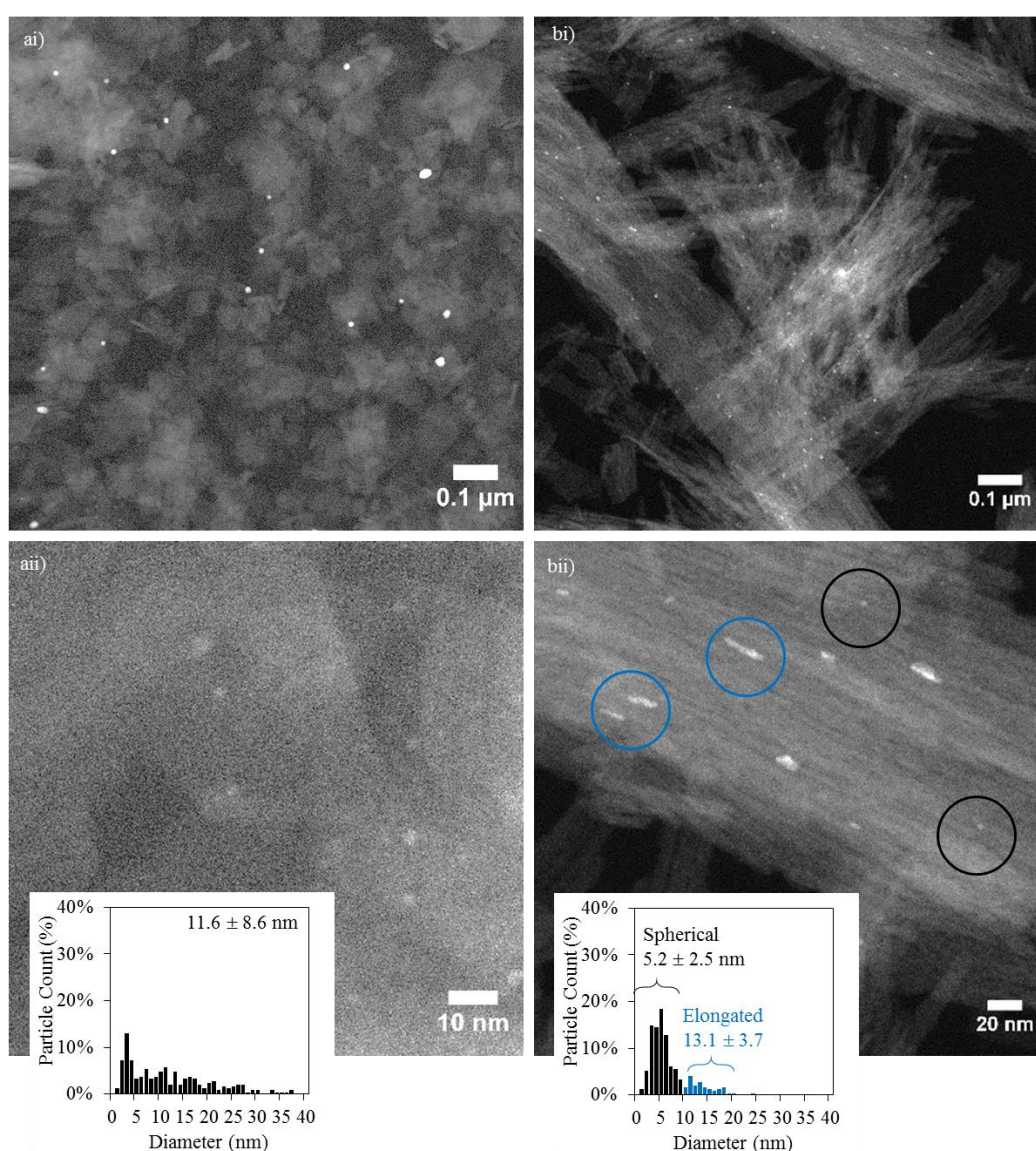


Figure 87. Representative HAADF-STEM micrographs and gold particle size distributions for a) *1.0Au/plate-ads-wash-red200* and b) *0.5Au/10hthin-ads-wash-red200*. Low magnification (i) and high magnification (ii).

7.2.4 Catalytic testing of Au/ γ -Al₂O₃-adsorption catalysts

All of the catalysts prepared by adsorption were tested for CO oxidation in order to study the effect of the support morphology and gold loading on the particle size and resulting catalytic activity. The catalysts were tested in a standard three consecutive run test with *in situ* pre-reduction at 200 °C. The third run catalytic data is presented in Figure 88 and Table 43 presents some catalytic activity descriptors.

The CO oxidation activity is notably different as a result of changing the morphology of the γ -Al₂O₃ support and the gold loading. In general, increasing the gold loading increases the conversion, however, this is not true for *0.5Au/10hthin-ads-wash*, which is more active per mol of gold than *1.9Au/10hthin-ads-wash*. The CO oxidation activation energies vary from ~ 47 to 68 kJ·mol⁻¹, with differences occurring across a series on a given support. For example with the plate support, a low activation energy of ~ 47 kJ·mol⁻¹ is obtained for samples with less than 0.08 wt% Au and a high activation energy ~ 68 kJ·mol⁻¹ for higher loading (0.98 to 1.22 wt% Au). For very low loadings < 0.02 wt% Au, the TOF at 450 °C is exceptionally high per mol of gold, with the highest rate of CO₂ production (9976.2 mol_{CO₂}·mol_{Au}⁻¹·h⁻¹) obtained with *0.02Au/40hfat-ads-wash*. No gold particles in this sample were visible by bright and dark field electron microscopy, which may be due to the low loading or the small size below detection capabilities (< 1 nm). However, particles less than 1 nm are reportedly inactive for CO oxidation so it is unlikely that the sample contains particles smaller than 1 nm given the exceptionally high activity per mole of gold.¹⁰⁸

The three catalysts supported on the *commercial* support exhibit very poor activity, regardless of the loading. The T₅₀ for all the catalysts ranges from approximately 370 to 450 °C, with some catalysts with lower loadings not achieving 50 % conversion within the studied temperature range. At high gold loading (> 1 wt%) with the *commercial* support, the colour of the spent catalyst is a distinct burgundy.

The change in activity of the catalysts after the three consecutive catalytic runs is summarised in Table 43. In most cases the TOF decreases i.e. the catalyst deactivates. The degree of deactivation varies from 2.3 to 71.8 % of the TOF value with *1.2Au/plate-ads-wash-red200* and *0.4Au/commercial-ads-wash-red200* deactivating the least and most respectively. However, in some cases with very low loading (< 0.02 wt% Au) the catalyst activates such as with *0.01Au/plate-ads-wash* and *0.02Au/40hfat-ads-wash*.

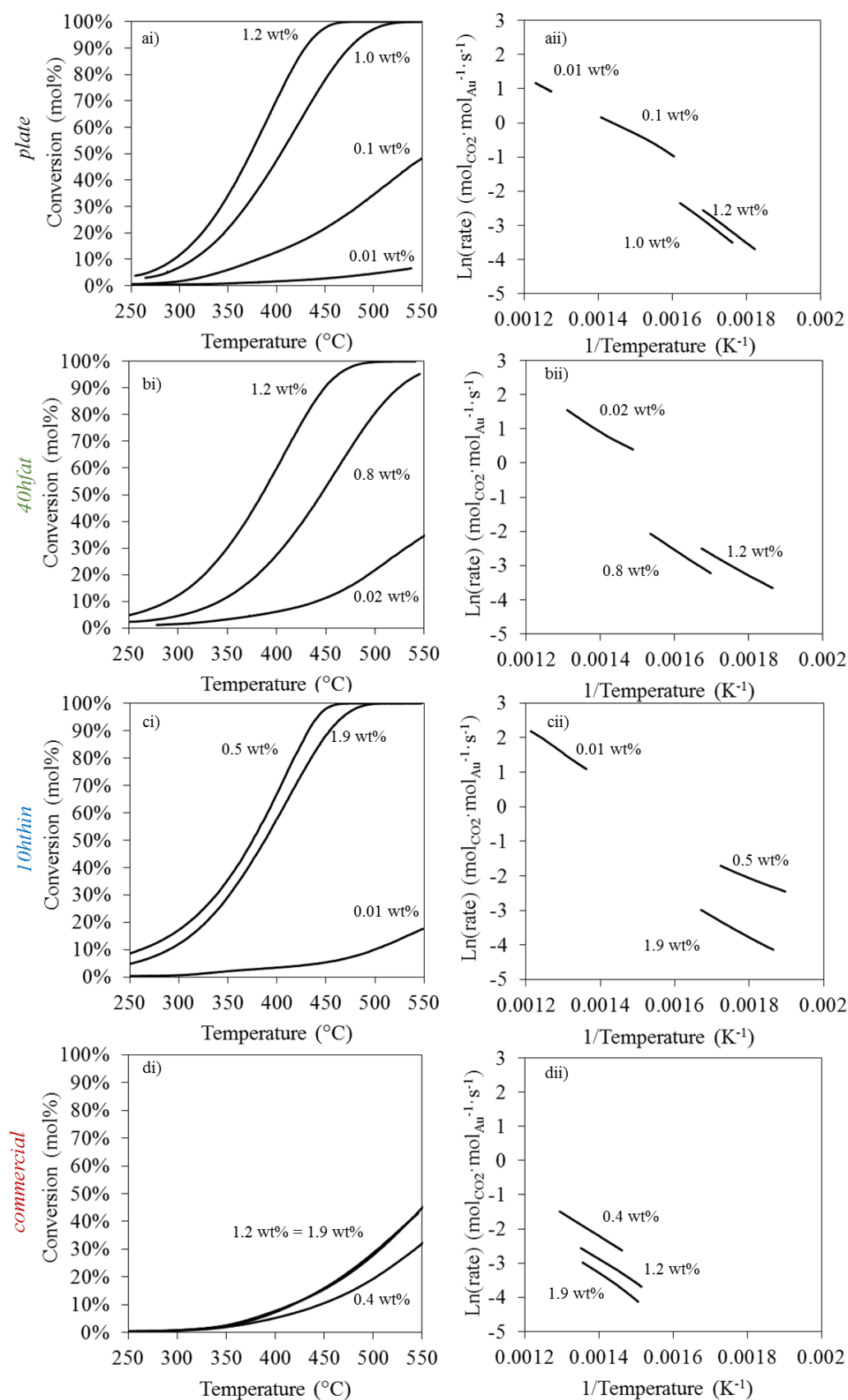


Figure 88. CO oxidation catalytic activity for $Au/\gamma-Al_2O_3$ -ads-wash catalysts pre-reduced at 200 °C under H_2 flow. Conversion as a function of temperature (i) and Arrhenius plot (ii). Supported on a) plate, b) 40hfat, c) 10hthin and c) commercial. $GHSV = 2160 \text{ mL}_{CO} \cdot \text{g}_{cat}^{-1} \cdot \text{h}^{-1}$.

Table 43. Third run CO oxidation catalytic data for different loadings of *Au/γ-Al₂O₃-ads-wash* catalysts supported on different γ -Al₂O₃ morphologies. GHSV = 2160 mL_{CO}·g_{cat}⁻¹·h⁻¹.

Catalyst	E _a (kJ·mol ⁻¹)	T ₅₀ ^a (°C)	TOF @ 450 °C (mol _{CO₂} ·mol _{Au} ⁻¹ ·h ⁻¹)	Stability over 3 runs ^b	Catalyst colour after test
<i>0.01Au/plate-ads-wash-red200</i>	47.7	-	4836.2	+9.4 % TOF	White
<i>0.1Au/plate-ads-wash-red200</i>	47.0	-	4796.5	-5.0 % TOF	Very pale pink
<i>1.0Au/plate-ads-wash-red200</i>	68.3	404.2	1408.6	-16.1 % TOF	Dark grey/pink
<i>1.2Au/plate-ads-wash-red200</i>	68.2	373.1	1417.1	-2.3 % TOF	Dark grey/mauve
<i>0.02Au/40hfat-ads-wash-red200</i>	54.4	-	9976.2	+24.4 % TOF	White
<i>0.8Au/40hfat-ads-wash-red200</i>	59.1	445.3	1246.3	-22.4 % TOF	Bright pink
<i>1.2Au/40hfat-ads-wash-red200</i>	50.3	385.2	1379.8	-3.2 % TOF	Light mauve
<i>0.01Au/10hthin-ads-wash-red200</i>	62.5	-	9487.8	-34.9 % TOF	White
<i>0.5Au/10hthin-ads-wash-red200</i>	35.6	375.5	3338.1	+1.4 % TOF	Light grey/pink
<i>1.9Au/10hthin-ads-wash-red200</i>	49.6	388.2	829.1	-9.4 % TOF	Dark grey
<i>0.4Au/commercial-ads-wash-red200</i>	56.2	-	444.3	-71.8 % TOF	Pale pink
<i>1.2Au/commercial-ads-wash-red200</i>	56.6	-	225.9	-54.2 % TOF	Burgundy
<i>1.9Au/commercial-ads-wash-red200</i>	63.0	-	151.7	-34.9 % TOF	Burgundy

^a Temperature at which 50 mol% conversion is achieved. – indicates 50 mol% conversion not reached within temperature range studied.

^b (-) indicates deactivation and (+) activation.

7.2.5 Discussion of the effect of loading, support morphology and synthesis method on CO oxidation catalytic activity

7.2.5.1 Effect of support morphology of *Au/γ-Al₂O₃-IWI* catalysts

For the series synthesised by IWI, the activity follows the trend: *0.2Au/40hfat-IWI-wash-red200* > *0.3Au/10hthin-IWI-wash-red200* > *0.7Au/plate-IWI-wash* >> *0.2Au/commercial-IWI-wash-red200*. The activity of *0.2Au/40hfat-IWI-wash-red200* is superior compared to the rest of the materials. This high activity is due to the average particle size of 2.9 nm, which is within the 2 to 3 nm optimum size range for CO oxidation. This suggests that in this case, the larger rod diameter is more effective at stabilising the small particles.¹⁰⁹

The reason for the very poor activity of *0.2Au/commercial-IWI-wash-red200* is unlikely to be due to chloride ions as the catalyst was washed nor due to sodium as the content is relatively

low (0.3 wt%) and unknown to have an effect for this application. Possibly, the average particle size of 2.1 nm results in a size distribution with a significant proportion of particles that are too small (< 1 nm) to exhibit catalytic activity.¹⁰⁸

It is possible that the difference in gold loading achieved results in the formation of different sized gold particles as a function of the strength of the metal-support interaction. This is certainly true for *0.7Au/plate-IWI-wash*, which contains the highest quantity of gold in the series and the largest average Au⁰ particle size. In contrast, *0.3Au/10hthin-IWI-wash-red200* and *0.2Au/commercial-IWI-wash-red200* have very similar gold loadings but different particle sizes and CO oxidation activity. The particle size of *0.2Au/commercial-IWI-wash-red200* is very similar to *0.2Au/40hfat-IWI-wash-red200* but their catalytic activities are not aligned.

Based on a comparison of the literature with similar gold loadings, impregnation methods usually result in larger particles (20 to 100 nm),¹¹² suggesting a strong metal-support interaction or good stabilisation effect with the supports used herein. This is justified by the small average particle sizes estimated from pulse CO chemisorption (2 to 18 nm). However, a few larger particles greater than 40 nm in diameter were spotted by HAADF-STEM. The distribution of all the particles visible by HAADF-STEM for *0.7Au/plate-IWI-wash-red200* and *0.3Au/10hthin-IWI-wash-red200* contain 13 and 30 % of highly active 2 to 3 nm particles, respectively. In addition, the larger average size estimated by CO chemisorption of the former suggests the formation of large inactive particles, resulting in a relatively lower catalytic activity of *0.7Au/plate-IWI-wash-red200* compared to the use of a nanorod support. Thus, it is clear that the particle size plays an important role in the CO oxidation catalytic activity, in agreement with the literature for inert, non-interacting supports such as γ -Al₂O₃.¹⁰⁹

The most common deactivation mechanism for CO oxidation is thought to be due to increased particle size by sintering. This is because gold does not easily form oxides due to the high Gibbs energy (+53.3 kJ·mol⁻¹), especially not under reductive carbonylation conditions.^{11,123} Deactivation is highest in *0.7Au/plate-IWI-wash*, possibly due to an increase in particle size as the flat *plate* support morphology does not sufficiently constraint the small, high energy metal nanoparticles.

7.2.5.2 Effect of gold loading and support morphology of $Au/\gamma-Al_2O_3$ -*ads-wash* catalysts

Due to the difference in loading across the catalyst series, the catalytic activity is adjusted by the amount of gold in the material when comparing performance. The gold loading is taken into account in the TOF values reported in Table 43 and in the Arrhenius plot (Figure 88). Based on these values, the theoretical 0.5 wt% Au catalysts on the nanostructured supports show the highest activity at 450 °C in the order $0.02Au/40hfat-ads-wash > 0.01Au/10hthin-ads-wash \gg 0.01Au/plate-ads-wash$.

The low loading of the catalysts relative to the theoretical value, particularly 0.5 wt% for the nanostructured supports, suggests either a slow rate of adsorption, weak adsorption capability, few nanoparticle anchoring points or a weak metal-support interaction enabling gold loss during washing. Given that the synthesis is carried out for three hours, which should be sufficient time to reach an equilibrium and the low gold reduction temperature observed in the TPR profiles (Figure 86), it is probable that there is a poor $Au-\gamma-Al_2O_3$ electrostatic interaction. By contrast, the *commercial* support has a higher adsorption capacity compared to the nanostructured $\gamma-Al_2O_3$ based on the higher gold loadings obtained.

Pulse CO chemisorption at -80 °C enables chemisorption at all gold surface sites in order to estimate the average particle size, allowing size comparison across the catalyst series. The range of sizes calculated for the series of catalysts with different loadings and support morphologies suggests that these factors determine the resulting particle size. In general, lower loading results in smaller gold particle sizes, however in some instances this trend is not followed. For example $0.8Au/40hfat-ads-wash$ contains larger average gold particles (9.5 nm) compared to $1.2Au/40hfat-ads-wash$ (4.6 nm), which may be due to the higher theoretical loading of 2.5 wt% in the former, encouraging the formation of larger particles.

Pulse chemisorption does not, however, provide any information about the distribution of sizes nor the shape of the particles. This information has, however, been obtained for two samples supported on *plate* and *10hthin* by HAADF-STEM as shown in Figure 87. The average particle size determined by HAADF-STEM is consistent with pulse chemisorption calculations. The $1.0Au/plate-ads-wash-red200$ (Figure 87a) contains only spherical particles with an average size of 11.6 nm and a fairly broad size distribution. Remarkable behaviour in terms of particle

shape and size distribution is observed by dark field imaging of a second sample, *0.5Au/10hthin-ads-wash-red200* (Figure 87bi), compared to *1.0Au/plate-ads-wash-red200*. The size distribution is much narrower and is comprised of a bimodal distribution of small, spherical particles less than 10 nm in diameter and elongated particles 10 to 20 nm in length.

Both samples analysed by HAADF-STEM contain approximately 20 % of 2 to 3 nm particles, which are likely responsible for the high catalytic activity. However, the TOF at 450 °C for *0.5Au/10hthin-ads-wash-red200* ($3338.1 \text{ mol}_{\text{CO}_2} \cdot \text{mol}_{\text{Au}}^{-1} \cdot \text{h}^{-1}$) is more than twice as high compared to *1.0Au/plate-ads-wash-red200* ($1408.6 \text{ mol}_{\text{CO}_2} \cdot \text{mol}_{\text{Au}}^{-1} \cdot \text{h}^{-1}$). Since spherical gold particles greater than 10 nm in diameter are believed to be inactive for CO oxidation, it is likely that the higher activity of *0.5Au/10hthin-ads-wash-red200* can be attributed to the presence of the elongated particles. Unlike spherical particles greater than 10 nm in diameter, the elongated particles are likely to still contain a high concentration of defect active sites usually found in 2 to 3 nm spherical nanoparticles. It is plausible that the elongated particles in *0.5Au/10hthin-ads-wash-red200* form during reduction at 200 °C due to physical confinement of the nanorod support which inhibits motion of the nanoparticles in all directions except along the length of the rod. By contrast, the reductive thermal treatment of *1.0Au/plate-ads-wash-red200* results in agglomeration into less active or inactive particles. The combined assessment of the dark field micrographs and the catalytic activity of these two materials highlights the implication of support morphology on metal nanoparticle stabilisation. It is shown that the use of the nanorod support provides stabilisation against agglomeration into less active, spherical particles. This data provides evidence for the stabilisation by physical confinement of metal nanoparticles on curved nanorod supports compared to conventional flat supports.

Often in the literature, nanoparticulate gold supported on a reducible support (e.g. TiO_2) is capable of catalysing CO oxidation at sub ambient conditions, with temperatures as low as -70 °C reported.¹⁵ However, due to the choice of a non-reducible support, the activity of the $\text{Au}/\gamma\text{-Al}_2\text{O}_3$ catalysts tested only starts above ~ 250 °C in most cases, despite the small average particle size in some samples. This highlights the requirement for both small particle size (2 to 3 nm) and interaction from a reducible support in order to achieve sub-ambient CO oxidation activity.

One clear distinction between the literature studies and the work carried out herein is the absence of a precipitant. In the previous chapter, the need for a precipitant in the synthesis of $\text{Co}/\gamma\text{-Al}_2\text{O}_3$ was justified in order to increase the solution pH above the point of zero charge to

enable cobalt adsorption without high CoAl_2O_4 formation. The same theory applies for loading gold and synthesis of gold nanoparticles by deposition are commonly carried out at pH greater than 8 using precipitants such as NaOH, urea and Na_2CO_3 .¹² This pH dependent behaviour is highlighted by CO oxidation of Au/ γ - Al_2O_3 catalysts synthesised by deposition-precipitation at increasing pH from 6.5 to 8.6, leading to an improvement in CO oxidation activity, reflected by a downward shift of T_{50} from 130 to 2 °C.¹² However, since gold was successfully loaded onto the support, albeit at lower loadings than the theoretical content but without the formation of “irreducible” oxidic compounds, a precipitant was not employed. The use of HAuCl_4 as the gold source decreases the synthesis pH from 10 (the support in water) to 4 or 5. Thus, it is plausible that carrying out the gold synthesis under acidic conditions rather than basic conditions results in a difference in surface chemistry, which inhibits the low temperature activity reported for Au/ γ - Al_2O_3 (Table 4). In any case, the purpose of testing the catalysts for CO oxidation is to provide evidence for the effect of support morphology on particle size and activity, for which it has been successful.

Another interesting observation of the catalytic data is the reason for the very poor activity observed for the lower loading *commercial* supported catalyst, *0.4Au/commercial-ads-wash-red200*. When compared with a catalyst with similar loading such as *0.5Au/10hthin-ads-wash-red200* the TOF at 450 °C is nearly an order of magnitude lower with the *commercial* support despite a smaller average size of 4.0 nm as estimated by pulse chemisorption for *0.4Au/commercial-ads-wash-red200* and 7.8 nm for *0.5Au/10hthin-ads-wash-red200*. This difference in activity may be due to a different size distribution or strength of interaction with the support, highlighting the beneficial effect of nanostructuring the support. For the catalysts supported on *commercial* γ - Al_2O_3 with more than 1 wt% Au, the poor activity can be attributed to the large particle sizes estimated by pulse chemisorption (25 to 38 nm) formed as a result of the higher loading, suggesting the support is not effective at inhibiting sintering under the reduction conditions at 200 °C.

7.2.5.3 Effect of gold synthesis method and support morphology

The choice of gold loading method determines the properties of the resulting catalyst such as particle size and thus the CO oxidation catalytic activity. This section discusses the implications of the method on the catalytic activity for the catalysts supported on different morphologies of γ -Al₂O₃.

The sodium content of the catalysts is lower in the materials produced by the adsorption method compared to IWI but this is unlikely to be the cause for the differences in catalytic activity as sodium has not been reported to affect CO oxidation activity.

The final gold loading in the Au/ γ -Al₂O₃ material is altered by both the loading method and the support morphology. For example, the theoretical 1.4 wt% Au series synthesised by IWI contain 0.2 to 0.7 wt% Au, whereas adsorption materials for the same theoretical content contain 0.1 to 1.2 wt% Au. The loading range is greater with the adsorption method but there is no clear trend for the support that favours the highest loading across both methods, suggesting that the final loading is not only dependent on the support type but also on the gold concentration in solution due to the effect on the nuclei size and the resulting metal-support interaction strength. For example higher loadings on the *commercial* support are favoured with adsorption compared to IWI. By contrast, IWI results in the highest loading on the *plate* support (0.7 wt%) but very low loadings from the adsorption method (0.01 and 0.08 wt% Au). The loading is significant because it may encourage the formation of different sized particles, which in turn affects the catalytic activity.

The range of gold reduction temperatures observed by TPR is greater for the adsorption catalysts compared to IWI, indicative of different metal-support interaction strengths. Furthermore, for both methods the resulting catalysts supported on the *commercial* support tend to have sharper reduction peaks. The fact that the average particle size determined from TEM and pulse chemisorption agrees for catalysts synthesised by adsorption but not by IWI, suggests that some very large particles are formed by the IWI method, (observed for *0.5Au/10hthin-ads-wash* in Figure 84bii, as a result of the weak metal-support interaction.

Interestingly, elongated particles were visible on the *10hrod* supported catalyst synthesised by adsorption (*0.5Au/10hthin-ads-wash*) but not by IWI (*0.3Au/10hthin-IWI-wash*) and not in any sample supported on the flat *plate*. The presence of these particles highlight two key points that

have been briefly touched upon earlier. Firstly, the adsorption method results in a stronger metal-support interaction; and secondly, provided the interaction is strong enough, nanorods are capable of stabilising small, unstable gold nanoparticles. These results provide evidence for the research hypothesis of stabilisation using curved supports.

In general the gold particle sizes are smaller due to the use of nanostructured supports and the use of the adsorption loading method. Consequently, significantly higher rates of CO oxidation for these materials are observed as the nanostructured support can effectively stabilise the small particles.

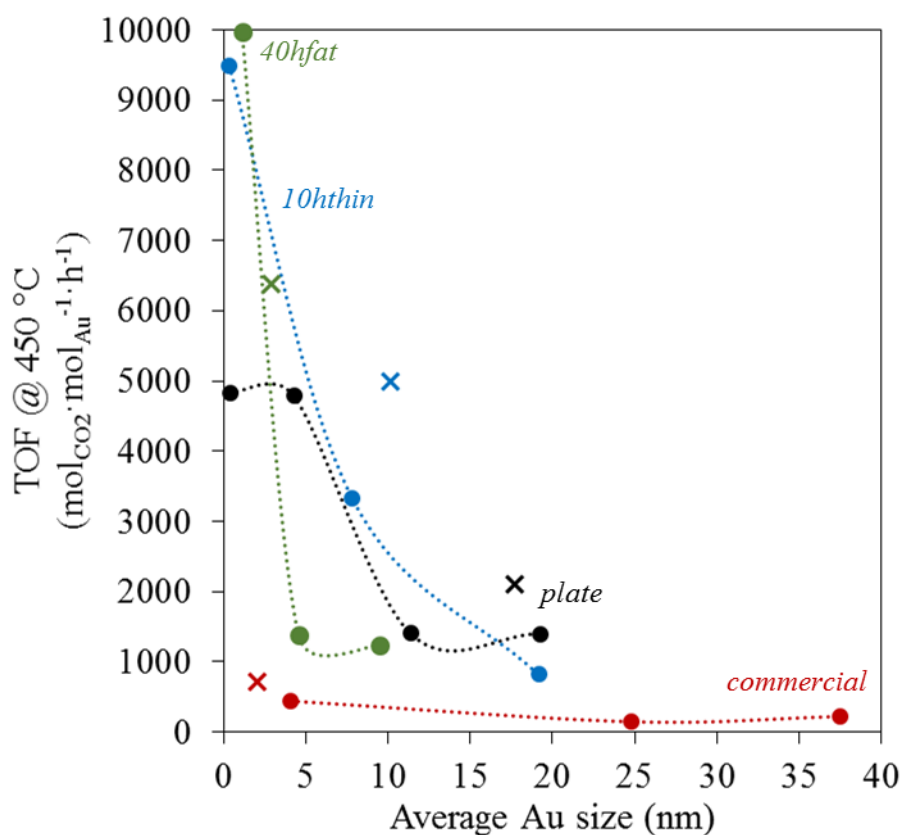


Figure 89. TOF at 450 °C with respect to average gold size calculated by pulse CO chemisorption for Au/ γ -Al₂O₃. Synthesised by IWI (x) and adsorption (●). Plate (black), 40hfat (green), 10hthin (blue) and commercial (burgundy).

Figure 89 compares the CO oxidation TOF at 450 °C for all the Au/ γ -Al₂O₃ materials discussed in this chapter, highlighting the strong dependency of catalytic activity on particle size and support morphology. As shown in Figure 89, for catalysts with less than 10 nm average gold size, the rate of CO₂ production at 450 °C is accelerated by the use of a nanostructured support. Note that the average particle size estimated from CO pulse chemisorption is used for simplicity in Figure 89 but the catalytic activity is essentially dependent on the proportion of

gold particles that are 2 to 3 nm in diameter. In the case of the *10hthin* and *plate* supported catalysts, the use of the adsorption method decreases the average particle size and increases the catalytic activity.

It is clear from Figure 89 that the materials supported on *commercial* γ -Al₂O₃ are highly inactive, regardless of the gold loading method and the small size estimated by chemisorption in some cases.

Since the TOF is calculated at 450 °C for the third run, it is possible that the catalysts supported on *plate* and *commercial* sinter to form larger, inactive particles during the first catalytic testing run resulting in the poor catalytic activity observed. This highlights the beneficial effect of the nanorod support in stabilising the active 2 to 3 nm gold nanoparticles. It is also evident that for gold particles with average diameters less than 5 nm estimated by pulse chemisorption the use of a nanorod support (*10hthin* or *40hfat*) accelerates the rate of reaction. This is observed in Figure 89 as the TOF at 450 °C is twice as high with a nanorod support compared to the use of *plate* support and tenfold higher compared to the use of *commercial* support.

In general, however, the T₅₀ values for the materials in this chapter range from 375 to 445 °C, significantly higher than values reported for CO oxidation by Au/ γ -Al₂O₃ in the literature which range from -28 to 333 °C (Table 4). This discrepancy may be due to the choice of method and the resulting synthesis pH, as the deposition-precipitation method at pH higher than 8 is usually used for the synthesis of Au/ γ -Al₂O₃ for sub-ambient CO oxidation activity.

The dependence of CO oxidation activity on synthesis pH is believed to be due to higher synthesis pH favouring the formation of smaller gold nanoparticles, due to the hydroxylation of AuCl₄⁻ under basic conditions to yield Au(OH)₄⁻.^{15,114} However, it has been demonstrated that IWI and adsorption at pH 4 to 5 used herein are capable of forming up to 30 % small 2 to 3 nm gold particles, likely from the use of nanostructured supports. Thus it is expected that acidic adsorption leads to an unfavourable difference in surface composition compared to the basic pH deposition-precipitation method. Following the water assisted CO oxidation mechanism valid for inert supported gold catalysts, the presence of OH⁻ is needed for reaction with CO.¹¹ Thus, catalysts prepared under acidic conditions are less active. This is in agreement with the reported increase in low temperature CO oxidation activity by Au/ γ -Al₂O₃ prepared by impregnation followed by a base wash to convert gold chloride into the hydroxide.¹¹³

7.3 Thermal stability of Au/ γ -Al₂O₃ catalysts

The most likely deactivation mechanism of CO oxidation catalysts is an increase in particle size via sintering.¹²³ Therefore the CO oxidation activity after high temperature stability tests is a useful indicator of the degree of sintering that has taken place and thus the level of stabilisation provided by the support.

The thermal stability of four of the Au/ γ -Al₂O₃ catalysts with less than 1 wt% Au loading were tested by sequentially increasing the CO oxidation reaction temperature from a base set point, ~ 370 °C. The selected catalysts tested were supported on *plate* and *10hthin* γ -Al₂O₃ to determine the effect of support curvature on the degree of stabilisation. In addition, both materials synthesised by IWI and adsorption were tested to compare the stability of the materials produced by the different methods. The activity of the *commercial* supported catalysts is too low to carry out a meaningful study and the activity of *40hfat* materials is similar to the use of *10hthin*, so neither were tested for thermal stability assays.

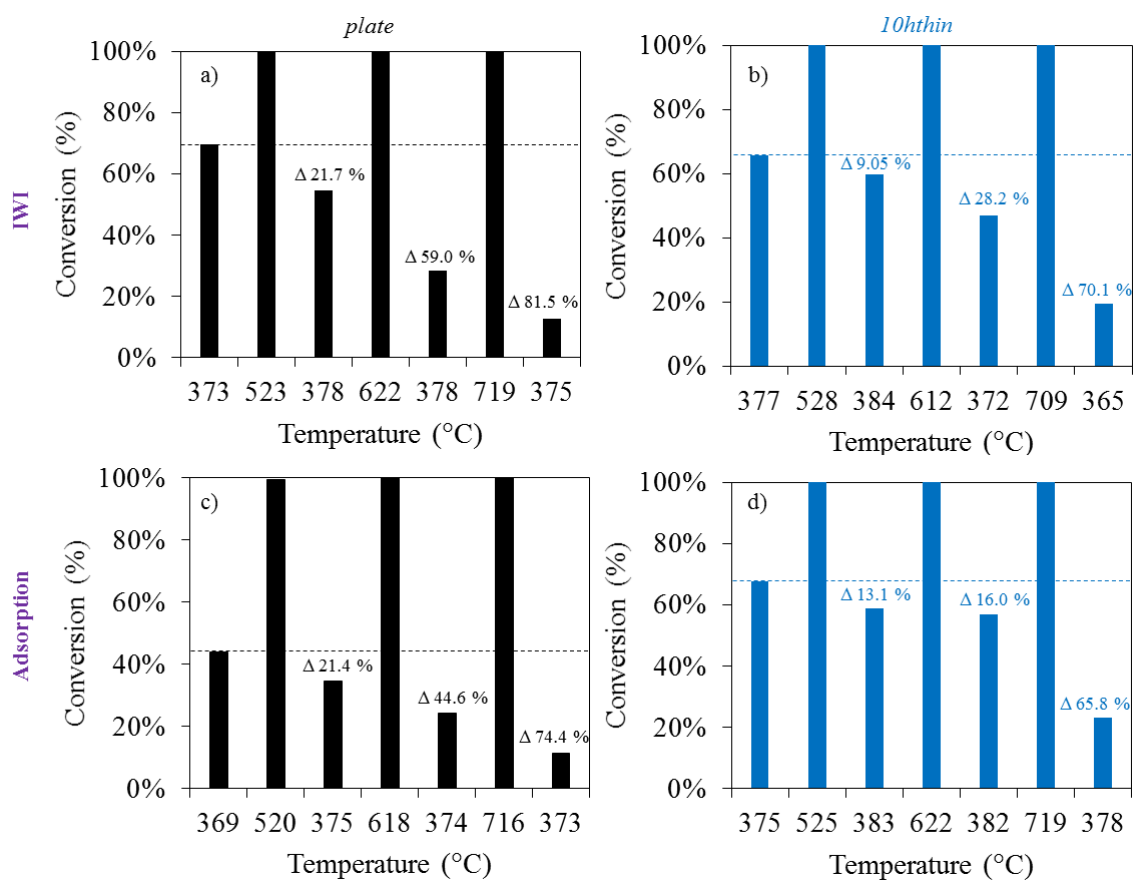


Figure 90. CO oxidation thermal stability test for Au/ γ -Al₂O₃-wash catalysts. a) 0.7Au/*plate*-IWI-wash, b) 0.3Au/*10hthin*-IWI-wash, c) 1.0Au/*plate*-ads-wash and d) 0.5Au/*10hthin*-ads-wash. Samples were pre-reduced *in situ* at 200 °C.

If the initial activity at the fixed base set point is considered to be 100 %, the modification in activity from the first run can be calculated as a percentage change at the next base set point, quantifying the degree of deactivation. The percentage change is presented above the set point bars of the catalytic stability test data shown in Figure 90.

The differences in degree of deactivation after ~ 610 °C conditions between the materials supported by *10hthin* and *plate* is noteworthy. For example, with the catalysts synthesised by IWI, the *plate* supported catalyst deactivates by 59.0 % whereas the use of the *10hthin* nanorod support only loses 28.2 % of its activity, representing a twofold improvement in stabilisation at ~ 610 °C from the use of nanorod support. The effect of stabilisation after ~ 610 °C by nanorods is demonstrated further with the adsorption synthesised catalysts in which 44.6 % compared to 16.0 % loss in activity is observed from the use of the *plate* support compared to *10hthin* nanorods respectively.

The degree of high temperature stabilisation after ~ 710 °C exposure is relatively higher for the materials synthesised by adsorption compared to IWI, suggesting a stronger metal-support interaction resulting from the former method, in agreement with the discussion in the previous section (7.2.5.3). In addition, approximately 10 % less deactivation after ~ 710 °C exposure is observed for the materials supported by *10hthin* compared to *plate* regardless of the method of gold preparation. This suggests that the nanorod support is capable of providing additional stabilisation due to the curvature of the surface restricting the mobility of the nanoparticles.

Chapter 7 conclusions

A set of experimental protocols for the preparation of Au/ γ -Al₂O₃ catalysts was determined by characterising and catalytically testing a theoretical 1.4 wt% Au catalyst synthesised by IWI with different work up procedures. The catalytic data highlights the deactivation by chlorine in the unwashed sample and by calcination at 250 °C, both of which are believed to encourage sintering. Reduction of the washed sample at 200 °C made a small improvement on catalytic activity and is therefore used in order to apply a consistent heat treatment to all subsequent materials. Using these synthesis conditions, a series of Au/ γ -Al₂O₃ catalysts with different gold loadings were synthesised by IWI and adsorption on γ -Al₂O₃ with four different morphologies.

The choice of method affects the metal-support interaction strength, the size of the resulting gold and thus the catalytic activity. The adsorption method resulted in the formation of the most active catalysts but these materials had lower metal loadings than the IWI series. Thermal stability tests confirm that the metal-support interaction is stronger for catalysts synthesised by adsorption compared to IWI, based on less deactivation in the materials synthesised by the latter after 710 °C reaction conditions independent of the support used. However, the thermal stability of catalysts synthesised on a flat support (*plate*) is lower than the analogous material supported on a curved support (*10hthin*). For example with the use of *plate* support after 610 °C reaction conditions, the catalyst deactivates 30 % more than with *10hthin* and after 710 °C deactivates by 10 % more, further highlighting the metal nanoparticle stabilisation capability of the nanorods.

Despite the common criticism of IWI for gold synthesis, TEM imaging of some of the IWI synthesised materials herein were found to contain 10 to 30 % of 2 to 3 nm active particles, possibly due to the washing step removing chlorine which encourages sintering. However, IWI also resulted in the formation of large, inactive gold particles greater than 40 nm. The thermal stability tests found that materials produced by IWI deactivated more than those synthesised by adsorption. In future, the deposition-precipitation method should be applied to these precursors and methods in order to improve the low temperature CO oxidation activity.

Lower gold loadings resulted in the formation of smaller gold nanoparticles, which are effectively stabilised by nanorods. More specifically, with less than 0.02 wt% Au loading, both the *40hfat* and *10hthin* support are effective at stabilising small particles, resulting in a high

rate of CO₂ production with the maximum rate of reaction at 450 °C achieved by *0.02Au/40hfat-ads-wash-red200*.

In all cases, the use of the *commercial* support results in poorly active catalysts due to the large particle size calculated. However, in one case a small size after reduction is calculated but the catalysts is still fairly inactive, possibly due to a weak metal-support interaction.

Thus, the morphology of the support is demonstrated to have a significant effect on the stabilisation of small (2 to 3 nm) gold nanoparticles, with nanorod supports resulting in fivefold or tenfold improvement in reaction rates compared to flat or *commercial* supports respectively. The improvement in activity may also be due to the presence of elongated particles observed by TEM. These elongated particles are only observed in a sample supported on thin nanorods (*0.5Au/10hthin-ads-wash-red200*) when the metal-support interaction is strong due to the use of the adsorption method. The presence of these particles provides unequivocal evidence for the stabilisation effect of curved supports for small gold nanoparticles due to their physical confinement.

Chapter 8 – Conclusions and future work

In this final chapter, the scientific evidence presented herein with regards to validation of the research hypothesis is summarised. Key conclusions from each research chapter are outlined, including areas for future work.

The overall aim of this thesis is to determine if metal nanoparticles can be stabilised by curved surfaces relative to conventional flat surfaces. The key results supporting the novel stabilisation strategy are summarised in Section 8.1. In order to approach this aim, four objectives were devised, the results from which have been presented in this thesis and the main conclusions are found in this chapter. Firstly, a route for the production of morphologically pure curved and flat support surfaces was achieved in Chapter 4. Secondly, the effects of gold and cobalt metal loading methods onto the support was presented in Chapters 5 and 7. Thirdly, the catalytic activity of metal nanoparticles supported on nanostructured γ -Al₂O₃ was carried out using model reactions in Chapter 5 to 7. Finally, the thermal stability of these catalysts was considered in Chapters 6 and 7.

8.1 Hypothesis of metal nanoparticle stabilisation by confinement using curved supports

The liquid-like properties of high-energy, small metal nanoparticles wetting a flat surface enables mobility and agglomeration with the provision of energy. Agglomeration results in irreversible deactivation for size-sensitive catalytic applications. This thesis hypothesises that stability can be provided to unstable metal nanoparticles by physical confinement on a curved surface. This is further enhanced by an increase in metal-support contact area.

Strong evidence has been presented herein which supports the hypothesis in the cases when the nanoparticle is a suitable size relative to the diameter of the nanorod. This was demonstrated not only for the *ICo/γ-Al₂O₃-NaOH* catalyst supported on thin nanorods (8 nm diameter) but also for strongly interacting Au/γ-Al₂O₃ catalysts supported on thin nanorods (8 nm diameter). For these materials, the formed particles are small enough in diameter (P) relative to the diameter of the rod (R), so P:R < 1.

In these cases, elongation of the particles was observed along the length of the rod as well as individual small, stabilised particles as shown in Figure 91. By contrast, only spherical, agglomerated particles were observed in samples supported on a flat support. The presence of these two classes of particles in the nanorod supported catalysts unequivocally confirm that curved surfaces offer additional stabilisation compared to flat surfaces. The reason for the elongation of the particles is because the surface can be considered flat along the direction of the rod, meaning that mobility is unrestricted. Nevertheless, the presence of highly strained, elongated particles may also be a contributing factor in the enhanced activity observed with the nanorod supported samples.

The multi-crystalline nature of the γ -Al₂O₃ nanorods synthesised herein may cause some degree of surface roughness as the surface is not perfectly smooth nor is it a perfectly cylindrical rod-shape as the model assumes (Figure 2). In addition, the strength of the metal-support interaction is also a factor that can affect the validity of the hypothesis. For example, in the case of Au/ γ -Al₂O₃ elongation of the particles was only observed in the sample synthesised by adsorption and not by IWI due to the difference in metal-support interaction.

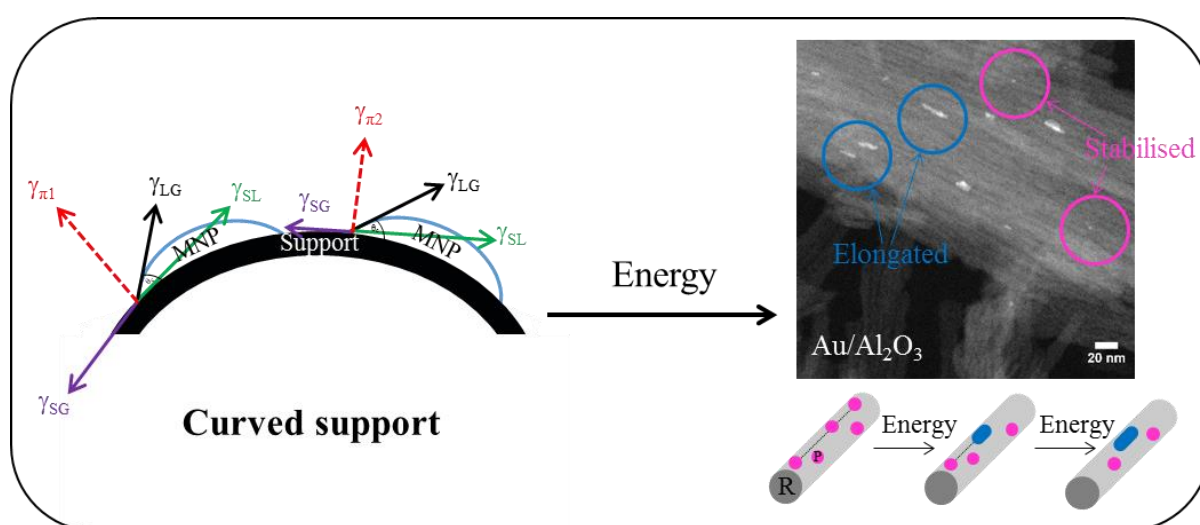


Figure 91. Metal nanoparticle stabilisation by confinement on curved supports.

The evidence presented in this thesis for Co/ γ -Al₂O₃ and Au/ γ -Al₂O₃ catalytic systems supports the conclusion that the hypothesis of nanoparticle stabilisation using curved supports is valid for cases when the ratio of the nanoparticle diameter (P) and the diameter of the nanorod support (R) is less than one, $P:R < 1$.

8.2 Hydrothermal synthesis of nanostructured γ - Al_2O_3

The controlled hydrothermal synthesis of pure γ - Al_2O_3 nanostructures was extensively covered in Chapter 4. The importance of the choice of synthesis parameters such as the NaOH:Al ratio, synthesis time and temperature was highlighted by the results. Not only does the NaOH:Al ratio affect the product yield, but also the morphology due to its influence on the synthesis pH. γ - Al_2O_3 nanorods are selectively synthesised under acidic conditions (pH 3.5) while γ - Al_2O_3 nanoplates are formed under basic conditions (pH > 11.2). The size of γ - Al_2O_3 nanorods obtained from hydrothermal synthesis can be tuned by varying the reaction time and temperature. The ability to tailor the morphology and curvature is facilitated by the elucidation of a detailed formation mechanism as the rate of individual steps can be varied with different synthesis conditions.

The morphological purity of the γ - Al_2O_3 nanorods can only be achieved at low aluminium yields and thus, the recyclability of the reaction supernatant has also been explored, providing an understanding of the different factors affecting the potential large-scale manufacturing of these materials. The results confirmed the feasibility to move from batch to semi-continuous synthesis, demonstrating the possibility of scale up of this technology.

Future work:

The next step in the synthesis of nanostructured γ - Al_2O_3 could be to try to decrease the synthesis time (currently 10 to 40 hours), possibly by the use of microwave-assisted hydrothermal methods, in order to streamline production of these materials. In addition, longer term recycle studies continuing the work exploring the possibility for sustainable scale up of these materials is of commercial relevance and importance due to the range of applications and beneficial properties offered by nanostructured materials.

8.3 Effect of cobalt loading methods on Co/ γ -Al₂O₃ properties and catalytic activity

In this chapter the γ -Al₂O₃ nanoplates produced in the previous chapter were used to support cobalt nanoparticles by a range of different loading methods. In addition, an experimental protocol was developed for the testing of catalysts for NH₃ decomposition in terms of calcination and reduction. The active species for Co-catalysed NH₃ decomposition was confirmed to be Co⁰ as the rate of reaction increased with higher reduction temperatures, consistent with observations from the TPR profiles.

The choice of method was found to alter the particle size, reducibility, composition and oxidation state, which ultimately affects the NH₃ decomposition activity. Specifically adsorption and precipitation by a borate buffer were found to be the least suitable methods to produce Co/ γ -Al₂O₃ due to the formation of either inactive cobalt aluminate or contamination (boron, chlorine and potassium), respectively. The carbonate buffer precipitation method produced the most active catalyst at high temperature, probably due to the smallest Co⁰ particle size (7.7 nm). However, this method resulted in some damage to the support which may affect the surface roughness. In some samples (from adsorption and urea precipitation methods), no metallic cobalt pXRD peaks were observed and since dark field TEM is difficult to access, detailed size-activity comparisons across the series was challenging.

Future work:

It would be interesting to complete imaging of all the reduced samples by dark field TEM. In addition, alternative methods for accurate particle size determination of Co/ γ -Al₂O₃ could be explored.

8.4 Effect of support morphology on Co/ γ -Al₂O₃ catalytic activity and stability

For practical reasons, the IWI and NaOH precipitation methods were chosen from the findings of the previous chapter to synthesise a range of Co/ γ -Al₂O₃ catalysts with different support morphologies and metal loadings. In order to provide a benchmark, these materials were

compared to analogous catalysts supported on a commercial γ -Al₂O₃ support. The materials were characterised and tested for NH₃ decomposition activity.

The tendency for Co to form irreducible cobalt aluminate using the IWI method of synthesis with low Co loading (1 wt% Co) is derived from the strong metal-support interaction, rendering this series inactive. However, the use of the NaOH method for the same low loading enabled the formation of Co⁰ nanoparticles suspected to be smaller than equipment detection capabilities (< 2 nm). The unprecedented high activity of these materials suggests B3 to be the active Co fcc (111) site for NH₃ decomposition. The difference in their catalytic activity as a function of support morphology is revealed due to the difference in stabilisation offered by the support. In this case, the thin nanorod support (8 nm average diameter) proves to be the most effective at stabilising the small nanoparticles, evidenced by the extremely high activity and elongation of particles along the length of the nanorod. Stabilisation is effective in this case because the particle size (P) is believed to be a suitable size with respect to the nanorod diameter (R) as their ratio is less than one (P:R < 1). By contrast, the analogous catalysts supported on the *commercial* support is less active by an order of magnitude. When higher loadings are used (> 5 wt%), the size of the resulting nanoparticle is no longer suitable in relation to the diameter of the rod, so the beneficial stabilisation effect of the curved support is not observed.

Future work:

Future work for this chapter could focus on increasing the abundance of the small particles stabilised at low loadings (1 wt% Co) by repeating the NaOH precipitation method to achieve a higher concentration of the small particles. This may help to shift the NH₃ decomposition temperature towards the 150 °C practical application target. If this can be achieved with a highly stable catalyst comprised of a less expensive metal than ruthenium (the current state-of-the-art catalyst), such as cobalt, the economic feasibility of NH₃ as a hydrogen storage vector becomes a realistic possibility for the future of renewable energy. Thermal stability catalytic tests of the 1 wt% series synthesised by NaOH precipitation catalysts stabilised by nanorods would be necessary to demonstrate the effectiveness of these materials for long term usage. Cobalt-metal alloys supported on nanorods should be explored for this application, using metals such as rhenium and molybdenum.

8.5 Effect of support morphology on Au/ γ -Al₂O₃ catalytic activity and stability

Gold nanoparticles are investigated as a second catalytic system to test the research hypothesis. The synthesis process variables were first considered in order to optimise the method. Washing and reduction at 200 °C were determined to be necessary steps for the Au/ γ -Al₂O₃ materials. A series of catalysts produced by different methods, with varied metal loading and support morphology were characterised and tested for CO oxidation. In order to carry out the catalytic tests of Au/ γ -Al₂O₃, a catalytic testing rig was designed, constructed, commissioned and operated as part of this project.

Characterisation, catalytic testing and stability tests suggests that the Au/ γ -Al₂O₃ support interaction is stronger for materials synthesised by adsorption compared to IWI. Provided this strong interaction and the use of a nanorod support, small gold particles were observed by TEM to have arranged themselves along the length of the rod forming an elongated particle. This phenomenon was not observed in the other imaged samples supported on nanoplates or synthesised by IWI but instead larger, agglomerated particles were observed. Thus, the stabilisation effect of a curved support is demonstrated again for the Au/ γ -Al₂O₃ system provided there is a sufficiently strong interaction.

Future work:

Au/ γ -Al₂O₃ catalysts supported on thin nanorods (8 nm diameter) should be synthesised by base precipitation. The change in surface chemistry combined with the stabilisation effect of the nanorod of small particles could be the answer to unlock sub-ambient CO oxidation by Au with an irreducible support.

Appendix

A selection of supplementary figures are included in this appendix section to support the results presented in Chapters 4 to 7. The “A” label in the figure names demonstrates that the figure is located in the appendix.

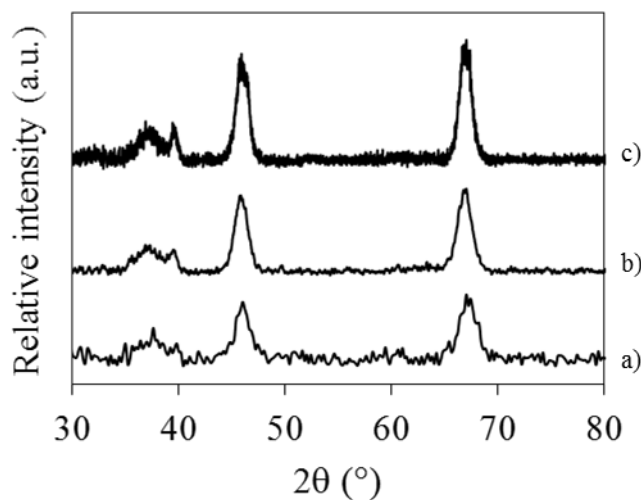


Figure A92. pXRD pattern for γ - Al_2O_3 rods synthesised with 0.77NaOH:1Al, 20 hours and different temperature. a) 170 °C b) 180 °C and c) 200 °C. (JCPDS Card No. 10-0425)

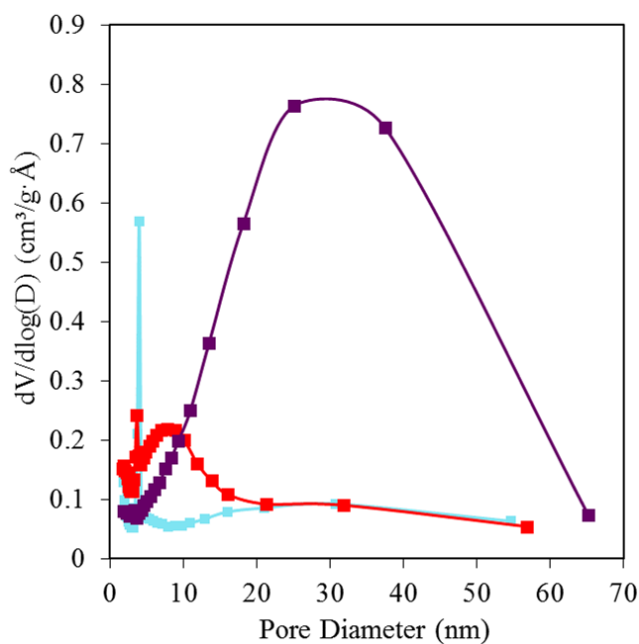


Figure A93. Pore size distributions of γ - Al_2O_3 synthesised with 0.77NaOH:1Al for 20 hours 170 °C (pale blue), 180 °C (red) and 200 °C (purple).

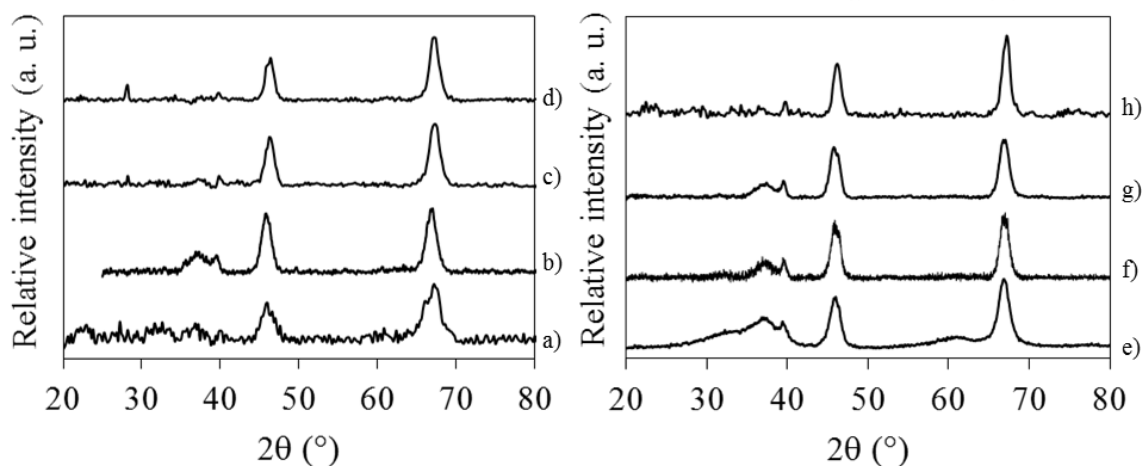


Figure A94. pXRD pattern for γ - Al_2O_3 rods synthesised with 0.77NaOH:1Al and different synthesis conditions. 180 °C for a) 10 hours b) 20 hours c) 40 hours and d) 80 hours. 200 °C for e) 10 hours f) 20 hours g) 40 hours and h) 80 hours. (JCPDS 10-0425)

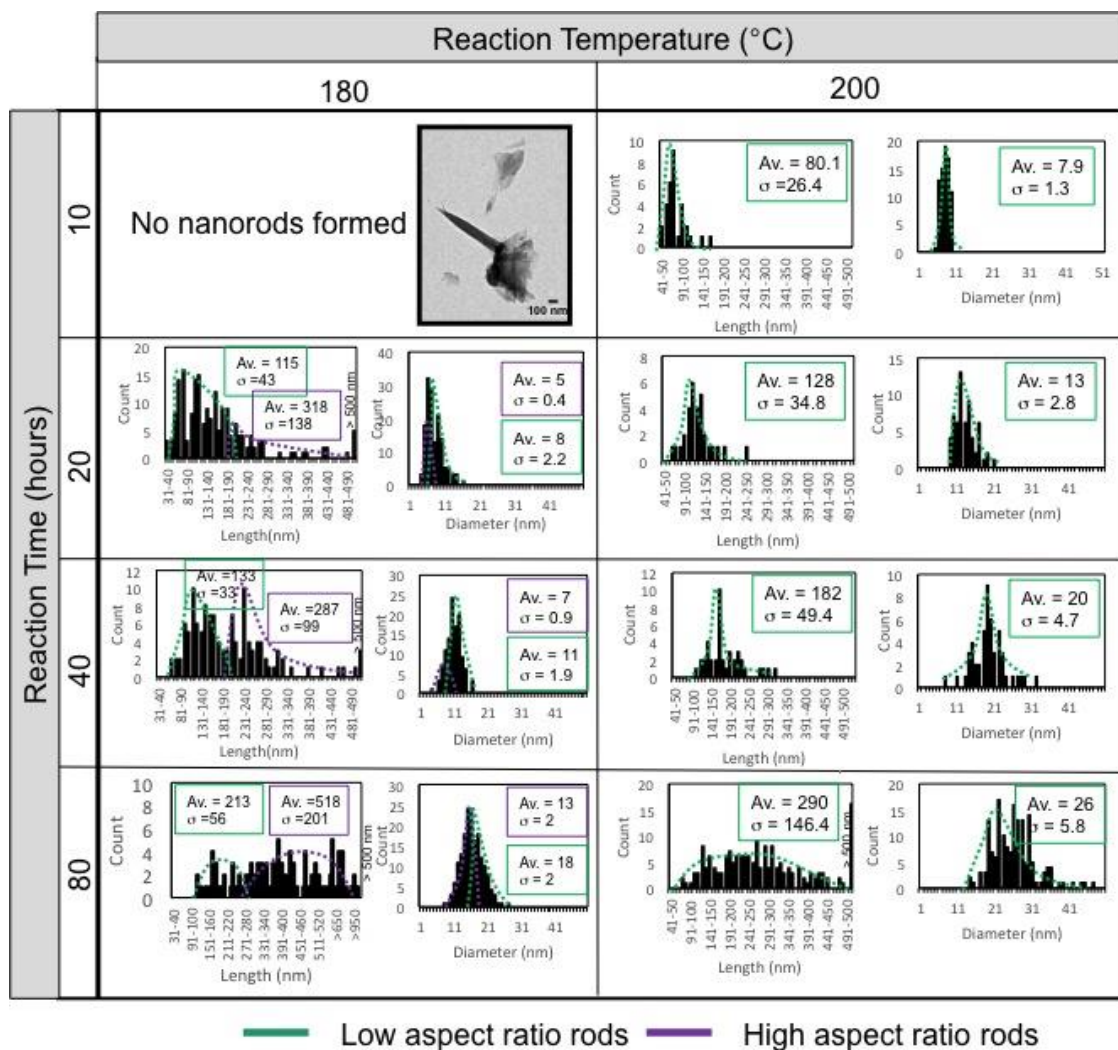


Figure A95. Length and diameter size distributions obtained from analysis of TEM micrographs of γ - Al_2O_3 rods. Synthesised for different times (10 to 80 hours) and temperatures (180 °C and 200 °C) with 0.77NaOH:1Al molar ratio. Green lines for *short/thick* nanorods and purple lines for *long/thin* nanorods.

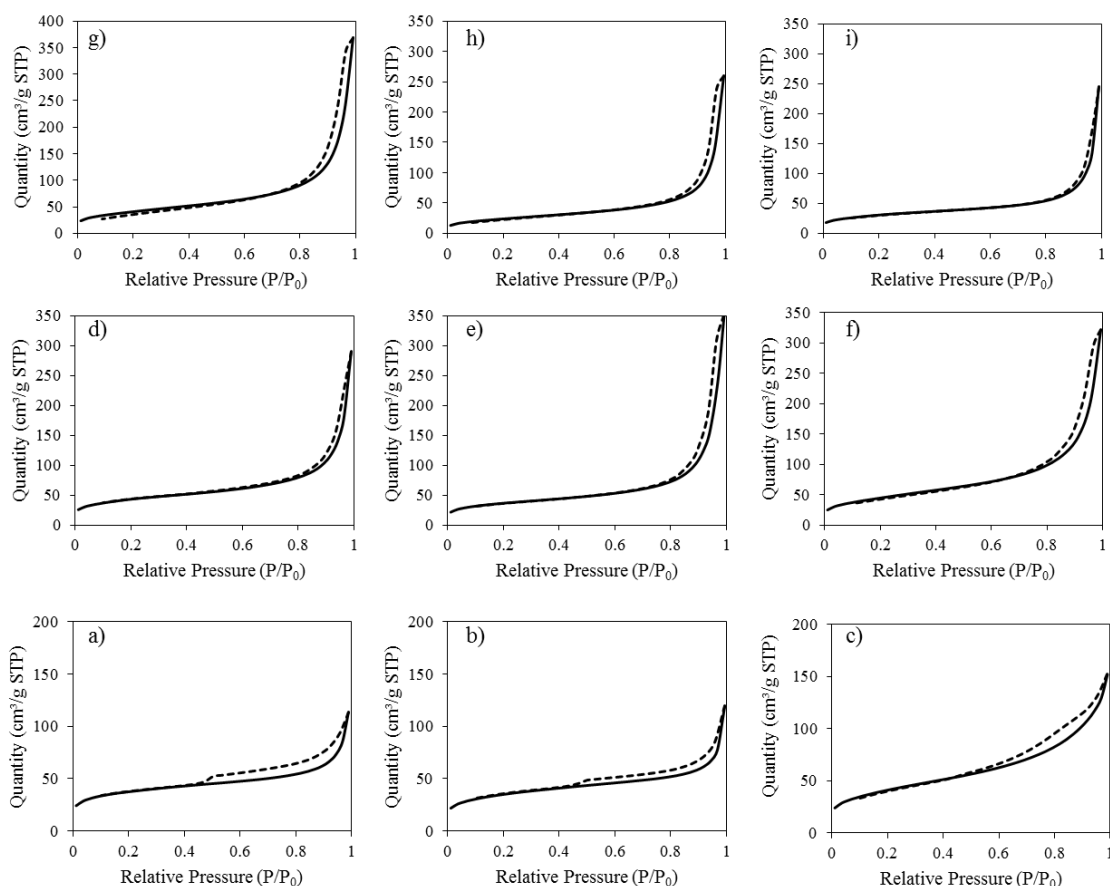


Figure A96. N₂ adsorption-desorption isotherms at -196 °C of γ -Al₂O₃ synthesised with 0.77 NaOH:Al molar ratio. a) 170 °C for 20 hours, b) 180 °C for 10 hours, c) 180 °C for 20 hours, d) 180 °C for 40 hours, e) 180 °C for 80 hours, f) 200 °C for 10 hours, g) 200 °C for 20 hours, h) 200 °C for 40 hours and i) 200 °C for 80 hours. Adsorption shown by the solid line and desorption is represented by the dashed line.

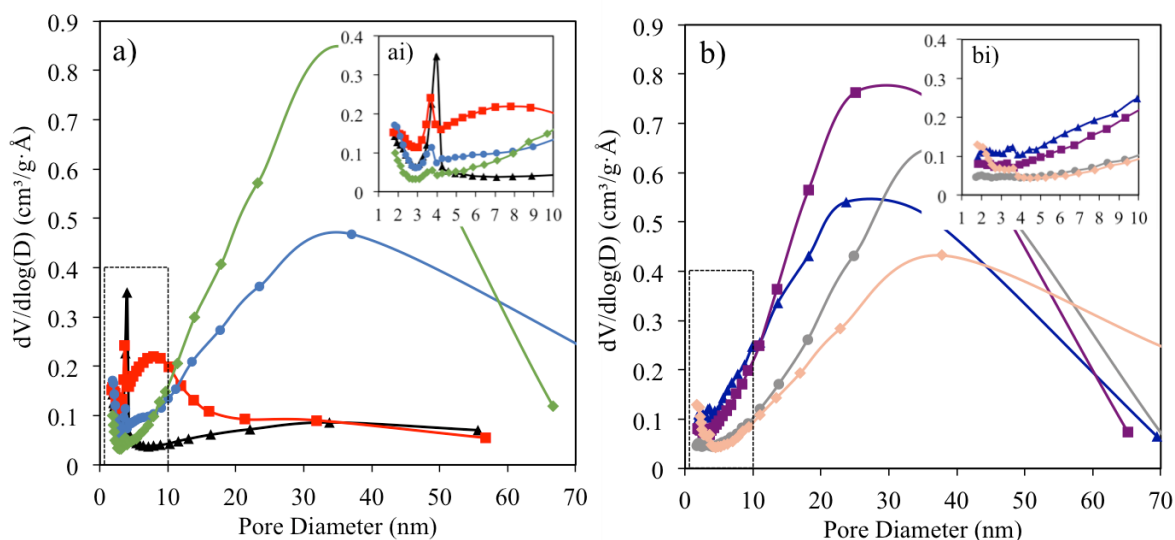


Figure A97. Pore size distributions of γ -Al₂O₃ synthesised with 0.77NaOH:1Al at a) 180 °C and b) 200 °C. Inserts in i) show the distribution from 1 to 10 nm. The marker shape distinguishes the different synthesis time: 10 hours (▲), 20 hours (■), 40 hours (●) and 80 hours (◆).

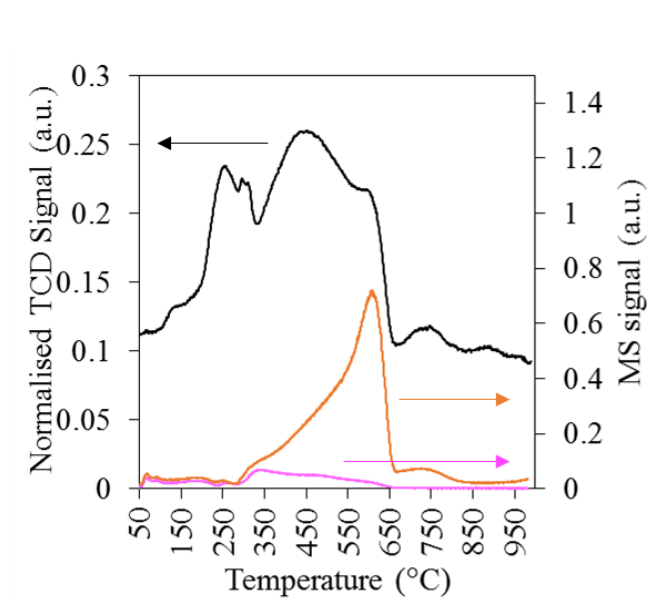


Figure A98. TPR (LHS) and MS (RHS) data for 6.8Co/plate-NaOH-cal250. Pink and orange lines correspond to MS traces for m/z 16 (CH_4) and 28 (N_2) respectively.

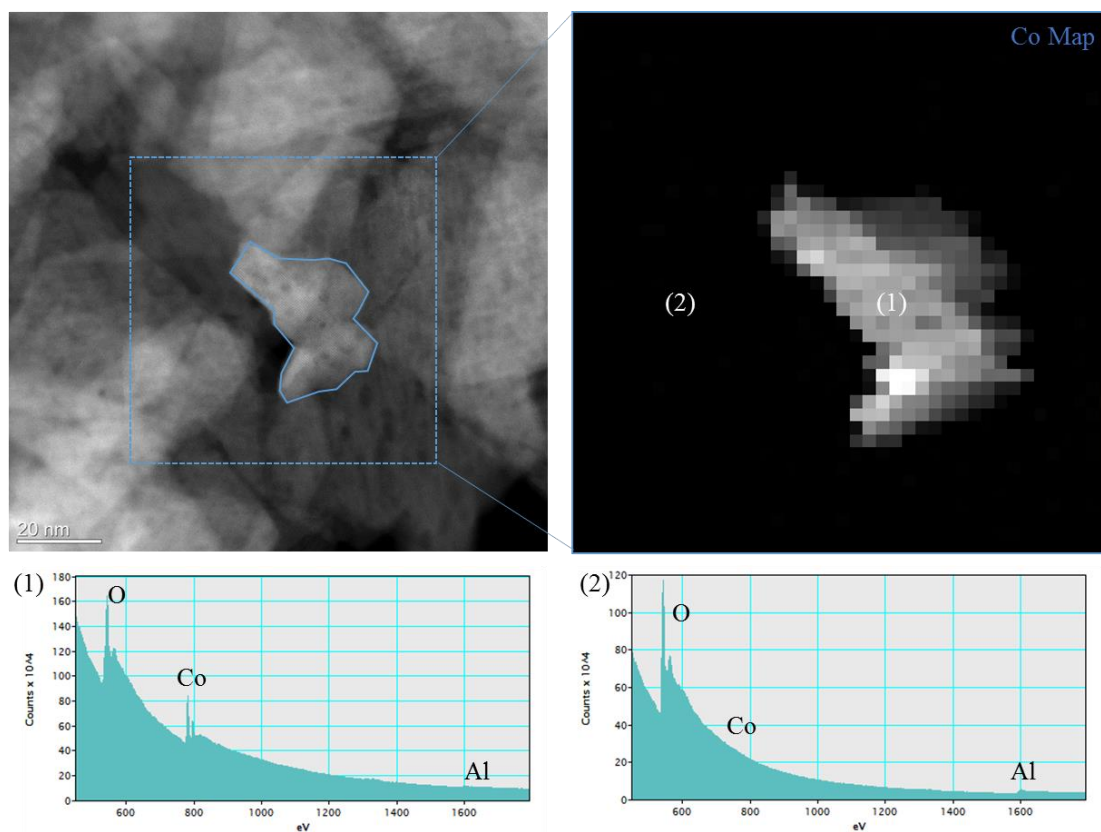


Figure A99. EELS mapping of 7.7Co/plate-IWI-cal250. Cobalt particles surrounded by solid blue line.

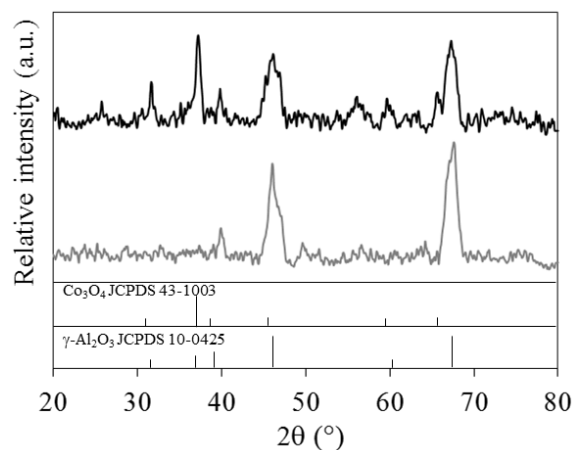


Figure A100. pXRD of *plate* γ -Al₂O₃ support (grey) and *9.1Co/plate-NaOH-cal500* calcined at 500 °C (black). (γ -Al₂O₃ JCPDS 10-0425, Co₃O₄ JCPDS 43-1003)

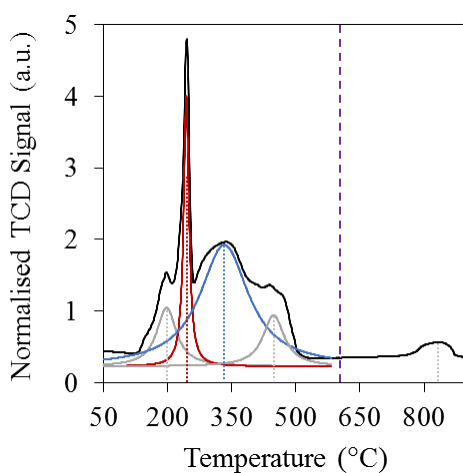


Figure A101. TPR profile of unsupported CoOOH (*42.6Co-unsupported*). Normalised TCD signal = black line, support = black dashed line, 580 °C employed reduction temperature = vertical purple dashed line, Co³⁺ → Co²⁺ = burgundy curve and Co²⁺ → Co⁰ = blue curve and removal of impurities = grey curve.

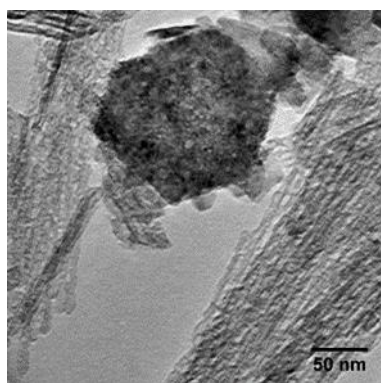


Figure A102. Bright field TEM micrographs of fresh *16.6Co/180thin-NaOH* showing a large hexagonal structure.

References

- 1 Oxford Economics, *The Economic Benefits of Chemistry Research to the UK*, 2010.
- 2 F. Diehl and A.Y. Khodakov, Promotion of Cobalt Fischer-Tropsch Catalysts with Noble Metals: a Review, *Oil Gas Sci. Technol. - Rev. l'IFP*, 2008, **64**, 11–24.
- 3 A. Moisala, A.G. Nasibulin and E.I. Kauppinen, The role of metal nanoparticles in the catalytic production of single-walled carbon nanotubes—a review, *J. Phys. Condens. Matter*, 2003, **15**, S3011–S3035.
- 4 M. José-Yacamán, C. Gutierrez-Wing, M. Miki, D.Q. Yang, K.N. Piyakis and E. Sacher, Surface Diffusion and Coalescence of Mobile Metal Nanoparticles, *J. Phys. Chem. B*, 2005, **109**, 9703–9711.
- 5 J. M. Campelo, D. Luna, R. Luque, J.M. Marinas and A.A. Romero, Sustainable Preparation of Supported Metal Nanoparticles and Their Applications in Catalysis, *ChemSusChem*, 2009, **2**, 18–45.
- 6 A. Cao, R. Lu and G. Veser, Stabilizing metal nanoparticles for heterogeneous catalysis, *Phys. Chem. Chem. Phys.*, 2010, **12**, 13499–13510.
- 7 Y.-F. Han, Z. Zhong, K. Ramesh, F. Chen and L. Chen, Effects of Different Types of γ - Al_2O_3 on the Activity of Gold Nanoparticles for CO Oxidation at Low-Temperatures, *J. Phys. Chem. C*, 2007, **111**, 3163–3170.
- 8 E. Roduner, Size matters: why nanomaterials are different, *Chem. Soc. Rev.*, 2006, **35**, 583–592.
- 9 N. Fischer, B. Clapham, T. Feltes, E. van Steen and M. Claeys, Size-Dependent Phase Transformation of Catalytically Active Nanoparticles Captured In Situ, *Angew. Chemie Int. Ed.*, 2014, **53**, 1342–1345.
- 10 P. Munnik, P.E. De Jongh and K.P. De Jong, Recent Developments in the Synthesis of Supported Catalysts, *Chem. Rev.*, 2015, **115**, 6687–6718.
- 11 M. Haruta, Spiers Memorial Lecture : Role of perimeter interfaces in catalysis by gold nanoparticles, *Faraday Discuss.*, 2011, **152**, 11–32.

- 12 A. Wolf and F. Schuth, A systematic study of the synthesis condition for the preparation of highly active gold catalysts, *Appl. Catal., A*, 2002, **226**, 1–13.
- 13 M. Campanati, G. Fornasari and A. Vaccari, Fundamentals in the preparation of heterogeneous catalysts, *Catal. Today*, 2003, **77**, 299–314.
- 14 C.N. Satterfield, *Heterogeneous catalysis in practice*, McGraw-Hill, 1980.
- 15 M. Haruta, Size- and support-dependency in the catalysis of gold, *Catal. Today*, 1997, **36**, 153–166.
- 16 K. Phiwdang, S. Suphankij, W. Mekprasart and W. Pecharapa, Synthesis of CuO Nanoparticles by Precipitation Method Using Different Precursors, *Energy Procedia*, 2013, **34**, 740–745.
- 17 M. Bowker, A. Nuhu and J. Soares, High activity supported gold catalysts by incipient wetness impregnation, *Catal. Today*, 2007, **122**, 245–247.
- 18 T. W. Hansen, A.T. DeLaRiva, S.R. Challa and A.K. Datye, Sintering of Catalytic Nanoparticles: Particle Migration or Ostwald Ripening?, *Accounts Chem. Res.*, 2013, **46**, 1720–1730.
- 19 D. Farrusseng and A. Tuel, Perspectives on zeolite-encapsulated metal nanoparticles and their applications in catalysis, *New J. Chem.*, 2016, **40**, 3933–3949.
- 20 W.J. Stark, P.R. Stoessel, W. Wohlleben and A. Hafner, Industrial applications of nanoparticles, *Chem. Soc. Rev.*, 2015, **44**, 5793–5805.
- 21 Q. Yang, The reaction conditions influence on hydrothermal synthesis of boehmite nanorods, *Inorg. Mater.*, 2010, **46**, 953–958.
- 22 M. Ma, Y. Zhu, G. Cheng and Y. Huang, Solvothermal Synthesis of Boehmite and γ -Alumina Nanorods, *J. Mater. Sci. Technol.*, 2008, **24**, 637–640.
- 23 J.S. Lee, B. Min, K. Cho, S. Kim, J. Park, Y.T. Lee, N.S. Kim, M.S. Lee, S.O. Park and J.T. Moon, Al₂O₃ nanotubes and nanorods fabricated by coating and filling of carbon nanotubes with atomic-layer deposition, *J. Cryst. Growth*, 2003, **254**, 443–448.
- 24 W. Cai, Y. Hu, J. Chen, G. Zhang and T. Xia, Synthesis of nanorod-like mesoporous γ -Al₂O₃ with enhanced affinity towards Congo red removal: Effects of anions and structure-directing agents, *CrystEngComm*, 2012, **14**, 972–977.

- 25 G. Busca, The surface of transitional aluminas: A critical review, *Catal. Today*, 2014, **226**, 2–13.
- 26 W. Brostow and T. Datashvili, Chemical Modification and Characterization of Boehmite Particles, *Chem. Chem. Technol.*, 2008, **2**, 27–32.
- 27 A. Boumaza, L. Favaro, J. Lédion, G. Sattonnay, J.B. Brubach, P. Berthet, A.M. Huntz, P. Roy and R. Tétot, Transition alumina phases induced by heat treatment of boehmite: An X-ray diffraction and infrared spectroscopy study, *J. Solid State Chem.*, 2009, **182**, 1171–1176.
- 28 S.J. Wilson, The dehydration of boehmite, γ -AlOOH, to γ -Al₂O₃, *J. Solid State Chem.*, 1979, **30**, 247–255.
- 29 J. Lee, H. Jeon, D.G. Oh, J. Szanyi and J.H. Kwak, Morphology-dependent phase transformation of γ -Al₂O₃, *Appl. Catal. A Gen.*, 2015, **500**, 58–68.
- 30 B. Kasprzyk-Hordern, Chemistry of alumina, reactions in aqueous solution and its application in water treatment, *Adv. Colloid Interfac.*, 2004, **110**, 19–48.
- 31 X.Y. Chen, H.S. Huh and S.W. Lee, Hydrothermal synthesis of boehmite (γ -AlOOH) nanoplatelets and nanowires: pH-controlled morphologies, *Nanotechnology*, 2007, **18**, 285608–285612.
- 32 M. Trueba and S.P. Trasatti, γ -Alumina as a Support for Catalysts: A Review of Fundamental Aspects, *Eur. J. Inorg. Chem.*, 2005, **2005**, 3393–3403.
- 33 X. Krokidis, P. Raybaud, A.-E. Gobichon, B. Rebours, P. Euzen and H. Toulhoat, Theoretical Study of the Dehydration Process of Boehmite to γ -Alumina, *J. Phys. Chem. B*, 2001, **105**, 5121–5130.
- 34 L. Qu, C. He, Y. Yang, Y. He and Z. Liu, Hydrothermal synthesis of alumina nanotubes templated by anionic surfactant, *Mater. Lett.*, 2005, **59**, 4034–4037.
- 35 L. Torrente-Murciano, A. Gilbank, B. Puertolas, T. Garcia, B. Solsona and D. Chadwick, Shape-dependency activity of nanostructured CeO₂ in the total oxidation of polycyclic aromatic hydrocarbons, *Appl. Catal. B Environ.*, 2013, **132–133**, 116–122.
- 36 L. Torrente-Murciano, A.A. Lapkin and D. Chadwick, Synthesis of high aspect ratio titanate nanotubes, *J. Mater. Chem.*, 2010, **20**, 6484–6489.
- 37 M. de Beer, A. Kunene, D. Nabaho, M. Claeys and E. van Steen, Technical and

- economic aspects of promotion of cobalt-based Fischer-Tropsch catalysts by noble metals – a review, *J. South. African Inst. Min. Metall.*, 2014, **114**, 157–165.
- 38 S.C. Shen, Q. Chen, P.S. Chow, G.H. Tan, X.T. Zeng, Z. Wang and R. B.H. Tan, Steam-Assisted Solid Wet-Gel Synthesis of High-Quality Nanorods of Boehmite and Alumina, *J. Phys. Chem. C*, 2006, **111**, 700–707.
- 39 J.-C. Gabriel and P. Davidson, in *Top Curr. Chem.*, ed. M. Antonietti, Springer Berlin Heidelberg, 2003, vol. 226, pp. 119–172.
- 40 X.Y. Chen, Z.J. Zhang, X.L. Li and S.W. Lee, Controlled hydrothermal synthesis of colloidal boehmite (γ -AlOOH) nanorods and nanoflakes and their conversion into γ -Al₂O₃ nanocrystals, *Solid State Commun.*, 2008, **145**, 368–373.
- 41 Z. Wang, H. Du, J. Gong, S. Yang, J. Ma and J. Xu, Facile synthesis of hierarchical flower-like γ -AlOOH films via hydrothermal route on quartz surface, *Colloid. Surface. A.*, 2014, **450**, 76–82.
- 42 M. Digne, P. Sautet, P. Raybaud, P. Euzen and H. Toulhoat, Use of DFT to achieve a rational understanding of acid–basic properties of γ -alumina surfaces, *J. Catal.*, 2004, **226**, 54–68.
- 43 Y. Li and W.J. Shen, Morphology-dependent nanocatalysts: Rod-shaped oxides, *Chem. Soc. Rev.*, 2014, **43**, 1543–1574.
- 44 J. Bugosh, Colloidal Alumina—The Chemistry and Morphology of Colloidal Boehmite, *J. Phys. Chem.*, 1961, **65**, 1789–1793.
- 45 T. He, L. Xiang and S. Zhu, Hydrothermal Preparation of Boehmite Nanorods by Selective Adsorption of Sulfate, *Langmuir*, 2008, **24**, 8284–8289.
- 46 T. He, L. Xiang and S. Zhu, Different nanostructures of boehmite fabricated by hydrothermal process: effects of pH and anions, *CrystEngComm*, 2009, **11**, 1338–1342.
- 47 F.A. Dar, A.H. Sofi and M.A. Shah, Boehmite (AlOOH) nanostrips and their growth mechanism, *Int Nano Lett*, 2015, **5**, 67–70.
- 48 H. Hou, Y. Xie, Q. Yang, Q. Guo and C. Tan, Preparation and Characterization of γ -AlOOH Nanotubes and Nanorods, *Nanotechnology*, 2005, **16**, 741–745.
- 49 P. Pardo, N. Montoya and J. Alarcon, Tuning the size and shape of nano-boehmites by a free-additive hydrothermal method, *CrystEngComm*, 2015, **17**, 2091–2100.

- 50 J. Wang, K. Shang, Y. Guo and W.-C. Li, Easy hydrothermal synthesis of external mesoporous γ -Al₂O₃ nanorods as excellent supports for Au nanoparticles in CO oxidation, *Microporous Mesoporous Mater.*, 2013, **181**, 141–145.
- 51 S. Ghosh, R. Das and M.K. Naskar, Morphologically Tuned Aluminum Hydrous Oxides and Their Calcined Products, *J. Am. Ceram. Soc.*, 2016, **99**, 2273–2282.
- 52 Z. Lendzion-Bielun, U. Narkiewicz and W. Arabczyk, Cobalt-based Catalysts for Ammonia Decomposition, *Materials (Basel)*, 2013, **6**, 2400–2409.
- 53 G. Jacobs, Y. Ji, B.H. Davis, D. Cronauer, A.J. Kropf and C. L. Marshall, Fischer–Tropsch synthesis: Temperature programmed EXAFS/XANES investigation of the influence of support type, cobalt loading, and noble metal promoter addition to the reduction behavior of cobalt oxide particles, *Appl. Catal. A Gen.*, 2007, **333**, 177–191.
- 54 C. Lancelot, V.V. Ordonsky, O. Stéphan, M. Sadeqzadeh, H. Karaca, M. Lacroix, D. Curulla-Ferré, F. Luck, P. Fongarland, A. Griboval-Constant and A.Y. Khodakov, Direct Evidence of Surface Oxidation of Cobalt Nanoparticles in Alumina-Supported Catalysts for Fischer–Tropsch Synthesis, *ACS Catal.*, 2014, 4510–4515.
- 55 H. Zhang, Y.A. Alhamed, A. Al-Zahrani, M. Daous, H. Inokawa, Y. Kojima and L.A. Petrov, Tuning catalytic performances of cobalt catalysts for clean hydrogen generation via variation of the type of carbon support and catalyst post-treatment temperature, *Int. J. Hydrogen Energy*, 2014, **39**, 17573–17582.
- 56 O.O. James and S. Maity, Temperature programme reduction (TPR) studies of cobalt phases in γ -alumina supported cobalt catalysts, *J. Pet. Technol. Altern. Fuels*, 2016, **7**, 1–12.
- 57 S. Podila, Y.A. Alhamed, A.A. AlZahrani and L.A. Petrov, Hydrogen production by ammonia decomposition using Co catalyst supported on Mg mixed oxide systems, *Int. J. Hydrogen Energy*, 2015, **40**, 15411–15422.
- 58 R.-J. Wu, J.-G. Wu, T.-K. Tsai and C.-T. Yeh, Use of cobalt oxide CoOOH in a carbon monoxide sensor operating at low temperatures, *Sensors Actuators B Chem.*, 2006, **120**, 104–109.
- 59 D.J. Moodley, A.M. Saib, J. van de Loosdrecht, C.A. Welker-Nieuwoudt, B.H. Sigwebela and J.W. Niemantsverdriet, The impact of cobalt aluminate formation on the deactivation of cobalt-based Fischer–Tropsch synthesis catalysts, *Catal. Today*, 2011, **171**, 192–200.

- 60 G. Jacobs, W. Ma and B. Davis, Influence of Reduction Promoters on Stability of Cobalt/ γ -Alumina Fischer-Tropsch Synthesis Catalysts, *Catalysts*, 2014, **4**, 49–76.
- 61 S.F. Yin, B.Q. Xu, X.P. Zhou and C.T. Au, A mini-review on ammonia decomposition catalysts for on-site generation of hydrogen for fuel cell applications, *Appl. Catal. A Gen.*, 2004, **277**, 1–9.
- 62 A. Hill and L. Torrente Murciano, In-situ H₂ production via low temperature decomposition of ammonia: insights into the role of cesium as a promoter, *Int. J. Hydrogen Energy*, 2014, **39**, 7646–7654.
- 63 R. Lan, J.T.S. Irvine and S. Tao, Ammonia and related chemicals as potential indirect hydrogen storage materials, *Int. J. Hydrogen Energy*, 2012, **37**, 1482–1494.
- 64 A. Klerke, C.H. Christensen, J.K. Nørskov and T. Vegge, Ammonia for hydrogen storage: challenges and opportunities, *J. Mater. Chem.*, 2008, **18**, 2304.
- 65 F. Schüth, R. Palkovits, R. Schlögl and D.S. Su, Ammonia as a possible element in an energy infrastructure: catalysts for ammonia decomposition, *Energy Environ. Sci.*, 2012, **5**, 6278–6289.
- 66 S. Satyapal, J. Petrovic, C. Read, G. Thomas and G. Ordaz, The U.S. Department of Energy's National Hydrogen Storage Project: Progress towards meeting hydrogen-powered vehicle requirements, *Catal. Today*, 2007, **120**, 246–256.
- 67 A. Wojcik, H. Middleton, I. Damopoulos and J. Van Herle, Ammonia as a fuel in solid oxide fuel cells, *J. Power Sources*, 2003, **118**, 342–348.
- 68 C. Zamfirescu and I. Dincer, Ammonia as a green fuel and hydrogen source for vehicular applications, *Fuel Process. Technol.*, 2009, **90**, 729–737.
- 69 L. Green, An ammonia energy vector for the hydrogen economy, *Int. J. Hydrogen Energy*, 1982, **7**, 355–359.
- 70 M. Feyen, C. Weidenthaler, R. Güttel, K. Schlichte, U. Holle, A.-H. Lu and F. Schüth, High-temperature stable, iron-based core-shell catalysts for ammonia decomposition., *Chemistry*, 2011, **17**, 598–605.
- 71 A.K. Hill and L. Torrente-Murciano, Low temperature H₂ production from ammonia using ruthenium-based catalysts: Synergetic effect of promoter and support, *Appl. Catal. B Environ.*, 2015, **172-173**, 129–135.

- 72 S. Mukherjee, S.V. Devaguptapu, A. Sviripa, C.R.F. Lund and G. Wu, Low-temperature ammonia decomposition catalysts for hydrogen generation, *Appl. Catal. B Environ.*, 2018, **226**, 162–181.
- 73 J.C. Ganley, F.S. Thomas, E.G. Seebauer and R.I. Masel, A Priori Catalytic Activity Correlations: The Difficult Case of Hydrogen Production from Ammonia, *Catal. Letters*, 2004, **96**, 117–122.
- 74 D.A. Hansgen, D.G. Vlachos and J.G. Chen, Using first principles to predict bimetallic catalysts for the ammonia decomposition reaction, *Nat Chem*, 2010, **2**, 484–489.
- 75 L. Wang, Y. Zhao, C. Liu, W. Gong and H. Guo, Plasma driven ammonia decomposition on a Fe-catalyst: eliminating surface nitrogen poisoning., *Chem. Commun.*, 2013, **49**, 3787–9.
- 76 M. Appl, *Ullmann's Encyclopedia of Industrial Chemistry*, Wiley-VCH Verlag GmbH & Co, Weinheim, Germany, 2000.
- 77 L. Yao, Y. Li, J. Zhao, W. Ji and C. Au, Core-shell structured nanoparticles (M@ SiO₂, Al₂O₃, MgO; M= Fe, Co, Ni, Ru) and their application in CO_x-free H₂ production via NH₃ decomposition, *Catal. Today*, 2010, **158**, 401–408.
- 78 D. Varisli and N.G. Kaykac, CO_x free hydrogen production over cobalt incorporated silicate structured mesoporous catalysts, *Appl. Catal. B Environ.*, 2012, **127**, 389–398.
- 79 D. Varisli and N.G. Kaykac, Hydrogen from ammonia over cobalt incorporated silicate structured catalysts prepared using different cobalt salts, *Int. J. Hydrogen Energy*, 2016, **41**, 5955–5968.
- 80 Y.-Q. Gu, Z. Jin, H. Zhang, R.-J. Xu, M.-J. Zheng, Y.-M. Guo, Q.-S. Song and C.-J. Jia, Transition metal nanoparticles dispersed in an alumina matrix as active and stable catalysts for CO_x-free hydrogen production from ammonia, *J. Mater. Chem. A*, 2015, **3**, 17172–17180.
- 81 H. Zhang, Y.A. Alhamed, Y. Kojima, A.A. Al-Zahrani and L.A. Petrov, Cobalt supported on carbon nanotubes. An efficient catalyst for ammonia decomposition, *Comptes Rendus L'Academie Bulg. des Sci.*, 2013, **66**, 519–524.
- 82 H. Zhang, Y. Alhamed and W. Chu, Controlling Co-support interaction in Co/MWCNTs catalysts and catalytic performance for hydrogen production via NH₃ decomposition, *Appl. Catal. A Gen.*, 2013, **464-465**, 156–164.

- 83 Ł. Czekajlo and Z. Lendzion-Bielun, Effect of preparation conditions and promoters on the structure and activity of the ammonia decomposition reaction catalyst based on nanocrystalline cobalt, *Chem. Eng. J.*, 2016, **289**, 254–260.
- 84 L. Li, R. Jiang, W. Chu, H. Cang, H. Chena and J. Yan, Cobalt nanoparticles embedded in a porous carbon matrix as an efficient catalyst for ammonia decomposition, *Catal. Sci. Technol.*, 2017, **7**, 1363–1371.
- 85 S. Podila, H. Driss, S.F. Zaman, Y.A. Alhamed, A.A. AlZahrani, M.A. Daous and L.A. Petrov, Hydrogen generation by ammonia decomposition using Co/MgO–La₂O₃ catalyst: Influence of support calcination atmosphere, *J. Mol. Catal. A Chem.*, 2016, **414**, 130–139.
- 86 J. Zhang, M. Comotti and F. Schüth, Commercial Fe-or Co-containing carbon nanotubes as catalysts for NH₃ decomposition, *Chem. Commun.*, 2007, 1916–1918.
- 87 C. Zhao, Y. Yang, Z. Wu, M. Field and X. Fang, Synthesis and facile size control of well-dispersed cobalt nanoparticles supported on ordered mesoporous carbon, *J. Mater. Chem. A*, 2014, **2**, 19903.
- 88 M. Rønning, N. E. Tsakoumis, A. Voronov, R.E. Johnsen, P. Norby, W. van Beek, Ø. Borg, E. Rytter and A. Holmen, Combined {XRD} and {XANES} studies of a Re-promoted Co/γ-Al₂O₃ catalyst at Fischer–Tropsch synthesis conditions, *Catal. Today*, 2010, **155**, 289–295.
- 89 S.K. Beaumont, M. Rønning, Ø. Borg, E. Rytter, A. Holmen, C.J. Brooks, M.A. Marcus, J. Guo, Z. Liu, N. Kruse, G.A. Somorjai, W.F. Pong, J.H. Guo, R. Perez, F. Besenbacher and M. Salmeron, Recent developments in the application of nanomaterials to understanding molecular level processes in cobalt catalysed Fischer–Tropsch synthesis, *Phys. Chem. Chem. Phys.*, 2014, **16**, 5034.
- 90 E. Rytter and A. Holmen, On the support in cobalt Fischer–Tropsch synthesis—Emphasis on alumina and aluminates, *Catal. Today*, 2016, **275**, 11–19.
- 91 A.T. Najafabadi, A.A. Khodadadi, M.J. Parnian and Y. Mortazavi, Atomic layer deposited Co/γ-Al₂O₃ catalyst with enhanced cobalt dispersion and Fischer–Tropsch synthesis activity and selectivity, *Appl. Catal. A Gen.*, 2016, **511**, 31–46.
- 92 G.L. Bezemer, J.H. Bitter, H.P.C.E. Kuipers, H. Oosterbeek, J.E. Holewijn, X. Xu, F. Kapteijn, A.J. van Dillen and K.P. de Jong, Cobalt Particle Size Effects in the Fischer–Tropsch Reaction Studied with Carbon Nanofiber Supported Catalysts, *J. Am. Chem. Soc.*, 2006, **128**, 3956–3964.

- 93 Y. Liu, L. Jia, B. Hou, D. Sun and D. Li, Cobalt aluminate-modified alumina as a carrier for cobalt in Fischer–Tropsch synthesis, *Appl. Catal. A Gen.*, 2017, **530**, 30–36.
- 94 P. van Helden, I.M. Ciobîcă and R.L.J. Coetzer, The size-dependent site composition of FCC cobalt nanocrystals, *Catal. Today*, 2016, **261**, 48–59.
- 95 L.B. László Guzzi, Györgyi Stefler, Zsuzsa Koppány, CO Hydrogenation over Re-Co Bimetallic Catalysts Supported over SiO₂, Al₂O₃ and NaY Zeolite, *React. Kinet. Catal. Lett.*, 2001, **74**, 259–269.
- 96 K. Shimura, T. Miyazawa, T. Hanaoka and S. Hirata, Fischer–Tropsch synthesis over alumina supported cobalt catalyst: Effect of promoter addition, *Appl. Catal. A Gen.*, 2015, **494**, 1–11.
- 97 G. Jacobs, W. Ma, P. Gao, B. Todic, T. Bhatelia, D.B. Bukur and B.H. Davis, The application of synchrotron methods in characterizing iron and cobalt Fischer–Tropsch synthesis catalysts, *Catal. Today*, 2013, **214**, 100–139.
- 98 N.E. Tsakoumis, M. Rønning, Ø. Borg, E. Rytter and A. Holmen, Deactivation of cobalt based Fischer–Tropsch catalysts: A review, *Catal. Today*, 2010, **154**, 162–182.
- 99 J. van de Loosdrecht, M. van der Haar, A.M. van der Kraan, A.J. van Dillen and J.W. Geus, Preparation and properties of supported cobalt catalysts for Fischer–Tropsch synthesis, *Appl. Catal. A Gen.*, 1997, **150**, 365–376.
- 100 C. Liu, Y. Zhang, Y. Zhao, L. Wei, J. Hong, L. Wang, S. Chen, G. Wang, J. Li, A. Griboval-Constant and A. Y. Khodakov, The effect of the nanofibrous Al₂O₃ aspect ratio on Fischer–Tropsch synthesis over cobalt catalysts, *Nanoscale*, 2017, **9**, 570–581.
- 101 M. Minnermann, H.K. Grossmann, S. Pokhrel, K. Thiel, H. Hagelin-Weaver, M. Bäumer and L. Mädler, Double flame spray pyrolysis as a novel technique to synthesize alumina-supported cobalt Fischer–Tropsch catalysts, *Catal. Today*, 2013, **214**, 90–99.
- 102 A. Voronov, N.E. Tsakoumis, N. Hammer, W. van Beek, H. Emerich and M. Rønning, The state and location of Re in Co–Re/Al₂O₃ catalysts during Fischer–Tropsch synthesis: Exploring high-energy XAFS for in situ catalysts characterisation, *Catal. Today*, 2014, **229**, 23–33.
- 103 M. Haruta, Nanoparticulate Gold Catalysts for Low-Temperature CO Oxidation, *J. New. Mat. Electrochem. Syst.*, 2004, **7**, 163–172.
- 104 N.F.P. Ribeiro, F.M.T. Mendes, C.A.C. Perez, M.M.V.M. Souza and M. Schmal,

- Selective CO oxidation with nano gold particles-based catalysts over Al₂O₃ and ZrO₂, *Appl. Catal. A Gen.*, 2008, **347**, 62–71.
- 105 M. Haruta, T. Kobayashi, H. Sano and N. Yamada, Novel gold catalysts for the oxidation of carbon monoxide at a temperature far below 0 °C., *Chem. Lett.*, 1987, **16**, 405–408.
- 106 D.-Q. Han, C.-Q. Zhou, H.-M. Yin, D.-J. Zhang and X.-H. Xu, Reactivity of the Alkaline Pretreated Nanoporous Gold for the CO Oxidation, *Catal. Letters*, 2011, **141**, 1026–1031.
- 107 L. Liotta, New Trends in Gold Catalysts, *Catalysts*, 2014, **4**, 299–304.
- 108 J. Saavedra, C. J. Pursell and B.D. Chandler, CO Oxidation Kinetics over Au/TiO₂ and Au/Al₂O₃ Catalysts: Evidence for a Common Water-Assisted Mechanism, *J. Am. Chem. Soc.*, 2018, **140**, 3712–3723.
- 109 A.-Q. Wang, C.-M. Chang and C.-Y. Mou, Evolution of Catalytic Activity of Au–Ag Bimetallic Nanoparticles on Mesoporous Support for CO Oxidation, *J. Phys. Chem. B*, 2005, **109**, 18860–18867.
- 110 L. Delannoy, R.L. Chantry, S. Casale, Z.Y. Li, Y. Borensztein and C. Louis, HRTEM and STEM-HAADF characterisation of Au–TiO₂ and Au–Al₂O₃ catalysts for a better understanding of the parameters influencing their properties in CO oxidation, *Phys. Chem. Chem. Phys.*, 2013, **15**, 3473–3479.
- 111 J.-X. Liu, I.A.W. Filot, Y. Su, B. Zijlstra and E.J.M. Hensen, Optimum Particle Size for Gold-Catalyzed CO Oxidation, *J. Phys. Chem. C*, 2018, **122**, 8327–8340.
- 112 G.C. Bond and D.T. Thompson, Catalysis by Gold, *Catal. Rev.*, 1999, **41**, 319–388.
- 113 Q. Xu, K.C.C. Kharas and A.K. Datye, The Preparation of Highly Dispersed Au/Al₂O₃ by Aqueous Impregnation, *Catal. Letters*, 2003, **85**, 229–235.
- 114 S. Ivanova, C. Petit and V. Pitchon, A new preparation method for the formation of gold nanoparticles on an oxide support, *Appl. Catal., A*, 2004, **267**, 191–201.
- 115 S. Ivanova, V. Pitchon, C. Petit, H. Herschbach, A. Van Dorsselaer and E. Leize, Preparation of alumina supported gold catalysts: Gold complexes genesis, identification and speciation by mass spectrometry, *Appl. Catal. A Gen.*, 2006, **298**, 203–210.
- 116 A.I. Kozlov, A.P. Kozlova, H. Liu and Y. Iwasawa, A new approach to active supported Au catalysts, *Appl. Catal. A Gen.*, 1999, **182**, 9–28.

- 117 M. Okumura, S. Nakamura, S. Tsubota, T. Nakamura, M. Azuma and M. Haruta, Chemical vapor deposition of gold on Al₂O₃, SiO₂, and TiO₂ for the oxidation of CO and of H₂, *Catal. Letters*, 1998, **51**, 53–58.
- 118 S. Ivanova, C. Petit and V. Pitchon, Application of alumina supported gold-based catalysts in total oxidation of CO and light hydrocarbons mixture, *Catal. Today*, 2006, **113**, 182–186.
- 119 S. Ivanova, V. Pitchon and C. Petit, Application of the direct exchange method in the preparation of gold catalysts supported on different oxide materials, *J. Mol. Catal. A Chem.*, 2006, **256**, 278–283.
- 120 J. Wang, A.-H. Lu, M. Li, W. Zhang, Y.-S. Chen, D.-X. Tian and W.-C. Li, Thin Porous Alumina Sheets as Supports for Stabilizing Gold Nanoparticles, *ACS Nano*, 2013, **7**, 4902–4910.
- 121 Y.-X. Miao, L. Shi, L.-N. Cai and W.-C. Li, Alumina hollow microspheres supported gold catalysts for low-temperature CO oxidation: effect of the pretreatment atmospheres on the catalytic activity and stability, *Gold Bull.*, 2014, **47**, 275–282.
- 122 L. Wen, J.-K. Fu, P.-Y. Gu, B.-X. Yao, Z.-H. Lin and J.-Z. Zhou, Monodispersed gold nanoparticles supported on γ -Al₂O₃ for enhancement of low-temperature catalytic oxidation of CO, *Appl. Catal. B Environ.*, 2008, **79**, 402–409.
- 123 C. K. Costello, J. Guzman, J.H. Yang, Y.M. Wang, M.C. Kung, B.C. Gates and H.H. Kung, Activation of Au/ γ -Al₂O₃ Catalysts for CO Oxidation: Characterization by X-ray Absorption Near Edge Structure and Temperature Programmed Reduction, *J. Physiscal Chem. B*, 2004, **108**, 12529–12536.
- 124 J. Guzman and B.C. Gates, Catalysis by supported gold: Correlation between catalytic activity for CO oxidation and oxidation states of gold, *J. Am. Chem. Soc.*, 2004, **126**, 2672–2673.
- 125 P.A. Webb and C. Orr, *Analytical Methods in Fine Particle Technology*, 1st edn., 1997.
- 126 J.L.G. Fierro, J.F.G. De and L. Banda, Chemisorption of Probe Molecules on Metal Oxides Chemisorption of Probe Molecules on Metal Oxides, *Catal. Rev. Sci. Eng.*, 1986, **28**, 265–333.
- 127 L. Torrente-Murciano, The importance of particle-support interaction on particle size determination by gas chemisorption, *J. Nanoparticle Res.*, 2016, **18**, 87.

- 128 R.C. Reuel and C.H. Bartholomew, The stoichiometries of H₂ and CO adsorptions on cobalt: Effects of support and preparation, *J. Catal.*, 1984, **85**, 63–77.
- 129 C.H. Bartholomew and R.C. Reuel, Cobalt-Support Interactions: Their Effects on Adsorption and CO Hydrogenation Activity and Selectivity Properties, *Ind. Eng. Chem. Prod. Res. Dev.*, 1985, **22**, 56–61.
- 130 F.A. Reboredo and G. Galli, Size and Structure Dependence of Carbon Monoxide Chemisorption on Cobalt Clusters, *J. Phys. Chem. B*, 2006, **110**, 7979–7984.
- 131 E. Miyazaki, Chemisorption of diatomic molecules (H₂, N₂, CO) on transition d-metals, *J. Catal.*, 1980, **65**, 84–94.
- 132 B.R. Cuenya and F. Behafarid, Nanocatalysis: size- and shape-dependent chemisorption and catalytic reactivity, *Surf. Sci. Rep.*, 2015, **70**, 135–187.
- 133 J.W. Olesik, Elemental analysis using ICP-OES and ICP/MS, *Anal. Chem.*, 1991, **63**, 12A–21A.
- 134 J.F. Watts and J. Wolstenholme, *An Introduction to Surface Analysis by XPS and AES*, John Wiley & Sons, Ltd, Chichester, UK, 2003.
- 135 A. Hill, University of Bath, 2014, *PhD Thesis*.
- 136 K. Snavely and B. Subramaniam, Thermal conductivity detector analysis of hydrogen using helium carrier gas and Hayesep® D columns, *J. Chromatogr. Sci.*, 1998, **36**, 191–196.
- 137 S. Bi, C. Wang, Q. Cao and C. Zhang, Studies on the mechanism of hydrolysis and polymerization of aluminum salts in aqueous solution: correlations between the ‘Core-links’ model and ‘Cage-like’ Keggin-Al₁₃ model, *Coord. Chem. Rev.*, 2004, **248**, 441–455.
- 138 G. Fu, L.F. Nazar and A.D. Bain, Aging processes of alumina sol-gels: characterization of new aluminum polyoxycations by aluminum-27 NMR spectroscopy, *Chem. Mater.*, 1991, **3**, 602–610.
- 139 S.M. Bradley, R.A. Kydd and R.F. Howe, The Structure of Al Gels Formed through the Base Hydrolysis of Al³⁺ Aqueous Solutions, *J. Colloid Interface Sci.*, 1993, **159**, 405–412.

- 140 C. V. Ruiz Madroñero and J. E. Rodríguez Paéz, Sodium aluminates obtained from the $\text{Al}(\text{NO}_3)_3 \cdot 9\text{H}_2\text{O}$ - NaOH system using the controlled precipitation method, *Ing. e Investig.*, 2010, **30**, 16–24.
- 141 H. Zhao, H. Liu and J. Qu, Effect of pH on the aluminum salts hydrolysis during coagulation process: Formation and decomposition of polymeric aluminum species, *J. Colloid Interface Sci.*, 2009, **330**, 105–112.
- 142 G. Furrer, C. Ludwig and P. W. Schindler, On the chemistry of the Keggin Al_{13} polymer, *J. Colloid Interface Sci.*, 1992, **149**, 56–67.
- 143 R.J.M.J. Vogels, J.T. Kloprogge, P.A. Buining, D. Seykens, J.B.H. Jansen and J.W. Geus, The tridecameric aluminum complex as an appropriate precursor for fibrous boehmite: A ^{27}Al NMR study on the partial hydrolysis of aluminum sec-butoxide, *J. Non. Cryst. Solids*, 1995, **191**, 38–44.
- 144 J.F. Keggin, Structure of the Molecule of 12-Phosphotungstic Acid, *Nature*, 1933, **131**, 908–909.
- 145 J.T. Kloprogge, D. Seykens, J.B.H. Jansen and J.W. Geus, A ^{27}Al nuclear magnetic resonance study on the optimization of the development of the Al_{13} polymer, *J. Non. Cryst. Solids*, 1992, **142**, 94–102.
- 146 X. Xu, Y. Liu, Z. Li, Z. Lv, J. Song, M. He, Q. Wang, L. Yan and Z. Li, Thermal study of boehmite nanofibers with controlled particle size, *J. Therm. Anal. Calorim.*, 2014, **115**, 1111–1117.
- 147 M.-G. Ma, Y.-J. Zhu and Z.-L. Xu, A new route to synthesis of γ -alumina nanorods, *Mater. Lett.*, 2007, **61**, 1812–1815.
- 148 M. Thommes, Characterization of nanoporous materials, *Chemie Ing. Tech.*, 2010, **82**, 1059–1073.
- 149 L. Zhang, X. Jiao, D. Chen and M. Jiao, γ - AlOOH Nanomaterials with Regular Shapes: Hydrothermal Fabrication and $\text{Cr}_2\text{O}_7^{2-}$ Adsorption, *Eur. J. Inorg. Chem.*, 2011, **2011**, 5258–5264.
- 150 J. Ge, K. Deng, W. Cai, J. Yu, X. Liu and J. Zhou, Effect of structure-directing agents on facile hydrothermal preparation of hierarchical γ - Al_2O_3 and their adsorption performance toward Cr (VI) and CO_2 , *J. Colloid Interface Sci.*, 2013, **401**, 34–39.
- 151 H.Y. Zhu, X.P. Gao, D.Y. Song, S.P. Ringer, Y.X. Xi and R.L. Frost, Manipulating the

- size and morphology of aluminum hydrous oxide nanoparticles by soft-chemistry approaches, *Micropor. Mesopor. Mat.*, 2005, **85**, 226–233.
- 152 J.A. Kaduk and S. Pei, The Crystal Structure of Hydrated Sodium Aluminate, $\text{NaAlO}_2 \cdot 5/4\text{H}_2\text{O}$, and Its Dehydration Product, *J. Solid State Chem.*, 1995, **115**, 126–139.
- 153 L. Torrente-Murciano, A.K. Hill and T.E. Bell, Ammonia decomposition over cobalt/carbon catalysts—Effect of carbon support and electron donating promoter on activity, *Catal. Today*, 2017, **286**, 131–140.
- 154 P.H. Bolt, F.H.P.M. Habraken and J.W. Geus, Formation of Nickel, Cobalt, Copper, and Iron Aluminates from α - and γ -Alumina-Supported Oxides: A Comparative Study, *J. Solid State Chem.*, 1998, **135**, 59–69.
- 155 JCPDS Associateship, New X-Ray Powder Diffraction Patterns from the JCPDS Associateship, *Powder Diffr.*, 1986, **1**, 77–99.
- 156 D.R. Baer, D.J. Gaspar, P. Nachimuthu, S.D. Techane and D.G. Castner, Application of surface chemical analysis tools for characterization of nanoparticles., *Anal. Bioanal. Chem.*, 2010, **396**, 983–1002.
- 157 M.C. Biesinger, B.P. Payne, A.P. Grosvenor, L.W.M. Lau, A.R. Gerson and R.S.C. Smart, Resolving surface chemical states in XPS analysis of first row transition metals, oxides and hydroxides: Cr, Mn, Fe, Co and Ni, *Appl. Surf. Sci.*, 2011, **257**, 2717–2730.
- 158 J. Yang, H. Cheng and R. L. Frost, Synthesis and characterisation of cobalt hydroxy carbonate $\text{Co}_2\text{CO}_3(\text{OH})_2$ nanomaterials, *Spectrochim. Acta Part A Mol. Biomol. Spectrosc.*, 2011, **78**, 420–428.
- 159 J.D. Donaldson, D. Beyersmann, J.D. Donaldson and D. Beyersmann, in *Ullmann's Encyclopedia of Industrial Chemistry*, Wiley-VCH Verlag GmbH & Co. KGaA, Weinheim, Germany, 2005.
- 160 M. Haruta, Low-Temperature Oxidation of CO over Gold Supported on TiO_2 , $\alpha\text{-Fe}_2\text{O}_3$, and Co_3O_4 , *J. Catal.*, 1993, **144**, 175–192.
- 161 T.E. Bell and L. Torrente-Murciano, H_2 Production via Ammonia Decomposition Using Non-Noble Metal Catalysts: A Review, *Top. Catal.*, 2016, **59**, 1438–1457.
- 162 Z. Kowalczyk, J. Sentek, S. Jodzis, M. Muhler and O. Hinrichsen, Effect of Potassium on the Kinetics of Ammonia Synthesis and Decomposition over Fused Iron Catalyst at

- Atmospheric Pressure, *J. Catal.*, 1997, **169**, 407–414.
- 163 F.R. García-García, A. Guerrero-Ruiz, I. Rodríguez-Ramos, A. Goguet, S.O. Shekhtman and C. Hardacre, TAP studies of ammonia decomposition over Ru and Ir catalysts, *Phys. Chem. Chem. Phys.*, 2011, **13**, 12892.
- 164 M. Digne, P. Sautet, P. Raybaud, P. Euzen and H. Toulhoat, Hydroxyl Groups on γ -Alumina Surfaces: A DFT Study, *J. Catal.*, 2002, **211**, 1–5.
- 165 Ø. Borg, S. Eri, E.A. Blekkan, S. Storsæter, H. Wigum, E. Rytter and A. Holmen, Fischer–Tropsch synthesis over γ -alumina-supported cobalt catalysts: Effect of support variables, *J. Catal.*, 2007, **248**, 89–100.
- 166 X. Xie, Y. Li, Z.-Q. Liu, M. Haruta and W. Shen, Low-temperature oxidation of CO catalysed by Co_3O_4 nanorods, *Nature*, 2009, **458**, 746–9.